

Copyright

by

Kyana Yvette Garza

2021

**The Dissertation Committee for Kyana Yvette Garza Certifies that this is the approved version of the following Dissertation:**

**Molecular Characterization of Biological Samples by Ambient Ionization Mass Spectrometry to Advance Clinical Assessment of Human Disease**

**Committee:**

Livia Schiavinato Eberlin, Supervisor

Jennifer S. Brodbelt

Richard M. Crooks

Alastair Thompson

**Molecular Characterization of Biological Samples by Ambient  
Ionization Mass Spectrometry to Advance Clinical Assessment of  
Human Disease**

**by**

**Kyana Yvette Garza**

**Dissertation**

Presented to the Faculty of the Graduate School of

The University of Texas at Austin

in Partial Fulfillment

of the Requirements

for the Degree of

**Doctor of Philosophy**

**The University of Texas at Austin**

**August 2021**

## **Dedication**

To my family, Leonardo, Yvette, Kalie, Chris, and Gabby.

## **Acknowledgements**

There are many people that deserve recognition for supporting me throughout this journey to obtain my PhD. First, thank you to my incredible parents, Leonardo and Yvette, for their unconditional and endless love and support throughout these last five years. The both of you have selflessly dedicated your life to your family, and for that, I will forever be indebted to you. Mom, I am constantly in awe of everything you do. Thank you for continuously applauding my achievements and being there for me when I need you. Dad, your determination, work ethic, and strong mentality serve as an inspiration to me every day. You constantly challenge me to be the best at what I do and encourage me to keep my head up when things get tough. I am eternally grateful to the both of you for everything you have done for me, and I love you dearly. I feel honored my past and future scientific contributions will bare both of your names. Kalie, Chris, and Gabby, I could have not asked for better siblings. The three of you are my best friends, and I feel so blessed to have you in my life. I could not have achieved this milestone without you. Thank you for constantly supporting me in all my decisions. To my niece and nephews, Moriah, Aaron, and Eli, you are absolute joy to be around, time spent with you has helped relieve the stress of graduate school. I look forward to watching the three of you continue to grow and learn. Thank you all for your love, support, and guidance. I love you, and this degree is as much mine as it is yours.

To my advisor, Professor Livia S. Eberlin, thank you for all that you have done for me these last five years. I think back to when I first joined your lab and realize how much I have grown, in large part to you. You have constantly challenged me to think critically, be proactive, and to work hard, and I am forever grateful to you for pushing me to be a better scientist. I admire your dedication and commitment to both your work and your

family, and I hope to find and imitate that balance in my life. I cannot express how thankful I am for the opportunities you have given me and your guidance and support while navigating graduate school. To my committee members, Dr. Jennifer Brodbelt, Dr. Richard Crooks, and Dr. Alastair Thompson, thank you for your time and support throughout my PhD.

To the past and current members of Eberlin Lab, seeing, working, talking with you all kept me sane during my PhD journey. Rachel and Alena, both of you have continuously supported me throughout these last five years, and I am so appreciative of both of you. We have made so many memories together from Plano Pedro to our own fifth year happy hours, and although I will miss seeing you, I am grateful that we got to share our graduate school experience together. I'm so proud of you. To Clara and Marta, thank you for everything you have taught me and taking me under your wings when I first joined the lab. I have no doubt that the both of you will have successful careers, and I can't wait to hear about them. To Mary, Anna, and Abby, I have watched the three of you grow so much and really come into your own. You should be proud of what you have accomplished thus far, and although it might not feel like it, there is a light at the end of the tunnel. I will miss the fun that you three brought to our group. Mike, Sydney, and Monica, I have enjoyed watching the three of you forge your own path and make your mark on the lab. It's remarkable how independent you've become in three short years. I'm so glad I got to work with you three, and I wish you the very best in your last few years. To Meredith and Charlie, you have started off graduate school so strong. I know you both have a bright future ahead of you, regardless of the career path you choose. To Jialing, thank you for having the patience to work with me as a first year. You taught me so much about mass spectrometry and working with you was an invaluable experience. Sunil, you were such a great addition to the lab. You are so knowledgeable, and I wish I would have been able to work more with you. To

our past a current undergraduates, John, Shirley, Isabel, Praj, Ashish, and Iñaki, you are such an important part of the lab and all your effort does not go unnoticed. I am so appreciative of all your hard work, and best of luck in the future. I am so fortunate to have met each and every one of you. You are now some of my closest friends and were the best coworkers. Thank you for being my family away from family.

To my great collaborators, thank you for your dedication, resources, time, and support. To those at Baylor College of Medicine, Dr. James Suliburk, Dr. Chandandeep Nagi, Dr. Stacey Carter, Dr. Alastair Thompson, and Dr. Elizabeth Bonefas, working with you all has been one of the best experiences. Your dedication and contribution to our projects has been invaluable. To one of my frequent collaborators in Brazil, Dr. Andreia Porcari, thank you for all your time and effort on our joint projects. It has been an absolute pleasure working with and learning from you. To the collaborators within the University of Texas including Dr. Jennifer Brodbelt and Dr. Dustin Klein, thank you for wisdom, help, and support. I have learned so much from working with the both of you.

I would like to express my sincerest gratitude to Department of Chemistry, the College of Natural Science, and the Graduate school for the several fellowships that have supported me over the last five years. I would also like to thank the funding agencies, the National Institute of Health, the National Cancer Institute, and the Welch Foundation, for their financial support throughout the last five years.

To Josh Pender, who has become one of my best friends during my stay at UT. Your support throughout the four years we have known each other has made this process a lot easier. Thank you for always being there when I needed you.

Thank you once again to everyone who has supported and helped me on this journey toward my PhD. It means more than I can express.

## **Abstract**

# **Molecular Characterization of Biological Samples by Ambient Ionization Mass Spectrometry to Advance Clinical Assessment of Human Disease**

Kyana Yvette Garza, Ph.D.

The University of Texas at Austin, 2021

Supervisor: Livia Schiavinato Eberlin

Ambient ionization mass spectrometry (MS) approaches have revolutionized the way diagnostic molecular information can be obtained from biological and clinical samples, requiring minimal to no sample pretreatment, being operationally simple, and most importantly, providing near real time assessment of molecular information directly from biospecimens. Ambient ionization approaches have been widely applied to various clinical applications including screening of inborn errors of metabolism, therapeutic drug monitoring, and disease diagnosis and subtyping, with the goal of evaluating their use for addressing complex challenges in human health. Desorption electrospray ionization (DESI) MS is the most extensively used ambient ionization method for the investigation of molecular changes in tissue biospecimens, showing great potential for providing complimentary information to routine histopathology. Since its inception, a variety of other ambient ionization MS methods have been developed, with newer techniques, such as the MasSpec Pen, envisioned for the intraoperative analysis of *in vivo* and *ex vivo* tissue specimen during surgery. This dissertation describes the development and application of

ambient ionization MS methods for the investigation of various human diseases. Chapter 2 provides discussion on the robustness of DESI-MS for breast cancer tissue section evaluation and receptor status determination in a multi-center study, providing evidence of its potential use to compliment routine histopathological assessment. Chapter 3 describes the optimization of DESI-MS to expand the molecular information obtained from a single tissue section, demonstrating for the first time the detection of proteins directly from tissue sections by DESI-MS. Chapters 4 and 5 discuss the clinical translation of the MasSpec Pen into an operating room for feasibility testing as well as the evaluation of the technology for improving intraoperative surgical margin evaluation during breast cancer surgeries. Lastly, Chapter 6 discusses the modification of the MasSpec Pen to better analyze clinical nasal swabs and its application toward screening of COVID-19 disease using lipid information.

## Table of Contents

List of Tables .....	xvi
List of Figures .....	xviii
List of Illustrations .....	xxiii
Chapter 1: Introduction .....	1
Current Mass Spectrometry based technologies used in the clinical lab .....	1
Ambient ionization mass spectrometry and its potential to be used in a clinical setting .....	2
Research Objectives .....	7
Evaluating the robustness of DESI-MS imaging for breast cancer diagnosis .....	8
Integrating ion mobility into the DESI-MS imaging workflow to expand molecular coverage .....	9
Clinical translation of the MasSpec Pen into the operating room .....	10
Application of the MasSpec Pen for breast cancer tissue evaluation .....	11
Screening of COVID-19 using the MasSpec Pen system .....	13
References .....	15
Chapter 2: A Multi-Center Study Using Desorption Electrospray Ionization Mass Spectrometry Imaging for Breast Cancer Diagnosis .....	20
Introduction .....	20
Materials and Methods .....	24
Tissue Collection .....	24
Human Breast Tissue .....	25
DESI-MSI .....	27
Histopathology and light microscopy .....	29

Statistical Analysis.....	29
Results.....	30
Molecular imaging of breast tissues by DESI-MSI.....	30
DESI-MSI of breast tissue samples from patients of a different race .....	33
Inter-laboratory assessment of the reproducibility of DESI-MSI.....	36
Predictive models of IDC based on lipid DESI-MSI data .....	37
Intra- and inter-laboratory validation of the predictive power of the Lasso classification model.....	38
Predictive features selected by Lasso .....	40
Prediction of Breast Cancer Hormone Receptor and Her2 Status .....	42
Discussion.....	44
Conclusion .....	49
References.....	50
Chapter 3: Desorption Electrospray Ionization Mass Spectrometry Imaging of Proteins Directly from Biological Tissue Sections.....	56
Introduction.....	56
Materials and Methods.....	59
Tissue samples .....	59
Lipid analysis.....	59
Protein analysis.....	60
S/N calculation.....	60
In tandem DESI-UVPD .....	61
Protein extraction.....	61
Top down UVPD .....	61

Bottom up proteomics.....	63
Results and Discussion .....	63
Optimization of DESI-MS geometric parameters for protein imaging .....	63
FAIMS operation and optimization .....	67
Spray voltage and inlet capillary temperature optimization .....	69
Effect of FAIMS on ions detected .....	69
Identification of detected proteins using top-down and bottom-up proteomics.....	70
DESI-FAIMS-MS imaging of proteins in mouse brain tissue sections.....	73
Multimodal imaging of lipids and proteins in mouse brain tissue sections..	75
DESI-FAIMS-MS imaging of proteins in human normal and cancerous ovarian tissue sections .....	77
DESI-FAIMS-MS imaging of proteins in human normal and cancerous breast tissue sections .....	77
Conclusion .....	80
References.....	82
Chapter 4: Clinical Translation and Evaluation of the MasSpec Pen Technology for Surgical Use .....	86
Introduction.....	86
Methods and Materials.....	88
Chemicals and Reagents .....	88
MasSpec Pen Device and Operation.....	89
Dual path MasSpec Pen Operation .....	89
Mass spectrometry .....	91
Data analysis .....	91

Permissions .....	91
Results.....	92
Design and Translation of the MasSpec Pen System for Surgical Use .....	92
Clinical Use by Surgeons and Surgical Staff.....	96
Molecular Analysis of <i>In Vivo</i> and Freshly Excised Tissues.....	102
Intraoperative Detection of Blood and Exogenous Species.....	109
Discussion.....	110
Conclusion .....	115
References.....	116
Chapter 5: Development of the MasSpec Pen for Rapid Evaluation of Surgical Margins During Breast Conserving Surgeries .....	120
Introduction.....	120
Methods and Materials.....	122
Banked tissue samples .....	122
MasSpec Pen analysis of banked breast tissue samples .....	122
Pathological evaluation of tissue sections .....	123
Intraoperative clinical testing of the MasSpec Pen during breast cancer surgeries.....	123
Statistical analyses .....	124
Results.....	125
Molecular analysis and statistical prediction of banked breast tissue samples.....	125
Intraoperative MasSpec Pen analysis during breast cancer surgeries.....	128
Discussion.....	130
Conclusion .....	135

References.....	136
Chapter 6: Rapid Screening of COVID-19 Disease Directly from Clinical Nasopharyngeal Swabs using the MasSpec Pen Technology.....	140
Introduction.....	140
Methods and Materials.....	144
Chemicals.....	144
Design and fabrication of the adapted MasSpec Pen-ESI system .....	144
Clinical nasopharyngeal swabs .....	145
MasSpec Pen-ESI analysis and data acquisition.....	146
Statistical analysis.....	149
Results.....	150
Design of the MasSpec Pen-ESI System .....	150
Optimization of the MasSpec Pen-ESI system for swab analysis .....	153
Molecular analysis of clinical nasopharyngeal swabs .....	155
Statistical prediction of COVID-19 infection .....	158
Discussion .....	164
Conclusion .....	170
References.....	172
Chapter 7: Conclusions and Perspectives .....	177
References.....	184
Appendices.....	185
Appendix A: Supplementary Material for Chapter 2.....	185
Appendix B: Supplementary Material for Chapter 3.....	189
Appendix C: Supplementary Material for Chapter 4.....	196

Appendix E: Supplementary Material for Chapter 6 .....	220
Bibliography .....	227
Chapter 1 .....	227
Chapter 2 .....	232
Chapter 3 .....	238
Chapter 4 .....	242
Chapter 5 .....	246
Chapter 6 .....	250
Chapter 7 .....	255
Vita .....	256

## List of Tables

Table 2.1: Demographic and clinicopathologic characteristics of samples used in our study.....	26
Table 2.2: Summary of the main experimental parameters used in the USA and Brazil DESI-MSI experiments. ....	28
Table 2.3: Tentatively identified species selected by the Lasso as significant contributors to the molecular model for IDC and normal breast tissue classification with attributed statistical weights. ....	41
Table 3.1: DESI-MS parameters for protein and lipid analysis. ....	64
Table 4.1: Summary of patient demographics, clinical indications, and procedures. ....	98
Table 5.1: Summary of the classification results for the training, validation and test sets of data.....	129
Table 6.1: Summary of patient demographics, clinical indications, and procedures. ....	147
Table 6.2: Confusion matrices of the Lasso results for Classifiers 1 and 2.....	161
Table A2.1: Cosine similarity values of the data obtained in USA and Brazil for same Brazilian normal and cancer samples. ....	187
Table A2.2: Summary of Lasso prediction results for distinguishing between normal and IDC breast samples for USA training set, USA test set, and Brazil test set.....	188
Table B3.1: Comparison of the S/N of alpha globin in mouse kidney tissue sections detected by DESI-MS imaging with and without FAIMS.....	189
Table B3.2: Identified proteins and their corresponding sequence coverages for mouse brain, human ovary, and human breast tissue samples.....	192
Table C4.1: Cosine similarity results between the mass spectra obtained with different tubing lengths of the MasSpec Pen.....	198

Table C4.2: Droplet transport time from pen tip to mass spectrometer through various tubing lengths.....	199
Table C4.3: Clinical and demographic information for the 100 patients included in this study.....	200
Table C4.4: Proposed attributions, molecular formula, and mass error for the species annotated. Abbreviations: FA – fatty acid, PE – glycerophosphoethanolamine, PS – glycerophosphoserine, PI – glycerophosphoinositol, TG – triacylglycerol. ....	210
Table E6.1: Demographic and detailed clinical information for the 26 symptomatic negative patients.....	220
Table E6.2: Observed $m/z$ , mass error, and identification for the features selected by Lasso for Classifier 1 and 2. ....	224

## List of Figures

Figure 1.1: Applications of ambient ionization MS in the research laboratory with a focus on DESI-MS imaging.....	3
Figure 1.2: Ambient ionization MS and potential applications in a clinical setting including surgical margin evaluation and COVID-19 screening.....	6
Figure 2.1: Negative ion mode DESI-MSI of IDC and normal breast tissues. ....	32
Figure 2.2: DESI-MS and principal component analysis of IDC tissues from patients of different races and country collection sites. ....	34
Figure 2.3: Predictive performance of the IDC classification model. ....	39
Figure 2.4: Per-pixel and per-patient prediction results for positive and negative receptor status classification. ....	43
Figure 3.1: Representative positive ion mode DESI mass spectra.....	66
Figure 3.2: DESI-MS ion images obtained from mouse brain tissue sections both with and without FAIMS. ....	68
Figure 3.3: Representative protein DESI-MS spectra of mouse kidney tissue, both with and without FAIMS. ....	68
Figure 3.4: MS/MS spectrum obtained using CID of the isotope envelope surrounding $m/z$ 1153.298, identified as alpha globin, while using DESI-MS.....	71
Figure 3.5: Tandem DESI-UVPD mass spectrum of $m/z$ 938.180, identified as a proteoform of alpha globin. ....	72
Figure 3.6: Representative DESI-FAIMS mass spectrum and ion images of a washed mouse brain tissue section. ....	74

Figure 3.7: DESI-MS spectra and ion images of the same mouse brain tissue section analyzed by both negative mode lipid DESI-MS imaging, followed by positive mode protein DESI-MS imaging.....	76
Figure 3.8: Representative DESI-FAIMS mass spectrum and ion images of a washed human normal and cancerous ovarian tissue sections.....	78
Figure 3.9: Representative DESI-FAIMS mass spectrum and ion images of a washed human normal and cancerous breast tissue sections. ....	79
Figure 4.1: Incorporation of the MasSpec Pen system in the OR. ....	93
Figure 4.2: Mass spectra acquired with different MasSpec Pen tubing lengths. ....	95
Figure 4.3: Mass spectra obtained during a total thyroidectomy for papillary thyroid cancer (TH0011). ....	99
Figure 4.4: Intraoperative use of the MasSpec Pen for <i>in vivo</i> and <i>ex vivo</i> tissue analyses. ....	101
Figure 4.5: Mass spectra obtained from <i>in vivo</i> MasSpec Pen analyses of various tissues in multiple surgical procedures. ....	103
Figure 4.6: Comparison between mass spectra obtained with the MasSpec Pen <i>in vivo</i> and <i>ex vivo</i> . ....	104
Figure 4.7: <i>Ex vivo</i> mass spectrum obtained from MasSpec Pen analysis of an excised lymph node sample during a right mastectomy procedure with sentinel node biopsy on a patient with grade III intraductal carcinoma (BR0001).....	107
Figure 4.8: Mass spectrum obtained from MasSpec Pen <i>ex vivo</i> analysis of an excised breast specimen during a second surgery right breast lumpectomy for re-excision of a positive ductal carcinoma in situ margin (BR0003).....	108

Figure 5.1: MasSpec Pen and statistical analysis of normal breast and primary IDC tissue. ....	127
Figure 6.1: Comparison of mass spectra obtained using the MasSpec Pen with ESI or solvent assisted inlet ionization to analyze a 20 ppm CL 72:4 lipid standard. ....	154
Figure 6.2: Comparison of mass spectra of swabs containing a 10 $\mu$ M PG 36:2 ( $m/z$ 773.533) and PE 36:2 ( $m/z$ 742.539) lipid standard mixture with and without heat inactivation. ....	156
Figure 6.3: MasSpec Pen-ESI MS analysis of asymptomatic negative, symptomatic negative, and symptomatic positive samples. ....	157
Figure 6.4: Statistical analysis results for Classification models 1 and 2. ....	159
Figure 6.5: Lasso classification features. ....	163
Figure A2.1: PCA analysis of normal breast tissue by race and ethnicity. ....	185
Figure A2.2: Negative ion mode DESI-MS ion images and mass spectra acquired in the USA and Brazil. ....	186
Figure B3.1: Comparison of the S/N and number of detected protein species at different spray voltages using DESI-FAIMS-MS. ....	190
Figure B3.2: Comparison of the S/N and number of detected protein species at different inlet temperatures using DESI-FAIMS-MS. ....	191
Figure B3.3: DESI-MS ion images of three serial mouse brain tissue sections ....	193
Figure B3.4: Representative negative ion mode MS/MS spectra of PS 40:6 and ST C24:1 obtained using DESI. ....	194
Figure B3.5: DESI-MS ion images of mouse brain tissue sections obtained both with and without previous analysis by DESI-MS imaging in negative ion mode. ....	195

Figure C4.1: MasSpec Pen control interface front panel. ....	196
Figure C4.2: Assembling of MasSpec Pen devices. ....	197
Figure C4.3: Comparison between mass spectra obtained <i>ex vivo</i> (A-C) and <i>in vivo</i> (D) from a parathyroid collected with the MasSpec Pen during a parathyroidectomy procedure for primary hyperparathyroidism (PT0010). ....	208
Figure C4.4: Images of two different MasSpec Pen devices after being used <i>in vivo</i> by surgeons for tissue analyses. ....	209
Figure C4.5: Comparison of total ion count values obtained from MasSpec Pen analyses in the operating room and laboratory setting for (A) breast and (B) thyroid specimens. ....	213
Figure C4.6: (A) Isotopic distribution of heme (on the top) observed <i>in vivo</i> from MasSpec Pen analysis of parathyroid tissue during a parathyroidectomy procedure for primary hyperparathyroidism (PT0012) and theoretical mass spectrum of heme (at the bottom) in negative ion mode using isotope simulation function available in Thermo XCalibur Qual Browser. ....	214
Figure C4.7: Detection and identification of heme and hexafluoroisopropyl sulfonate. .	215
Figure C4.8: Multiply charged peaks detected from <i>in vivo</i> analysis of thyroid tissue using MasSpec Pen during a right hemithyroidectomy procedure of an indeterminate nodule (TH0025) were tentatively assigned as hemoglobin $\alpha$ and hemoglobin $\beta$ subunits. ....	216
Figure C4.9: Negative ion mode mass spectra obtained of 10 $\mu$ L of human blood deposited onto a glass slide and analyzed with the MasSpec Pen. ....	217

Figure C4.10: MasSpec Pen *in vivo* analysis of a thyroid nodule during a total thyroidectomy and parathyroidectomy for a thyroid neoplasm and primary hyperparathyroidism (TH0024), showing interferences in the mass spectrum resulting from saline irrigation.....218

Figure C4.11: Identification of  $m/z$  246.950 as hexafluoroisopropyl sulfonate (HFIPS).....219

Figure E6.1: Representative mass spectrum from the MasSpec Pen-ESI MS analysis of a nylon flock swab dipped in 20 ppm CL 72:4 ( $m/z$  727.510) lipid standard.....223

## List of Illustrations

Illustration 2.1: Scheme of DESI-MS imaging of breast tissue sections across multiple centers for validation of the diagnostic potential of lipid markers.....	23
Illustration 3.1: Scheme of DESI-FAIMS-MS imaging of biological tissue sections.....	58
Illustration 6.1: Schematic of the MasSpec Pen-ESI-MS system for the diagnosis of COVID-19 infection. ....	152

## Chapter 1: Introduction

### CURRENT MASS SPECTROMETRY BASED TECHNOLOGIES USED IN THE CLINICAL LAB

Mass spectrometry (MS) has become routinely used in several areas of clinical diagnostics to detect molecules from various types of biological specimens *in vitro*. The unparalleled chemical specificity, high analytical sensitivity, and multiplexing capabilities achieved by MS have transformed the practice of laboratory medicine and established it as a key technique for the diagnosis of disease and metabolic disorders, immunoassays, and microbial identification, among others.<sup>1-2</sup> In addition to the high analytical performance of MS, its success in clinical labs can be contributed to the development of electrospray ionization (ESI) and matrix assisted laser desorption/ionization (MALDI) MS. Liquid chromatography (LC) coupled to ESI-MS, for example, is now considered the gold standard for the multiplex screening of inborn errors of metabolism in newborns.<sup>3-4</sup> MALDI-MS has enabled the identification of bacterium species and genus in a fraction of the time compared to conventional methods, ultimately revolutionizing bacterial identification, and becoming an invaluable tool in clinical microbiology labs.<sup>5-7</sup> Although various MS based techniques have been implemented in routine clinical practice to enable clinical decision making, they often require extensive sample processing and preparation prior to MS analysis, limiting their applications in diagnostic medicine where rapid turnaround times are highly needed.

## **AMBIENT IONIZATION MASS SPECTROMETRY AND ITS POTENTIAL TO BE USED IN A CLINICAL SETTING**

The development of ambient ionization MS in the early 2000s greatly expanded the potential of MS in the clinic.<sup>8</sup> Ambient ionization MS techniques share essential operational features that are well suited for a clinical lab including minimal sample preparation requirements and open-air sampling. Ambient MS approaches have been used for various applications ranging from therapeutic drug monitoring<sup>9</sup> and newborn screening<sup>3-4</sup>, both of which are currently being performed in the clinic using MS, to oncological and non-malignant disease detection and diagnosis.<sup>10-11</sup> Since its inception, the field of ambient ionization MS has been largely focused on analyzing various types of healthy and diseased tissue samples<sup>12</sup>, detecting alterations in the molecular profiles that are associated with cell metabolism and dysregulated biochemical pathways involved in cancer cell proliferation and malignant growth. Additionally, these approaches have been employed to analyze biofluids, different types of bacteria and bacteria cultures<sup>13</sup>, and medical swabs.<sup>11, 14</sup> While ambient ionization MS techniques have yet to be translated to the clinic, analytical and clinical advances in ambient ionization MS are currently being pursued to facilitate implementation of these methods into a clinical setting. Additionally, many studies utilizing ambient ionization MS approaches have incorporated machine learning to build classification models based on molecular information predictive of disease state.<sup>2</sup> The incorporation of predictive classification models into software packages with interpretable diagnostic readouts should further aid in the clinical translation of ambient ionization MS.

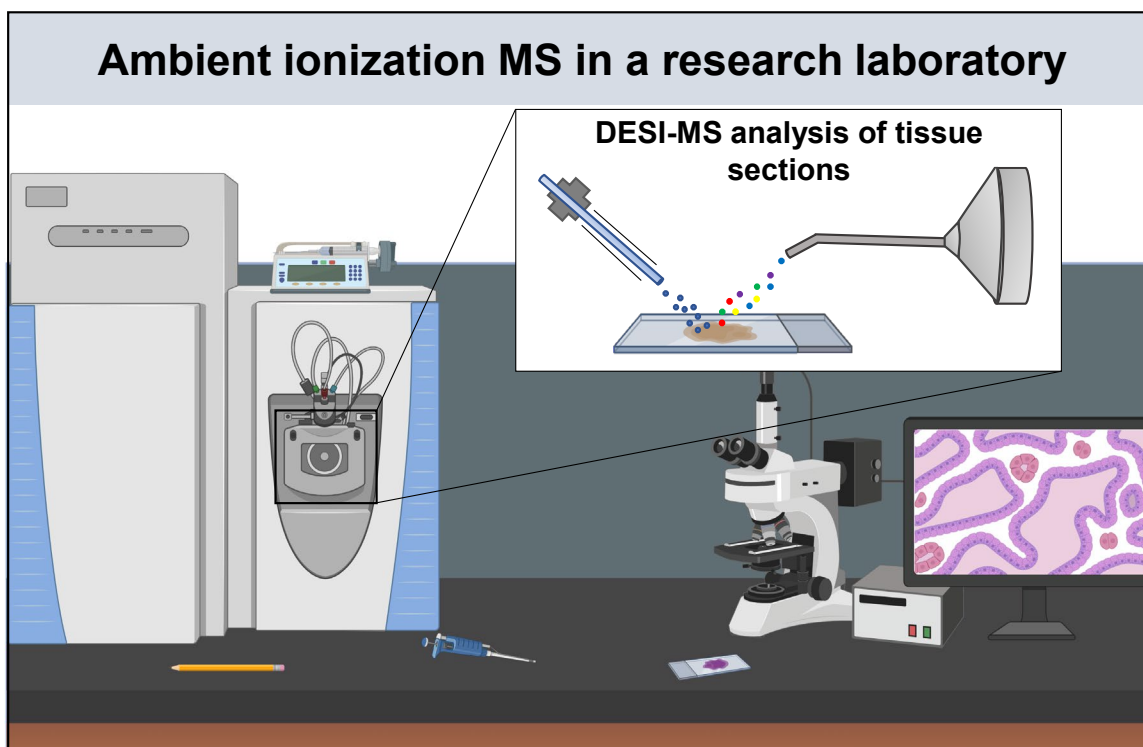


Figure 1.1: Applications of ambient ionization MS in the research laboratory with a focus on DESI-MS imaging.

Figure created with BioRender.com.

The field of ambient ionization MS remains largely focused on *in situ* analysis of biological tissue specimens. The most widely employed ambient ionization MS technique for the analysis of biological tissue sections is desorption electrospray ionization (DESI) MS. DESI utilizes a spray of charged solvent microdroplets that are directed towards a sample surface to extract analytes from the sample through a solid/liquid extraction process.<sup>8</sup> The secondary microdroplets formed through the continuous spray and splashing process are then aspirated through an inlet transfer tube directly into the mass spectrometer for chemical analysis. DESI can be used in the imaging mode, known as DESI-MS imaging, by rastering the spray across the sample surface, which generates molecular images showing the spatial distribution of the molecules detected. Recent advances in DESI-MS imaging have expanded the molecular coverage of this technique to include the detection of proteins directly from tissue sections through integration with ion mobility.<sup>15-</sup>  
<sup>16</sup> Notably, the development of histologically compatible solvent systems has enabled acquisition of rich metabolite and lipid information from tissue sections by DESI without significant damage to sample histology or morphology.<sup>17</sup> These solvent systems have enabled single tissue sections to undergo hematoxylin and eosin (H&E) or immunohistochemistry (IHC) staining and pathological evaluation after DESI-MS analysis, thereby allowing unambiguous correlation between chemical and histologic information. This advance is critical in enabling the incorporation of DESI-MS into the clinical workflow at various stages of routine histopathological evaluation. Further, the speed, relative ease of use, and minimal to no sample preparation requirements have propelled DESI as a tool for rapid and direct analysis of biological samples in clinical

research (Figure 1.1). In fact, DESI-MS has been used to investigate many types of cancers, including breast<sup>18-20</sup>, ovarian<sup>21-22</sup>, thyroid<sup>23-24</sup>, brain<sup>25-27</sup>, and prostate<sup>28-30</sup>, among others<sup>10, 12</sup>, allowing for discrimination between normal and cancerous tissue based on alterations in their metabolic and lipid profiles, and therefore showcasing the potential of DESI-MS as a powerful approach for the detection, subtyping<sup>18</sup>, and staging of cancer as well as surgical margin evaluation.<sup>20, 31</sup>

The development of handheld and surgical devices for direct tissue analysis, with a specific focus on *in vivo* use in the operating room, has been a major research aim in the field of clinical ambient ionization MS in the last decade as these technologies could provide clinical professionals with MS-based tools capable of extracting informative molecular information from tissues *in vivo* and freshly excised specimens. In the case of oncological surgeries, for example, handheld MS devices could assist surgeons in guiding tissue resection to assist in the complete removal of tumor tissue, identify regions of normal tissues, and pinpoint sites of cancer metastasis, thus mitigating many challenges in tissue evaluation that commonly occur during surgical procedures (Figure 1.2). The first handheld MS-based device developed for intraoperative use was rapid evaporative ionization MS (REIMS), otherwise known as the iKnife, which employs an electrocauterization device commonly used in surgical procedures to generate gaseous molecular ions of cellular components that are then transported to the MS through the tubing system for analysis.<sup>32-</sup>  
<sup>33</sup> Since its development, additional handheld MS-based technologies utilizing liquid, laser, and solid extraction processes have been developed and used for the molecular characterization of healthy and diseased tissue samples<sup>12</sup>, with intent to be used

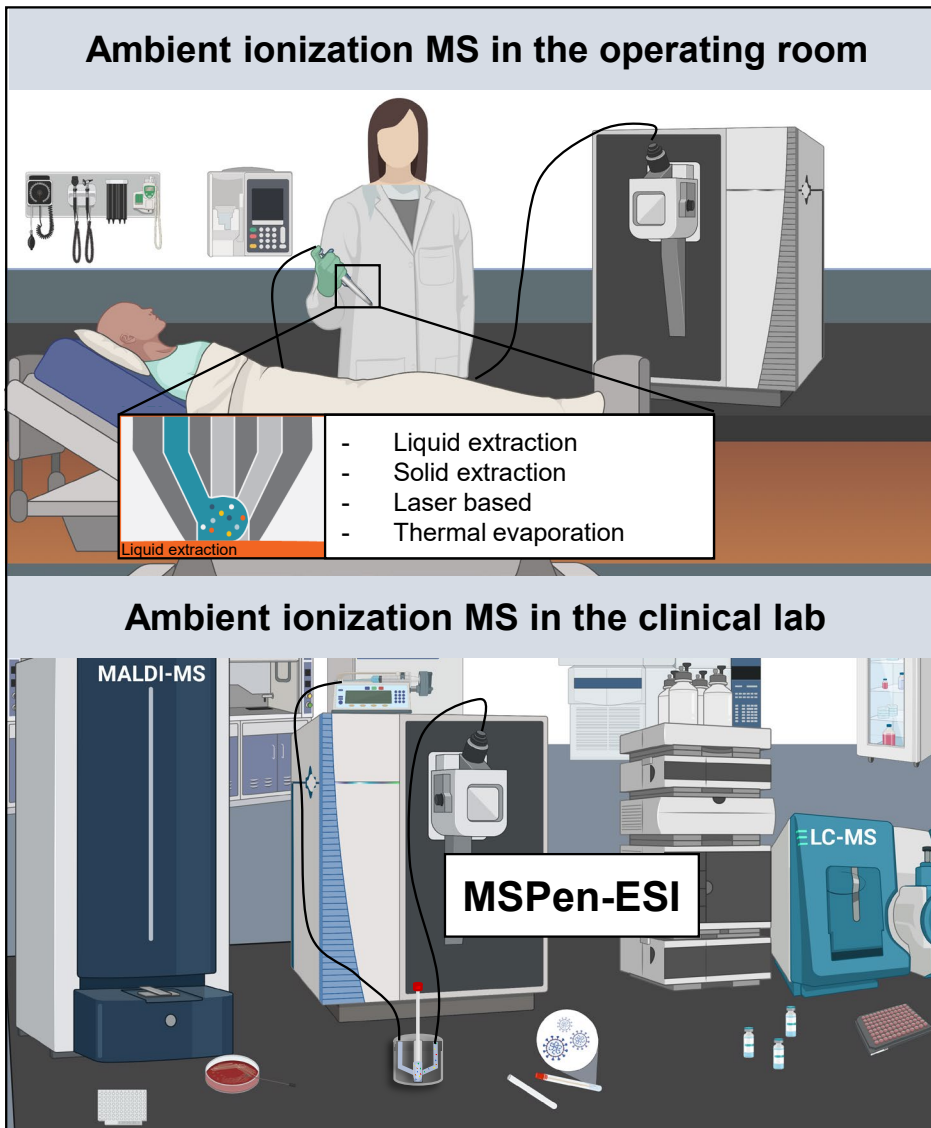


Figure 1.2: Ambient ionization MS and potential applications in a clinical setting including surgical margin evaluation and COVID-19 screening.

Figure created with BioRender.com.

intraoperatively for *in vivo* and *ex vivo* analyses of tissue specimens. The MasSpec Pen, which was developed in our lab, utilizes a simple and gentle liquid extraction process to extract molecules from tissue samples which are then transferred to a mass spectrometer for chemical analysis.<sup>34-35</sup> Altogether, these technologies have been used to investigate various types of cancer including breast<sup>34, 36</sup>, brain<sup>33, 37</sup>, colon<sup>33</sup>, and ovarian<sup>38-40</sup>, among others<sup>41</sup>, successfully differentiating between normal and cancerous tissue based on molecular information. Although more rigorous validation of these technologies for intraoperative use is needed, they show promise for rapid intraoperative evaluation tissue samples, with potential to expand the applications of MS in a clinical environment.

## **RESEARCH OBJECTIVES**

Technologies that provide molecular characterization of biological samples offer the exciting opportunity to incorporate molecular markers into clinical decision making for various types of human diseases. Molecular technologies, such as ambient ionization MS, can detect changes in the relative abundances of molecular species characteristic of altered energy metabolism and dysregulated cellular and metabolic pathways. Capitalizing on this, my research has been focused on developing and applying ambient ionization MS methods to molecularly characterize multiple types of biological samples to evaluate their feasibility for detecting human diseases, including breast cancer and COVID-19 infection. The main objectives were to evaluate the robustness of DESI-MS imaging for the rapid discrimination of normal and cancerous breast tissue in a multi-center study, integrating DESI-MS with ion mobility to expand its molecular coverage for the analysis of biological tissue sections, and to develop liquid extraction-based sampling approaches for the direct

analysis and molecular characterization nasal of swabs as well as *in vivo* and *ex vivo* normal and cancerous breast tissue specimens, evaluating their potential for clinical use.

### **Evaluating the robustness of DESI-MS imaging for breast cancer diagnosis**

Breast cancer is a heterogenous and complex disease that affects approximately one in eight women during their lifetime. Breast cancer is diagnosed pre-operatively at both the histological and molecular levels. Invasive ductal carcinoma (IDC) is the most common histological subtype of breast cancer and is subtyped at the molecular level based on the overexpression of estrogen receptor (ER), progesterone receptor (PR), and human epidermal growth factor receptor 2 (HER2). Rapid and accurate diagnosis of histological subtype and receptor status plays an essential role in selecting the appropriate treatment options for patients. Immunohistochemistry, the gold standard for ER, PR, and HER2 receptor status determination, can be time and labor intensive, subjective, and requires experienced research personnel for interpretation to perform the assay and interpret the results.<sup>42</sup> Chapter 2 of my dissertation describes the application of DESI-MS imaging for the molecular analysis healthy breast and invasive ductal carcinoma tissue section from patients of different races and countries of origins in a multi-center study between the United States and Brazil. DESI-MS imaging allowed for spatial correlation of molecular information with histopathologically validated regions of IDC and normal breast tissue. The molecular information obtained from the IDC tissue samples was further correlated with ER, PR, and HER2 status. The least absolute shrinkage and selection operator statistical method was used to build classification models for discriminating IDC from normal breast tissue based on 44 lipid markers from data collected in the United States,

yielding over a 95% accuracy when predicting on an independent test set of data acquired in Brazil using a different orbitrap platform. For receptor status determination, over an 88% accuracy was achieved for ER, PR, and hormone receptor (ER/PR) status determination was achieved for cross validation. This multi-center study demonstrates DESI-MS imaging as a robust technology for rapid breast cancer diagnosis as well as showcases the predictive power of lipid information obtained by DESI-MS imaging for breast cancer prediction as well as ER and PR status determination.

### **Integrating ion mobility into the DESI-MS imaging workflow to expand molecular coverage**

Ambient ionization mass spectrometry imaging has been extensively used for the untargeted molecular analysis of biological tissue sections, detecting thousands of small molecules including metabolite, fatty acid, and lipid species simultaneously. However, analysis of larger biomolecules has proven challenging with these methodologies due to the inefficient desorption of larger biomolecules, ion suppression from the complex biological matrix, and competitive ionization from smaller molecular species, all of which can lead to a lower abundance for the molecules of interest. Several direct liquid extraction ambient ionization MS methods have found success in detecting proteins in biological tissue section by incorporating ion mobility into the MS workflow.<sup>43-45</sup> Ion mobility separates molecules in the gas phase based on size, charge, and shape and enables selective transmission of molecules of interest. Chapter 3 of my dissertation describes the successful optimization of DESI-MS, a spray based ambient MS approach, to detect intact proteins directly from tissue sections, and the integration of DESI-MS to a high field asymmetric

waveform ion mobility (FAIMS) device for protein imaging. FAIMS acts as an ion filter, separating molecules based on their differential ion mobility when the appropriate electric field is applied.<sup>46-47</sup> The integration of FAIMS with DESI-MS enabled the semi-selective transmission and detection of proteins in biological tissue sections by separating and filtering out small interfering molecules and chemical noise. Optimized DESI-FAIMS-MS parameters were used to image mouse kidney, mouse brain, and human ovarian and breast tissue samples, allowing detection of 11, 16, 14, and 16 proteoforms, respectively. Identification of protein species detected by DESI-MS was performed on-tissue by top-down ultraviolet photodissociation (UVPD) and collision induced dissociation (CID), as well as using tissue extracts by bottom-up CID and top-down UVPD. Alterations in the relative abundances of protein species within healthy and diseased human ovarian and breast tissues were observed. These results demonstrate that DESI-MS imaging is suitable for the analysis of the distribution of proteins within biological tissue sections.

### **Clinical translation of the MasSpec Pen into the operating room**

Intraoperative tissue analysis and identification are critical to guide surgical procedures and improve patient outcomes. Evaluation of tissue specimens during cancer surgeries is essential to determine the extent of tumor resection and surgical margin status. Intraoperative tissue evaluation can currently be accomplished by gross examination through palpation, imaging of resected bulk tissue, and histopathological analysis of frozen tissue sections although these methods are not widely used across multiple centers due to various challenges. Beyond cancer surgeries, surgical procedures for non-malignant

conditions, such as those affecting the thyroid or parathyroid glands, can be hindered by difficulties in distinguishing between and correctly identifying tissues with similar gross anatomy. Chapter 4 of this dissertation focuses on the clinical translation and evaluation of the MasSpec Pen technology for molecular analysis and evaluation of *in vivo* and freshly excised tissues in the OR. Detection of mass spectral profiles from 715 *in vivo* and *ex vivo* analyses performed on thyroid, parathyroid, lymph node, breast, pancreatic, and bile duct tissues during parathyroidectomies, thyroidectomies, breast, and pancreatic neoplasia surgeries was achieved. The MasSpec Pen enabled gentle extraction and sensitive detection of various molecular species including small metabolites and lipids using a droplet of sterile water without causing apparent tissue damage. Notably, effective molecular analysis was achieved while no limitations to sequential histologic tissue analysis were identified and no device-related complications were reported for any of the patients. This study shows that the MasSpec Pen system can be successfully incorporated into the operating room, allowing direct detection of rich molecular profiles from tissues with a seconds-long turnaround time that could be used to inform surgical and clinical decisions without disrupting tissue analysis workflows.

#### **Application of the MasSpec Pen for breast cancer tissue evaluation**

Breast cancer is the most common cancer among women in the United States and is the second leading cause of cancer deaths among female patients. Breast conserving surgery (BCS) is one of the first steps in the surgical management of women diagnosed with early stage breast cancer. This procedure involves the removal of most of or all the

tumor as well as a rim of surrounding normal breast tissue. It is paramount that the surgeon maximizes the extent of tumor resection during primary BCS as positive margins, defined by the presence of tumor cells at the edge of the excised specimen, are associated with increased risk of local recurrence and poorer outcomes.<sup>48-49</sup> However, complete removal of tumor tissue during BCS remains a challenge for surgeons due to difficulties in precisely identifying microscopic disease through gross assessment. Margin status is often evaluated postoperatively as current pathology and imaging based intraoperative tissue assessment methods have limited sensitivity and can lengthen the time the patient is under anesthesia.<sup>50-53</sup> As such, clinical reports show that ~20-40% of breast cancer patients need multiple surgeries to ensure complete cancer removal.<sup>50, 54-55</sup> Additional surgeries for complete tumor removal are associated with increased morbidity and patient anxiety, poorer cosmetic outcome, and increased health costs.<sup>49</sup>

Chapter 5 of this dissertation outlines the development and application of the MasSpec Pen for the rapid evaluation of breast tissue. The least absolute shrinkage and selection operator was used to build a classification model using data collected from the analysis of banked normal and IDC breast tissue, achieving over a 90% agreement with pathology for an independent test set of data. The classification model was built using 10 metabolite and lipid species. Additionally, this chapter describes the clinical translation and assessment of the MasSpec Pen technology for intraoperative use and evaluation of breast tissue. The MasSpec Pen was used during 24 breast surgeries for malignant and benign conditions and diseases. Similar molecular information was obtained intraoperatively compared to the mass spectra collected in the laboratory. The statistical

classifier was used to predict on the data obtained from the in vivo and ex vivo analyses of breast tissue in an independent test set. An 95.2% agreement with final postoperative pathology was achieved, demonstrating the ability of the MasSpec Pen for intraoperative breast tissue assessment.

### **Screening of COVID-19 using the MasSpec Pen system**

The outbreak of COVID-19 has created an unprecedented global crisis. While PCR is the gold standard method for detecting active SARS-CoV-2 infection, alternative high-throughput diagnostic tests are of significant value to meet universal testing demands. Alternative diagnostic tests that require minimal reagents, can be processed quickly, and provide a rapid diagnosis are highly valuable for the screening of COVID-19. Alternative methods capable of rapidly screening for COVID-19 disease are thus still needed to increase testing capacity and throughput. Chapter 6 describes a new design of the MasSpec Pen technology integrated to ESI for direct analysis of clinical swabs and investigate the diagnostic potential of lipid species for COVID-19 screening. Lipids are a major component of the virion cellular membrane and are acquired from the host during budding. It is well known that the lipid composition of the viral membrane is distinct from that of host cells as well as other viruses, making lipid species promising detection targets for SARS-CoV-2 viral infection. The redesigned MasSpec Pen system incorporates a disposable sampling device refined for uniform and efficient analysis of swab tips via liquid extraction directly coupled to a ESI source. Using this system, we analyzed nasopharyngeal swabs from 244 individuals including symptomatic COVID-19 positive,

symptomatic negative, and asymptomatic negative individuals, enabling rapid detection of rich lipid profiles. Two statistical classifiers were generated based on the lipid information acquired. Classifier 1 was built to distinguish symptomatic PCR-positive from asymptomatic PCR-negative individuals, yielding cross-validation accuracy of 83.5%, sensitivity of 76.6%, and specificity of 86.6%, and validation set accuracy of 89.6%, sensitivity of 100%, and specificity of 85.3%. Classifier 2 was built to distinguish symptomatic PCR-positive patients from negative individuals including symptomatic PCR-negative patients with moderate to severe symptoms and asymptomatic individuals, yielding a cross-validation accuracy of 78.4% accuracy, specificity of 77.21%, and sensitivity of 81.8%. Collectively, this study suggests that the lipid profiles detected directly from nasopharyngeal swabs using MasSpec Pen-ESI MS allows fast (under a minute) screening of COVID-19 disease using minimal operating steps and no specialized reagents, thus representing a promising alternative high-throughput method for screening of COVID-19.

## REFERENCES

1. Jannetto, P. J.; Fitzgerald, R. L., Effective Use of Mass Spectrometry in the Clinical Laboratory. *Clin Chem* **2016**, *62* (1), 92-8.
2. Banerjee, S., Empowering Clinical Diagnostics with Mass Spectrometry. *ACS Omega* **2020**, *5* (5), 2041-2048.
3. Ombrone, D.; Giocaliere, E.; Forni, G.; Malvagìa, S.; la Marca, G., Expanded newborn screening by mass spectrometry: New tests, future perspectives. *Mass Spectrom Rev* **2016**, *35* (1), 71-84.
4. Ismail, I. T.; Showalter, M. R.; Fiehn, O., Inborn Errors of Metabolism in the Era of Untargeted Metabolomics and Lipidomics. *Metabolites* **2019**, *9* (10).
5. Tsuchida, S.; Umemura, H.; Nakayama, T., Current Status of Matrix-Assisted Laser Desorption/Ionization-Time-of-Flight Mass Spectrometry (MALDI-TOF MS) in Clinical Diagnostic Microbiology. *Molecules* **2020**, *25* (20).
6. Hou, T. Y.; Chiang-Ni, C.; Teng, S. H., Current status of MALDI-TOF mass spectrometry in clinical microbiology. *J Food Drug Anal* **2019**, *27* (2), 404-414.
7. Kostrzewa, M., Application of the MALDI Biotyper to clinical microbiology: progress and potential. *Expert Rev Proteomics* **2018**, *15* (3), 193-202.
8. Takats, Z.; Wiseman, J. M.; Gologan, B.; Cooks, R. G., Mass spectrometry sampling under ambient conditions with desorption electrospray ionization. *Science* **2004**, *306* (5695), 471-3.
9. Garg, U.; Zhang, Y. V., Mass Spectrometry in Clinical Laboratory: Applications in Therapeutic Drug Monitoring and Toxicology. *Methods Mol Biol* **2016**, *1383*, 1-10.
10. Ifa, D. R.; Eberlin, L. S., Ambient Ionization Mass Spectrometry for Cancer Diagnosis and Surgical Margin Evaluation. *Clin Chem* **2016**, *62* (1), 111-23.
11. Feider, C. L.; Krieger, A.; DeHoog, R. J.; Eberlin, L. S., Ambient Ionization Mass Spectrometry: Recent Developments and Applications. *Anal Chem* **2019**, *91* (7), 4266-4290.
12. Zhang, J.; Sans, M.; Garza, K. Y.; Eberlin, L. S., Mass Spectrometry Technologies to Advance Care for Cancer Patients in Clinical and Intraoperative Use. *Mass Spectrom Rev* **2020**.
13. Bardin, E. E.; Cameron, S. J. S.; Perdones-Montero, A.; Hardiman, K.; Bolt, F.; Alton, E.; Bush, A.; Davies, J. C.; Takats, Z., Metabolic Phenotyping and Strain Characterisation of *Pseudomonas aeruginosa* Isolates from Cystic Fibrosis Patients Using Rapid Evaporative Ionisation Mass Spectrometry. *Sci Rep* **2018**, *8* (1), 10952.
14. Pirro, V.; Llor, R. S.; Jarmusch, A. K.; Alfaro, C. M.; Cohen-Gadol, A. A.; Hattab, E. M.; Cooks, R. G., Analysis of human gliomas by swab touch spray-mass spectrometry: applications to intraoperative assessment of surgical margins and presence of oncometabolites. *Analyst* **2017**, *142* (21), 4058-4066.

15. Garza, K. Y.; Feider, C. L.; Klein, D. R.; Rosenberg, J. A.; Brodbelt, J. S.; Eberlin, L. S., Desorption Electrospray Ionization Mass Spectrometry Imaging of Proteins Directly from Biological Tissue Sections. *Anal Chem* **2018**, *90* (13), 7785-7789.
16. Towers, M. W.; Karancsi, T.; Jones, E. A.; Pringle, S. D.; Claude, E., Optimised Desorption Electrospray Ionisation Mass Spectrometry Imaging (DESI-MSI) for the Analysis of Proteins/Peptides Directly from Tissue Sections on a Travelling Wave Ion Mobility Q-ToF. *J Am Soc Mass Spectrom* **2018**.
17. Eberlin, L. S.; Ferreira, C. R.; Dill, A. L.; Ifa, D. R.; Cheng, L.; Cooks, R. G., Nondestructive, histologically compatible tissue imaging by desorption electrospray ionization mass spectrometry. *Chembiochem* **2011**, *12* (14), 2129-32.
18. Porcari, A. M.; Zhang, J. L.; Garza, K. Y.; Rodrigues-Peres, R. M.; Lin, J. Q.; Young, J. H.; Tibshirani, R.; Nagi, C.; Paiva, G. R.; Carter, S. A.; Sarian, L. O.; Eberlin, M. N.; Eberlin, L. S., Multicenter Study Using Desorption-Electrospray-Ionization-Mass-Spectrometry Imaging for Breast-Cancer Diagnosis. *Analytical Chemistry* **2018**, *90* (19), 11324-11332.
19. Guenther, S.; Muirhead, L. J.; Speller, A. V.; Golf, O.; Strittmatter, N.; Ramakrishnan, R.; Goldin, R. D.; Jones, E.; Veselkov, K.; Nicholson, J.; Darzi, A.; Takats, Z., Spatially resolved metabolic phenotyping of breast cancer by desorption electrospray ionization mass spectrometry. *Cancer Res* **2015**, *75* (9), 1828-37.
20. Calligaris, D.; Caragacianu, D.; Liu, X.; Norton, I.; Thompson, C. J.; Richardson, A. L.; Golshan, M.; Easterling, M. L.; Santagata, S.; Dillon, D. A.; Jolesz, F. A.; Agar, N. Y., Application of desorption electrospray ionization mass spectrometry imaging in breast cancer margin analysis. *Proc Natl Acad Sci U S A* **2014**, *111* (42), 15184-9.
21. Doria, M. L.; McKenzie, J. S.; Mroz, A.; Phelps, D. L.; Speller, A.; Rosini, F.; Strittmatter, N.; Golf, O.; Veselkov, K.; Brown, R.; Ghaem-Maghami, S.; Takats, Z., Epithelial ovarian carcinoma diagnosis by desorption electrospray ionization mass spectrometry imaging. *Scientific Reports* **2016**, *6*, 11.
22. Sans, M.; Gharpure, K.; Tibshirani, R.; Zhang, J.; Liang, L.; Liu, J.; Young, J. H.; Dood, R. L.; Sood, A. K.; Eberlin, L. S., Metabolic Markers and Statistical Prediction of Serous Ovarian Cancer Aggressiveness by Ambient Ionization Mass Spectrometry Imaging. *Cancer Res* **2017**, *77* (11), 2903-2913.
23. Zhang, J.; Feider, C. L.; Nagi, C.; Yu, W.; Carter, S. A.; Suliburk, J.; Cao, H. S. T.; Eberlin, L. S., Detection of Metastatic Breast and Thyroid Cancer in Lymph Nodes by Desorption Electrospray Ionization Mass Spectrometry Imaging. *J. Am. Soc. Mass Spectrom.* **2017**, *28* (6), 1166-1174.
24. DeHoog, R. J.; Zhang, J.; Alore, E.; Lin, J. Q.; Yu, W.; Woody, S.; Almendariz, C.; Lin, M.; Engelsman, A. F.; Sidhu, S. B.; Tibshirani, R.; Suliburk, J.; Eberlin, L. S., Preoperative metabolic classification of thyroid nodules using mass spectrometry imaging of fine-needle aspiration biopsies. *Proc Natl Acad Sci U S A* **2019**, *116* (43), 21401-21408.
25. Cooks, R. G.; Alfaro, C.; Jarmusch, A.; Pirro, V.; Baird, Z.; Hattab, E.; Cohen-Gadol, A. In *Intrasurgical diagnosis of human brain tumor tissue and surgical margin characterization by DESI-MS*, American Chemical Society: 2017; pp ANYL-284.

26. Eberlin, L. S.; Dill, A. L.; Golby, A. J.; Ligon, K. L.; Wiseman, J. M.; Cooks, R. G.; Agar, N. Y., Discrimination of human astrocytoma subtypes by lipid analysis using desorption electrospray ionization imaging mass spectrometry. *Angew Chem Int Ed Engl* **2010**, *49* (34), 5953-6.
27. Jarmusch, A. K.; Pirro, V.; Baird, Z.; Hattab, E. M.; Cohen-Gadol, A. A.; Cooks, R. G., Lipid and metabolite profiles of human brain tumors by desorption electrospray ionization-MS. *Proc. Natl. Acad. Sci. U. S. A.* **2016**, *113* (6), 1486-1491.
28. Banerjee, S.; Zare, R. N.; Tibshirani, R. J.; Kunder, C. A.; Nolley, R.; Fan, R.; Brooks, J. D.; Sonn, G. A., Diagnosis of prostate cancer by desorption electrospray ionization mass spectrometric imaging of small metabolites and lipids. *Proc. Natl. Acad. Sci. U. S. A.* **2017**, *114* (13), 3334-3339.
29. Kerian, K. S.; Jarmusch, A. K.; Pirro, V.; Koch, M. O.; Masterson, T. A.; Cheng, L.; Cooks, R. G., Differentiation of prostate cancer from normal tissue in radical prostatectomy specimens by desorption electrospray ionization and touch spray ionization mass spectrometry. *Analyst* **2015**, *140* (4), 1090-1098.
30. Eberlin, L. S.; Dill, A. L.; Costa, A. B.; Ifa, D. R.; Cheng, L.; Masterson, T.; Koch, M.; Ratliff, T. L.; Cooks, R. G., Cholesterol sulfate imaging in human prostate cancer tissue by desorption electrospray ionization mass spectrometry. *Anal Chem* **2010**, *82* (9), 3430-4.
31. Eberlin, L. S.; Tibshirani, R. J.; Zhang, J.; Longacre, T. A.; Berry, G. J.; Bingham, D. B.; Norton, J. A.; Zare, R. N.; Poultides, G. A., Molecular assessment of surgical-resection margins of gastric cancer by mass-spectrometric imaging. *Proc Natl Acad Sci U S A* **2014**, *111* (7), 2436-41.
32. Schafer, K. C.; Denes, J.; Albrecht, K.; Szaniszlo, T.; Balog, J.; Skoumal, R.; Katona, M.; Toth, M.; Balogh, L.; Takats, Z., In vivo, in situ tissue analysis using rapid evaporative ionization mass spectrometry. *Angew Chem Int Ed Engl* **2009**, *48* (44), 8240-2.
33. Balog, J.; Sasi-Szabo, L.; Kinross, J.; Lewis, M. R.; Muirhead, L. J.; Veselkov, K.; Mirnezami, R.; Dezso, B.; Damjanovich, L.; Darzi, A.; Nicholson, J. K.; Takats, Z., Intraoperative tissue identification using rapid evaporative ionization mass spectrometry. *Sci Transl Med* **2013**, *5* (194), 194ra93.
34. Zhang, J.; Rector, J.; Lin, J. Q.; Young, J. H.; Sans, M.; Katta, N.; Giese, N.; Yu, W.; Nagi, C.; Suliburk, J.; Liu, J.; Bensussan, A.; DeHoog, R. J.; Garza, K. Y.; Ludolph, B.; Sorace, A. G.; Syed, A.; Zahedivash, A.; Milner, T. E.; Eberlin, L. S., Nondestructive tissue analysis for ex vivo and in vivo cancer diagnosis using a handheld mass spectrometry system. *Sci Transl Med* **2017**, *9* (406).
35. Keating, M. F.; Zhang, J.; Feider, C. L.; Retailleau, S.; Reid, R.; Antaris, A.; Hart, B.; Tan, G.; Milner, T. E.; Miller, K.; Eberlin, L. S., Integrating the MasSpec Pen to the da Vinci Surgical System for In Vivo Tissue Analysis during a Robotic Assisted Porcine Surgery. *Anal Chem* **2020**, *92* (17), 11535-11542.
36. St John, E. R.; Balog, J.; McKenzie, J. S.; Rossi, M.; Covington, A.; Muirhead, L.; Bodai, Z.; Rosini, F.; Speller, A. V. M.; Shousha, S.; Ramakrishnan, R.; Darzi, A.; Takats, Z.; Leff, D. R., Rapid evaporative ionisation mass spectrometry of electrosurgical vapours for the identification of

breast pathology: towards an intelligent knife for breast cancer surgery. *Breast Cancer Res* **2017**, *19* (1), 59.

37. Woolman, M.; Ferry, I.; Kuzan-Fischer, C. M.; Wu, M.; Zou, J.; Kiyota, T.; Isik, S.; Dara, D.; Aman, A.; Das, S.; Taylor, M. D.; Rutka, J. T.; Ginsberg, H. J.; Zarrine-Afsar, A., Rapid determination of medulloblastoma subgroup affiliation with mass spectrometry using a handheld picosecond infrared laser desorption probe. *Chem. Sci.* **2017**, *8* (9), 6508-6519.

38. Phelps, D. L.; Balog, J.; Gildea, L. F.; Bodai, Z.; Savage, A.; El-Bahrawy, M. A.; Speller, A. V.; Rosini, F.; Kudo, H.; McKenzie, J. S.; Brown, R.; Takats, Z.; Ghaem-Maghani, S., The surgical intelligent knife distinguishes normal, borderline and malignant gynaecological tissues using rapid evaporative ionisation mass spectrometry (REIMS). *Br J Cancer* **2018**, *118* (10), 1349-1358.

39. Fatou, B.; Saudemont, P.; Leblanc, E.; Vinatier, D.; Mesdag, V.; Wisztorski, M.; Focsa, C.; Salzert, M.; Ziskind, M.; Fournier, I., In vivo Real-Time Mass Spectrometry for Guided Surgery Application. *Scientific Reports* **2016**, *6*.

40. Sans, M.; Zhang, J.; Lin, J. Q.; Giese, N.; Liu, J.; Sood, A. K.; Eberlin, L. S., Evaluating the Performance of the MasSpec Pen for Rapid Diagnosis of Ovarian Cancer. *Clinical Chemistry under review*.

41. Mason, S.; Manoli, E.; Poynter, L.; Alexander, J.; Paizs, P.; Adebessin, A.; Goldin, R.; Darzi, A.; Takats, Z.; Kinross, J., Mass spectrometry transanal minimally invasive surgery (MS-TAMIS) to promote organ preservation in rectal cancer. *Surg Endosc* **2020**, *34* (8), 3618-3625.

42. Yaziji, H.; Barry, T., Diagnostic Immunohistochemistry: what can go wrong? *Adv Anat Pathol* **2006**, *13* (5), 238-46.

43. Sarsby, J.; Griffiths, R. L.; Race, A. M.; Bunch, J.; Randall, E. C.; Creese, A. J.; Cooper, H. J., Liquid Extraction Surface Analysis Mass Spectrometry Coupled with Field Asymmetric Waveform Ion Mobility Spectrometry for Analysis of Intact Proteins from Biological Substrates. *Anal Chem* **2015**, *87* (13), 6794-800.

44. Feider, C. L.; Elizondo, N.; Eberlin, L. S., Ambient Ionization and FAIMS Mass Spectrometry for Enhanced Imaging of Multiply Charged Molecular Ions in Biological Tissues. *Anal Chem* **2016**, *88* (23), 11533-11541.

45. Griffiths, R. L.; Creese, A. J.; Race, A. M.; Bunch, J.; Cooper, H. J., LESA FAIMS Mass Spectrometry for the Spatial Profiling of Proteins from Tissue. *Anal Chem* **2016**, *88* (13), 6758-66.

46. Guevremont, R., High-field asymmetric waveform ion mobility spectrometry (FAIMS). *Can. J. Anal. Sci. Spectrosc.* **2004**, *49* (3), 105-113.

47. Cooper, H. J., To What Extent is FAIMS Beneficial in the Analysis of Proteins? *J Am Soc Mass Spectrom* **2016**, *27* (4), 566-77.

48. Houssami, N.; Marinovich, M. L., Margins in Breast-Conserving Surgery for Early Breast Cancer: How Much is Good Enough? *Curr Breast Cancer R* **2016**, *8* (2), 127-134.

49. Pilewskie, M.; Morrow, M., Margins in breast cancer: How much is enough? *Cancer* **2018**, *124* (7), 1335-1341.

50. Cabioglu, N.; Hunt, K. K.; Sahin, A. A.; Kuerer, H. M.; Babiera, G. V.; Singletary, S. E.; Whitman, G. J.; Ross, M. I.; Ames, F. C.; Feig, B. W.; Buchholz, T. A.; Meric-Bernstam, F., Role for intraoperative margin assessment in patients undergoing breast-conserving surgery. *Ann Surg Oncol* **2007**, *14* (4), 1458-71.
51. Bakhshandeh, M.; Tutuncuoglu, S. O.; Fischer, G.; Masood, S., Use of imprint cytology for assessment of surgical margins in lumpectomy specimens of breast cancer patients. *Diagn Cytopathol* **2007**, *35* (10), 656-9.
52. Weber, W. P.; Engelberger, S.; Viehl, C. T.; Zanetti-Dallenbach, R.; Kuster, S.; Dirnhofer, S.; Wruk, D.; Oertli, D.; Marti, W. R., Accuracy of frozen section analysis versus specimen radiography during breast-conserving surgery for nonpalpable lesions. *World J Surg* **2008**, *32* (12), 2599-606.
53. Dener, C.; Inan, A.; Sen, M.; Demirci, S., Intraoperative Frozen Section for Margin Assessment in Breast Conserving Surgery. *Scand J Surg* **2009**, *98* (1), 34-40.
54. Pleijhuis, R. G.; Graafland, M.; de Vries, J.; Bart, J.; de Jong, J. S.; van Dam, G. M., Obtaining adequate surgical margins in breast-conserving therapy for patients with early-stage breast cancer: current modalities and future directions. *Ann Surg Oncol* **2009**, *16* (10), 2717-30.
55. Fisher, S.; Yasui, Y.; Dabbs, K.; Winget, M., Re-excision and survival following breast conserving surgery in early stage breast cancer patients: a population-based study. *BMC Health Serv Res* **2018**, *18* (1), 94.

## Chapter 2: A Multi-Center Study Using Desorption Electrospray Ionization Mass Spectrometry Imaging for Breast Cancer Diagnosis<sup>1</sup>

### INTRODUCTION

Breast cancer is a complex and heterogeneous disease, and the leading cause of cancer deaths among females worldwide<sup>1-2</sup>. Breast cancer exhibits distinct gene expression patterns depending on the molecular subtype defined mostly by the estrogen receptor (ER), progesterone receptor (PR), and human epidermal growth factor receptor 2 (Her2) status. Precise diagnosis and subtyping of breast cancer at the molecular level is pivotal to manage cancer patients since each subtype presents distinct clinical outcomes and therefore require targeted treatment regimens<sup>3</sup>. Diagnosis and molecular subtyping of breast cancer is routinely performed in the clinic based on histopathologic interpretation of hematoxylin and eosin (H&E) staining of tissue sections, immunohistochemistry (IHC) assays that are specific for ER, PR determination, and fluorescence *in situ* hybridization (FISH) for the evaluation of the overamplification of the Her2 gene<sup>4-7</sup>. Although relatively simple techniques, H&E and IHC are time consuming assays that may present bias due to reaction conditions and subjectivity in data interpretation<sup>8</sup>. FISH assays are time consuming and require experienced personnel to perform and interpret results<sup>9-10</sup>. Implementation of new clinical technologies that provide precise and rapid diagnosis and characterization of breast

---

<sup>1</sup> Adapted with permission from “Porcari, A. M.; Zhang, J. L.; Garza, K. Y.; Rodrigues-Peres, R. M.; Lin, J. Q.; Young, J. H.; Tibshirani, R.; Nagi, C.; Paiva, G. R.; Carter, S. A.; Sarian, L. O.; Eberlin, M. N.; Eberlin, L. S., Multicenter Study Using Desorption-Electrospray-Ionization-Mass-Spectrometry Imaging for Breast-Cancer Diagnosis. *Analytical Chemistry* **2018**, *90* (19), 11324-11332.” Copyright 2018 American Chemical Society. A.M.Porcari. and J.L. contributed equally to this work and are co-first-authors. K.Y.G. and R.M.R.-P. contributed equally to this work and are co-second-authors. A.M. Porcari, J. Zhang, and L.S. Eberlin prepared and edited the manuscript. All authors revised the manuscript.

cancer are therefore desirable to guide treatment and improve patient care. Molecular technologies offer the opportunity to incorporate cancer-specific biomarkers into clinical decision making. Genetic mutational signatures associated with the molecular and clinical differences of breast cancers, for example, have been incorporated into clinical workflows<sup>11-12</sup>. New technologies that allow rapid assessment of metabolic and protein alterations in breast cancer have also been increasingly explored and have shown great potential for clinical use to expedite diagnosis and treatment decisions<sup>13</sup>.

Mass spectrometry imaging (MSI) technologies offer a powerful tool for chemical and spatial characterization of biological tissues with high specificity and sensitivity, and have been widely explored for human cancer tissue analysis<sup>14-19</sup>, including breast cancer<sup>20-26</sup>. Ambient ionization MSI techniques, such as desorption electrospray ionization (DESI), allow analysis of tissue sections with high-throughput and minimal sample pre-processing<sup>27</sup>, features that are attractive for clinical use in pre-operative cancer diagnosis and intraoperative surgical margin evaluation<sup>28</sup>. A few studies have employed DESI-MSI to investigate metabolic information of human breast cancer in an effort to improve diagnosis and surgical margin evaluation<sup>26, 29-30</sup>. Dill *et al* used DESI to image altered glycerophospholipids in a small set of breast cancer tissue samples<sup>29</sup>. Calligaris *et al* used DESI-MSI to analyze 61 breast tissue samples from 14 patients who had undergone mastectomy<sup>30</sup>. Guenther *et al* used DESI-MSI to characterize surgical biopsies from lesions (28 patients, 28 samples) and tumor bed (22 patients, 98 samples), and achieved an overall accuracy of 98.2% for breast cancer diagnosis<sup>26</sup>. The latter two studies also showed correlation between hormone receptor (HR) status, which combine PR and ER status into

a single HR category, although no correlation between lipid information and Her2 status were found. More recently, we have used DESI-MSI to detect and characterize metastatic breast cancer in lymph nodes <sup>31</sup>. Whereas these studies strongly showcase the potential of MSI techniques to complement histological and histochemical characterization and diagnosis of breast cancer, these isolated investigations have not evaluated the validity of determining biomarker status for breast cancer or the analytical performance of the methods for breast cancer diagnosis across different patient populations and laboratories. Racial, dietary, and environmental traits have been associated with molecular and prognostic differences within breast cancer patients, which may result in molecular variability and thus failure to properly categorize tissue samples <sup>32-33</sup>. Analytically, tissue preparation, tissue storage conditions, choice of instrumentation and experimental parameters have been associated with variabilities in imaging and mass spectra quality by MSI <sup>34</sup>, which could affect the method's performance. Larger studies using a diverse cohort of samples are therefore needed to properly evaluate the robustness of molecular markers and workflows of DESI-MSI for clinical use in breast cancer diagnosis and characterization. Herein, we report a multicenter study using DESI-MSI to investigate the lipid signatures of a diverse set of breast tissues and to validate the predictive performance of the method for breast cancer diagnosis. Samples from 103 patients of various races were independently investigated in the USA and Brazil to validate predictive molecular signatures and evaluate the sensitivity, specificity, and accuracy of the method for breast cancer diagnosis.

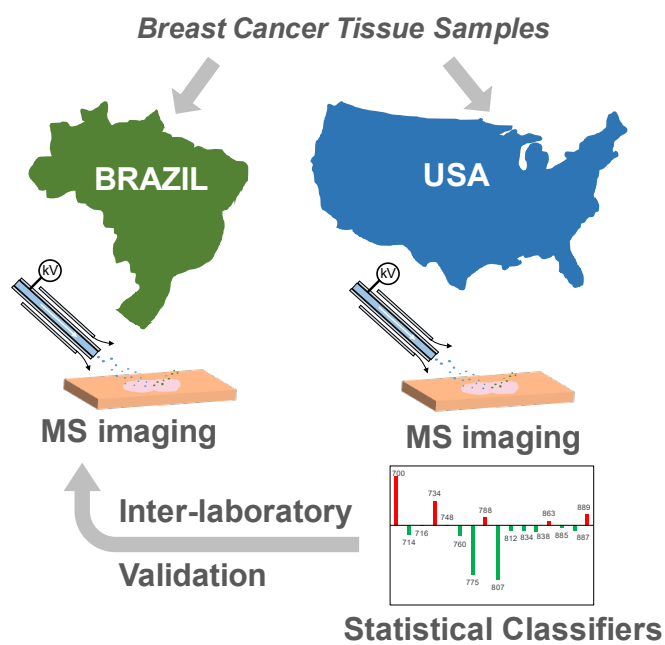


Illustration 2.1: Scheme of DESI-MS imaging of breast tissue sections across multiple centers for validation of the diagnostic potential of lipid markers.

## **MATERIALS AND METHODS**

### **Tissue Collection**

Samples from Brazil were collected from women who agreed to participate in the study and signed the consent form for this purpose before their surgery were collected. Both normal and cancer tissue were collected from women undergoing mastectomy or quadrantectomy as part of their cancer treatment in the Division of Gynecological Oncology and Breast Pathology of CAISM. Immediately after the removal of the surgical specimen, the tissue was taken to the Pathology Laboratory next to the surgical center. The specimen was then macroscopically assessed, and the tumor area was identified. If the tumor area had a sufficient size for diagnostic purposes and research (at least 0.8cm), a sample of the tumor as well as one from the normal glandular area from the same breast (5 cm away from tumor edge) were taken with a scalpel. Both tumor and normal tissues were later confirmed through histopathology by expert pathologist. Samples were snap frozen using liquid N<sub>2</sub> a maximum of four hours after the surgical removal. Then, samples were stored at  $-80^{\circ}\text{C}$  until they were sectioned for DESI-MSI. The medical records were reviewed to obtain their clinical and epidemiological data. Tissue sections of the Brazilian samples were shipped to the USA in dry ice (2-day international shipment).

Samples from European, Asian, and American patients were acquired from the Cooperative Human Tissue Network or Asterand Biosciences. Normal breast samples were acquired from contralateral breasts from bilateral mastectomies, breast reduction surgeries of non-neoplastic purposes, and prophylactic mastectomies as well as from non-cancerous regions adjacent to the tumor. Cancer tissue was selected from invasive mammary ductal

carcinoma of the breast from patients undergoing mastectomy or lumpectomy. Following surgical resection, samples were immediately transported to Surgical Pathology, where they were microscopically evaluated by pathologist, pathology assistant, or a pathology resident. Sterile instruments and equipment including towels, gloves, and ink are used by the pathologist during the examination of the specimen. After a quality control diagnosis, the samples were frozen in vapor phase liquid N<sub>2</sub>, on dry ice, or in liquid nitrogen within 1 to 4 hours of resection. Prior to shipment, all samples were stored in vapor phase liquid N<sub>2</sub>. Samples were shipped in dry ice and stored at -80°C until sectioned and subjected to DESI-MS analysis.

### **Human Breast Tissue**

131 frozen human breast tissue samples were obtained for our study. Demographic and clinicopathologic characteristics of the samples are provided in Table 2.1. Tissue procurement, handling and shipment were performed under approved IRB protocols at the respective institutions. Samples from Brazil were prospectively collected from a clinic at the CAISM Hospital da Mulher Prof. Dr. José Aristodemo Pinotti, at the University of Campinas (Campinas, Sao Paulo, Brazil). All other samples were obtained in the USA from the Cooperative Human Tissue Network (CHTN) or Asterand Biosciences (Detroit, MI). Tissue samples were sectioned at 16 µm thick sections using a CryoStar<sup>TM</sup> NX50 cryostat (Thermo Scientific, San Jose, CA) and stored in a -80°C freezer. Prior to MS imaging, all the glass slides were dried for ~15 min in ambient conditions. After DESI-MSI, the same

Table 2.1: Demographic and clinicopathologic characteristics of samples used in our study.

	Normal Samples, n	IDC Samples, n
<b>Country of Collection</b>	45	86
<b>USA</b>	10	7
<b>Brazil</b>	31	50
<b>Eastern Europe</b>	2	16
<b>Vietnam</b>	2	5
<b>Unknown</b>	0	8
<b>Race</b>		
<b>African American</b>	8	8
<b>Caucasian</b>	35	64
<b>Asian</b>	2	13
<b>ER Status</b>		
<b>Negative</b>		31
<b>Positive</b>		46
<b>Undetermined</b>		6
<b>PR Status</b>		
<b>Negative</b>		41
<b>Positive</b>		36
<b>Undetermined</b>		6
<b>HER2 Status</b>		
<b>Negative</b>		48
<b>Positive</b>		19
<b>Undetermined</b>		22

tissue sections analyzed by DESI-MS imaging were subjected afterwards to standard H&E staining protocol.

Tissue samples were composed of areas corresponding to *in situ* ductal carcinoma, invasive ductal carcinoma, fibrosis within neoplasia, pure fibrosis, necrosis, adipose tissue, vessels, normal glands, hyperplasia, cistus, elastosis and inflammatory infiltrates. All these characteristics were annotated per slide by the pathologist and only the regions of interest (well defined as invasive ductal carcinoma or normal glands/fibrosis) were used for statistical evaluation. Although all the samples collected in Brazil and in the USA had already been histologically characterized in the occasion of their collection, all the samples were stained for H&E and reviewed by the pathologists after analysis by DESI-MSI, thus testifying the classification of the samples.

## **DESI-MSI**

2D Omni Spray DESI imaging platforms (Prosolia Inc., Indianapolis, IN) coupled to an Exactive (Thermo Fisher Scientific, San Jose, CA) in Brazil and an LTQ-Orbitrap Elite (Thermo Fisher Scientific, San Jose, CA) in the USA were used for tissue imaging. Lab-built sprayers were adapted to the commercial DESI imaging stages. DESI-MSI was performed using the histologically compatible solvent system dimethylformamide: acetonitrile (DMF:ACN) 1:1 (v/v) in the negative ion mode<sup>35</sup>. Other experimental parameters for each center are described in Table 2.2. Ion images were assembled using Biomap and MSiReader software<sup>36</sup>. For ion identification, high mass resolution/accuracy

Table 2.2: Summary of the main experimental parameters used in the USA and Brazil DESI-MSI experiments.

	<b>USA</b>	<b>Brazil</b>
<b>Mass Spectrometer</b>	LTQ-Orbitrap Elite	Q-Exactive Hybrid Quadrupole-Orbitrap
<b>S lens RF value</b>	60	100
<b>Resolving Power</b>	60,000	70,000
<b><i>m/z</i> range</b>	100-1500	100-1200
<b>DESI solvent</b>	ACN:DMF (1:1)	ACN:DMF (1:1)
<b>DESI gas pressure</b>	180 psi	150 psi
<b>DESI flow rate</b>	1.5 $\mu\text{L}/\text{mL}$	0.7-1.2 $\mu\text{L}/\text{mL}$
<b>Spatial Resolution</b>	250 $\mu\text{m}$	200 $\mu\text{m}$

measurements were conducted using CID and HCD methods, using the Orbitrap for analysis.

### **Histopathology and light microscopy**

The same tissue sections analyzed by DESI-MS imaging were subjected afterwards to standard H&E staining protocol. Pathologic evaluation was performed by Dr. Geisilene Paiva in Brazil, and Dr. Chandandeep Nagi in the USA using light microscopy. Regions of clear diagnosis were assigned and delineated in the glass slides. Light microscopy images of the H&E stained slides were taken using the EVOS FL Auto Cell Imaging System (Invitrogen, Thermo Fisher Scientific, Waltham, Massachusetts, USA). ER, PR and Her2 status were established using IHC and/or FISH analyses during clinical workflow. The expression of ER and PR was determined by histopathologic analysis for 77 IDC tissue samples based on the percent of cells stained using IHC. Her2 status was first evaluated by histopathologic analysis using IHC, resulting in negative, indeterminate or positive results. For samples with indeterminate Her2 status by IHC, FISH analysis was performed, yielding a final Her2 status determination for 67 of the IDC tissue samples. For our study, samples with staining higher than 10% were considered positive for ER or PR, whereas samples with no positive stain were considered negative.

### **Statistical Analysis**

MS data corresponding to the areas of interest were extracted from the ion images using MSiReader software<sup>36</sup>. Data pre-processing and statistical analysis were performed using the same methodology on the DESI mass spectra profiles from Brazil and USA to identify

predictive ion markers and evaluate the performance of the classifiers for cancer diagnosis. The  $m/z$  range was discretized using binning size of 0.01. Peaks appearing in more than 10% of the pixels were kept for analysis. Pixels were then normalized by sum of intensities after any mass range restriction. After data pre-processing, logistic regression was performed with Lasso regularization using the “glmnet” package in the R language. Regularization parameters were determined by 5-fold cross-validation (CV) analysis. The data acquired in the USA was randomly divided in a training and validation set of samples, 75%-25% per patient basis. The data acquired in Brazil was independently evaluated as a test set using the same methodology. PCA was performed by centering the pre-processed data to mean zero and computing principal components using the `prcomp` function in R. To quantify tissue similarity, the cosine similarity method was used from the `lsa` package in CRAN. All pixels from each condition (USA normal, USA cancer, Brazil normal, Brazil cancer) were averaged to representative spectra. The same DESI mass spectra data ( $m/z > 700$ ) extracted from cancer regions used to build the classification model for IDC diagnosis were used to build classification models to predict positive or negative status for ER, PR and Her2, using a 5-fold CV approach.

## **RESULTS**

### **Molecular imaging of breast tissues by DESI-MSI**

DESI-MSI in the negative ion mode was performed on a total of 131 human breast tissue samples including 86 invasive ductal carcinomas (IDC) and 45 normal breast tissue samples obtained from 103 breast cancer patients. IDC is the most common histologic

subtype of breast cancer, accounting for approximately 80% of all invasive breast tumors. Due to its high incidence and relevance, only IDC tumors were used for our study. IDC tissue sections typically present regions of predominantly tumor cells neighboring adjacent stroma and adipose tissues. Figure 2.1A and 2.1C show a representative mass spectrum extracted from the tumor region of an IDC sample, selected ion images, and optical images of the H&E stained tissue section. The spatial resolution used for DESI-MSI (250  $\mu\text{m}$ ) enabled visualization of histologic features within the IDC tissues, allowing correlation between histology and molecular information. For example, the distribution of the ions corresponding to deprotonated PI(34:1), PI(36:1), and FA(20:4) spatially correlate with regions of IDC (outlined in red), whereas PI(38:4) was detected throughout the entire tissue section, including regions of adjacent normal stroma tissue (outlined in blue). A magnification of the optical image obtained from the H&E stained tissues section shows an overlap between the spatial distribution of PI (36:1) and regions of IDC, and a decrease in abundance of this ion within the surrounding normal stroma cells.

Normal breast tissues typically present stroma and/or adipose tissue surrounding focal regions of normal epithelial glands. Note that tissues classified as “normal” correspond to specimens deemed grossly normal at the time of specimen allocation and further confirmed by histopathologic evaluation. Normal samples were acquired from different breast regions depending on the patient including contralateral breasts from bilateral mastectomies, breast reduction surgeries of non-neoplastic purposes, prophylactic mastectomies, as well as from non-cancerous regions adjacent to the tumor. Figure 2.1B and 2.1D shows representative mass spectrum extracted from normal epithelial cells of a

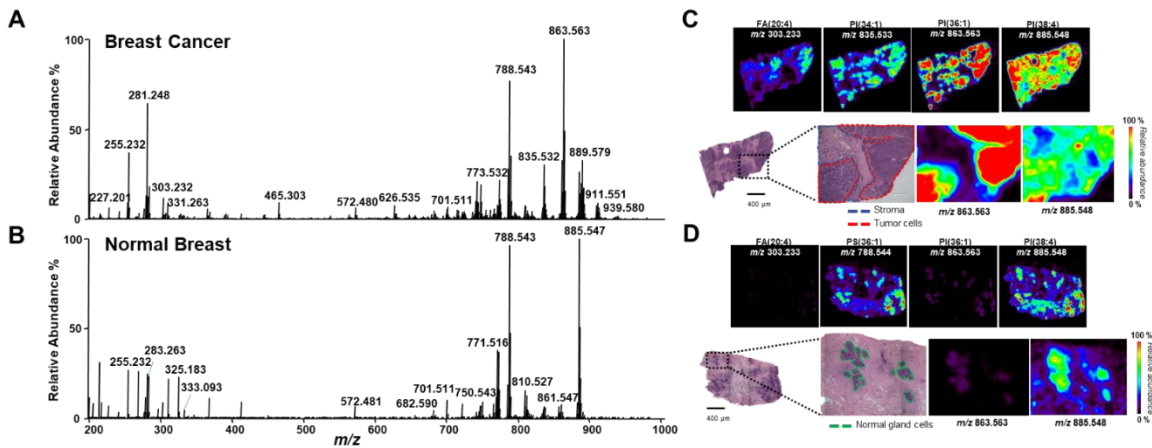


Figure 2.1: Negative ion mode DESI-MSI of IDC and normal breast tissues.

A) Representative metabolic profile for the IDC tissue region. B) Representative metabolic profile for the normal breast tissue region. C) Representative ion images for IDC tissue sample. D) Representative ion images for normal tissue sample. Tumor areas are outlined in red on H&E slides. Areas of red intensity within the ion images represent highest (100%) and black lowest (0%) relative abundances. PI: glycerophosphoinositol; PS: glycerophosphoserine FA: fatty acid. Lipid species are described by number of fatty acid chain carbons and double bonds.

normal tissue sample, selected ion images, and optical images of the H&E stained tissue section. DESI-MSI allowed visualization of focal epithelial glands (outlined in green) within adjacent stroma, which spatially overlapped with regions of high relative abundances of PS(36:1) and PI(38:4), for example. Qualitatively, the mass spectra from normal epithelial glands and IDC tissues presented distinct molecular profiles. For example, lower relative abundance of the ion of  $m/z$  863.563, attributed to PI(36:1) was observed in the mass spectra of normal epithelial glands when compared to that for IDC, whereas the relative abundance of the ion of  $m/z$  771.516, PG(36:3), was higher in the mass spectra of normal epithelial glands. These results showcase the usefulness of DESI-MSI in spatially investigating the lipid profiles of IDC and normal breast cancer tissues, even within fine histological features.

### **DESI-MSI of breast tissue samples from patients of a different race**

Next, we evaluated whether the metabolite and lipid profiles obtained from breast tissues by DESI-MSI were consistent across patients of different race/ethnicity. Normal and cancerous tissue samples from a diverse patient population were obtained from collection sites at different countries including 81 tissue samples from 53 patients from Brazil, 17 tissue samples from 17 patients from the United States of America (USA), 18 tissue samples from 18 patients from Europe, 7 tissue samples from 7 patients from Vietnam, as well as 8 tissue samples from Asia (specific country of origin unavailable) (Figure 2.2A and Table 2.1). For racial classification, we grouped white Americans and white Hispanics into a single “White” group, and afro American and afro Hispanic into a single

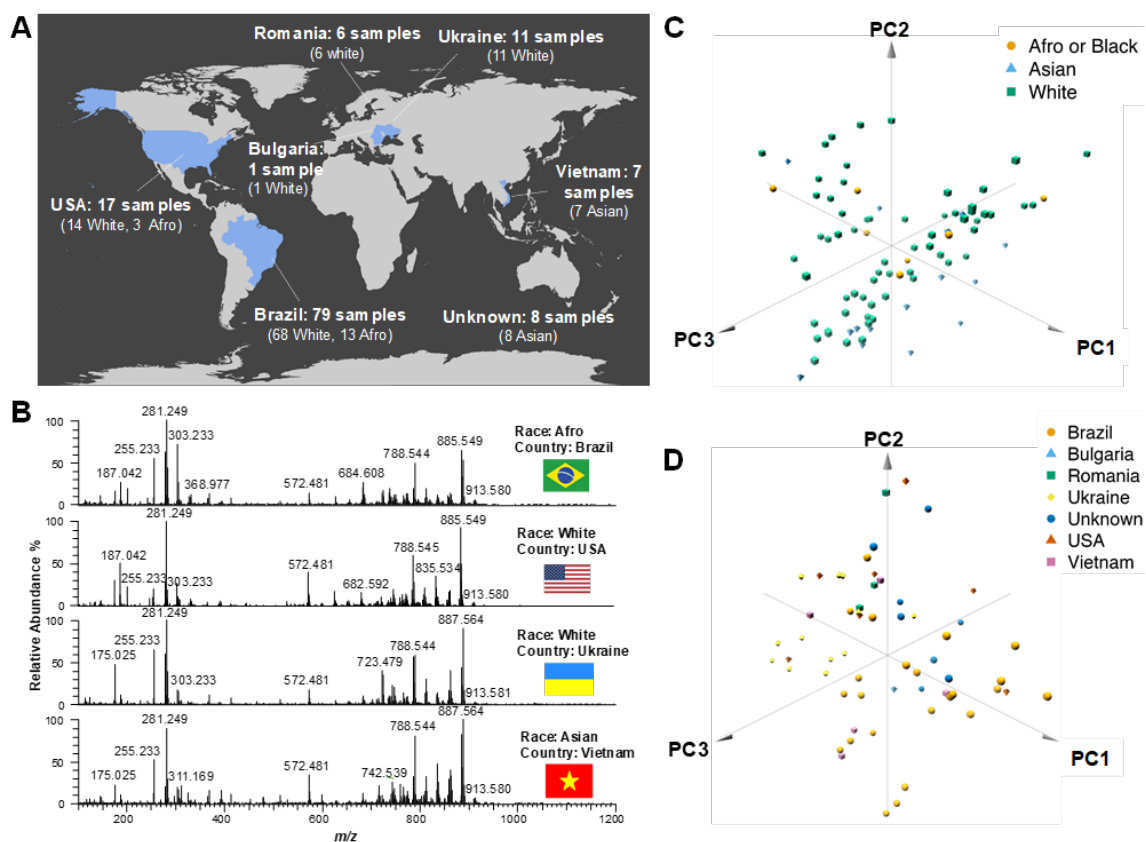


Figure 2.2: DESI-MS and principal component analysis of IDC tissues from patients of different races and country collection sites.

A) DESI-MSI was performed on a large cohort of human tissue samples collected from different country sites and from patients of different races. B) Similar negative ion mode DESI mass spectra were obtained for breast IDC tissue samples from patients of different races and country collection site. Projections of the 86 mass spectra from breast IDC tissue samples onto the first three principal components (PC) do not separate patients by C) race, or D) country of collection, as observed in the 3D PCA plots. The first three PCs explain 72.5% of the total variance of the full dataset.

“Afro” group, resulting in three possible racial groups: White (99 tissue samples from 76 patients), Afro (16 tissue samples from 11 patients), and Asian (15 tissue samples from 15 patients)<sup>37</sup>. In the USA, all tissue samples were analyzed using standardized DESI-MSI experimental parameters. Figure 2.2B shows representative DESI mass spectra obtained from IDC tissue samples from an Afro patient from Brazil, a white patient from the USA, a white patient from Ukraine, and an Asian patient from Vietnam. Overall, consistent trends in the relative abundances of the molecular species (deprotonated molecules) were observed across the mass spectra. For example, the ion of  $m/z$  281.249, attributed to FA(18:1) was detected at the highest relative abundance in comparison to other FA species. In the higher  $m/z$  range where complex lipids are detected, high relative abundances of the ions of  $m/z$  835.533, PI(34:1),  $m/z$  861.550, PI(36:2),  $m/z$  863.563, PI(36:1),  $m/z$  885.548, PI(38:4), and  $m/z$  887.564, PI(38:3), were seen across all mass spectra, although with some variations in their relative abundances. To evaluate the level of variance in the mass spectra from all the patients, we employed unsupervised PCA. No significant separation was observed in the score plots due to patient race based on the DESI mass spectra for cancer (Figure 2.2C) or normal tissues (Figure A2.1A). Further, no significant separation was seen in the score plots due to country of collection site based for cancer (Figure 2.2D) or normal tissues (Figure A2.1B). These results suggest that the metabolite and lipid profiles obtained by DESI-MSI are characteristic of IDC and normal breast tissues across different patient races and unrelated to sample collection site.

### **Inter-laboratory assessment of the reproducibility of DESI-MSI**

Assessment of inter-laboratory reproducibility is essential to demonstrate the robustness of an analytical technology for a targeted application. We evaluated the inter-laboratory reproducibility of DESI-MS for breast cancer tissue imaging by independently analyzing serial tissue sections of the same tissue sample in the USA and in Brazil, using similar experimental parameters (Table 2.2 and Figure A2.2). The mass spectra obtained in the USA and Brazil from the same region of the tissue sections showed similar patterns, with variations in the low mass range from  $m/z$  100-700 observed more clearly for normal tissue samples. Cosine similarity analyses were conducted to quantitatively evaluate similarity between the mass spectra obtained in Brazil and in the USA. As Table A2.1 summarizes, a low cosine value of 0.51 was obtained when comparing the full mass spectra of the normal samples analyzed in Brazil with the normal samples analyzed in the USA. When the  $m/z$  range was restricted to  $m/z$  700-1,200, the cosine value increased to 0.85, reflecting higher similarity at the higher  $m/z$  range. Further evaluation of the inter-laboratory data revealed inconsistencies in the relative and total abundances of metabolites, FA, and background ions detected at the low  $m/z$  range. As the DESI ion images and mass spectra of Figure A2.2A show, higher relative abundance of ions attributed to ascorbic acid and FA(20:4) were detected within the tissue sections analyzed in the USA compared to the adjacent tissue sections analyzed in Brazil. An unidentified background ion of  $m/z$  415.140 was only observed in the data acquired in Brazil. Higher consistency in the relative and total ion abundances and spatial distribution was observed for the complex lipid region of the mass spectra ( $m/z > 700$ ), where glycerophospholipids are commonly seen. The

inconsistency in the ions detected at low  $m/z$  range was not as pronounced for data obtained from cancer regions of IDC samples (Figure 2.2B), which is reflected in the similar cosine values obtained for the full  $m/z$  range (0.91) and the restricted  $m/z$  range (0.92).

### **Predictive models of IDC based on lipid DESI-MSI data**

To evaluate if the metabolite and lipid information obtained by DESI-MSI are predictive of breast cancer, we used the Lasso method to build a classification model for IDC<sup>38-39</sup>. DESI mass spectra data were extracted from areas within the ion images that presented predominantly IDC tumor or normal epithelial glands, yielding a total of 36,426 individual pixels/mass spectra for all data acquired (USA and Brazil). The data was restricted to the high range of  $m/z$  700-1,200, which provided reproducible results as previously described. Next, 44 samples from 27 of the 53 Brazilian patients were randomly selected and excluded from sample set with the goal of being used as an independent inter-laboratory validation set in our study. The remaining 87 tissue samples were randomly divided into a training set and a validation set using a 75%-25% split, respectively. The training set (45 IDC and 21 normal) yielded a total of 18,691 pixels (17,606 IDC and 1,085 normal, all acquired in the USA), which were used to build the classification model. Note that many of the normal breast tissue samples analyzed were predominantly composed of fat, therefore the total number of pixels extracted from focal regions presenting epithelial cells were limited. The remaining set of samples (15 IDC and 6 normal) were later used as an independent intra-laboratory validation set. Prediction results are presented as sensitivity, specificity, and overall agreement on a per-pixel and per-patient basis (Figure

2.3 and Table A2.2). For the training set, 97.6% sensitivity, 96.7% specificity and 97.6% accuracy were achieved on a per-pixel basis for IDC diagnosis using 5-fold cross-validation (Figure 2.3A). On a per-patient analysis, just a single cancer tissue sample was misclassified as normal tissue.

### **Intra- and inter-laboratory validation of the predictive power of the Lasso classification model**

We have also evaluated the robustness and performance of our classification model in predicting breast cancer diagnosis from the DESI data ( $m/z$  700-1,200) acquired from independent sample sets analyzed in the USA (intra-laboratory) and in Brazil (inter-laboratory). Our model was first tested using the held-out test set analyzed in the USA (15 IDC and 6 normal), which yielded a total of 6,385 pixels (6,173 IDC and 185 normal). Excellent performance was achieved, that is, 99.1% sensitivity, 99.5% specificity and 99.2% accuracy per-pixel, as well as 100.0% sensitivity, specificity and accuracy per-patient (Figure 2.3B). The classification model was then used to predict on data acquired in Brazil for the held-out validation set of 44 tissue samples from 27 Brazilian patients, which yielded a total of 11,377 pixels (9,290 IDC and 2,087 normal). Remarkably, excellent performance was seen on a per-pixel basis for IDC diagnosis (Figure 2.3C): 94.7% sensitivity, 97.8% specificity and 95.3% accuracy. On a per-patient analysis, only a single cancer sample was misclassified as normal. These results suggest that a single Lasso model built from DESI-MSI data ( $m/z$  700-1200) can be used to classify intra- and inter-laboratory data acquired under optimized conditions from independent sample sets.

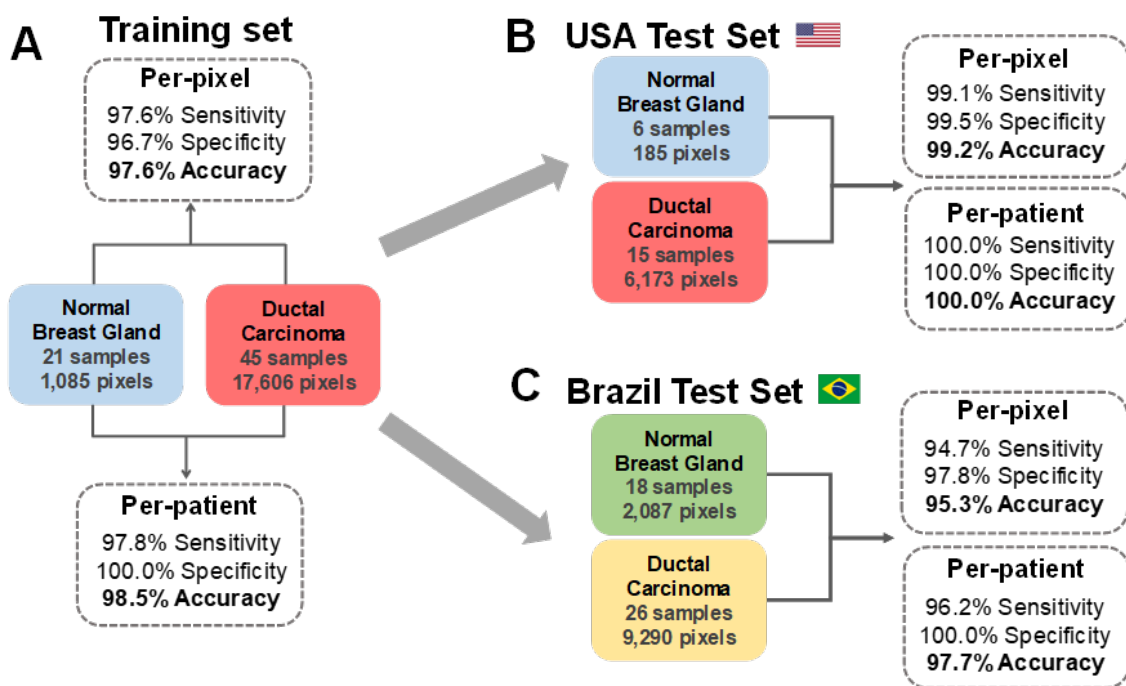


Figure 2.3: Predictive performance of the IDC classification model.

Classification per-pixel and per-patient prediction results are shown for normal and IDC, including sensitivity, specificity, and overall accuracy in A) Cross-validation performed with data acquired in the USA, B) test set with data acquired in the USA, and C) test set with data acquired in Brazil.

Further, the predictive complex lipids selected by the Lasso model are robust for breast cancer diagnosis.

### **Predictive features selected by Lasso**

A total of 44 predictive  $m/z$  values were selected for the classification model with assigned mathematical weights related to their importance in distinguishing between IDC and normal tissues. Positive weights were attributed by the Lasso to 17  $m/z$  values that were important in characterizing IDC, whereas negative weights were given to 27 values which were important to characterizing normal tissue. Identification of the ions corresponding to the selected  $m/z$  values were performed using tandem MS experiments and high mass accuracy measurements followed by comparison to lipid databases (Table 2.3). The five largest negative weights were assigned to PE(36:2) of  $m/z$  742.539, PG(36:4) of  $m/z$  769.502, PC(34:2) of  $m/z$  792.530, PE(O/P-38:5) of  $m/z$  750.545, and PS(36:2) of  $m/z$  786.529, which are the ions indicative of normal breast tissue. For IDC tissue classification, however, the highest five positive weights were assigned by the Lasso to PI(36:2) ions of  $m/z$  861.549, PG(34:1) of  $m/z$  747.517, PG(40:7) of  $m/z$  819.517, PS(38:4) of  $m/z$  810.525, and PE(38:4) of  $m/z$  766.539. Note also that the weights assigned to these ions corroborate with trends observed in the mass spectra and DESI ion images for IDC and normal tissues, which showcases the power of the Lasso statistical model in selecting predictive features that are potential biomarkers of disease states.

Table 2.3: Tentatively identified species selected by the Lasso as significant contributors to the molecular model for IDC and normal breast tissue classification with attributed statistical weights.

	Measured $m/z$	Lipid Assignment	Exact $m/z$	Mass Error (ppm)	Proposed Formula	Lasso Weight
Characteristic of Normal Breast Tissue	742.539	PE(36:2)	742.539	-0.4	C <sub>41</sub> H <sub>77</sub> NO <sub>8</sub> P	-213
	769.502	PG(36:4)	769.503	-0.9	C <sub>42</sub> H <sub>74</sub> O <sub>10</sub> P	-189.6
	792.53	PC(34:2)	792.532	2.5	C <sub>42</sub> H <sub>80</sub> O <sub>8</sub> PCl	-174.7
	750.545	PE(O-38:5)	750.544	0.7	C <sub>43</sub> H <sub>77</sub> NO <sub>7</sub> P	-169.4
	786.529	PS(36:2)	786.529	-0.4	C <sub>42</sub> H <sub>77</sub> NO <sub>10</sub> P	-166.3
	778.539	PE(39:5)	778.539	-0.6	C <sub>44</sub> H <sub>77</sub> NO <sub>8</sub> P	-149.5
	748.528	PE(O-38:6)	748.529	-0.8	C <sub>43</sub> H <sub>75</sub> NO <sub>7</sub> P	-148.1
	727.527	PA(38:2)	727.528	-1.9	C <sub>41</sub> H <sub>76</sub> O <sub>8</sub> P	-133.6
	734.534	PS(O-33:0)	734.534	-0.3	C <sub>39</sub> H <sub>77</sub> NO <sub>9</sub> P	-105
	891.722	TG(52:3)	891.721	0.3	C <sub>55</sub> H <sub>100</sub> O <sub>6</sub> Cl	-104.6
	770.534	PS(P-36:2) or PS(O-36:3)	770.534	0.1	C <sub>42</sub> H <sub>77</sub> NO <sub>9</sub> P	-39.8
	700.602	Cer(t42:1)	700.602	0.4	C <sub>42</sub> H <sub>83</sub> NO <sub>4</sub> Cl	-38.8
	816.576	PS(38:1)	816.576	-0.6	C <sub>44</sub> H <sub>83</sub> NO <sub>10</sub> P	-32.9
	788.545	PS(36:1)	788.544	0.6	C <sub>42</sub> H <sub>79</sub> NO <sub>10</sub> P	-25.3
	752.553	PE(O-38:4)	752.56	-9	C <sub>43</sub> H <sub>79</sub> NO <sub>7</sub> P	-24.8
	885.55	PI(38:4)	885.55	-0.3	C <sub>47</sub> H <sub>82</sub> O <sub>13</sub> P	-19.9
	837.547	PI(34:0)	837.55	-3.9	C <sub>43</sub> H <sub>82</sub> O <sub>13</sub> P	-14.3
	794.55	PC(34:1)	794.547	-3.8	C <sub>42</sub> H <sub>82</sub> O <sub>8</sub> NPCl	-14.1
	723.478	CL(72:8)	723.479	-0.8	C <sub>81</sub> H <sub>140</sub> O <sub>17</sub> P <sub>2</sub>	-4.7
724.485	CL(72:7)	724.487	-2.6	C <sub>81</sub> H <sub>142</sub> O <sub>17</sub> P <sub>2</sub>	-2.5	
Characteristic of IDC Tissue	846.657	PS(O-41:0)	846.659	-3.3	C <sub>47</sub> H <sub>93</sub> NO <sub>9</sub> P	12.3
	835.534	PI(34:1)	835.534	-0.7	C <sub>43</sub> H <sub>80</sub> O <sub>13</sub> P	17.2
	887.564	PI(38:3)	887.566	-2.3	C <sub>47</sub> H <sub>84</sub> O <sub>13</sub> P	18.1
	838.559	PS(40:4)	838.56	-1.6	C <sub>46</sub> H <sub>81</sub> NO <sub>10</sub> P	34.3
	773.533	PG(36:2)	773.534	-0.8	C <sub>42</sub> H <sub>78</sub> O <sub>10</sub> P	56.2
	760.513	PS(34:1)	760.513	-0.3	C <sub>40</sub> H <sub>75</sub> NO <sub>10</sub> P	90.8
	766.539	PE(38:4)	766.539	0	C <sub>43</sub> H <sub>77</sub> NO <sub>8</sub> P	116.4
	810.525	PS(38:4)	810.529	-4.9	C <sub>44</sub> H <sub>77</sub> NO <sub>10</sub> P	120.4
	819.517	PG(40:7)	819.518	-0.9	C <sub>46</sub> H <sub>76</sub> O <sub>10</sub> P	169.3
	747.517	PG(34:1)	747.518	-0.9	C <sub>40</sub> H <sub>76</sub> O <sub>10</sub> P	187.9
	861.549	PI(36:2)	861.55	-0.7	C <sub>45</sub> H <sub>82</sub> O <sub>13</sub> P	237.7

## Prediction of Breast Cancer Hormone Receptor and Her2 Status

Next, we investigated if the molecular information obtained by DESI-MSI enabled prediction of positive or negative status for ER, PR, combined hormone receptor (HR), and Her2 by building classification models for each class using IHC or FISH results as the gold standard. For the 77 IDC samples with ER status, 46 samples were ER+ (16,163 pixels), and 31 samples were ER- (14,315 pixels). The classification model built to predict ER status achieved 86.1% sensitivity, 91.6% specificity and 88.7% accuracy on a per-pixel basis (Figure 2.4). On a per-patient analysis, five ER+ tissue samples were misclassified as ER- tissues, and two ER- tissue samples were misclassified as ER+ tissues, resulting in 89.1% sensitivity, 93.5% specificity and 90.9% accuracy. For PR status, the classification model built using 36 PR+ samples (12,700 pixels) and 41 PR- samples (17,720 pixels) yielded 95.5% sensitivity, 84.3% specificity and 89.0% accuracy on a per-pixel basis. On a per-patient analysis, eight PR- tissue samples were misclassified as PR+ tissues. Samples were further combined into hormone receptor (HR) positive (ER+ and PR+) and HR negative (ER- and PR-) groups based on the combined ER and PR status. The classification model built using 36 HR- samples (14,315 pixels) and 31 HR+ samples (12,700 pixels) yielded 96.2% sensitivity, 95.2% specificity and 95.7% accuracy on a per-pixel basis, and 100.0% sensitivity, specificity and accuracy on a per-patient analysis. These accuracies are similar to the overall 96.0% accuracy achieved on a per-patient analysis (n=27) for HR positive and negative status described by Guenther *et al.*,<sup>26</sup> and corroborate with the PCA clustering observed for HR+ versus HR- samples (n=14) by Calligaris *et al.*<sup>30</sup> Next, we built a Her2 classification model using 19 Her2+ samples (8,536 pixels) and 48 Her2-

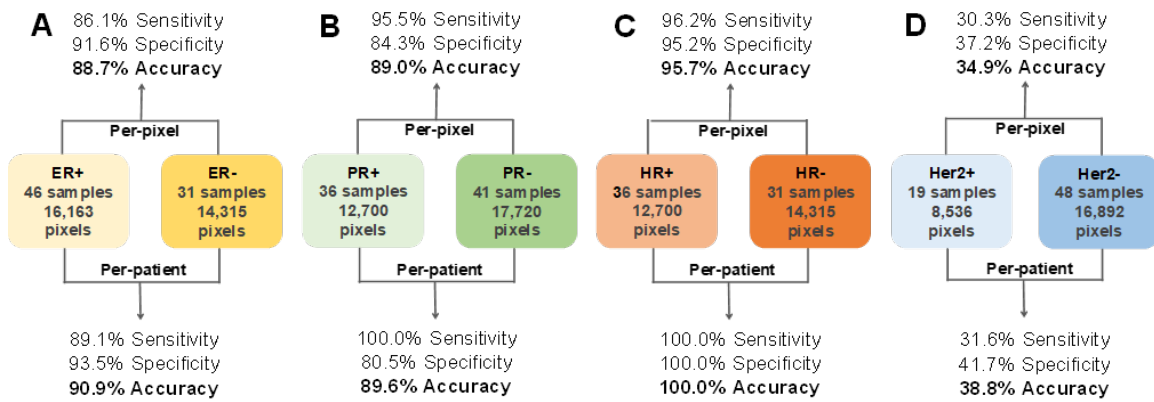


Figure 2.4: Per-pixel and per-patient prediction results for positive and negative receptor status classification.

Per-pixel and per-patient sensitivity, specificity and overall accuracy prediction results for positive or negative A) ER, B) PR, C) HR, and D) Her2 status. Prediction results were obtained using a 5-fold CV approach.

samples (16,892 pixels), but poor classification results were achieved (30.3% sensitivity, 37.2% specificity and 34.9% accuracy on a per-pixel basis). Interestingly, no separation or discrimination was achieved based on the Her2 status previously reported by Guenther *et al* (n=27) and Calligaris *et al* (n=14), which again corroborate with our results.

## **DISCUSSION**

We have performed a multicenter study using DESI-MSI to investigate the metabolic signatures of a diverse set of 131 breast tissue samples from 103 breast cancer patients from various countries including USA, Brazil, Ukraine, Vietnam, and others. DESI-MSI enabled clear visualization of fine histologic features in breast tissues and thus a detailed investigation of metabolic profiles characteristic of breast cancer, normal breast glands and adjacent stroma. Using tissue samples obtained from patients from various countries, we showed that DESI-MSI allows detection of lipid profiles that are characteristic of cancer tissue independent of patient race or ethnicity. These molecular profiles, when used to build classification models for cancer diagnosis, provide high sensitivity, specificity and accuracies for both training and test sample sets using data acquired in the USA and revealed predictive lipid markers. Most notably, the molecular classifiers showed high performance for cancer diagnosis for an independent dataset acquired in a laboratory in Brazil using standardized experimental conditions. Classifiers built to characterize PR and ER status in breast cancer samples also showed high accuracy to determine hormone receptor status. Altogether, our study provides strong evidence that DESI-MSI is a robust molecular technology able to provide rapid diagnosis and

characterization of breast tissues, with potential use in the clinical setting across different institutions.

Alterations in the abundances of FA and glycerophospholipids were detected in our study, which reflect known abnormalities in cancer cell metabolism<sup>40</sup> and breast cancer tissue<sup>13, 41-42</sup>. Fatty acid synthesis, for example, is highly relevant in breast cancer tumor biology due to the ability of these molecules to modulate the fluidity of lipid membranes and to affect cellular machinery<sup>43</sup>. Several separate, single-center studies suggest that lipid MSI signatures are diagnostic of breast cancer<sup>22, 25, 30</sup>. A MALDI-MSI study has reported increased relative abundances of monounsaturated FA in comparison to polyunsaturated FA in breast cancer than in adjacent normal tissues<sup>22</sup>. Chen *et al.* also found the FA(18:2) and FA(18:1) to be more abundant in cancer tissue when compared to normal tissue analyzed by air flow-assisted ionization MSI<sup>25</sup> whereas Agar *et al.* also reported FA(18:1) as a DESI-MSI discriminator for cancer detection and margin analysis<sup>44</sup>. Similarly, we consistently noted high relative abundances of FA(18:1), at  $m/z$  281.249, in breast cancer tissues in our study and identified several glycerophospholipid ions as predictive markers of breast cancer, with increased relative abundance in malignant histologic regions of tissue sections. Also using MALDI-MSI, Toi *et al.* have previously reported altered relative abundances of PIs in malignant epithelial regions of breast cancer tissues<sup>20</sup>. In their study, PI(36:1), for example, was observed in high relative abundances in cancer tissue when compared to benign epithelial regions, while PI(38:3) was putatively associated with cancer cell invasion. Similarly, high relative abundances of the PI(36:1) ion of  $m/z$  863.563 as well as PI(36:2) of  $m/z$  861.549 were consistently observed in breast cancer tissues in

comparison to normal tissue samples (Figure 2.1C), hence PI(36:2) was selected and shown to be highly predictive of breast IDC tissue by the Lasso classification model. Lipid information acquired by DESI-MSI was also used by Takats *et al.* to build classification models for breast cancer diagnosis based on a subset of 19 predictive features, including various FA and glycerophospholipids such as PE, PC and PI<sup>45</sup>. Within these, three glycerophospholipid species, PC(34:2), PC(34:1) and PI(38:3), were also selected as predictive markers by our classifier. Our study now confirms with comprehensive data that lipid profiles are robust diagnostic markers of breast cancer and that such markers are valid across different patient populations. Our PCA results also showed great similarity for the breast IDC DESI-MS data regardless of race, further demonstrating a commonality of diagnostic lipid profiles. Future studies are needed to validate these findings on larger patient cohorts.

The main goal of our multi-center study was to evaluate the performance of DESI-MSI workflow in producing reproducible data for breast cancer diagnosis across institutions and operators. A few multicenter studies have been performed to evaluate the performance of proteomics analysis for breast cancer diagnosis using traditional proteomics assay<sup>46</sup> and MALDI-MSI<sup>47</sup>. In the MALDI-MSI study, 40 breast cancer tissues were analyzed in two centers in Europe (n=12 in Munich, and n=18 in Leiden) using independent sample sets, methods, and operators<sup>47</sup>. Hierarchical clustering yielded 100% and 80.9% classification accuracies for discriminating extratumoral and intratumoral stromal profiles in the Munich and Leiden data sets, respectively. In our study, sample exchange among centers was implemented and a standardized experimental workflow was

adopted to ensure uniformity in the analytical approach of DESI-MSI employed in the USA and Brazil, despite differences in the mass spectrometer platforms and minor operational parameters. Our inter-laboratory analysis using the same tissue samples analyzed in Brazil and the USA revealed high mass spectra similarity in the high  $m/z$  region ( $m/z$  700-1200) of the data for both normal (cosine similarity = 0.86) and cancer (cosine similarity = 0.93) tissues, and moderate similarity in the relative abundances of low  $m/z$  ions ( $m/z < 400$ ) were observed for normal breast tissues (cosine similarity = 0.48). The DESI mass spectra in the low  $m/z$  region is mostly comprised of ions identified as background solvent peaks, small metabolites, and fatty acids. Whereas variations in chemical noise and background ions were anticipated across different mass spectrometers, differences in the relative abundances of biologically-relevant ions such as FA were unexpected. We suggest that these differences could be due to small variations in the DESI spray geometry parameters and/or the mass spectrometer S-lens ion optics RF values, which may lead to more efficient desorption and/or transmission of ions. Further, these differences could be due to lipid degradation owing to possible variations in temperatures and freezing conditions during international sample shipment in dry ice, factors which have been associated to increase in FA abundance in DESI mass spectra profiles (see Methods: Tissue Collection)<sup>48</sup>. As normal breast tissue provides poorer molecular profiles than IDC, higher variance was observed in the low  $m/z$  range. Nevertheless, high reproducibility in the higher  $m/z$  range in which glycerophospholipids and other complex lipid markers are detected was seen for normal and cancer tissues analyzed in the USA and Brazil. Lasso classifiers built using 44 predictive features detected at the restrictive  $m/z$  range provided outstanding performance

in cross-validation both per-pixel (97.6% accuracy, n=18,691) and per-patient (98.5% accuracy, n=66). The classification models provided high accuracy in cancer diagnosis using an independent dataset acquired in USA (99.2% per-pixel accuracy, n=6,358) and, most remarkably, acquired in Brazil (95.3% per-pixel accuracy, n=11,377). These results validate the predictive power of the lipid ion markers and classification models built from DESI-MSI data for breast cancer diagnosis and provides strong evidence that this technology is robust for breast cancer diagnosis across centers and populations.

Determining ER, PR and Her2 status is essential for identifying breast cancer molecular subtypes to help guide treatment for patients. Previous studies have also suggested a relationship between lipid profiles and breast cancer molecular subtypes<sup>42</sup>. In our study, we further evaluated the ability of using the lipid data acquired by DESI-MSI in the USA to build predictive models for positive or negative status of Her2, PR, and ER separately, as well as combined HR status. Per-patient accuracy of 90.9% was achieved for predicting positive or negative ER status (n=77), whereas 89.6% per-patient accuracy was achieved for predicting positive or negative PR status (n=77). When evaluating the combined HR status, we achieved 100% per-patient accuracy. Although prediction of combined HR status has been previously reported by DESI-MSI (accuracy of 86.7%, n=27), our results now indicate that the lipid information is also predictive of ER and PR status separately. When evaluating Her2 status, we found no relationship between lipid profiles detected by DESI-MSI and Her2 status (38.8% per-patient accuracy, n=67), as previously found using DESI-MSI. This confusion could be due to intra-tumor heterogeneity of Her2 positive breast cancers<sup>49-50</sup>, which may lead to variations in lipid

metabolism within the cancer tissue regions from which mass spectra were extracted for statistical analysis. The use of FISH to determine HER2 status was also only employed when IHC results was “undetermined”, potentially leading to higher incidence of inaccurate Her2 status <sup>51</sup>. Further studies using IHC and FISH assays to investigate the spatial expression of Her2 in each tissue section correlated to lipid abundances will be performed to better investigate these observations. In addition, further studies using larger sample cohorts will be performed to investigate possible correlations between lipids profiles detected by DESI-MS imaging and other patient and clinical characteristics including breast cancer molecular subtypes, stage, and treatment choice.

## **CONCLUSION**

In conclusion, our study provides strong evidence that the lipid information acquired by DESI-MSI is highly accurate in predicting breast cancer, as well as ER and PR status. Most importantly, our multi-center study has demonstrated that DESI-MSI is a robust, highly reproducible technology for rapid breast cancer tissue diagnosis and may be useful in the clinical setting.

## REFERENCES

1. Koboldt, D. C.; Fulton, R. S.; McLellan, M. D.; Schmidt, H.; Kalicki-Veizer, J.; McMichael, J. F.; Fulton, L. L.; Dooling, D. J.; Ding, L.; Mardis, E. R.; Wilson, R. K.; Ally, A.; Balasundaram, M.; Butterfield, Y. S. N.; Carlsen, R.; Carter, C.; Chu, A.; Chuah, E.; Chun, H.-J. E.; Coope, R. J. N.; Dhalla, N.; Guin, R.; Hirst, C.; Hirst, M.; Holt, R. A.; Lee, D.; Li, H. I.; Mayo, M.; Moore, R. A.; Mungall, A. J.; Pleasance, E.; Robertson, A. G.; Schein, J. E.; Shafiei, A.; Sipahimalani, P.; Slobodan, J. R.; Stoll, D.; Tam, A.; Thiessen, N.; Varhol, R. J.; Wye, N.; Zeng, T.; Zhao, Y.; Birol, I.; Jones, S. J. M.; Marra, M. A.; Cherniack, A. D.; Saksena, G.; Onofrio, R. C.; Pho, N. H.; Carter, S. L.; Schumacher, S. E.; Tabak, B.; Hernandez, B.; Gentry, J.; Huy, N.; Crenshaw, A.; Ardlie, K.; Beroukhim, R.; Winckler, W.; Getz, G.; Gabriel, S. B.; Meyerson, M.; Chin, L.; Park, P. J.; Kucherlapati, R.; Hoadley, K. A.; Auman, J. T.; Fan, C.; Turman, Y. J.; Shi, Y.; Li, L.; Topal, M. D.; He, X.; Chao, H.-H.; Prat, A.; Silva, G. O.; Iglesia, M. D.; Zhao, W.; Usary, J.; Berg, J. S.; Adams, M.; Booker, J.; Wu, J.; Gulabani, A.; Bodenheimer, T.; Hoyle, A. P.; Simons, J. V.; Soloway, M. G.; Mose, L. E.; Jefferys, S. R.; Balu, S.; Parker, J. S.; Hayes, D. N.; Perou, C. M.; Malik, S.; Mahurkar, S.; Shen, H.; Weisenberger, D. J.; Triche, T., Jr.; Lai, P. H.; Bootwalla, M. S.; Maglinte, D. T.; Berman, B. P.; Van den Berg, D. J.; Baylin, S. B.; Laird, P. W.; Creighton, C. J.; Donehower, L. A.; Getz, G.; Noble, M.; Voet, D.; Saksena, G.; Gehlenborg, N.; DiCara, D.; Zhang, J.; Zhang, H.; Wu, C.-J.; Liu, S. Y.; Lawrence, M. S.; Zou, L.; Sivachenko, A.; Lin, P.; Stojanov, P.; Jing, R.; Cho, J.; Sinha, R.; Park, R. W.; Nazaire, M.-D.; Robinson, J.; Thorvaldsdottir, H.; Mesirov, J.; Park, P. J.; Chin, L.; Reynolds, S.; Kreisberg, R. B.; Bernard, B.; Bressler, R.; Erkkila, T.; Lin, J.; Thorsson, V.; Zhang, W.; Shmulevich, I.; Ciriello, G.; Weinhold, N.; Schultz, N.; Gao, J.; Cerami, E.; Gross, B.; Jacobsen, A.; Sinha, R.; Aksoy, B. A.; Antipin, Y.; Reva, B.; Shen, R.; Taylor, B. S.; Ladanyi, M.; Sander, C.; Anur, P.; Spellman, P. T.; Lu, Y.; Liu, W.; Verhaak, R. R. G.; Mills, G. B.; Akbani, R.; Zhang, N.; Broom, B. M.; Casant, T. D.; Wakefield, C.; Unruh, A. K.; Baggerly, K.; Coombes, K.; Weinstein, J. N.; Haussler, D.; Benz, C. C.; Stuart, J. M.; Benz, S. C.; Zhu, J.; Szeto, C. C.; Scott, G. K.; Yau, C.; Paul, E. O.; Carlin, D.; Wong, C.; Sokolov, A.; Thusberg, J.; Mooney, S.; Sam, N.; Goldstein, T. C.; Ellrott, K.; Grifford, M.; Wilks, C.; Ma, S.; Craft, B.; Yan, C.; Hu, Y.; Meerzaman, D.; Gastier-Foster, J. M.; Bowen, J.; Ramirez, N. C.; Black, A. D.; Pyatt, R. E.; White, P.; Zmuda, E. J.; Frick, J.; Lichtenberg, T.; Brookens, R.; George, M. M.; Gerken, M. A.; Harper, H. A.; Leraas, K. M.; Wise, L. J.; Tabler, T. R.; McAllister, C.; Barr, T.; Hart-Kothari, M.; Tarvin, K.; Saller, C.; Sandusky, G.; Mitchell, C.; Iacocca, M. V.; Brown, J.; Rabeno, B.; Czerwinski, C.; Petrelli, N.; Dolzhansky, O.; Abramov, M.; Voronina, O.; Potapova, O.; Marks, J. R.; Suchorska, W. M.; Murawa, D.; Kycler, W.; Ibbs, M.; Korski, K.; Spsychala, A.; Murawa, P.; Brzezinski, J. J.; Perz, H.; Lazniak, R.; Teresiak, M.; Tatka, H.; Leporowska, E.; Bogusz-Czerniewicz, M.; Malicki, J.; Mackiewicz, A.; Wiznerowicz, M.; Xuan Van, L.; Kohl, B.; Nguyen Viet, T.; Thorp, R.; Nguyen Van, B.; Sussman, H.; Bui Duc, P.; Hajek, R.; Nguyen Phi, H.; Tran Viet The, P.; Huynh Quyet, T.; Khan, K. Z.; Penny, R.; Mallery, D.; Curley, E.; Shelton, C.; Yena, P.; Ingle, J. N.; Couch, F. J.; Lingle, W. L.; King, T. A.; Gonzalez-Angulo, A. M.; Mills, G. B.; Dyer, M. D.; Liu, S.; Meng, X.; Patangan, M.; Waldman, F.; Stoeppler, H.; Rathmell, W. K.; Thorne, L.; Huang, M.; Boice, L.; Hill, A.; Morrison, C.; Gaudioso, C.; Bshara, W.; Daily, K.; Egea, S. C.; Pegram, M. D.; Gomez-Fernandez, C.; Dhir, R.; Bhargava, R.; Brufsky, A.; Shriver, C. D.; Hooke, J. A.; Campbell, J. L.; Mural, R. J.; Hu, H.; Somiari, S.; Larson, C.; Deyarmin, B.; Kvecher, L.; Kovatich, A. J.; Ellis, M. J.; King, T. A.; Hu, H.; Couch, F. J.; Mural, R. J.; Stricker, T.; White, K.; Olopade, O.; Ingle, J. N.; Luo, C.; Chen, Y.; Marks, J. R.; Waldman, F.; Wiznerowicz, M.; Bose, R.; Chang, L.-W.; Beck, A. H.; Gonzalez-Angulo, A. M.; Pihl, T.; Jensen, M.; Sfeir, R.; Kahn, A.; Chu, A.; Kothiyal, P.; Wang, Z.; Snyder, E.; Pontius, J.; Ayala, B.; Backus, M.; Walton, J.; Baboud, J.; Berton, D.; Nicholls, M.; Srinivasan,

D.; Raman, R.; Girshik, S.; Kigonya, P.; Alonso, S.; Sanbhadti, R.; Barletta, S.; Pot, D.; Sheth, M.; Demchok, J. A.; Shaw, K. R. M.; Yang, L.; Eley, G.; Ferguson, M. L.; Tarnuzzer, R. W.; Zhang, J.; Dillon, L. A. L.; Buetow, K.; Fielding, P.; Ozenberger, B. A.; Guyer, M. S.; Sofia, H. J.; Palchik, J. D.; Canc Genome Atlas, N., Comprehensive molecular portraits of human breast tumours. *Nature* **2012**, *490* (7418), 61-70.

2. Jemal, A.; Bray, F.; Center, M. M.; Ferlay, J.; Ward, E.; Forman, D., Global Cancer Statistics. *Ca-a Cancer Journal for Clinicians* **2011**, *61* (2), 69-90.

3. Esserman, L. J.; Berry, D. A.; DeMichele, A.; Carey, L.; Davis, S. E.; Buxton, M.; Hudis, C.; Gray, J. W.; Perou, C.; Yau, C.; Livasy, C.; Krontiras, H.; Montgomery, L.; Tripathy, D.; Lehman, C.; Liu, M. C.; Olopade, O. I.; Rugo, H. S.; Carpenter, J. T.; Dressler, L.; Chhieng, D.; Singh, B.; Mies, C.; Rabban, J.; Chen, Y. Y.; Giri, D.; van 't Veer, L.; Hylton, N., Pathologic complete response predicts recurrence-free survival more effectively by cancer subset: results from the I-SPY 1 TRIAL--CALGB 150007/150012, ACRIN 6657. *Journal of clinical oncology : official journal of the American Society of Clinical Oncology* **2012**, *30* (26), 3242-9.

4. Kos, Z.; Dabbs, D. J., Biomarker assessment and molecular testing for prognostication in breast cancer. *Histopathology* **2016**, *68* (1), 70-85.

5. Perou, C. M.; Sorlie, T.; Eisen, M. B.; van de Rijn, M.; Jeffrey, S. S.; Rees, C. A.; Pollack, J. R.; Ross, D. T.; Johnsen, H.; Akslén, L. A.; Fluge, O.; Pergamenschikov, A.; Williams, C.; Zhu, S. X.; Lonning, P. E.; Borresen-Dale, A. L.; Brown, P. O.; Botstein, D., Molecular portraits of human breast tumours. *Nature* **2000**, *406* (6797), 747-52.

6. Perou, C. M., Molecular stratification of triple-negative breast cancers. *The oncologist* **2010**, *15* Suppl 5, 39-48.

7. Sorlie, T.; Perou, C. M.; Tibshirani, R.; Aas, T.; Geisler, S.; Johnsen, H.; Hastie, T.; Eisen, M. B.; van de Rijn, M.; Jeffrey, S. S.; Thorsen, T.; Quist, H.; Matese, J. C.; Brown, P. O.; Botstein, D.; Lonning, P. E.; Borresen-Dale, A. L., Gene expression patterns of breast carcinomas distinguish tumor subclasses with clinical implications. *Proceedings of the National Academy of Sciences of the United States of America* **2001**, *98* (19), 10869-74.

8. Yaziji, H.; Barry, T., Diagnostic immunohistochemistry: What can go wrong? *Advances in Anatomic Pathology* **2006**, *13* (5), 238-246.

9. Hicks, D. G.; Tubbs, R. R., Assessment of the HER2 status in breast cancer by fluorescence in situ hybridization: a technical review with interpretive guidelines. *Hum Pathol* **2005**, *36* (3), 250-61.

10. Furrer, D.; Sanschagrin, F.; Jacob, S.; Diorio, C., Advantages and disadvantages of technologies for HER2 testing in breast cancer specimens. *Am J Clin Pathol* **2015**, *144* (5), 686-703.

11. Frampton, G. M.; Fichtenholtz, A.; Otto, G. A.; Wang, K.; Downing, S. R.; He, J.; Schnall-Levin, M.; White, J.; Sanford, E. M.; An, P.; Sun, J.; Juhn, F.; Brennan, K.; Iwanik, K.; Maillet, A.; Buell, J.; White, E.; Zhao, M.; Balasubramanian, S.; Terzic, S.; Richards, T.; Banning, V.;

Garcia, L.; Mahoney, K.; Zwirko, Z.; Donahue, A.; Beltran, H.; Mosquera, J. M.; Rubin, M. A.; Dogan, S.; Hedvat, C. V.; Berger, M. F.; Pusztai, L.; Lechner, M.; Boshoff, C.; Jarosz, M.; Vietz, C.; Parker, A.; Miller, V. A.; Ross, J. S.; Curran, J.; Cronin, M. T.; Stephens, P. J.; Lipson, D.; Yelensky, R., Development and validation of a clinical cancer genomic profiling test based on massively parallel DNA sequencing. *Nat. Biotechnol.* **2013**, *31* (11), 1023-+.

12. Alexandrov, L. B.; Nik-Zainal, S.; Wedge, D. C.; Aparicio, S.; Behjati, S.; Biankin, A. V.; Bignell, G. R.; Bolli, N.; Borg, A.; Borresen-Dale, A. L.; Boyault, S.; Burkhardt, B.; Butler, A. P.; Caldas, C.; Davies, H. R.; Desmedt, C.; Eils, R.; Eyfjord, J. E.; Foekens, J. A.; Greaves, M.; Hosoda, F.; Hutter, B.; Ilcic, T.; Imbeaud, S.; Imielinski, M.; Jager, N.; Jones, D. T. W.; Jones, D.; Knappskog, S.; Kool, M.; Lakhani, S. R.; Lopez-Otin, C.; Martin, S.; Munshi, N. C.; Nakamura, H.; Northcott, P. A.; Pajic, M.; Papaemmanuil, E.; Paradiso, A.; Pearson, J. V.; Puente, X. S.; Raine, K.; Ramakrishna, M.; Richardson, A. L.; Richter, J.; Rosenstiel, P.; Schlesner, M.; Schumacher, T. N.; Span, P. N.; Teague, J. W.; Totoki, Y.; Tutt, A. N. J.; Valdes-Mas, R.; van Buuren, M. M.; van't Veer, L.; Vincent-Salomon, A.; Waddell, N.; Yates, L. R.; Zucman-Rossi, J.; Futreal, P. A.; McDermott, U.; Lichter, P.; Meyerson, M.; Grimmond, S. M.; Siebert, R.; Campo, E.; Shibata, T.; Pfister, S. M.; Campbell, P. J.; Stratton, M. R.; Australian Pancreatic Canc, G.; Consortium, I. B. C.; Consortium, I. M.-S.; PedBrain, I., Signatures of mutational processes in human cancer. *Nature* **2013**, *500* (7463), 415-+.

13. Budczies, J.; Brockmoller, S. F.; Muller, B. M.; Barupal, D. K.; Richter-Ehrenstein, C.; Kleine-Tebbe, A.; Griffin, J. L.; Oresic, M.; Dietel, M.; Denkert, C.; Fiehn, O., Comparative metabolomics of estrogen receptor positive and estrogen receptor negative breast cancer: alterations in glutamine and beta-alanine metabolism. *Journal of proteomics* **2013**, *94*, 279-288.

14. Heeren, R. M. A., Getting the picture: The coming of age of imaging MS. **2015**, *377*, 672–680.

15. Golf, O.; Strittmatter, N.; Karancsi, T.; Pringle, S. D.; Speller, A. V.; Mroz, A.; Kinross, J. M.; Abbassi-Ghadi, N.; Jones, E. A.; Takats, Z., Rapid evaporative ionization mass spectrometry imaging platform for direct mapping from bulk tissue and bacterial growth media. *Analytical chemistry* **2015**, *87* (5), 2527-34.

16. Laskin, J.; Heath, B. S.; Roach, P. J.; Cazares, L.; Semmes, O. J., Tissue Imaging Using Nanospray Desorption Electrospray Ionization Mass Spectrometry. *Analytical chemistry* **2011**, *84* (1), 141-148.

17. Walsh, C. M.; Reschke, B. R.; Fortney, J.; Piktel, D.; Razunguzwa, T. T.; Powell, M. J.; Gibson, L. F., A novel laser ablation electrospray ionization mass spectrometry (LAESI-MS) platform for biomarker discovery in cancer cells. *Cancer Research* **2012**, *72* (8), Abstract 4793.

18. Hsu, C.-C.; Dorrestein, P. C., Visualizing life with ambient mass spectrometry. *Current Opinion in Biotechnology* **2015**, *31*, 24-34.

19. Laskin, J.; Lanekoff, I., Ambient Mass Spectrometry Imaging Using Direct Liquid Extraction Techniques. *Analytical chemistry* **2015**, *88* (1), 52-73.

20. Kawashima, M.; Iwamoto, N.; Kawaguchi-Sakita, N.; Sugimoto, M.; Ueno, T.; Mikami, Y.; Terasawa, K.; Sato, T. A.; Tanaka, K.; Shimizu, K.; Toi, M., High-resolution imaging mass spectrometry reveals detailed spatial distribution of phosphatidylinositols in human breast cancer. *Cancer science* **2013**, *104* (10), 1372-9.
21. Tata, A.; Woolman, M.; Ventura, M.; Bernards, N.; Ganguly, M.; Gribble, A.; Shrestha, B.; Bluemke, E.; Ginsberg, H. J.; Vitkin, A.; Zheng, J.; Zarrine-Afsar, A., Rapid Detection of Necrosis in Breast Cancer with Desorption Electrospray Ionization Mass Spectrometry. *Scientific Reports* **2016**, *6*:35374.
22. Guo, S.; Wang, Y.; Zhou, D.; Li, Z., Significantly increased monounsaturated lipids relative to polyunsaturated lipids in six types of cancer microenvironment are observed by mass spectrometry imaging. *Scientific Reports*, Published online: 5 August 2014; | doi:10.1038/srep05959 **2014**.
23. Bluestein, B. M.; Morrish, F.; Graham, D. J.; Guenthoer, J.; Hockenbery, D.; Porter, P. L.; Gamble, L. J., An unsupervised MVA method to compare specific regions in human breast tumor tissue samples using ToF-SIMS. *The Analyst* **2016**, *141* (6), 1947-57.
24. Rauser, S.; Marquardt, C.; Balluff, B.; Deininger, S. O.; Albers, C.; Belau, E.; Hartmer, R.; Suckau, D.; Specht, K.; Ebert, M. P.; Schmitt, M.; Aubele, M.; Hofler, H.; Walch, A., Classification of HER2 receptor status in breast cancer tissues by MALDI imaging mass spectrometry. *J Proteome Res* **2010**, *9* (4), 1854-63.
25. Mao, X.; He, J.; Li, T.; Lu, Z.; Sun, J.; Meng, Y.; Abliz, Z.; Chen, J., Application of imaging mass spectrometry for the molecular diagnosis of human breast tumors. *Sci Rep* **2016**, *6*, 21043.
26. Guenther, S.; Muirhead, L. J.; Speller, A. V. M.; Golf, O.; Strittmatter, N.; Ramakrishnan, R.; Goldin, R. D.; Jones, E.; Veselkov, K.; Nicholson, J.; Darzi, A.; Takats, Z., Spatially Resolved Metabolic Phenotyping of Breast Cancer by Desorption Electrospray Ionization Mass Spectrometry. *Cancer Research* **2015**, *75* (9), 1828-1837.
27. Alberici, R. M.; Simas, R. C.; Sanvido, G. B.; Romao, W.; Lalli, P. M.; Benassi, M.; Cunha, I. B. S.; Eberlin, M. N., Ambient mass spectrometry: bringing MS into the "real world". *Analytical and Bioanalytical Chemistry* **2010**, *398* (1), 265-294.
28. Ifa, D. R.; Eberlin, L. S., Ambient Ionization Mass Spectrometry for Cancer Diagnosis and Surgical Margin Evaluation. *Clinical Chemistry* **2016**, *62* (1), 111-123.
29. Dill, A. L.; Ifa, D. R.; Manicke, N. E.; Zheng, O.; Cooks, R. G., Mass spectrometric imaging of lipids using desorption electrospray ionization. *Journal of Chromatography B-Analytical Technologies in the Biomedical and Life Sciences* **2009**, *877* (26), 2883-2889.
30. Calligaris, D.; Caragacianu, D.; Liu, X.; Norton, I.; Thompson, C. J.; Richardson, A. L.; Golshan, M.; Easterling, M. L.; Santagata, S.; Dillon, D. A.; Jolesz, F. A.; Agar, N. Y. R., Application of desorption electrospray ionization mass spectrometry imaging in breast cancer margin analysis. *Proc. Natl. Acad. Sci. U. S. A.* **2014**, *111* (42), 15184-15189.

31. Zhang, J.; Feider, C. L.; Nagi, C.; Yu, W.; Carter, S. A.; Suliburk, J.; Cao, H. S.; Eberlin, L. S., Detection of Metastatic Breast and Thyroid Cancer in Lymph Nodes by Desorption Electrospray Ionization Mass Spectrometry Imaging. *Journal of the American Society for Mass Spectrometry* **2017**, *28* (6), 1166-1174.
32. Huo, D. Z.; Hu, H.; Rhie, S. K.; Gamazon, E. R.; Cherniack, A. D.; Liu, J. F.; Yoshimatsu, T. F.; Pitt, J. J.; Hoadley, K. A.; Troester, M.; Ru, Y. B.; Lichtenberg, T.; Sturtz, L. A.; Shelley, C. S.; Benz, C. C.; Mills, G. B.; Laird, P. W.; Shriver, C. D.; Perou, C. M.; Olopade, O. I., Comparison of Breast Cancer Molecular Features and Survival by African and European Ancestry in The Cancer Genome Atlas. *Jama Oncology* **2017**, *3* (12), 1654-1662.
33. Michels, K. B.; Mohllajee, A. R.; Roset-Bahmanyar, E.; Beehler, G. P.; Moysich, K. B., Diet and breast cancer - A review of the prospective observational studies. *Cancer* **2007**, *109* (12), 2712-2749.
34. Dill, A. L.; Eberlin, L. S.; Costa, A. B.; Ifa, D. R.; Cooks, R. G., Data quality in tissue analysis using desorption electrospray ionization. *Anal Bioanal Chem* **2011**, *401* (6), 1949-61.
35. Eberlin, L. S.; Ferreira, C. R.; Dill, A. L.; Ifa, D. R.; Cheng, L.; Cooks, R. G., Non-Destructive, Histologically Compatible Tissue Imaging by Desorption Electrospray Ionization Mass Spectrometry. *ChemBioChem* **2011**, *12* (14), 2129-2132.
36. Bokhart, M. T.; Nazari, M.; Garrard, K. P.; Muddiman, D. C., MSiReader v1.0: Evolving Open-Source Mass Spectrometry Imaging Software for Targeted and Untargeted Analyses. *Journal of the American Society for Mass Spectrometry* **2018**, *29* (1), 8-16.
37. O'Brien, K. M.; Cole, S. R.; Tse, C. K.; Perou, C. M.; Carey, L. A.; Foulkes, W. D.; Dressler, L. G.; Geradts, J.; Millikan, R. C., Intrinsic Breast Tumor Subtypes, Race, and Long-Term Survival in the Carolina Breast Cancer Study. *Clinical Cancer Research* **2010**, *16* (24), 6100-6110.
38. Eberlin, L. S.; Tibshirani, R. J.; Zhang, J.; Longacre, T. A.; Berry, G. J.; Bingham, D. B.; Norton, J. A.; Zare, R. N.; Poultides, G. A., Molecular assessment of surgical-resection margins of gastric cancer by mass-spectrometric imaging. *Proc Natl Acad Sci U S A* **2014**, *111* (7), 2436-41.
39. Sans, M.; Gharpure, K.; Tibshirani, R.; Zhang, J.; Liang, L.; Liu, J.; Young, J. H.; Dood, R. L.; Sood, A. K.; Eberlin, L. S., Metabolic Markers and Statistical Prediction of Serous Ovarian Cancer Aggressiveness by Ambient Ionization Mass Spectrometry Imaging. *Cancer Res* **2017**, *77* (11), 2903-2913.
40. Cairns, R. A.; Harris, I. S.; Mak, T. W., Regulation of cancer cell metabolism. *Nature Reviews Cancer* **2011**, *11* (2), 85-95.
41. Chughtai, K.; Jiang, L.; Greenwood, T. R.; Glunde, K.; Heeren, R. M., Mass spectrometry images acylcarnitines, phosphatidylcholines, and sphingomyelin in MDA-MB-231 breast tumor models. *Journal of lipid research* **2013**, *54* (2), 333-44.

42. Baumann, J.; Sevinsky, C.; Conklin, D. S., Lipid biology of breast cancer. *Biochim. Biophys. Acta Mol. Cell Biol. Lipids* **2013**, *1831* (10), 1509-1517.
43. Baenke, F.; Peck, B.; Miess, H.; Schulze, A., Hooked on fat: the role of lipid synthesis in cancer metabolism and tumour development. *Dis Model Mech* **2013**, *6* (6), 1353-63.
44. Calligaris, D.; Caragacianu, D.; Liu, X.; Norton, I.; Thompson, C. J.; Richardson, A. L.; Golshan, M.; Easterling, M. L.; Santagata, S.; Dillon, D. A.; Jolesz, F. A.; Agar, N. Y., Application of desorption electrospray ionization mass spectrometry imaging in breast cancer margin analysis. *Proc Natl Acad Sci U S A* **2014**, *111* (42), 15184-9.
45. Guenther, S.; Muirhead, L. J.; Speller, A. V.; Golf, O.; Strittmatter, N.; Ramakrishnan, R.; Goldin, R. D.; Jones, E.; Veselkov, K.; Nicholson, J.; Darzi, A.; Takats, Z., Spatially resolved metabolic phenotyping of breast cancer by desorption electrospray ionization mass spectrometry. *Cancer Res* **2015**, *75* (9), 1828-37.
46. Mertens, B. J. A., Proteomic diagnosis competition: Design, concepts, participants and first results. **2009**, *72* (5), 785-790.
47. Dekker, T. J.; Balluff, B. D.; Jones, E. A.; Schone, C. D.; Schmitt, M.; Aubele, M.; Kroep, J. R.; Smit, V. T.; Tollenaar, R. A.; Mesker, W. E.; Walch, A.; McDonnell, L. A., Multicenter matrix-assisted laser desorption/ionization mass spectrometry imaging (MALDI MSI) identifies proteomic differences in breast-cancer-associated stroma. *J Proteome Res* **2014**, *13* (11), 4730-8.
48. Dill, A. L.; Eberlin, L. S.; Costa, A. B.; Ifa, D. R.; Cooks, R. G., Data quality in tissue analysis using desorption electrospray ionization. *Analytical and Bioanalytical Chemistry* **2011**, *401* (6), 1949-1961.
49. Burstein, H. J., The distinctive nature of HER2-positive breast cancers. *New England Journal of Medicine* **2005**, *353* (16), 1652-1654.
50. Buckley, N. E.; Forde, C.; McArt, D. G.; Boyle, D. P.; Mullan, P. B.; James, J. A.; Maxwell, P.; McQuaid, S.; Salto-Tellez, M., Quantification of HER2 heterogeneity in breast cancer-implications for identification of sub-dominant clones for personalised treatment. *Scientific Reports* **2016**, *6*.
51. Wesola, M.; Jelen, M., A Comparison of IHC and FISH Cytogenetic Methods in the Evaluation of HER2 Status in Breast Cancer. *Advances in clinical and experimental medicine : official organ Wroclaw Medical University* **2015**, *24* (5), 899-903.

## Chapter 3: Desorption Electrospray Ionization Mass Spectrometry Imaging of Proteins Directly from Biological Tissue Sections<sup>2</sup>

### INTRODUCTION

Mass spectrometry (MS) imaging is a powerful tool to investigate the spatial distribution of molecular species directly from tissue samples.<sup>1,2</sup> Matrix assisted laser desorption/ionization (MALDI) is the most widely used MS imaging technique, which has been extensively explored to image and characterize metabolites, lipids, and proteins from biological tissue samples in a variety of biomedical applications.<sup>1,3</sup> In MALDI, application of matrix to the biological tissue sample as well as high-vacuum conditions are necessary for efficient desorption and ionization of molecules. Ambient ionization MS techniques have become increasingly used for biological tissue imaging as they allow analysis to be performed in the open environment with minimal sample preparation requirements, which is appealing for clinical applications.<sup>2, 4</sup> Desorption electrospray ionization (DESI) MS imaging, for example, is the most widely used ambient ionization MS technique that has been broadly explored tissue imaging.<sup>4</sup>

DESI-MS imaging has been successfully used to analyze biological tissue sections allowing efficient desorption and ionization of lipids and metabolites that are diagnostic of cancer including breast,<sup>5-7</sup> ovarian,<sup>8-9</sup> brain<sup>10-11</sup>, and others<sup>4</sup>. Although typically used for small molecule analysis, a few studies have described optimization of DESI-MS for protein

---

<sup>2</sup> Adapted with permission from “Garza, K. Y.; Feider, C. L.; Klein, D. R.; Rosenberg, J. A.; Brodbelt, J. S.; Eberlin, L. S., Desorption Electrospray Ionization Mass Spectrometry Imaging of Proteins Directly from Biological Tissue Sections. *Anal Chem* **2018**, *90* (13), 7785-7789.” Copyright 2018 American Chemical Society. K.Y. Garza contributed to the collection and analysis of data and preparation of the manuscript. C.L. Feider, D.R. Klein, and J.A. Rosenberg assisted in the collection of data. L.S. Eberlin and C.L. Feider assisted in the preparation and editing of the manuscript. All authors revised the manuscript

analysis from non-biological substrates.<sup>12-14</sup> For example, DESI-MS has been recently used to desorb membrane proteins in their native conformations from planar surfaces.<sup>14</sup> However, inefficient desorption of large biomolecules and chemical noise arising from the complex tissue matrix have impeded detection of proteins directly from biological tissue sections by DESI-MS. Recently, ambient ionization MS using liquid extraction techniques such as nanospray desorption electrospray ionization (nano-DESI),<sup>15</sup> liquid extraction surface analysis (LESA),<sup>16</sup> and the liquid microjunction surface sampling probe (LMJ-SSP)<sup>17</sup> were applied to image proteins from biological tissue sections. In the latter two studies, protein analysis was enhanced by integrating ion mobility separation into the workflow, which allowed selected transmission of protein ions and reduced chemical noise in the mass spectra.<sup>16-17</sup> For example, LESA coupled to a chip based high field asymmetric waveform ion mobility (FAIMS)<sup>18</sup> device allowed increase in the signal-to-noise ratio (S/N) and the number of proteins detected from biological tissue sections.<sup>16</sup> Similarly, integration of FAIMS with LMJ-SSP increased the S/N of a variety of protein species in rat and human tissue sections.<sup>17</sup> Here, we describe the optimization of DESI-MS imaging for protein analysis and further coupling of DESI to a FAIMS device for imaging proteins from biological tissue sections, indicating that this approach could be used for top-down proteomics studies in various biomedical applications.

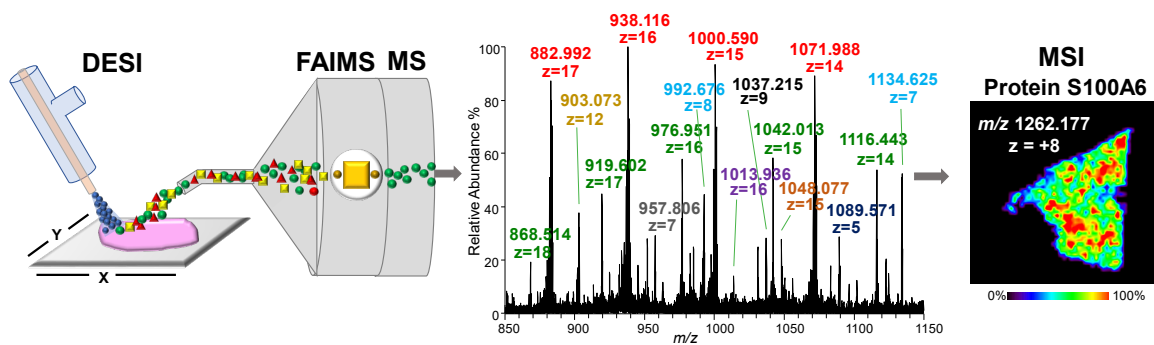


Illustration 3.1: Scheme of DESI-FAIMS-MS imaging of biological tissue sections.

## **MATERIALS AND METHODS**

### **Tissue samples**

Mice brain and kidney tissue samples were purchased from Bioreclamation IVT (Hicksville, NY). Human normal breast, breast cancer, and normal ovarian were purchased from the Cooperative Human Tissue Network (CHTN), and the ovarian cancer sample was purchased from the MD Anderson Cancer Center Tissue Bank under IRB approved protocol. Prior to sectioning, the samples were stored in a -80°C freezer. Tissue samples were sectioned at a thickness of 16 µm using a CryoStar NX50 cryostat (Thermo Scientific, San Jose, CA) and mounted onto glass slides. Tissue sections were stored in a -80°C freezer until DESI-MS analysis. Prior to DESI-MS imaging, glass slides were air dried for ~ 15 min. Tissue sections were washed twice with ethanol and chloroform for 10 sec each. Serial tissue sections were H&E stained and subjected to pathological evaluation.

### **Lipid analysis**

Lipid imaging experiments were performed using a DESI 2D system (Prosolia Inc., Indianapolis, IN) equipped with a lab-built DESI sprayer, mounted to the interface of a LTQ-Orbitrap Elite mass spectrometer (Thermo Fisher Scientific, San Jose, CA). DESI-MS imaging of mouse brain was performed in negative ion mode from  $m/z$  100-1500. The histologically compatible solvent system ACN:DMF was used for tissue imaging at a flow rate 1.2 µL/min. The spatial resolution used was 200 µm. The N<sub>2</sub> pressure was set to 180 psi, and the capillary temperature of the mass spectrometer was set to 300°C. Lipid species were identified using collision induced dissociation (CID) tandem mass spectrometry and high mass accuracy measurements.

### **Protein analysis**

Protein imaging experiments were performed using a DESI 2D system (Prosolia Inc., Indianapolis, IN) equipped with a lab-built DESI sprayer, mounted to the interface of a LTQ-Orbitrap Elite mass spectrometer (Thermo Fisher Scientific, San Jose, CA). An ultraFAIMS device (Owlstone Ltd., Cambridge, UK) modified with an extended transfer tube was coupled to mass spectrometer for ion mobility experiments. The FAIMS capillary used for these experiments had an inner diameter of 0.037 in and outer diameter of 0.0625 in. A spray angle of 55° relative to the sample surface was used for all experiments. The optimal spray to extended transfer capillary and DESI capillary to surface distances were found to be 2.5 mm and 3.5 mm, respectively. DESI-FAIMS-MS imaging was performed in positive ion mode from  $m/z$  700-2000 using a spatial resolution of 300  $\mu\text{m}$ . Although adding water to the solvent increased the sampling area and lowered the spatial resolution to 300  $\mu\text{m}$ , DESI-FAIMS-MS imaging allowed for the visualization of protein ions that localized to specific regions of the tissues. The Orbitrap Elite mass spectrometer allows for high mass resolution (60,000 resolving power) and high mass accuracy (<5 ppm). A solvent system of acetonitrile/water (ACN/H<sub>2</sub>O) 80:20 (v/v) with 0.2% formic acid was used for tissue analysis at a flow rate of 5  $\mu\text{L}/\text{min}$  with a spray voltage of 1 kV. The N<sub>2</sub> pressure was set to 200 psi, and the capillary temperature of the mass spectrometer was set to 300°C.

### **S/N calculation**

Optimization experiments were repeated using 3 serial mice kidney tissue sections. Data were extracted from three lines across each mouse kidney tissue section. Within each line, a total of 20 mass spectra were averaged to calculate the S/N. An average S/N for each

tissue section was then calculated from the three lines. The S/N reported in the manuscript is the average of the S/N obtained for the three kidney tissue sections.

### **In tandem DESI-UVPD**

Identification of intact proteins in positive ion mode was performed on a Thermo Orbitrap Elite mass spectrometer equipped with a 193 nm Coherent Excistar ArF excimer laser (Santa Clara, CA). 1 pulse at 3 mJ was used for all DESI-UVPD experiments. Prior to DESI-UVPD experiments, tissue sections were washed with ethanol and chloroform twice for 10 seconds each. ACN/H<sub>2</sub>O (v/v) with 0.2% formic acid at a flow rate of 5  $\mu$ L/min was used desorb proteins from the tissue sections. For these experiments, a 2000 ms injection time and 1 micro scan were used. For these experiments, the FAIMS device was not used.

### **Protein extraction**

Protein extracts were acquired through hand pipetting from glass slides of a serial section of tissue analyzed by DESI-FAIMS-MS. Tissue sections were washed with ethanol and chloroform twice for 10 sec each, followed by hand pipetting of 2  $\mu$ l of acetonitrile/water (ACN/H<sub>2</sub>O) 80:20 (v/v) with 0.2% formic acid onto the tissue section. The solvent was allowed to extract molecules from the tissue for ~10 sec and was then re-aspirated and collected. This process was repeated until adequate material was collected from protein identification.

### **Top down UVPD**

Prior to LC-MS analysis, tissue extracts were diluted with water to a final acetonitrile concentration of 5%. For each tissue sample, 1  $\mu$ L of the diluted extract was injected. The

chromatographic separation was performed with a Dionex UltiMate 3000 nanoLC system (Thermo-Fisher, San Jose, CA) using a PicoFrit column (New Objective, Ringoes, NJ) with an inner diameter of 75  $\mu$ M, packed to a length of 30 cm with polymer reverse-phase resin (Agilent, Santa Clara, CA) having a pore size of 1000 Angstroms. A 3 cm trap column with the same inner diameter and packing material was placed in front of the analytical column. Proteins were eluted using a gradient from 15% to 55% acetonitrile over 55 minutes, with 0.1% aqueous formic acid constituting the remainder of the mobile phase. Mobile phase A was 0.1% formic acid; mobile phase B was 99% acetonitrile. The flow rate was 300 nl/min. The LC system was interfaced to a Thermo Orbitrap Lumos tribrid mass spectrometer (Thermo-Fisher, San Jose, CA) equipped with 193 nm UVPD.<sup>18</sup> Eluting species were introduced to the mass spectrometer via electrospray with a spray voltage of 1.9 kV. The instrument was operated in the top-speed mode, with 7 seconds of MS<sup>2</sup> data collection for each MS<sup>1</sup> scan. During the 7 second MS<sup>2</sup> period, typically between 1 to 5 spectral acquisitions were performed. Proteins with a charge state of +7 or higher were isolated in the quadrupole and activated by UVPD (1.8 mJ, 1 pulse) in the low-pressure cell of the dual linear ion trap. MS<sup>1</sup> spectra were collected at a nominal resolution of 60,000 with 3 microscan averages per scan, while MS<sup>2</sup> spectra were collected at a resolution of 120,000 with 5 microscan averages. Each LC-MS run was searched against the Uniprot database of reviewed human proteins using the ProSightPD node of Thermo Proteome Discoverer 2.1. Peaks were identified with a mass tolerance of 100 Da for MS<sup>1</sup> or 10 ppm for MS<sup>2</sup> using an absolute-mass search workflow. Identified proteoforms were filtered

using an FDR value of 1%. Sequence coverage was determined using ProSight Lite software.

### **Bottom up proteomics**

Proteins were digested in-gel with trypsin and identified by LC-MS/MS on an Orbitrap Fusion Tribrid mass spectrometer, followed by Sequest HT database search and Scaffold validation in the CBRS Proteomics Facility using previously published methods.<sup>19</sup>

## **RESULTS AND DISCUSSION**

### **Optimization of DESI-MS geometric parameters for protein imaging**

Protein imaging from biological tissue sections by MALDI-MS is commonly performed by washing the tissue section with organic solvents prior to matrix application to remove endogenous lipids and biological salts that may affect efficiency of protein desorption and ionization.<sup>20</sup> Building on this knowledge, we first evaluated the effectiveness of a washing step on enhancing protein desorption and detection. DESI-MS imaging was performed on an unwashed mouse kidney tissue section in the positive ion mode using pure ACN as the solvent and typical DESI-MS lipid imaging parameters (Table 3.1).<sup>21</sup> As reported in previous DESI-MS lipid imaging studies,<sup>21</sup> ions identified as triacylglycerols and glycerophosphocholine lipids were detected at high relative abundances (Figure 3.1A), while multiply charged protein ions were not seen. Next, a solvent system of ACN:H<sub>2</sub>O (80:20) (v/v) with 0.2% formic acid previously reported to enhance protein desorption by nanoDESI was used for analysis of unwashed tissue sections, at a flow rate of 5  $\mu$ L/min.<sup>15</sup> Similar lipid species were detected at high relative abundances in addition to multiply

Table 3.1: DESI-MS parameters for protein and lipid analysis.

Summary of DESI-MS parameters used for lipid imaging in the negative ion mode, previously reported DESI-MS parameters for protein analysis from non-biological substrate in the positive ion mode<sup>13, 22</sup>, and the optimized DESI-MS parameters described in our study for protein detection from biological tissue sections in the positive ion mode.

	Lipid analysis	Protein standard analysis	Analysis of proteins from biological tissue
Solvent	ACN	MeOH:H <sub>2</sub> O (50:50) (v/v) with 0.1% formic acid	ACN:H <sub>2</sub> O (80:20) (v/v) with 0.2% formic acid
Spray angle	65°	60-90° <sup>13, 22</sup>	55°
Spray voltage	5 kV	1-6 kV <sup>13, 22</sup>	1 kV
Inlet temperature	300°C	200-350°C <sup>13, 22</sup>	300°C
Gas pressure	180 psi	250 psi <sup>2</sup>	200 psi
Flow rate	3 µL/min	0.1-7 µL/min <sup>13, 22</sup>	5 µL/min
Spatial resolution	200 µm	--	300 µm
Spray to sample distance	2-3 mm <sup>21</sup>	1-2 mm <sup>22</sup>	3.5 mm
Sample to inlet distance	4-8 mm <sup>21</sup>	--	2.5 mm

charged ions at low abundances that were tentatively identified as protein species (Figure 3.1B). A lipid washing step was then performed on an adjacent mouse kidney tissue section followed by DESI-MS imaging analysis at the same parameters (Figure 3.1C). While the washing step was effective at removing lipid species, the mass spectra obtained presented low total ion abundance of the multiple charged ions, suggesting that further optimization of DESI spray geometric parameters was needed to increase desorption and detection of protein species. Previous studies have reported that the desorption of protein standards from glass slides by DESI-MS is dependent on the spray angle and spray-to-surface distance.<sup>14, 22</sup> Thus, we performed optimization of DESI spray parameters for protein detection from biological tissue sections by tuning angle, spray-to-sample distance, and sample-to-inlet distance to 55°, 3.5 mm, and 2.5 mm, respectively. Performance was evaluated by the improvement in the total ion abundance of  $m/z$  938.117, the most abundant protein detected, later identified as an alpha-globin proteoform with an asparagine to a lysine substitution. While protein ions were detected in mouse kidney tissue at various spray-to-sample and sample-to-inlet distances, proteins were not detected above a S/N=3 using spray angles other than 55°, indicating that protein desorption and detection is more strongly dependent on the spray angle than other source parameters. At this optimized DESI-MS parameters for protein analysis, the alpha-globin proteoform was detected with S/N = 27.9 (average of n=3 tissue sections, n=3 lines/tissue section, n=20 mass spectra/line), as well as 10 other distinct protein species (Figure 3.1D).

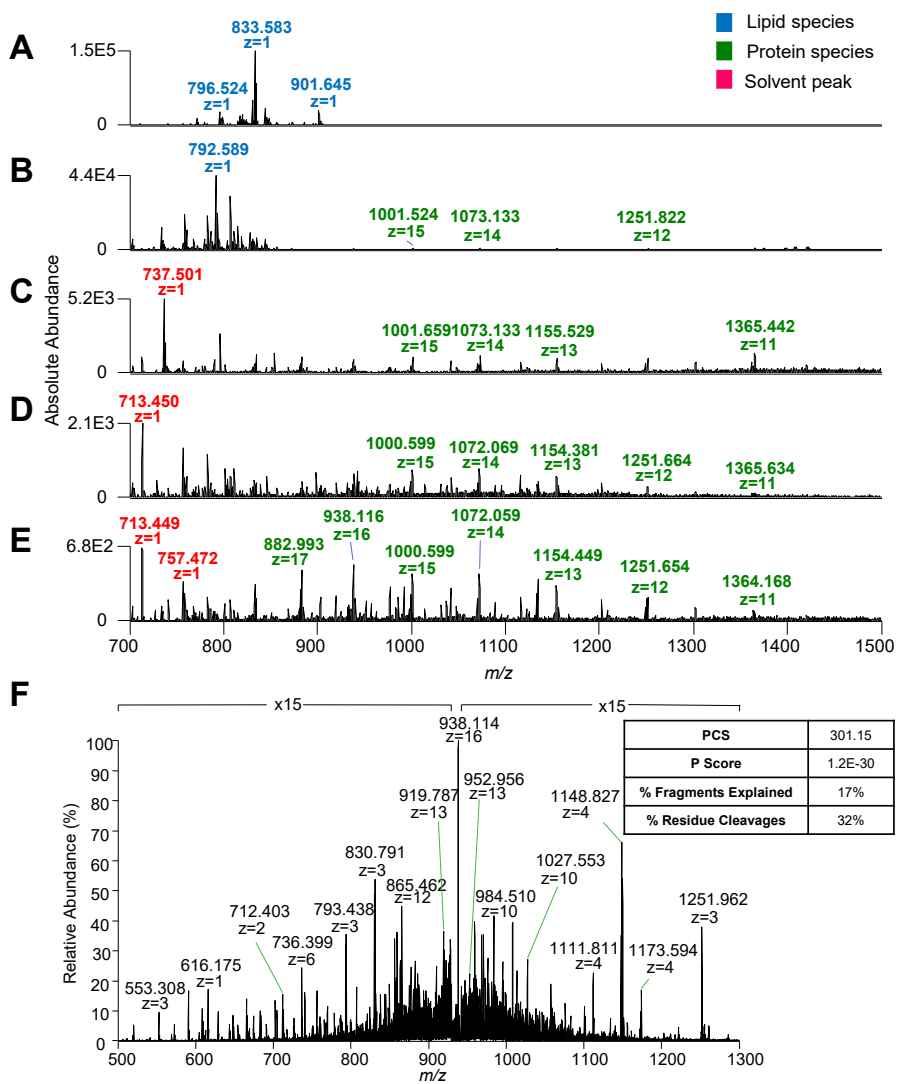


Figure 3.1: Representative positive ion mode DESI mass spectra.

Positive ion mode DESI mass spectra of A) Unwashed mouse kidney tissue section using lipid DESI-MS parameters and pure ACN as solvent system, B) unwashed mouse kidney tissue using lipid DESI-MS parameters with ACN:H<sub>2</sub>O 80:20 (v/v) and 0.2% formic acid as the solvent, C) washed mouse kidney tissue section using lipid DESI-MS parameters and ACN:H<sub>2</sub>O 80:20 (v/v) with 0.2% formic acid as the solvent, D) washed mouse kidney tissue section using protein DESI-MS parameters and ACN:H<sub>2</sub>O 80:20 (v/v) with 0.2% formic acid as the solvent, E) washed mouse kidney tissue section using protein DESI-FAIMS-MS parameters and ACN:H<sub>2</sub>O 80:20 (v/v) with 0.2% formic acid as the solvent. Mass spectra are an average of 25 scans. F) On-tissue UVPD mass spectrum of  $m/z$  938.117 using a mouse kidney tissue section. Spectrum is an average of 80 scans. PCS, P-score, and sequence coverage are reported for the protein identified as an alpha-globin proteoform.

### **FAIMS operation and optimization**

In an effort to further increase S/N of proteins, we integrated FAIMS to the DESI-MS imaging source and mass spectrometer interface as we have previously described.<sup>17</sup> FAIMS generates an alternating high and low electric field perpendicular to the ion travel path, known as a dispersion field (DF), which displaces the ions toward one of two electrodes.<sup>23</sup> To correct for this ion drift, a compensation field (CF) can be applied, allowing specific subsets of ions, such as multiply charged proteins, to be transmitted through the device.<sup>24</sup> In our experiments, the DF was stepped in 10 Townsend (Td) increments from 150 Td to 210 Td with a CF sweep of 0 Td to +4 Td occurring at each DF. Performance was evaluated by the improvement in the total ion abundance of  $m/z$  938.117, the most abundant protein within the spectra from washed mouse kidney tissue sections, later identified as alpha globin protein. The optimal parameters for protein detection were determined to be CF = +1.0 Td and DF = 180 Td. Under the optimized FAIMS parameters, a S/N=32.1 was achieved for the alpha-globin proteoform (average of n=3 tissue sections, n=3 lines/tissue section, n=20 mass spectra/line), as well as detection of 10 other distinct protein species (Table B3.1 and Figure 3.1E). The addition of FAIMS increased the S/N for all the proteins detected, thus improving image contrast and quality (Figure 3.2). The increase in the S/N of protein ions was due to the substantial filtering of interfering background species (~67% decrease), including abundant solvent peaks, and reduction of chemical noise (~60% decrease), despite an overall drop (~34%) in the absolute intensities of protein ions (Figure 3.3). Therefore, all further experiments were performed using the optimized FAIMS parameters.

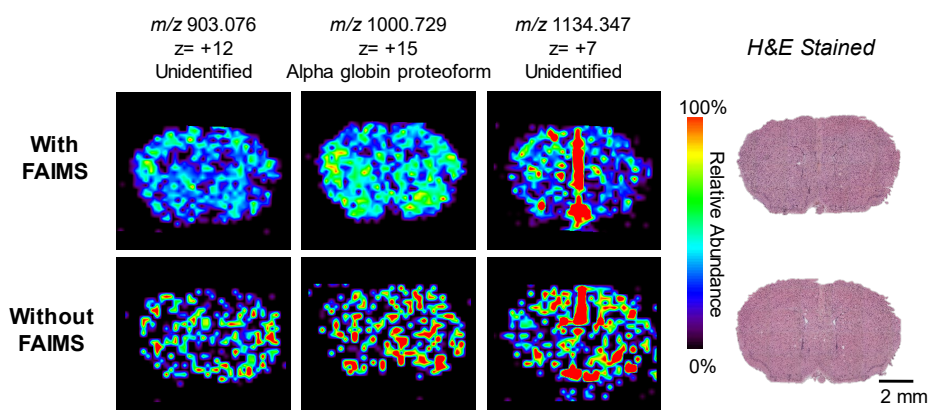


Figure 3.2: DESI-MS ion images obtained from mouse brain tissue sections both with and without FAIMS.

Ion images are in the same scale. H&E stained images are of a serial mouse brain tissue section as protein conditions are not histologically compatible.

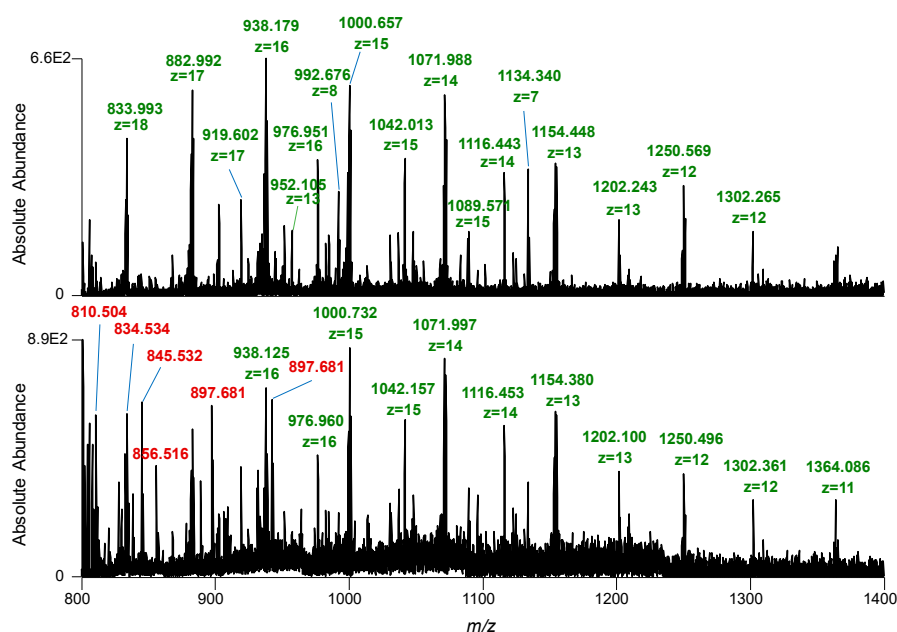


Figure 3.3: Representative protein DESI-MS spectra of mouse kidney tissue, both with and without FAIMS.

Solvent peaks are highlighted in red and protein species are highlighted in green. Spectra are averages of 25 scans.

### **Spray voltage and inlet capillary temperature optimization**

Spray voltage and transfer capillary temperature were also tuned to optimal values of 1 kV and 300°C for protein detection, respectively, using the optimized DESI-FAIMS parameters (Figure B3.1 and Figure B3.2). First, spray voltages from 1- 5 kV were tested in 1 kV increments. As shown in Figure B3.1, a S/N of 29.3 for alpha globin was achieved at 1 kV (average of n=3 tissue sections, n=3 lines/tissue section, n=20 mass spectra/line), in addition to the detection of ten other distinct protein species. While a similar S/N was achieved for other spray voltages tested, a larger number of proteins was detected using a voltage of 1 kV. Thus, the optimized voltage of 1 kV was used for all later experiments. Next, inlet temperatures from 100-400°C were tested in 100°C increments (Figure B3.2). The number of proteins detected at 200°C and 300°C (10 and 11, respectively) and S/N values (33.4 and 30.5, respectively, average of n=3 tissue sections, n=3 lines/tissue section, n=20 mass spectra/line) were similar. To assure efficient droplet desolvation at the 5  $\mu$ L/min solvent flow rate,<sup>25</sup> an inlet temperature of 300°C was chosen as the optimized temperature for the remaining experiments.

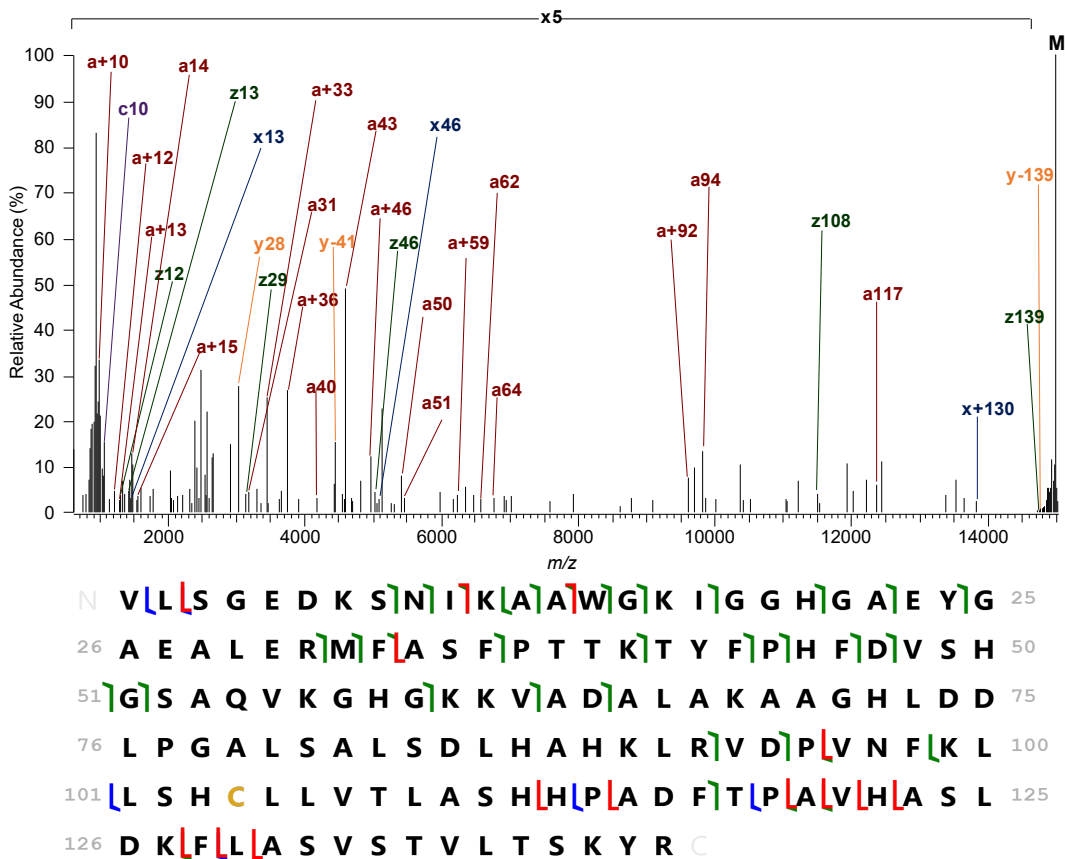
### **Effect of FAIMS on ions detected**

For mice kidney data, addition of FAIMS to the DESI imaging workflow resulted in 30% decrease in the ion intensity of  $m/z$  938.181 (assigned as the 16+ charge state of an alpha globin proteoform, MM = 14,985 Da), 68.5% decrease in the intensity of an interfering solvent peak at  $m/z$  713.442, and 43% decrease in the noise (n=3 sections, n=3 lines/section, n=25 mass spectra/line) when compared to the DESI imaging data acquired without FAIMS. For mice brain data, addition of FAIMS to the DESI imaging workflow

resulted in 36% decrease in the ion intensity of  $m/z$  1000.658 signal (assigned as the 15+ charge state of an alpha globin proteoform, MM = 14,985 Da), 66.2% decrease in the intensity of an interfering solvent peak at  $m/z$  713.442, and 77% decrease in the noise (n=2 sections, n=3 lines/section, n=25 mass spectra/line) when compared to the DESI imaging data acquired without FAIMS. Thus, although there is a loss in the total ion transmission in our experiments, FAIMS reduces noise as well as transmission of background/interfering ions, resulting in higher S/N of protein ions and thus improved imaging contrast and quality.

### **Identification of detected proteins using top-down and bottom-up proteomics**

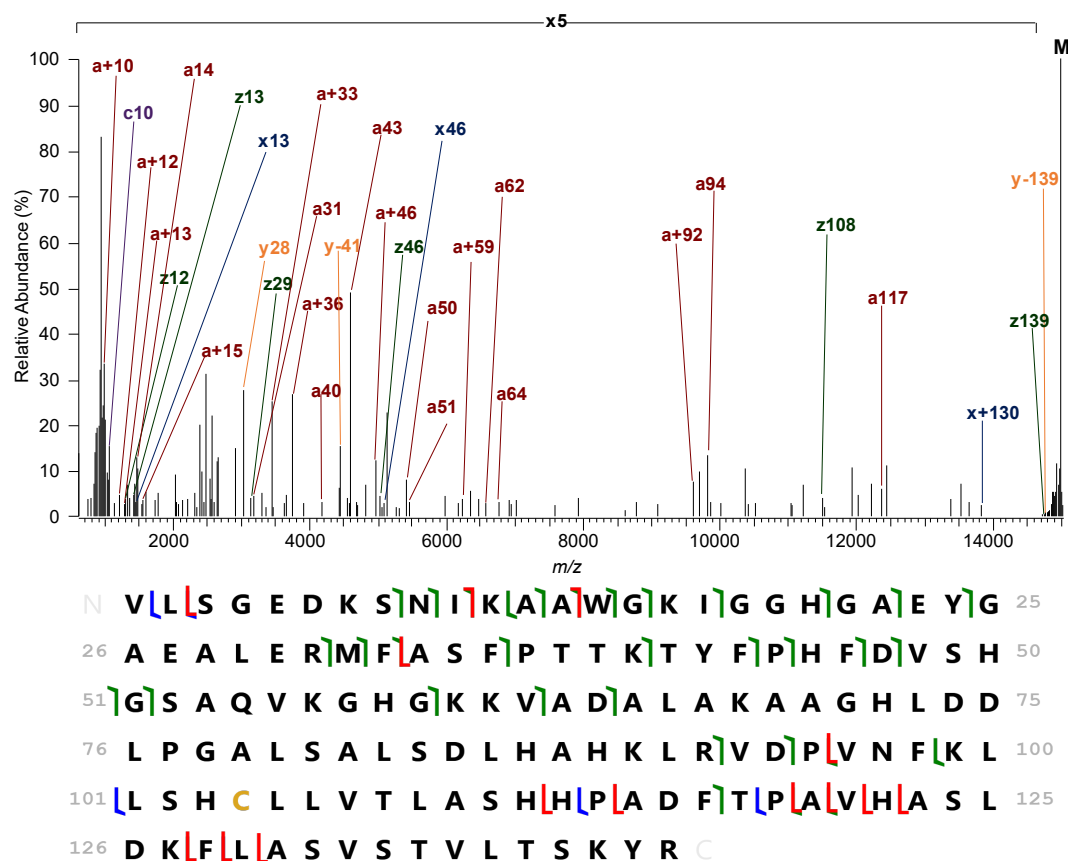
Top-down and bottom-up protein-sequencing methods were explored to identify the proteins detected. On-tissue CID was performed online by isolating and fragmenting the most abundant protein ions detected while directly profiling the tissue sections using DESI-MS alone (no FAIMS). Fragmentation of the 13+ charge state isotope envelope of the ion at  $m/z$  1,153.298 (MM = 15,085 Da, Figure 3.4) by CID allowed identification of this ion as the alpha globin protein (16% sequence coverage) in mouse kidney tissue section. Other proteoforms of alpha-globin were detected at high relative abundances, which are likely associated to the highly vascularized nature of the kidney tissue. In an effort to obtain higher sequence coverage for protein ions and therefore more accurate identification, UVPD was integrated with DESI-MS for on-tissue protein identification (no FAIMS).<sup>26</sup> The proteoform of alpha-globin presenting an asparagine to a lysine substitution (MM = 14,985 Da) used for method optimization was identified by on-tissue UVPD of  $m/z$



PCS	301.15
P Score	1.2E-30
% Fragments Explained	17%
% Residue Cleavages	32%

Figure 3.4: MS/MS spectrum obtained using CID of the isotope envelope surrounding  $m/z$  1153.298, identified as alpha globin, while using DESI-MS.

The sequence map of hemoglobin  $\alpha$  subunit is shown, demonstrating cleavages seen within the fragmentation spectrum.



PCS	301.15
P Score	1.2E-30
% Fragments Explained	17%
% Residue Cleavages	32%

Figure 3.5: Tandem DESI-UVPD mass spectrum of  $m/z$  938.180, identified as a proteoform of alpha globin.

The sequence map of the proteoform is shown, demonstrating cleavages seen within the fragmentation spectrum.

938.114 (16+ charge state), with 32% sequence coverage (Figure 3.1F and 3.5). Hemoglobin  $\alpha$  ( $m/z$  1009.335, 15+ charge state) was identified from normal human ovarian tissue using on-tissue UVPD (sequence coverage of 20%). These results demonstrate feasibility of UVPD for identification of abundant proteins detected using DESI-MS from biological tissue sections, and to the best of our knowledge represent the first application of UVPD for on-tissue protein identification. Nevertheless, further optimization of this integrated approach is needed for fragmentation and identification of lower abundant protein species. In addition to on-tissue fragmentation, top-down UVPD and bottom-up proteomics were performed on protein extracts obtained from tissues analyzed to assist in the identification of low abundance protein ions. Sequence coverage for proteins identified from tissues analyzed and the respective method used are provided in Table B3.2.

### **DESI-FAIMS-MS imaging of proteins in mouse brain tissue sections**

Next, we applied the optimized DESI-FAIMS approach to image proteins from biological tissue sections. As shown in Figure 3.6A, DESI-FAIMS allowed imaging of a variety of proteins from mouse brain tissue sections at distinct spatial distributions within the brain histologic structures. Figure 3.6B shows representative DESI-FAIMS ion images of selected protein ions. A distinct cluster of ions centered at  $m/z$  707.068 (20+ charge state, MM = 14,211 Da), identified as myelin basic protein (MBP) isoform 8 was observed at higher relative abundances within the white matter of the brain, while unidentified protein ions at  $m/z$  992.680 (8+ charge state) and  $m/z$  985.265 (11+ charge state) were distributed

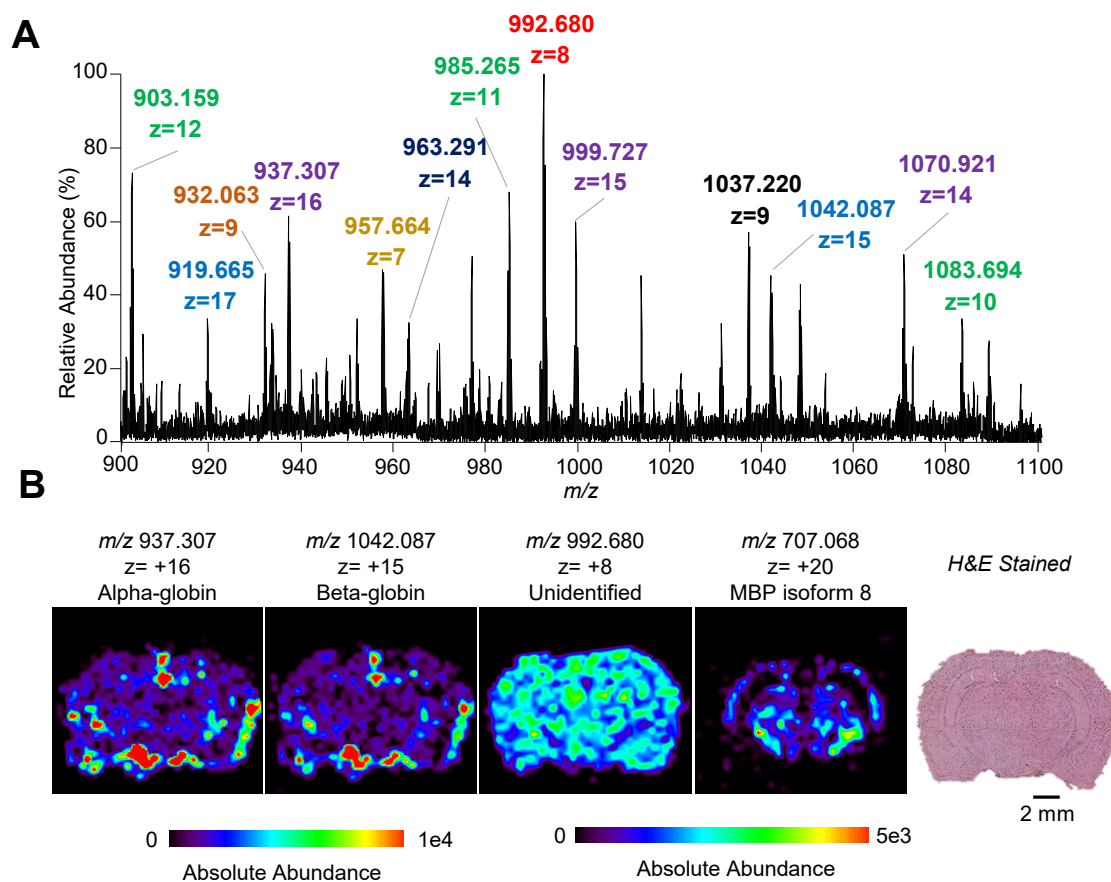


Figure 3.6: Representative DESI-FAIMS mass spectrum and ion images of a washed mouse brain tissue section.

A) Representative protein DESI mass spectra of a washed mouse brain tissue section with optimized FAIMS parameters. Mass spectra is an average of 25 scans. Different charge states of the same protein species are denoted by same colored labels. B) DESI-MS ion images of selected protein species as well as an optical image of a serial H&E stained mouse brain tissue section are shown.

throughout the tissue section. The relative abundance of alpha globin was higher in the outer portion of mouse brain tissue sections, likely correlating to regions containing blood vessels and arteries.<sup>15</sup> The spatial distribution of the protein ions detected was reproducible across multiple mouse brain tissue sections (Figure B3.3), and in agreement with what was previously reported by nanoDESI and LMJ-SSP.<sup>15, 17</sup>

### **Multimodal imaging of lipids and proteins in mouse brain tissue sections**

Multimodal MS imaging approaches that enable metabolite, lipid and protein imaging from a single tissue section are valuable to expand the molecular information achieved from tissues for a variety of applications.<sup>27-30</sup> To explore the potential of DESI imaging for collecting both lipid and protein information from the same tissue section, a mouse brain tissue section was first analyzed in negative ion mode using a histologically compatible solvent system (ACN:DMF) (Figure 3.7),<sup>31</sup> followed by a lipid-washing step, and then positive ion mode analysis using the DESI-FAIMS system optimized for protein detection. Negative ion mode DESI-MS imaging allowed detection of metabolites and lipid ions commonly seen in mouse brain tissue sections, including sulfatide C24:1 at  $m/z$  888.623 in the white matter, and glycerophosphoserine 40:6 at  $m/z$  834.529 in the grey matter (Figure B3.4). In the positive ion mode, the same protein ions detected from the tissue sections not previously analyzed were seen, including MBP at  $m/z$  707.021 in the white matter, despite a 10% decrease in signal intensity of the hemoglobin  $\alpha$  protein (Figure B3.5). These results demonstrate that DESI-MS imaging can be used to acquire

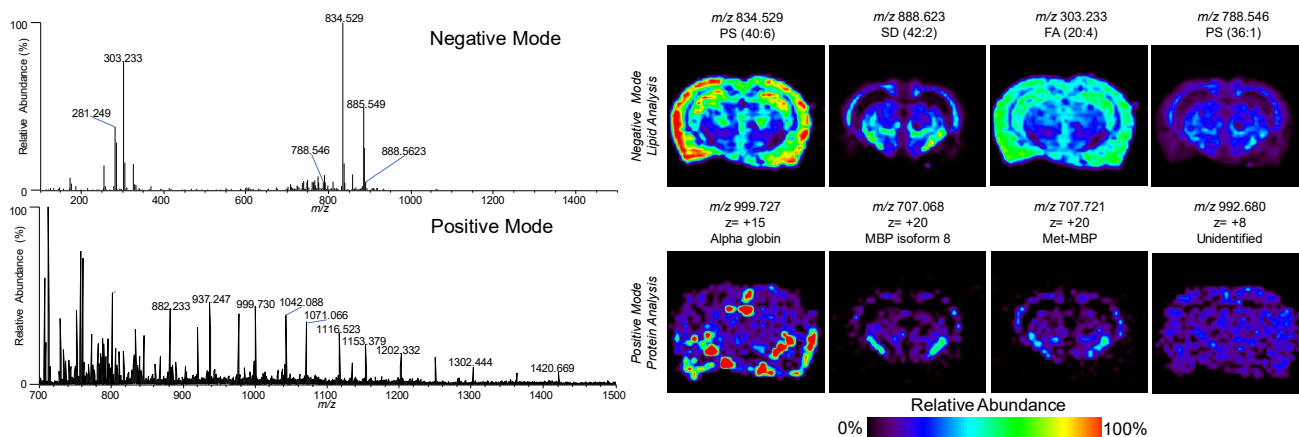


Figure 3.7: DESI-MS spectra and ion images of the same mouse brain tissue section analyzed by both negative mode lipid DESI-MS imaging, followed by positive mode protein DESI-MS imaging.

both lipid and protein information from the same tissue section, allowing a more comprehensive analysis of tissue molecular composition.

### **DESI-FAIMS-MS imaging of proteins in human normal and cancerous ovarian tissue sections**

We next employed DESI-FAIMS to image proteins from human normal and cancerous tissue sections. As shown in Figure 3.8A, the mass spectra obtained from normal ovarian and high-grade serous ovarian cancer (HGSC) tissue sections showed distinct relative abundances of protein ions. Hemoglobin  $\beta$  ( $m/z$  1443.318; 11+ charge state; MM = 15,998 Da), for example, was observed at high relative abundances in healthy ovarian tissue samples, while the S100A6 protein ( $m/z$  1442.339; 7+ charge state; MM = 10,180 Da), was observed at high relative abundances in HGSC tissue (Figure 3.8A). Note that although differing by  $\sim 1$   $m/z$  value, hemoglobin  $\beta$  and S100A6 were clearly resolved in the mass spectra (Figure 3.8B) and identified using a top-down approach. Increased abundance of S100A6 has been previously reported in a variety human cancers.<sup>32</sup> DESI-FAIMS ion images enabled clear visualization of protein ions within the heterogeneous regions of a single tissue sample (Figure 3.8C). These results corroborate previous findings in ovarian cancer tissue imaging described using LMJ-SSP and MALDI-MS.<sup>17, 33</sup>

### **DESI-FAIMS-MS imaging of proteins in human normal and cancerous breast tissue sections**

DESI-FAIMS-MS imaging of proteins was also performed on human normal and ductal breast carcinoma samples (Figure 3.9). As observed in Figure 3.9A, several proteins were detected from a normal breast and a Her2- breast cancer tissue sections. For

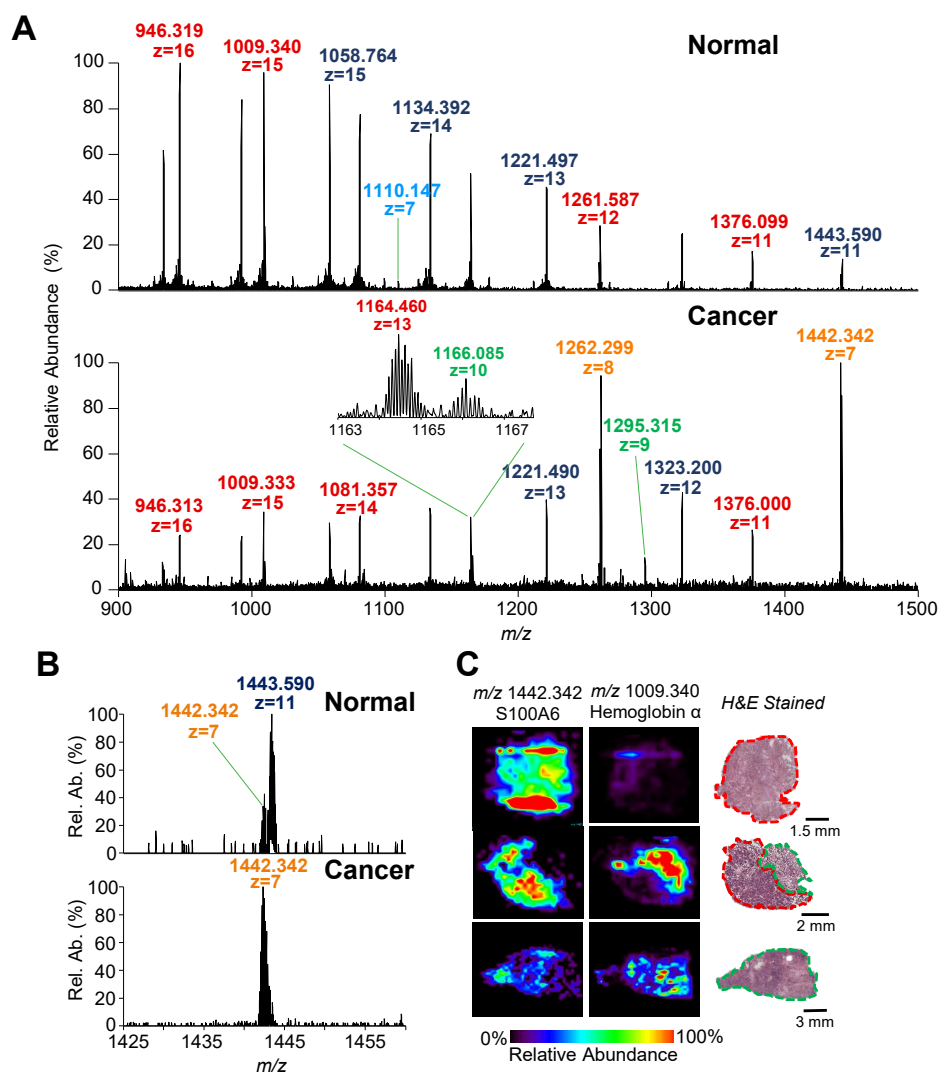


Figure 3.8: Representative DESI-FAIMS mass spectrum and ion images of a washed human normal and cancerous ovarian tissue sections.

A) Representative protein DESI-MS spectra of normal and HGSC ovarian tumor with optimized FAIMS parameters. Spectra are averages of 10 scans. Different charge states of the same protein species are denoted by same colored labels. B) Zoomed in spectra of normal and HGSC samples, highlighting the observance of  $m/z$  1442.339, identified as S100A6, within the cancer tissue. C) DESI-MS ion images obtained from normal, pure cancer, and mixed normal/cancer ovarian tissue sections. Ion images are in the same scale. H&E stained images are of a serial ovarian tissue sections as protein conditions are not histologically compatible.

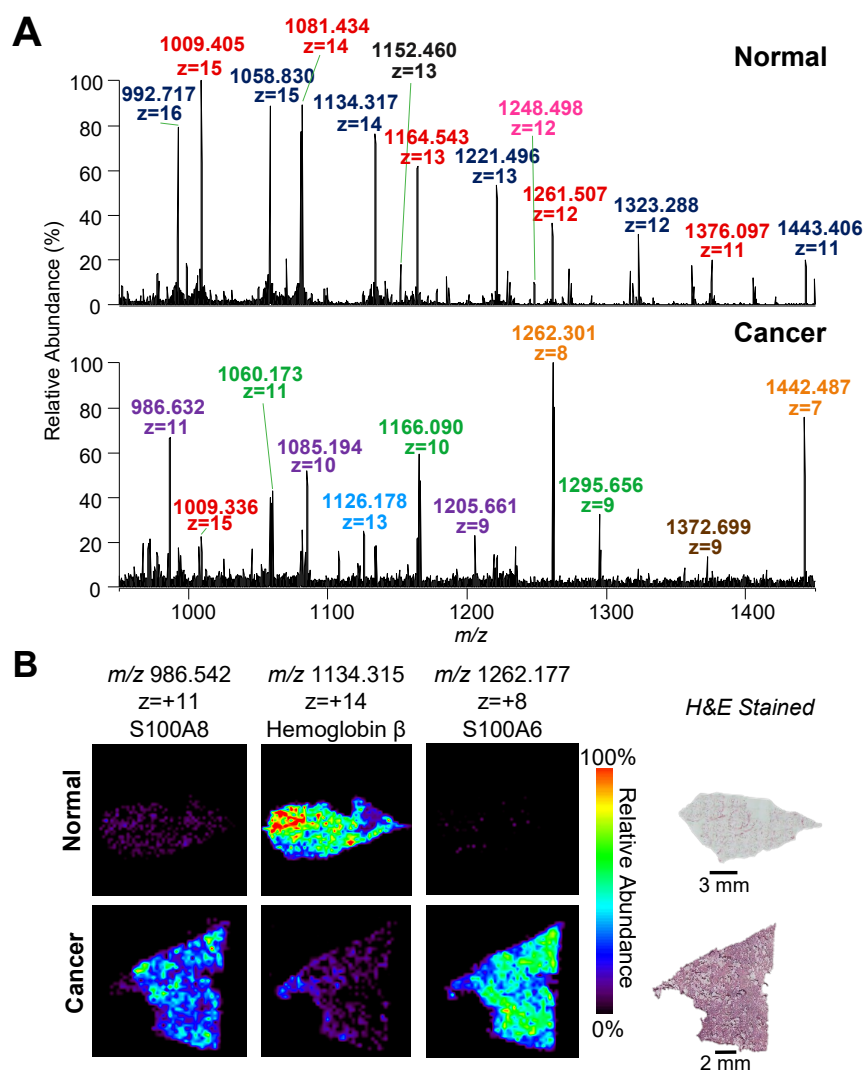


Figure 3.9: Representative DESI-FAIMS mass spectrum and ion images of a washed human normal and cancerous breast tissue sections.

A) Representative protein DESI-MS spectra of normal and breast cancer samples with optimized FAIMS parameters. Spectra are averages of 20 scans. Different charge states of the same protein species are denoted by same colored labels. B) DESI-MS ion images obtained from normal and breast cancer tissue sections. Ion images are in the same scale. H&E stained images are of a serial breast tissue sections as protein conditions are not histologically compatible.

example, profilin-1 at  $m/z$  1,152.460 (13+ charge state, MM = 15,054 Da) and hemoglobin  $\alpha$  at  $m/z$  1,009.536 (15+ charge state) were observed at higher relative abundance in a normal breast tissue. On the other hand, S100 proteins including S100A4 at  $m/z$  1058.893 (11+ charge state, MM = 11,279 Da), S100A8 at  $m/z$  986.633 (11+ charge state, MM = 10,835 Da), and S100A11 at  $m/z$  1,166.091 (10+ charge state, MM = 11,740 Da), were seen at higher relative abundances in breast cancer tissue (Figure 3.9B). Upregulation of members of the S100 family of proteins is known to occur in breast cancer and has been reported by MALDI-MS imaging and other techniques.<sup>34-36</sup> Galectin-1 ( $m/z$  1,126.177, 13+ charge state, MM = 14,716 Da), previously associated with Her2- breast cancer stromal tissue,<sup>37</sup> was also detected by DESI-FAIMS-MS at higher relative abundances in the Her2-cancer tissue analyzed.

## CONCLUSION

In conclusion, we describe the successful optimization of DESI for protein detection and further coupling to a FAIMS device for protein imaging directly from biological tissue sections. In our experiments, addition of FAIMS at parameters optimized for protein transmission reduced the mass spectra noise and transmission of background ions, resulting in a higher S/N of protein ions and thus improved imaging contrast and quality. We further demonstrate on-tissue top-down protein identification using UVPD and CID for identification of abundant protein ions detected by DESI-MS. While this study shows a noteworthy advancement for DESI-MS imaging, it represents an initial step towards in-depth tissue proteomics applications. Most protein species detected are highly

abundant in biological tissues, such as hemoglobin and S100 proteins. Thus, additional optimization of this platform is needed to improve the desorption efficiency of lower abundant proteins from thin tissue sections. Nevertheless, although protein coverage by DESI-MS imaging remains vastly poorer to the coverage achieved through traditional LC-MS/MS of tissue extracts and MALDI-MS imaging workflows,<sup>38-39</sup> the ability to rapidly image intact proteins from tissue sections with minimal sample preparation and under ambient conditions suggests DESI-MS as a promising tool for top-down proteomics, with potential applications in cancer imaging and diagnosis.

## REFERENCES

1. Schwamborn, K.; Caprioli, R. M., MALDI imaging mass spectrometry--painting molecular pictures. *Mol Oncol* **2010**, *4* (6), 529-38.
2. Wu, C.; Dill, A. L.; Eberlin, L. S.; Cooks, R. G.; Ifa, D. R., Mass spectrometry imaging under ambient conditions. *Mass Spectrom Rev* **2013**, *32* (3), 218-43.
3. Kriegsmann, M.; Casadonte, R.; Kriegsmann, J.; Dienemann, H.; Schirmacher, P.; Kobarg, J. H.; Schwamborn, K.; Stenzinger, A.; Warth, A.; Weichert, W., Reliable Entity Subtyping in Non-small Cell Lung Cancer by Matrix-assisted Laser Desorption/Ionization Imaging Mass Spectrometry on Formalin-fixed Paraffin-embedded Tissue Specimens. *Molecular & Cellular Proteomics* **2016**, *15* (10), 3081-3089.
4. Ifa, D. R.; Eberlin, L. S., Ambient Ionization Mass Spectrometry for Cancer Diagnosis and Surgical Margin Evaluation. *Clin Chem* **2016**, *62* (1), 111-23.
5. Calligaris, D.; Caragacianu, D.; Liu, X. H.; Norton, I.; Thompson, C. J.; Richardson, A. L.; Golshan, M.; Easterling, M. L.; Santagata, S.; Dillon, D. A.; Jolesz, F. A.; Agar, N. Y. R., Application of desorption electrospray ionization mass spectrometry imaging in breast cancer margin analysis. *Proc. Natl. Acad. Sci. U. S. A.* **2014**, *111* (42), 15184-15189.
6. Guenther, S.; Muirhead, L. J.; Speller, A. V.; Golf, O.; Strittmatter, N.; Ramakrishnan, R.; Goldin, R. D.; Jones, E.; Veselkov, K.; Nicholson, J.; Darzi, A.; Takats, Z., Spatially resolved metabolic phenotyping of breast cancer by desorption electrospray ionization mass spectrometry. *Cancer Res* **2015**, *75* (9), 1828-37.
7. Dill, A. L.; Ifa, D. R.; Manicke, N. E.; Ouyang, Z.; Cooks, R. G., Mass spectrometric imaging of lipids using desorption electrospray ionization. *J Chromatogr B Analyt Technol Biomed Life Sci* **2009**, *877* (26), 2883-9.
8. Sans, M.; Gharpure, K.; Tibshirani, R.; Zhang, J.; Liang, L.; Liu, J.; Young, J. H.; Dood, R. L.; Sood, A. K.; Eberlin, L. S., Metabolic Markers and Statistical Prediction of Serous Ovarian Cancer Aggressiveness by Ambient Ionization Mass Spectrometry Imaging. *Cancer Res* **2017**, *77* (11), 2903-2913.
9. Doria, M. L.; McKenzie, J. S.; Mroz, A.; Phelps, D. L.; Speller, A.; Rosini, F.; Strittmatter, N.; Golf, O.; Veselkov, K.; Brown, R.; Ghaem-Maghani, S.; Takats, Z., Epithelial ovarian carcinoma diagnosis by desorption electrospray ionization mass spectrometry imaging. *Scientific Reports* **2016**, *6*, 11.
10. Jarmusch, A. K.; Pirro, V.; Baird, Z.; Hattab, E. M.; Cohen-Gadol, A. A.; Cooks, R. G., Lipid and metabolite profiles of human brain tumors by desorption electrospray ionization-MS. *Proc. Natl. Acad. Sci. U. S. A.* **2016**, *113* (6), 1486-1491.
11. Eberlin, L. S.; Norton, I.; Orringer, D.; Dunn, I. F.; Liu, X. H.; Ide, J. L.; Jarmusch, A. K.; Ligon, K. L.; Jolesz, F. A.; Golby, A. J.; Santagata, S.; Agar, N. Y. R.; Cooks, R. G., Ambient mass

spectrometry for the intraoperative molecular diagnosis of human brain tumors. *Proc. Natl. Acad. Sci. U. S. A.* **2013**, *110* (5), 1611-1616.

12. Honarvar, E.; Venter, A. R., Ammonium Bicarbonate Addition Improves the Detection of Proteins by Desorption Electrospray Ionization Mass Spectrometry. *J Am Soc Mass Spectrom* **2017**, *28* (6), 1109-1117.

13. Shin, Y. S.; Drolet, B.; Mayer, R.; Dolence, K.; Basile, F., Desorption electrospray ionization-mass spectrometry of proteins. *Anal Chem* **2007**, *79* (9), 3514-8.

14. Ambrose, S.; Housden, N. G.; Gupta, K.; Fan, J.; White, P.; Yen, H. Y.; Marcoux, J.; Kleanthous, C.; Hopper, J. T. S.; Robinson, C. V., Native Desorption Electrospray Ionization Liberates Soluble and Membrane Protein Complexes from Surfaces. *Angew Chem Int Ed Engl* **2017**, *56* (46), 14463-14468.

15. Hsu, C. C.; Chou, P. T.; Zare, R. N., Imaging of Proteins in Tissue Samples Using Nanospray Desorption Electrospray Ionization Mass Spectrometry. *Anal. Chem.* **2015**, *87* (22), 11171-11175.

16. Griffiths, R. L.; Creese, A. J.; Race, A. M.; Bunch, J.; Cooper, H. J., LESA FAIMS Mass Spectrometry for the Spatial Profiling of Proteins from Tissue. *Anal. Chem.* **2016**, *88* (13), 6758-6766.

17. Feider, C. L.; Elizondo, N.; Eberlin, L. S., Ambient Ionization and FAIMS Mass Spectrometry for Enhanced Imaging of Multiply Charged Molecular Ions in Biological Tissues. *Anal. Chem.* **2016**, *88*, 11533-11541.

18. Klein, D. R.; Holden, D. D.; Brodbelt, J. S., Shotgun Analysis of Rough-Type Lipopolysaccharides Using Ultraviolet Photodissociation Mass Spectrometry. *Anal Chem* **2016**, *88* (1), 1044-51.

19. Li, Q.; Lex, R. K.; Chung, H.; Giovanetti, S. M.; Ji, Z.; Ji, H.; Person, M. D.; Kim, J.; Vokes, S. A., The Pluripotency Factor NANOG Binds to GLI Proteins and Represses Hedgehog-mediated Transcription. *The Journal of Biological Chemistry* **2016**, *291* (13), 7171-7182.

20. Seeley, E. H.; Oppenheimer, S. R.; Mi, D.; Chaurand, P.; Caprioli, R. M., Enhancement of protein sensitivity for MALDI imaging mass spectrometry after chemical treatment of tissue sections. *Journal of the American Society for Mass Spectrometry* **2008**, *19* (8), 1069-1077.

21. Eberlin, L. S.; Ferreira, C. R.; Dill, A. L.; Ifa, D. R.; Cooks, R. G., Desorption electrospray ionization mass spectrometry for lipid characterization and biological tissue imaging. *Biochim Biophys Acta* **2011**, *1811* (11), 946-60.

22. Takats, Z.; Wiseman, J. M.; Cooks, R. G., Ambient mass spectrometry using desorption electrospray ionization (DESI): instrumentation, mechanisms and applications in forensics, chemistry, and biology. *J Mass Spectrom* **2005**, *40* (10), 1261-75.

23. Guevremont, R., High-field asymmetric waveform ion mobility spectrometry (FAIMS). *Can. J. Anal. Sci. Spectrosc.* **2004**, *49* (3), 105-113.
24. Swearingen, K. E.; Moritz, R. L., High-field asymmetric waveform ion mobility spectrometry for mass spectrometry-based proteomics. *Expert Review of Proteomics* **2012**, *9* (5), 505-517.
25. Page, J. S.; Kelly, R. T.; Tang, K.; Smith, R. D., Ionization and transmission efficiency in an electrospray ionization-mass spectrometry interface. *J Am Soc Mass Spectrom* **2007**, *18* (9), 1582-90.
26. Klein, D. R.; Holden, D. D.; Brodbelt, J. S., Shotgun Analysis of Rough-Type Lipopolysaccharides Using Ultraviolet Photodissociation Mass Spectrometry. *Analytical Chemistry* **2016**, *88* (1), 1044-1051.
27. Hanrieder, J.; Oskar, K.; Brittebo, E. B.; Malmberg, P.; Ewing, A. G., Probing the lipid chemistry of neurotoxin-induced hippocampal lesions using multimodal imaging mass spectrometry. *Surf. Interface Anal.* **2014**, *46*, 375-378.
28. Chughtai, S.; Chughtai, K.; Cillero-Pastor, B.; Kiss, A.; Agrawal, P.; MacAleese, L.; Heeren, R. M. A., A multimodal mass spectrometry imaging approach for the study of musculoskeletal tissues. *Int. J. Mass Spectrom.* **2012**, *325*, 150-160.
29. Marshall, P.; Toteu-Djomte, V.; Bareille, P.; Perry, H.; Brown, G.; Baumert, M.; Biggadike, K., Correlation of Skin Blanching and Percutaneous Absorption for Glucocorticoid Receptor Agonists by Matrix-Assisted Laser Desorption Ionization Mass Spectrometry Imaging and Liquid Extraction Surface Analysis with Nano electrospray Ionization Mass Spectrometry. *Analytical Chemistry* **2010**, *82* (18), 7787-7794.
30. Eberlin, L. S.; Liu, X.; Ferreira, C. R.; Santagata, S.; Agar, N. Y.; Cooks, R. G., Desorption electrospray ionization then MALDI mass spectrometry imaging of lipid and protein distributions in single tissue sections. *Anal Chem* **2011**, *83* (22), 8366-71.
31. Eberlin, L. S.; Ferreira, C. R.; Dill, A. L.; Ifa, D. R.; Cheng, L.; Cooks, R. G., Nondestructive, histologically compatible tissue imaging by desorption electrospray ionization mass spectrometry. *Chembiochem* **2011**, *12* (14), 2129-32.
32. Bresnick, A. R.; Weber, D. J.; Zimmer, D. B., S100 proteins in cancer. *Nat Rev Cancer* **2015**, *15* (2), 96-109.
33. Delcourt, V.; Franck, J.; Leblanc, E.; Narducci, F.; Robin, Y. M.; Gimeno, J. P.; Quanico, J.; Wisztorski, M.; Kobeissy, F.; Jacques, J. F.; Roucou, X.; Salzet, M.; Fournier, I., Combined Mass Spectrometry Imaging and Top-down Microproteomics Reveals Evidence of a Hidden Proteome in Ovarian Cancer. *EBioMedicine* **2017**, *21*, 55-64.
34. Cross, S. S.; Hamdy, F. C.; Deloulme, J. C.; Rehman, I., Expression of S100 proteins in normal human tissues and common cancers using tissue microarrays: S100A6, S100A8, S100A9 and S100A11 are all overexpressed in common cancers. *Histopathology* **2005**, *46* (3), 256-69.

35. McKiernan, E.; McDermott, E. W.; Evoy, D.; Crown, J.; Duffy, M. J., The role of S100 genes in breast cancer progression. *Tumor Biol* **2011**, *32* (3), 441-450.
36. Sanders, M. E.; Dias, E. C.; Xu, B. J.; Mobley, J. A.; Billheimer, D.; Roder, H.; Grigorieva, J.; Dowsett, M.; Arteaga, C. L.; Caprioli, R. M., Differentiating proteomic biomarkers in breast cancer by laser capture microdissection and MALDI MS. *J Proteome Res* **2008**, *7* (4), 1500-7.
37. Grosset, A. A.; Labrie, M.; Vladoiu, M. C.; Yousef, E. M.; Gaboury, L.; St-Pierre, Y., Galectin signatures contribute to the heterogeneity of breast cancer and provide new prognostic information and therapeutic targets. *Oncotarget* **2016**, *7* (14), 18183-203.
38. Kompauer, M.; Heiles, S.; Spengler, B., Atmospheric pressure MALDI mass spectrometry imaging of tissues and cells at 1.4- $\mu\text{m}$  lateral resolution. *Nat Methods* **2017**, *14* (1), 90-96.
39. Palma, C. D.; Grassi, M. L.; Thome, C. H.; Ferreira, G. A.; Albuquerque, D.; Pinto, M. T.; Melo, F. U. F.; Kashima, S.; Covas, D. T.; Pitteri, S. J.; Faca, V. M., Proteomic Analysis of Epithelial to Mesenchymal Transition (EMT) Reveals Cross-talk between SNAIL and HDAC1 Proteins in Breast Cancer Cells. *Molecular & Cellular Proteomics* **2016**, *15* (3), 906-917.

## Chapter 4: Clinical Translation and Evaluation of the MasSpec Pen Technology for Surgical Use<sup>3</sup>

### INTRODUCTION

Clinical implementation of new technologies that can augment tissue assessment is highly desirable to improve disease diagnosis and to guide clinical and surgical decision-making<sup>1-3</sup>. Tissue evaluation is particularly critical in the surgical excision of solid cancers to assess completeness of tumor resection and surgical margin status<sup>4</sup>. Intraoperative tissue assessment is conventionally accomplished by palpation, imaging, and histopathological analysis of frozen tissue sections prepared from an excised surgical specimen. While these procedures have vastly improved patient care over the last century<sup>5</sup>, frozen section analysis in particular is time and labor intensive, susceptible to tissue processing artifacts that can lead to subjective and occasionally unconfirmed diagnoses, and requires specific training with a high level of anatomical pathology expertise. Beyond oncologic surgeries, surgical procedures for excision of tissues in benign pathologies including thyroid and parathyroid diseases are often hampered by difficulties in tissue identification due to organ similarities by gross anatomy<sup>6</sup>. Failed excisions can have devastating consequences for patients

---

<sup>3</sup> Adapted with permission from “Zhang, J., Sans, M., DeHoog, R. J., Garza, K. Y., King, M. E., Fieder, C. L., Bensussan, A., Keating, M. F., Lin, J. Q., Povilaitis, S. C., Katta, N., Milner, T. E., Wendong, Y., Nagi, C., Dhingra, S., Pirko, C., Brahmhatt, K. A., Van Buren, G., Carter, S. A., Thompson, A., Grogan, R. H., Suliburk, J., Eberlin, L. S., Clinical Translation and Evaluation of the MasSpec Pen Technology for Surgical Use. *Clinical Chemistry* 2021.” Copyright 2021 American Association of Clinical Chemistry. J.S. and L.S.E. conceived and designed the study. J.Z., M.S., R.J.D., K.Y.G., M.E.K., C.L.F., A.B. M.F.K., and J.Q.L. were responsible for mass spectrometry experiments in the OR. S.P. performed tandem mass spectrometry data analysis. L.S.E, J.Z., J.Q.L., N.K. and T.E.M. carried out engineering design of Dual Path MasSpec Pen control box. W.Y., C.N., and S.D. were responsible for pathological examination of the clinical tissues obtained in this study. C.P., K.A.B, G.V.B., S.C., A.T., R.H.G., and J.S. performed the surgeries and tissue analyses. L.S.E., J.Z., M.S. and J.S. wrote the manuscript. All authors contributed to data interpretation and revised and approved the final version of the manuscript.

including the need for re-excision surgery, additional therapies, and lifelong comorbidities<sup>7-9</sup>.

New technologies capable of providing real-time tissue assessment during surgery could greatly assist surgical decision-making, reduce operative time, and improve patient care and outcome. Several imaging and molecular technologies have been developed for intraoperative use. Fluorescence image-guided surgery has been in development for over two decades and implemented for *in vivo* tissue identification and visualization in surgical procedures<sup>10</sup>. Optical techniques including Raman spectroscopy<sup>11</sup>, optical coherence tomography<sup>12</sup>, reflectance spectroscopy<sup>13</sup>, and stimulated Raman scattering microscopy<sup>14</sup> have also been proposed for surgical guidance. Several mass spectrometry (MS) techniques have been explored for rapid molecular analysis and intraoperative tissue diagnosis<sup>15-26</sup>. The iKnife technology uses rapid evaporative ionization MS to analyze the surgical smoke generated by electrocauterization, allowing identification of normal and diseased tissues based on the detection of mass spectral profiles<sup>21, 27</sup>. Laser ablation MS techniques have also been proposed for intraoperative tissue analysis and identification through the molecular analysis of the plume formed through laser ablation<sup>18-20, 22, 28</sup>. We have described the development of the MasSpec Pen technology for rapid tissue analysis and cancer diagnosis based on the untargeted detection of molecular profiles characteristic of a disease state<sup>25-26</sup>. The MasSpec Pen operates via a liquid extraction mechanism in which a solvent droplet gently extracts molecules from a tissue for mass spectrometry (MS) analysis. We have previously reported performance for diagnosis of multiple cancer types using *ex vivo* human tissues acquired from tissue banks as frozen specimens and analyzed

in the laboratory and demonstrated feasibility for *in vivo* tissue analysis using a murine model<sup>25-26</sup>. Recently, we described the development of a laparoscopic MasSpec Pen and tested its use in a robotic surgery performed on a porcine model<sup>29</sup>. While our previous laboratory studies with human tissues and *in vivo* testing with animal models have shown feasibility of the technology for tissue analysis and diagnosis, amenability of use *in vivo* and on freshly excised tissues in human surgeries within the context and complexity of the surgical environment remained undetermined. Here, we describe the clinical translation of the MasSpec Pen technology to the operating room (OR) for *in vivo* and *ex vivo* tissue analysis in 100 surgical procedures over a 12-month period. Collectively, the results obtained show that MasSpec Pen technology can be successfully implemented in an OR and used by surgeons for non-destructive molecular analysis of tissues in human surgeries.

## **METHODS AND MATERIALS**

### **Chemicals and Reagents**

Sterile water (Deerfield, Illinois, USA) commonly used during surgery was provided by the clinical staff and used for all analyses. Human whole blood was purchased from BioIVT (Westbury, NY, USA). Silicon tubing, PTFE tubing, and heat shrink tubing were purchased from Kinesis (Vernon Hills, IL, USA), MilliporeSigma (Burlington, MA, USA), and Newark element14 (Chicago, IL, USA). Luer-locks were purchased from Cole-Parmer (Vernon Hills, Illinois, USA). The other materials used to 3D-print the MasSpec Pen devices were described in detail in our previous report<sup>26</sup>.

## **MasSpec Pen Device and Operation**

The MasSpec Pen devices were fabricated in the laboratory using 3D printing as previously described <sup>26</sup>. The devices contained a polydimethylsiloxane tip in which a reservoir is connected to three distinct conduits and two PTFE tubes (4.5 meters). Upon tissue contact, 20  $\mu$ L of sterile water was delivered through one of the PTFE tubes to the tip reservoir (2.7 mm of diameter), which was held in contact with the tissue (5 seconds). The water droplet containing the extracted molecules was then transferred via the second tube to the heated inlet of the mass spectrometer. The third conduit was left open to air to enable pressure balance and assist droplet transport. All devices were discarded after each surgery observing universal precautions. The MasSpec Pen interface/control box was designed and fabricated at the University of Texas at Austin (Figure C4.1).

## **Dual path MasSpec Pen Operation**

The MasSpec Pen interface/control box was designed and fabricated by the Instrument Design and Repair Services at the University of Texas at Austin Department of Chemistry (Figure C4.1). The interface houses an Arduino board (ELEGOO MEGA 2560 R3 Board), a lab-built circuit board, two three-way solenoid pinch valves (Masterflex, Gelsenkirchen, Germany). The “dual-path” MasSpec Pen interface was designed and programmed for the clinical studies with two parallel systems that allowed simultaneous channel operation under “analysis” or “priming” mode. Under the “priming” mode, the syringe pump was activated by pressing a “refill” button, allowing pumping of 2.5 mL of water to fill the 4.5 meter PTFE tube (~ 15 seconds). A lab-built extended metal capillary was inserted into the

mass spectrometer inlet, and to the third PTFE conduit of the MasSpec Pen connected to the metal capillary through a silicon tubing. Two syringe pumps (Chemyx Inc, Stafford, TX, USA) were connected to the control box, enabling parallel analysis and priming of the MasSpec Pen devices. The clinical staff used the MasSpec Pen following an informal and short training (~5 minutes) from the research team. At the time of tissue analysis, a foot pedal was used to activate the analysis by triggering the delivery of a discrete water volume (20  $\mu\text{L}$ ) to the MasSpec Pen tip, followed by 5 seconds of tissue analysis time, subsequent aspiration of the droplets to the mass spectrometer, and a water flush of the system (106  $\mu\text{L}$ ). After 5 seconds of tissue contact time, subsequent aspiration of the droplet to the mass spectrometer and a water flush of the system was performed automatically, as previously described <sup>26</sup>. Note that this new interface was developed to improve operational efficiency and did not entail any engineering or methodological changes to the device itself. To facilitate communication of analysis status within the surgical suite, an LED system was incorporated within the MasSpec Pen interface to announce data acquisition status during surgery. A yellow light was used to indicate solvent delivery to the MasSpec Pen tip, a purple light was used to indicate the tissue contact period, and a blue light was used to indicate solvent transport from the pen to the mass spectrometer. Audio feedback, which included a simple “ping” noise, was also incorporated to provide immediate feedback on the completion of the necessary tissue contact time (5 seconds) for one analysis to the attending surgeon(s) so that the surgeon(s) can remove the probe from the tissue site. Note that sterile water and disposable sterile syringes were used in all procedures.

## **Mass spectrometry**

Experiments were performed on a Q Exactive™ Hybrid Quadrupole-Orbitrap™ mass spectrometer (Thermo Fisher Scientific) suited with the lab-built MasSpec Pen interface, which was installed in an OR at a hospital affiliate of Baylor College of Medicine (Houston, TX). Analyses were carried out in full scan (centroid mode) in the negative ion mode from  $m/z$  120 to 1800, using a resolving power of 140,000, capillary temperature of 400 °C, and an S-lens radio frequency level of 100. Due to the strict time constraint for data acquisition in the OR, tandem MS experiments with *ex vivo* tissues and analyses of human blood were performed in the laboratory using a Q Exactive™ HF Hybrid Quadrupole-Orbitrap™ mass spectrometer.

## **Data analysis**

Mass spectral data was analyzed using XCalibur 3.1 Qual Browser. For cosine similarity analyses, four mass spectra for each analysis were first normalized to their total ion current and then averaged. Cosine similarity analyses were performed in the CRAN R language.

## **Permissions**

The study was reviewed and approved by the Institutional Review Board (IRB) of Baylor College of Medicine and the IRB of the University of Texas at Austin. The intraoperative use of the MasSpec Pen was restricted to research purposes on patients pre-scheduled to undergo surgery independently of our study. Written consent was obtained for all patients. The data from the analyses were not communicated to the surgical team nor used in clinical

decision-making. Patients scheduled to undergo parathyroidectomy, thyroidectomy, breast, and pancreatic cancer surgeries were approached by the clinical research assistants prior to surgery to participate in the study. Written consent was obtained for all patients that agreed to participate in the study. The research team was notified by clinical research assistants if the patient provided written consent to participate in the study so that MasSpec Pen analyses could take place during the surgical procedure. Patient information was de-identified by the clinical research assistants using a coding system, according to approved IRB protocol.

## **RESULTS**

### **Design and Translation of the MasSpec Pen System for Surgical Use**

We designed the MasSpec Pen as a disposable handheld device integrated to a lab-built interface that is connected to a high-performance mass spectrometer for direct, real-time molecular analysis of tissues<sup>26</sup> (Supplementary Methods). For this pilot clinical study, the disposable devices were assembled in the laboratory and transferred to the hospital facilities for sterilization by autoclaving before surgical use (Figure C4.2). The mass spectrometer was placed outside the OR sterile field, at a ~2 m distance from the operating table (Figure 4.1). Due to this distance and OR workspace constraint, the MasSpec Pen tubing length was extended to 4.5 m, which is three times longer than previously described (1.5 m) in laboratory experiments<sup>25-26</sup>, resulting in ~15s analysis time without significant impact on data quality (Tables C4.1 and C4.2). For example, Figure 4.2 shows the mass spectra obtained from serial sections of mouse brain tissue analyzed with a 2.7 mm

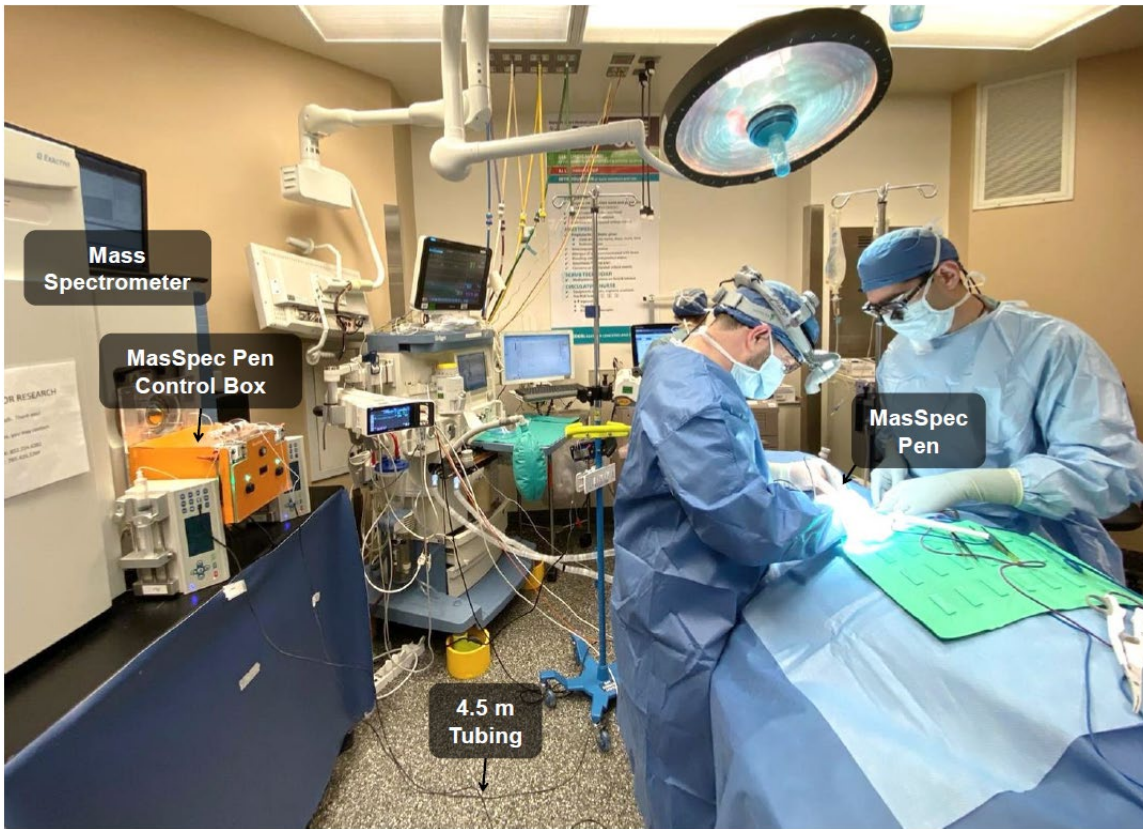


Figure 4.1: Incorporation of the MasSpec Pen system in the OR.

A Q Exactive Orbitrap mass spectrometer equipped with a MasSpec Pen Control Box was installed in the OR. MasSpec Pen devices with 4.5 m tubing were fabricated in the laboratory and autoclaved in the hospital prior to surgical use by the surgeons. The photo was obtained during *in vivo* MasSpec Pen use in a thyroidectomy surgical procedure.

MasSpec Pen probe connected to polytetrafluoroethylene (PTFE) tubing with 1.5 m, 3.0 m and 4.5 m lengths. The tubing length was measured from the MasSpec Pen handheld device to the mass spectrometer inlet. Similar molecular patterns were observed in the recorded mass spectra, displaying high relative abundances of a variety of negatively charged ions, identified as lipid species typically observed from mouse brain tissue sections using MasSpec Pen and other ambient ionization techniques. For example,  $m/z$  834.529 (identified as [PS(40:6)-H]<sup>-</sup>),  $m/z$  885.550 (identified as [PI(38:4)-H]<sup>-</sup>), and  $m/z$  790.539 (identified as [PE(40:6)-H]<sup>-</sup>), were observed at high relative abundances in the mass spectra obtained from the grey matter of mouse brain. Please note that less similarity was observed in the mass spectra profiles in the  $m/z$  120-400 range, where fluctuations in the intensities of background ions including  $m/z$  297.153,  $m/z$  311.168, and  $m/z$  325.164 are often observed in our MasSpec Pen analyses. These ions are not biologically related and likely arise from impurities in the water used or the PTFE tubing. Biologically related ions at the lower  $m/z$  range including  $m/z$  146.044 (identified as glutamate),  $m/z$  175.023 (identified as ascorbate), and  $m/z$  255.233 (identified as FA 16:0), are consistently detected in the mass spectra. As shown in Figure 4.2, the signal intensity or total ion count obtained for the mass spectra acquired using the 1.5 meter tubing length was 2.21 E5, using the 3.0 meters tubing length was 5.27 E5, and using the 4.5 meters tubing length it decreased to 3.29 E4. An average cosine similarity of 0.93 (n=12) was achieved for the mass spectra obtained with various tube lengths, which indicates that the molecular information obtained is reproducible and independent of tube length (Table C4.1). Additionally, the transfer time of the entire droplet volume plus flush used from the pen tip to the mass spectrometer

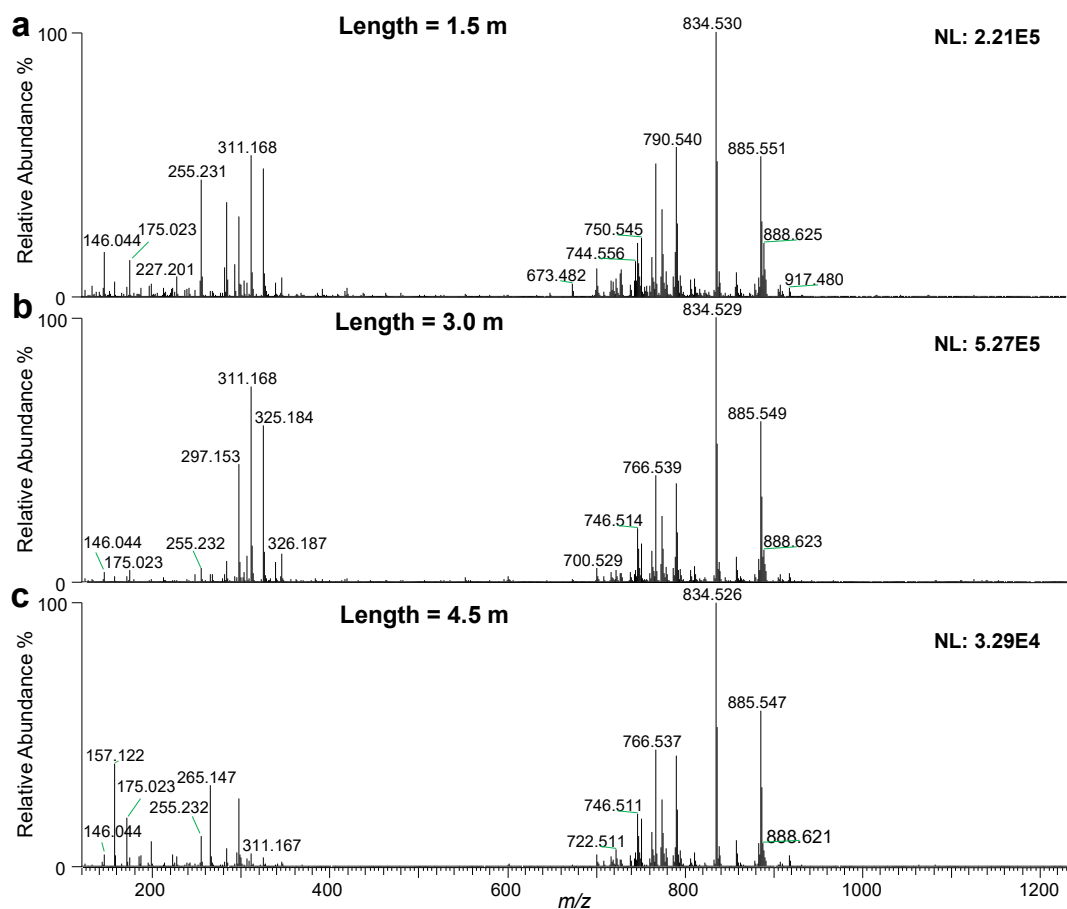


Figure 4.2: Mass spectra acquired with different MasSpec Pen tubing lengths.

The data quality obtained at different tubing was evaluated using mouse brain tissue sections. As observed, similar molecular profiles were obtained at different transfer times using (A) 1.5 m, (B) 3.0 m, and (C) 4.5 m tube lengths, although a lower total ion count (NL) was detected with the 4.5 m tube.

inlet was measured for each length tested, yielding  $3.8 \text{ s} \pm 0.5 \text{ s}$  (n=10),  $5.8 \text{ s} \pm 0.7 \text{ s}$  (n=10), for tube lengths of 1.5 m, 3.0 m, and 4.5 meters, respectively (Table C4.2). Thus, to maximize safety in our study by allowing flexibility in the placement of the tubing between the operating table and the mass spectrometer and avoid a potential tripping hazard, the 4.5-meter MasSpec Pen device was implemented in the OR, yielding a total analysis time of ~15 seconds from tissue contact to completion of mass spectra data acquisition without impact on data quality, and  $7.5 \text{ s} \pm 0.4 \text{ s}$  (n=10).

The “dual-path” MasSpec Pen interface was designed and programmed with two parallel systems allowed simultaneous channel operation under “analysis” or “priming” mode, and negligible time lag when using a new device (Figure C4.1). To facilitate communication in the OR, an LED and audio signaling system incorporated within the interface were used to announce data acquisition status during surgery, providing immediate feedback to the attending surgeon(s).

### **Clinical Use by Surgeons and Surgical Staff**

The MasSpec Pen technology was used by 7 different surgeons and surgical teams to analyze multiple tissue sites *in vivo* along with freshly excised tissue specimens during 100 surgical procedures (September 2018-August 2019). Prior to each surgery, MasSpec Pen devices were brought onto the sterile field by the surgical technologists, connected to the interface, and set up by the research team. To perform the analyses, the surgeon positioned the MasSpec Pen tip on the desired tissue site and the system was activated via a foot pedal.

Note that the research team was not permitted to cross onto the sterile field nor operate the devices during the surgical procedures.

Tables 4.1 and C4.3 provide detailed information on patient cases. In total, 270 MasSpec Pen devices were used to collect mass spectral profiles from 715 *in vivo* and *ex vivo* analyses of healthy and diseased thyroid, parathyroid, lymph node, breast, pancreatic and bile duct tissues, with 1-6 MasSpec Pen devices used per surgery. While multiple analyses were obtained with the same MasSpec Pen when amenable and at the surgeon's discretion (Figure C4.3), a different device was used for different tissue types to prevent any potential cross-contamination between different tissue types. A "water wash" was employed between devices when surgical timing allowed to do so, in order to evaluate background signal and thus potential contamination of the system and mass spectrometer interface. The "water wash" background was collected by triggering the pedal and conducting the analysis without touching a tissue. Figure. 4.3 shows the mass spectra obtained from a water background and tissue analyses during a total parathyroidectomy procedure. In the surgery, a first pen was used to analyze parathyroid tissue. After analysis, a new pen was activated and a water wash background was collected, as shown in the top mass spectra in panel A. As observed, the water background mass spectra did not present the characteristic lipid and metabolite profiles obtained from tissue analysis, regardless of previous tissue analyses performed with other MasSpec Pen devices during the surgery. Following the water wash, analyses of a lymph node were performed, yielding rich mass spectral profiles with many biologically relevant species (center mass spectra in panel A). A third pen was then activated in the system for subsequent analysis of thyroid tissue. As

Table 4.1: Summary of patient demographics, clinical indications, and procedures.

	Demographics						Clinical Indication and Procedure	
	Number of Patients (N)	Median Age, Years	Age Range, Years	Gender	Ethnicity	Race	Indication (N)	Procedure (N)
				(Female, Male)	(Hispanic or Latino, not Hispanic or Latino)	(Asian, Black or African American, Native Hawaiian or Other Pacific Islander, White or Caucasian, Other)		
<b>Thyroidectomy</b>	33	42	26 - 70	(28, 5)	(5, 28)	(4, 8, 0, 18, 3)	Graves' Disease (6), Indeterminate Nodule (11), Papillary Thyroid Cancer (7), Toxic Multinodular Goiter (3), Other (6)	Hemithyroidectomy (16), Total Thyroidectomy (14), Other (3)
<b>Parathyroidectomy</b>	42	59	31 - 81	(32, 10)	(5, 37)	(0, 10, 1, 30, 1)	Primary Hyperparathyroidism (35), Secondary Hyperparathyroidism (1), Tertiary Hyperparathyroidism (6)	Parathyroidectomy (22), Subtotal Parathyroidectomy (13), Revisional Parathyroidectomy (7)
<b>Breast</b>	11	58	45 - 84	(11, 0)	(3, 8)	(0, 1, 1, 9, 0)	Invasive Ductal Carcinoma (2), Infiltrating Lobular Carcinoma (4), Other (5)	Mastectomy (1), Bilateral Mastectomy (5), Lumpectomy (5)
<b>Pancreas</b>	14	62.5	38 - 77	(7, 7)	(4, 10)	(0, 1, 0, 12, 1)	Pancreatic Adenocarcinoma (4), Pancreatic Mass (5), Other (5)	Whipple (12), Distal Pancreatectomy (2)

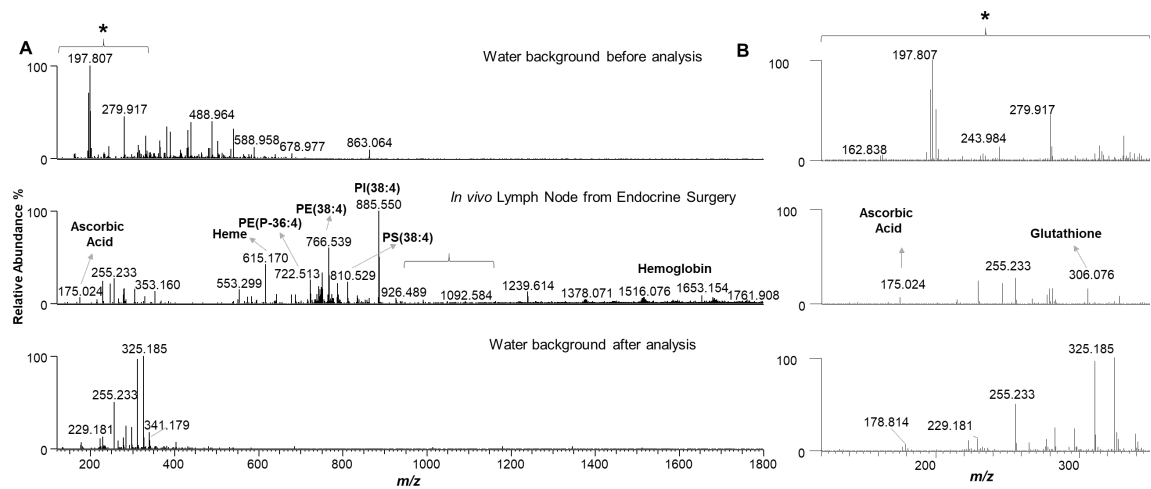


Figure 4.3: Mass spectra obtained during a total thyroidectomy for papillary thyroid cancer (TH0011).

A) A water background mass spectrum (top) was first collected using a new MasSpec Pen device prior to sampling a lymph node *in vivo* (center). After tissue analysis, the MasSpec Pen was discarded, and a new device was used for subsequent sampling. The water background mass spectrum obtained with the new MasSpec Pen device is shown in the bottom. (B) Zoom in the metabolite region from  $m/z$  100-350.

seen in the bottom mass spectra in panel A, the background mass spectrum obtained with the third pen did not present biological peaks associated with tissue analyses, with the exception of palmitic acid at  $m/z$  255.233, often detected as a background ion. A zoom-in the low  $m/z$  region is shown in panel B to facilitate visualization of detected metabolites. Note that due to the limited time available for tissue analysis in the OR and the constraints of the surgical workflow, systematic evaluation of the extent of cross-contamination between analyses using the same pen was not pursued, and will be further explored in future laboratory and OR studies. Also note that variation in the mass spectra obtained from water backgrounds was commonly observed in our experiments, which we have presumably associated with variations in residual compounds from the autoclaving process, pen materials, and/or water impurities.

Figure 4.4A shows images of the MasSpec Pen being used to analyze a thyroid on the operative field prior to its excision during a thyroidectomy (left image, TH0001) and breast cancer tissue prior to excision during a bilateral lumpectomy (right image, BR0006). Images of a freshly excised thyroid specimen before, during, and after analysis are shown in Figure 4.4B. No apparent macroscopic damage to any of the tissues analyzed *in vivo* or *ex vivo* due to MasSpec Pen analysis was observed by the surgical and research team, corroborating previous findings<sup>26</sup>. Further, no apparent microscopic damage was identified by the pathologists for cases where frozen section analyses were performed on the same tissues analyzed by the MasSpec Pen, as shown in selected H&E images of clinical frozen (breast tissue sections (BR0006, Figure 4.4C). Accordingly, while some macroscopic

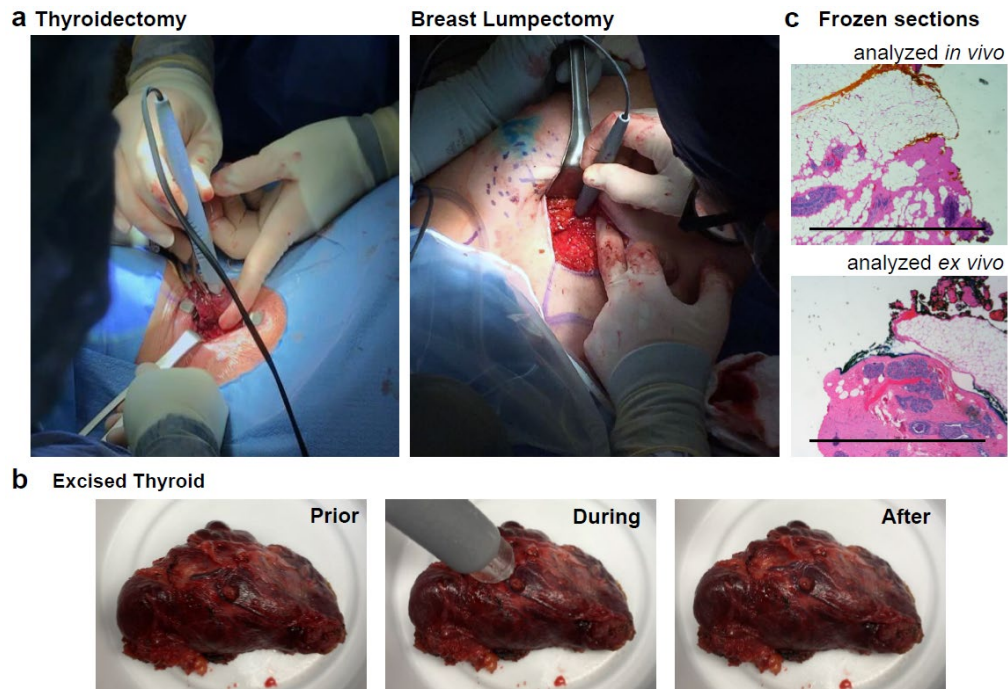


Figure 4.4: Intraoperative use of the MasSpec Pen for *in vivo* and *ex vivo* tissue analyses.

**A)** Images showing *in vivo* MasSpec Pen analysis of a thyroid gland (TH0001, left) during thyroidectomy procedure, and analysis of breast tissue in a lumpectomy prior to surgical excision (BR0006, right). **(B)** Images of a freshly excised thyroid specimen prior, during, and after *ex vivo* MasSpec Pen analysis. **(C)** Optical images provided by the pathology department of H&E stained frozen tissue sections from specimens analyzed with the MasSpec Pen *in vivo* (top) and *ex vivo* (bottom) during a lumpectomy procedure (BR0006). Scale bar = 1 mm

blood staining was expected and noted on the tissue contact portion of the device, no observable tissue fragments were seen in the pen tip or tubing (Figure C4.4).

### **Molecular Analysis of *In Vivo* and Freshly Excised Tissues**

Rich molecular profiles were detected intraoperatively with the MasSpec Pen, showing high relative abundances of various metabolites and lipid species previously characterized as potential disease markers in human tissues<sup>16, 24-27, 30</sup>. Figure 4.5 shows negative ion mode mass spectra obtained from various tissue types analyzed *in vivo* during separate surgical procedures. Proposed attributions, molecular formulae, and mass errors for annotated species are provided in Table C4.4. Figure 4.5A shows an *in vivo* mass spectrum obtained from a right thyroid gland prior to its excision during a hemithyroidectomy performed on a patient with papillary thyroid cancer (TH0003). Among many peaks, high relative abundance of peaks tentatively identified as iodine, ascorbate, hexose, fatty acid [FA] 18:1, FA 20:4, glycerophosphoethanolamine [PE] 38:4, glycerophosphoserine [PS] 36:1,  $m/z$  822.477 (unidentified), and glycerophosphoinositol [PI] 38:4 were detected. These molecular species were consistently detected in the mass spectra from thyroid tissues analyzed *in vivo* across various surgical procedures, a few of which are color-coded in the mass spectra provided in the top panel of Figure 4.6A for a benign thyroid analyzed *in vivo* during a subtotal parathyroidectomy procedure for tertiary parathyroidism (PT0008). Similar species were also detected intraoperatively on the excised thyroid tissue (Figure 4.6A, middle panel) for the same procedure (PT0008), and have been previously described in banked thyroid tissues analyzed in the laboratory *ex vivo* using the MasSpec Pen (Figure

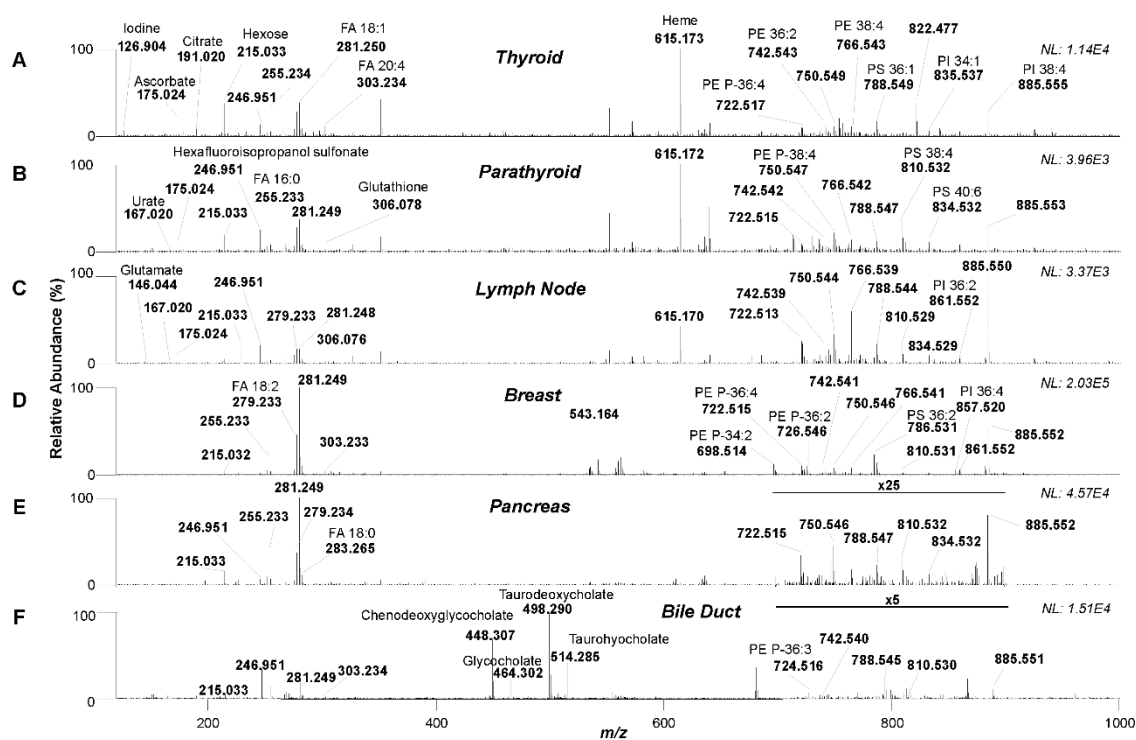


Figure 4.5: Mass spectra obtained from *in vivo* MasSpec Pen analyses of various tissues in multiple surgical procedures.

Molecular data were obtained from (A) thyroid tissue during a right hemithyroidectomy procedure for papillary thyroid cancer (TH0003, average of 15 scans), (B) right inferior parathyroid during a parathyroidectomy procedure for primary hyperparathyroidism (PT0040, average of 29 scans), (C) lymph node during a total parathyroidectomy procedure for papillary thyroid cancer (TH0011, average of 23 scans), (D) breast tissue during a right mastectomy for grade III intraductal carcinoma (BR0001, average of 4 scans), (E) pancreatic tissue during a Whipple procedure for a pancreatic mass (PN0011, average of 4 scans) and (F) bile duct margin during a Whipple procedure for a cholangiocarcinoma (PN0004, average of 13 scans). Note that *in vivo* analysis of the bile duct yielded a distinct mass spectrum with high relative abundance of bile acids in addition to metabolites and lipid species, including ions at  $m/z$  448.307,  $m/z$  464.302,  $m/z$  498.290, and  $m/z$  514.285, identified as the bile acids chenodeoxyglycocholate, glycocholate, taurodeoxycholate, taurohyocholate, respectively. Annotations for a subset of species are provided. Molecular formulas and mass errors are provided in Table C4.4. Abbreviations: FA – fatty acid, PE – glycerophosphoethanolamine, PS – glycerophosphoserine, PI – glycerophosphoinositol. Total ion count (NL) for the mass spectra are shown in each panel.

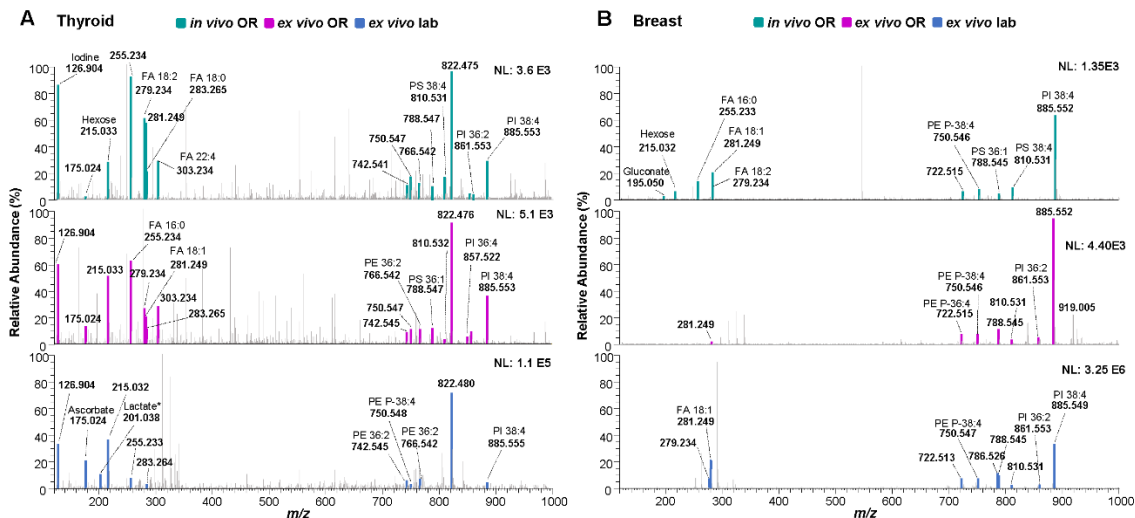


Figure 4.6: Comparison between mass spectra obtained with the MasSpec Pen *in vivo* and *ex vivo*.

(A) Comparison between mass spectra obtained *in vivo* (average of 9 scans) and *ex vivo* (average of 11 scans) in the OR from the analysis of the same benign thyroid with the MasSpec Pen during a subtotal parathyroidectomy procedure for tertiary parathyroidism (PT0008), and *ex vivo* mass spectrum (average of 7 scans) obtained from a thawed banked benign thyroid tissue that was previously acquired in the laboratory by researchers using the same instrument but with a 1.5 m tube length MasSpec Pen device<sup>26</sup>. (B) Comparison between mass spectra obtained *in vivo* (average of 12 scans) and *ex vivo* (average of 12 scans) in the OR from the same breast tissue in a lumpectomy procedure (BR0006), and the *ex vivo* mass spectrum (average of 9 scans) obtained from a thawed banked benign breast tissue acquired in the laboratory by researchers using the same instrument but with a 1.5 m tube length MasSpec Pen device<sup>26</sup>. A few representative peaks corresponding to molecules previously identified in thyroid and breast tissues are color-coded to facilitate their visualization within the mass spectra. Annotations are also provided for a subset of the species. Note that the peak annotated as lactate in the bottom mass spectrum of panel A corresponds to the sodium bound dimer. Total ion count (NL) for the mass spectra are shown in each panel.

4.6A, bottom panel) <sup>26</sup>. Note, however, that variations in the mass spectral profiles and a significant decrease in the total ion count were observed when comparing the intraoperative data with the data previously acquired by researchers from banked tissues in our laboratory, as shown in Figure C4.5. To evaluate changes in total ion count obtained in the mass spectra acquired intraoperatively with mass spectra obtained previously in the controlled laboratory environment, we calculated the average total ion counts (NL units) for all the mass spectra acquired *in vivo*, *ex vivo*, and in the laboratory (as we reported in reference 17), and used a Wilcoxon test to evaluate if the change was significant. For breast, a total of 42 *in vivo* OR mass spectra, 31 *ex vivo* OR mass spectra, and 45 *ex vivo* laboratory mass spectra were considered. For thyroid, a total of 120 *in vivo* OR mass spectra, 71 *ex vivo* OR mass spectra, and 56 *ex vivo* laboratory mass spectra were considered. As shown in Figure C4.5, no statistically significant change was observed when comparing the total ion counts obtained *in vivo* versus *ex vivo* in the OR ( $p > 0.05$ ), while a statistically significant change in the total ion abundance was observed when compared to the lab data obtained from frozen-thawed tissues ( $p < 0.05$ ). We speculate that several variables could contribute to the lower total ion counts observed in the mass spectra obtained from the OR: tube length, fresh versus frozen-thawed tissue, user experience, among others. Note that changes in total ion abundance are common in techniques that employ direct analysis by mass spectrometry, and that profiles or S/N ratios for selected peaks are a more meaningful way to compare similarities in the data achieved

*In vivo* analyses were also performed in 11 breast cancer operations, yielding mass spectra with high relative abundances of several metabolites and lipids previously

characterized in breast tissues with the MasSpec Pen and other MS techniques<sup>16, 26, 30</sup>. For example, Figure 4.5D shows the mass spectrum obtained from breast tissue *in vivo* during a right mastectomy performed on a patient with grade III intraductal carcinoma (BR0001). As observed, high relative abundance of peaks tentatively identified as FA 18:2, FA 18:1, PE plasmalogen [PE-P] 36:4, PE-P 38:4, PS 36:2, PI 36:2, and PI 38:4 were detected among many other peaks. A sentinel lymph node (SLN) biopsy was also performed during the procedure on patient BR0001. The specimen was analyzed *ex vivo* using the MasSpec Pen prior to processing for frozen section analysis (Figure 4.7). Analyses of lymph nodes both *in vivo* and *ex vivo* were conducted in 5 of the 11 breast cancer procedures (Table C4.3). *Ex vivo* measurements of excised breast specimens were also performed in all but one of the procedures (BR0008). Figure 4.6B shows the mass spectra obtained *in vivo* of a healthy breast tissue in a breast lumpectomy procedure prior to excision (BR0006), *ex vivo* from a different region of the healthy breast tissue immediately following its resection, and *ex vivo* from a banked healthy breast tissue previously analyzed in the laboratory using the MasSpec Pen<sup>26</sup>. Several peaks corresponding to molecules previously identified in breast tissues are color-coded to facilitate their visualization within the mass spectra (Figure 4.6B) (27). As observed, several metabolites, fatty acids, and lipids were commonly detected intraoperatively, as also seen in other breast cancer procedures tissues analyzed in the OR (BR0003, Figure 4.8). Yet, many metabolites detected *in vivo* were not detected in the *ex vivo* analysis for this specific tissue, which is likely due to sampling of different tissue regions *in vivo* (performed by the surgeon) and *ex vivo* (performed by the surgical assistant) within the breast specimen. The MasSpec Pen was also used to

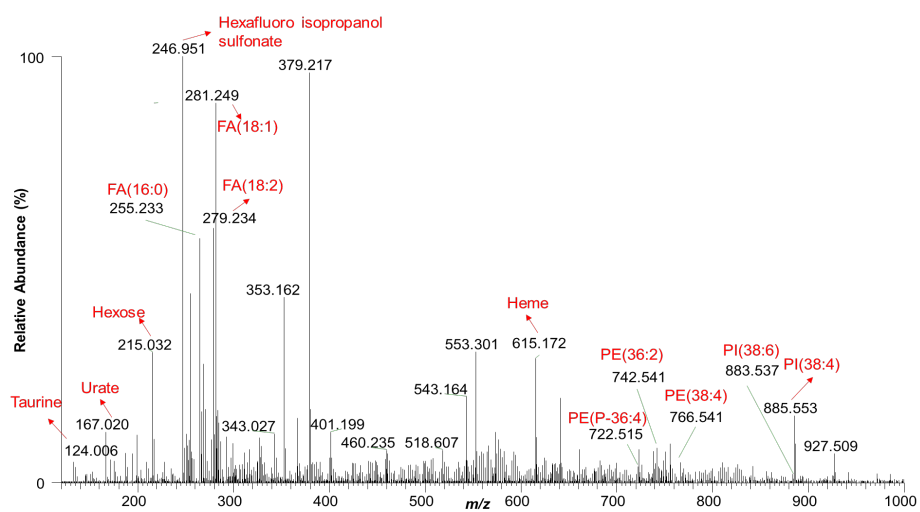


Figure 4.7: *Ex vivo* mass spectrum obtained from MasSpec Pen analysis of an excised lymph node sample during a right mastectomy procedure with sentinel node biopsy on a patient with grade III intraductal carcinoma (BR0001).

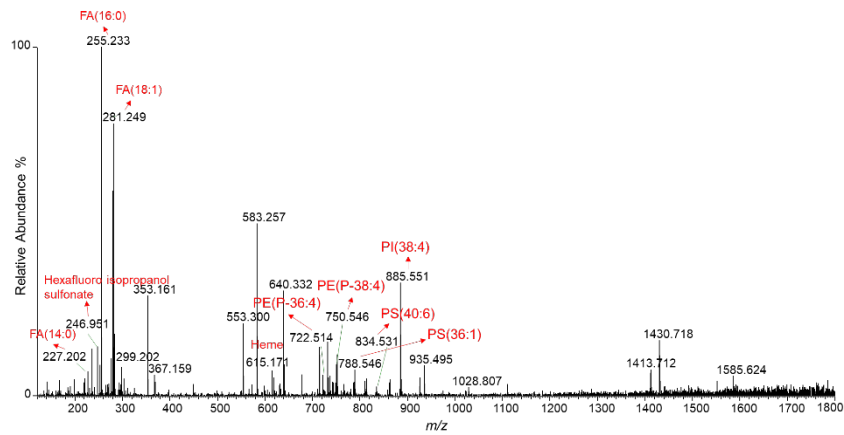


Figure 4.8: Mass spectrum obtained from MasSpec Pen *ex vivo* analysis of an excised breast specimen during a second surgery right breast lumpectomy for re-excision of a positive ductal carcinoma in situ margin (BR0003).

analyze pancreatic and bile duct tissues *in vivo* and *ex vivo* during 14 pancreatic surgical procedures. Results for pancreatic and bile duct tissue analyses are exemplified in Figure 4.5E (PN00011) and Figure 4.5F (PN00004).

### **Intraoperative Detection of Blood and Exogenous Species**

Blood-related ions were observed at generally higher relative abundances in the mass spectra collected from *in vivo* and freshly excised tissues when compared to *ex vivo* mass spectra previously acquired in the laboratory with banked tissues (Figure 4.5, Figure C4.6)<sup>25-26</sup>. In particular,  $m/z$  615.171, identified as deprotonated heme (Figure C4.6 and Figure C4.7), and a series of multiply charged ions in the  $m/z$  1200-1800 range, identified as deprotonated hemoglobin subunits (Figure C4.8), were detected at varied relative abundances in the mass spectra acquired intraoperatively. Heme and hemoglobin were also detected when directly analyzing human blood, with heme in particular detected at high relative abundances (Figure C4.9). Other exogenous species including sodium chloride cluster peaks from  $m/z$  200-1300 associated to the saline solution used for irrigation (Figure C4.10), a heavy fluorinated compound ( $C_3HF_6SO_4^-$ ) at  $m/z$  246.951 (Figure 4.5 and 4.6)<sup>31</sup>, identified as hexafluoroisopropyl sulfonate (HFIPS), a suspected secondary metabolite of the anesthetic compound sevoflurane (Figure C4.11)<sup>32</sup>, and an ion at  $m/z$  543.164 (Figure 4.5D, Figure 4.6B) identified as isosulfan blue (lymphazurin), the blue dye used as a SLN mapping agent in breast surgeries<sup>33</sup>, were also detected in the mass spectra acquired in several surgical cases. HFIPS had also been previously detected in our laboratory by desorption electrospray ionization mass spectrometry analysis of prospectively collected

specimens from endometriosis surgeries <sup>31</sup>, and was identified as a heavy fluorinated compound (C<sub>3</sub>HF<sub>6</sub>SO<sub>4</sub>) of possible anesthetic origin. The detection of *m/z* 246.951 at high relative abundances in the mass spectra collected in this study with the MasSpec Pen from *in vivo* and freshly excised specimens during surgery supported the identification of this species as hexafluoroisopropyl sulfonate (HFIPS), a suspected secondary metabolite of sevoflurane, an anesthetic compound used during surgery. To corroborate this hypothesis, we performed an experiment to biosynthesize HFIPS by incubating HFIP, a known metabolite of sevoflurane produced by Cytochrome P450 2E1, with rat liver S9 and 3'-Phosphoadenosine-5'-phosphosulfate.<sup>32</sup> The resulting product was analyzed by ESI-MS/MS revealing similar fragmentation patterns to those obtained from tissue samples, thus supporting its identification as HFIP-sulfonate (Figure C4.11).

## DISCUSSION

In this study, we report the clinical implementation of the MasSpec Pen technology in an OR and its direct use by surgeons and clinical staff to effectively and rapidly acquire molecular data during surgical procedures. The MasSpec Pen interface was re-designed to improve efficiency of use and communication to the clinical staff while minimizing disruptions to the surgical workflow. To maximize safety for patients and surgical staff, a tube length of 4.5 meters was used in all surgical procedures, all materials were sterilized before use, and sterile water and syringes were used. The surgical teams indicated the MasSpec Pen analysis procedure was efficient, well-tolerated, and no device specific intraoperative or postoperative complications to patients were reported.

The MasSpec Pen allowed gentle and effective extraction of biomolecules *in vivo* and from freshly excised tissues using a small volume (20  $\mu$ L) of sterile water, without causing any apparent microscopic or macroscopic tissue damage. Mass spectral profiles were obtained *in vivo* and *ex vivo* from a total of 177 organs during 100 surgeries, including healthy and diseased thyroid, parathyroid, lymph node, breast, pancreatic and bile duct tissues. The capability to obtain molecular information *in vivo* and from fresh specimens while preserving tissue integrity is critical to ensure patient safety and avoid damage to healthy tissues, as well as to facilitate integration with standard-of-care procedures. Other MS technologies proposed for intraoperative use rely on more invasive methods to achieve molecular analysis, such as vaporization or laser ablation, which may impede pathologic evaluation of the tissue area analyzed and/or damage tissues *in vivo*. In this study, no limitations to histologic tissue processing or diagnosis were identified via frozen section and/or final pathology analyses by the pathology department due to MasSpec Pen use in the surgical procedures and tissues analyzed, as exemplified by the H&E images of breast tissue sections obtained from clinical frozen sections analysis of the tissue regions analyzed *in vivo* and *ex vivo* by the MasSpec Pen (Figure 4.4C).

The molecular spectral profiles obtained intraoperatively from *in vivo* and *ex vivo* analyses showed high relative abundances of metabolites and lipid species previously characterized as disease markers in human tissues using the MasSpec Pen and many other MS techniques<sup>16, 24-27, 30</sup>. Several of the detected molecules have been described to have biological significance in disease progression or treatment<sup>34-36</sup>. Note that tissue analysis with the MasSpec Pen does not directly yield quantitative molecular information and that

a decrease in total ion counts was observed in the mass spectra acquired intraoperatively when compared to laboratory data (Figure 4.6), which could be associated with the fresh versus frozen-thawed nature of the tissue analyzed, the user experience, longer tube length, and/or other variables. As expected in surgical procedures, detection of blood-related ions was observed in the mass spectra obtained from *in vivo* and freshly excised tissues (Figure 4.5, 4.6, 4.7, 4.8, C4.7, C4.8, and C4.9). Spectral interferences due to blood during intraoperative tissue analysis have been previously described for other technologies, including fluorescence-guided surgeries<sup>37-38</sup>. For example, presence of blood has been shown to affect the fluorescence of molecular probes used in fluorescence-guided brain tumor surgeries, causing both quenching and increases in overall signal<sup>37</sup>. Moreover, contamination of optical devices with blood have been shown to block light transmission in fluorescence-guided procedures<sup>37</sup>. These challenges have been largely mitigated through the implementation of device cleaning protocols and development of computational methods for spectral subtraction of the blood-related effects observed in the fluorescence signal<sup>38</sup>. Using MS, the most prominent spectral features associated with blood can be identified with high mass accuracy/resolution and the chemical specificity provided by MS. The data acquired in our study suggests that the detection of heme and hemoglobin ions due to residual blood on *in vivo* and freshly excised tissues does not strongly contribute to or preclude detection of lipid and metabolite profiles from tissues. Similarly, other exogenous compounds, such as HFIPS and isosulfan blue detected in various mass spectra acquired did not hinder detection of endogenous molecular species. Thus, while the intraoperative data obtained shows evidence that the MasSpec Pen allows extraction and

detection of biologically relevant molecules *in vivo* and from freshly excised specimens, including molecules that we have previously reported as predictive features in statistical models (27), additional studies are needed to systematically evaluate the effect of interfering compounds on the molecular profiles and, more relevantly, on statistical prediction results.

A few operational and technical challenges were identified during the intraoperative studies. A decrease in instrument performance due to contamination of the first-stage ion optics following consecutive surgeries was noted within the first two months of the study, similar to what reported by others <sup>21,39</sup>. A momentary loss in system status occurred in 9 of the 100 surgeries due to vacuum instability, requiring instrument reboot. In one of the surgeries (PN0010), the instrument performance was below operational standards, precluding data acquisition. Following this occurrence, we implemented standard cleaning and calibration procedures at approximately every 10 surgeries. Multiple practical approaches are being explored to reduce contamination and improve instrument robustness and ease of maintenance. For example, a rapid and automated washing flush that is diverted from the mass spectrometer into a waste bottle is being incorporated into the programmed analysis steps to reduce buildup in the ion optics and the total volume of water introduced to the mass spectrometer per analysis, as well as to improve reusability of the device during surgery. Efforts to reduce contamination of the mass spectrometer during *in vivo* use by redesign of the ion optics components have been reported by other methods <sup>21,39</sup>, and may be explored in future iterations of a clinical mass spectrometer to improve robustness and ease of maintenance. We have previously tested the performance

of the MasSpec Pen to differentiate normal from cancerous ovarian tissues *ex vivo* using a lower performance ion trap mass spectrometer, which is smaller and less costly than the Orbitrap, as a potential alternative mass spectrometer for selected intraoperative applications<sup>25</sup>. Concerns regarding the mass spectrometer size (95 x 83 x 91 cm) and vacuum pump noise levels (~70 dB) were reported by OR personnel. However, no identified effects on patient care or progress of the surgical procedures was reported as a result of the instrumentation. The challenges and opportunities identified in this pilot study give rise to the potential for the development of a console-type mass spectrometer as a portable wheeled unit to facilitate implementation and allow use across multiple ORs. Importantly, the surgical and clinical staff universally confirmed the potential of the technology warrants further investigation and development in order to benefit future patient care.

Note that there are limitations to this study. Foremost, this is a prospective cohort pilot study conducted at a single clinical center to evaluate technical feasibility of a new intraoperative technology and was not powered or designed to evaluate diagnostic performance or differences in clinical outcomes. Thus, surgical procedures for various clinical indications were included in this study to reflect the variety of surgeries, techniques, and specialties at the clinical center. Future studies with larger cohorts of patients and procedures are needed to evaluate the data obtained per each tissue type and to enable a rigorous comparison between the mass spectra from normal and diseased tissues and diagnostic performance in the intraoperative setting. A clinical protocol for tissue annotation is being optimized to allow precise pathological evaluation of the tissue area

analyzed as sample marking for pathology correlation was not incorporated in this initial study. Statistical modeling and prediction of a larger dataset will be systematically performed for each indication in consecutive studies to evaluate the diagnostic and intraoperative performance of the MasSpec Pen for tissue identification and surgical margin evaluation.

## **CONCLUSION**

To conclude, we describe the successful translation and intraoperative use of the MasSpec Pen technology by surgical teams for direct molecular analysis of *in vivo* tissues on diverse operative fields and of freshly excised tissues from 100 patients undergoing a variety of surgical procedures. Importantly, implementation of the MasSpec Pen technology did not impact pathologic tissue evaluation nor cause any reported complications to the patients. Following clinical studies with larger cohorts of patients undergoing cervical, breast, and pancreatic cancer operations will be pursued to evaluate diagnostic performance and potential in guiding surgical decision-making.

## REFERENCES

1. Yokoyama, Y.; Nimura, Y.; Nagino, M., Advances in the treatment of pancreatic cancer: Limitations of surgery and evaluation of new therapeutic strategies. *Surg. Today* **2009**, *39* (6), 466-475.
2. Jaafar, H., Intra-Operative Frozen Section Consultation: Concepts, Applications and Limitations. *Malays. J. Med. Sci.* **2006**, *13* (1), 4-12.
3. Lee, K.; Yoon, K.; Lee, J.; Lee, H.; Kim, J.; Kim, S. I.; Cho, Y. U.; Park, B. W.; Park, H. S.; Alshahrani, M. A., The potential role of frozen sections of tumors in decision making of axillary procedure in breast conserving surgery for DCIS at preoperative diagnosis. *Breast* **2019**, *44*, S119-S119.
4. Orosco, R. K.; Tapia, V. J.; Califano, J. A.; Clary, B.; Cohen, E. E. W.; Kane, C.; Lippman, S. M.; Messer, K.; Molinolo, A.; Murphy, J. D.; Pang, J.; Sacco, A.; Tringale, K. R.; Wallace, A.; Nguyen, Q. T., Positive Surgical Margins in the 10 Most Common Solid Cancers. *Sci. Rep.* **2018**, *8*.
5. Gal, A. A.; Cagle, P. T., The 100-year anniversary of the description of the frozen section procedure. *J. Am. Med. Assoc.* **2005**, *294* (24), 3135-3137.
6. Hughes, D. T.; White, M. L.; Miller, B. S.; Gauger, P. G.; Burney, R. E.; Doherty, G. M., Influence of prophylactic central lymph node dissection on postoperative thyroglobulin levels and radioiodine treatment in papillary thyroid cancer. *Surgery* **2010**, *148* (6), 1100-6; discussion 1006-7.
7. Buchholz, T. A.; Somerfield, M. R.; Griggs, J. J.; El-Eid, S.; Hammond, M. E. H.; Lyman, G. H.; Mason, G.; Newman, L. A., Margins for Breast-Conserving Surgery With Whole-Breast Irradiation in Stage I and II Invasive Breast Cancer: American Society of Clinical Oncology Endorsement of the Society of Surgical Oncology/American Society for Radiation Oncology Consensus Guideline. *Journal of Clinical Oncology* **2014**, *32* (14), 1502-+.
8. Moran, M. S.; Schnitt, S. J.; Giuliano, A. E.; Harris, J. R.; Khan, S. A.; Horton, J.; Klimberg, S.; Chavez-MacGregor, M.; Freedman, G.; Houssami, N.; Johnson, P. L.; Morrow, M., Society of Surgical Oncology-American Society for Radiation Oncology Consensus Guideline on Margins for Breast-Conserving Surgery With Whole-Breast Irradiation in Stages I and II Invasive Breast Cancer. *Journal of Clinical Oncology* **2014**, *32* (14), 1507-+.
9. King, T. A.; Sakr, R.; Patil, S.; Gurevich, I.; Stempel, M.; Sampson, M.; Morrow, M., Clinical management factors contribute to the decision for contralateral prophylactic mastectomy. *J. Clin. Oncol.* **2011**, *29* (16), 2158-64.
10. Stummer, W.; Pichlmeier, U.; Meinel, T.; Wiestler, O. D.; Zanella, F.; Hans-Jürgen, R.; Grp, A.-G. S., Fluorescence-guided surgery with 5-aminolevulinic acid for resection of malignant glioma: a randomised controlled multicentre phase III trial. *Lancet Oncol.* **2006**, *7* (5), 392-401.

11. Jermyn, M.; Mok, K.; Mercier, J.; Desroches, J.; Pichette, J.; Saint-Arnaud, K.; Bernstein, L.; Guiot, M. C.; Petrecca, K.; Leblond, F., Intraoperative brain cancer detection with Raman spectroscopy in humans. *Sci. Transl. Med.* **2015**, *7* (274), 274ra19.
12. Kut, C.; Chaichana, K. L.; Xi, J. F.; Raza, S. M.; Ye, X. B.; McVeigh, E. R.; Rodriguez, F. J.; Quinones-Hinojosa, A.; Li, X. D., Detection of human brain cancer infiltration ex vivo and in vivo using quantitative optical coherence tomography. *Science Translational Medicine* **2015**, *7* (292).
13. Rajaram, N.; Aramil, T. J.; Lee, K.; Reichenberg, J. S.; Nguyen, T. H.; Tunnell, J. W., Design and validation of a clinical instrument for spectral diagnosis of cutaneous malignancy. *Applied Optics* **2010**, *49* (2), 142-152.
14. Orringer, D. A.; Pandian, B.; Niknafs, Y. S.; Hollon, T. C.; Boyle, J.; Lewis, S.; Garrard, M.; Hervey-Jumper, S. L.; Garton, H. J. L.; Maher, C. O.; Heth, J. A.; Sagher, O.; Wilkinson, D. A.; Snuderl, M.; Venneti, S.; Ramkissoon, S. H.; McFadden, K. A.; Fisher-Hubbard, A.; Lieberman, A. P.; Johnson, T. D.; Xie, X. S.; Trautman, J. K.; Freudiger, C. W.; Camelo-Piragua, S., Rapid intraoperative histology of unprocessed surgical specimens via fibre-laser-based stimulated Raman scattering microscopy. *Nat. Biomed. Eng.* **2017**, *1* (2), 0027.
15. Banerjee, S.; Zare, R. N.; Tibshirani, R. J.; Kunder, C. A.; Nolley, R.; Fan, R.; Brooks, J. D.; Sonn, G. A., Diagnosis of prostate cancer by desorption electrospray ionization mass spectrometric imaging of small metabolites and lipids. *Proc. Natl. Acad. Sci. U. S. A.* **2017**, *114* (13), 3334-3339.
16. Calligaris, D.; Caragacianu, D.; Liu, X. H.; Norton, I.; Thompson, C. J.; Richardson, A. L.; Golshan, M.; Easterling, M. L.; Santagata, S.; Dillon, D. A.; Jolesz, F. A.; Agar, N. Y. R., Application of desorption electrospray ionization mass spectrometry imaging in breast cancer margin analysis. *Proc. Natl. Acad. Sci. U. S. A.* **2014**, *111* (42), 15184-15189.
17. Calligaris, D.; Feldman, D. R.; Norton, I.; Olubiyi, O.; Changelian, A. N.; Machaidze, R.; Vestal, M. L.; Laws, E. R.; Dunn, I. F.; Santagata, S.; Agar, N. Y. R., MALDI mass spectrometry imaging analysis of pituitary adenomas for near-real-time tumor delineation. *Proc. Natl. Acad. Sci. U. S. A.* **2015**, *112* (32), 9978-9983.
18. Fatou, B.; Saudemont, P.; Leblanc, E.; Vinatier, D.; Mesdag, V.; Wisztorski, M.; Focsa, C.; Salzet, M.; Ziskind, M.; Fournier, I., In vivo Real-Time Mass Spectrometry for Guided Surgery Application. *Sci Rep* **2016**, *6*, 25919.
19. Woolman, M.; Kuzan-Fischer, C. M.; Ferry, I.; Kiyota, T.; Luu, B.; Wu, M. G.; Munoz, D. G.; Das, S.; Aman, A.; Taylor, M. D.; Rutka, J. T.; Ginsberg, H. J.; Zarrine-Afsar, A., Picosecond Infrared Laser Desorption Mass Spectrometry Identifies Medulloblastoma Subgroups on Intrasurgical Timescales. *Cancer Res.* **2019**, *79* (9), 2426-2434.
20. Ogrinc, N.; Saudemont, P.; Balog, J.; Robin, Y. M.; Gimeno, J. P.; Pascal, Q.; Tierny, D.; Takats, Z.; Salzet, M.; Fournier, I., Water-assisted laser desorption/ionization mass spectrometry for minimally invasive in vivo and real-time surface analysis using SpiderMass. *Nat. Protoc.* **2019**, *14* (11), 3162-3182.

21. Balog, J.; Kumar, S.; Alexander, J.; Golf, O.; Huang, J. Z.; Wiggins, T.; Abbassi-Ghadi, N.; Enyedi, A.; Kacska, S.; Kinross, J.; Hanna, G. B.; Nicholson, J. K.; Takats, Z., In Vivo Endoscopic Tissue Identification by Rapid Evaporative Ionization Mass Spectrometry (REIMS). *Angew. Chem. Int. Ed.* **2015**, *54* (38), 11059-11062.
22. Woolman, M.; Ferry, I.; Kuzan-Fischer, C. M.; Wu, M. G.; Zou, J.; Kiyota, T.; Isik, S.; Dara, D.; Aman, A.; Das, S.; Taylor, M. D.; Rutka, J. T.; Ginsberg, H. J.; Zarrine-Afsar, A., Rapid determination of medulloblastoma subgroup affiliation with mass spectrometry using a handheld picosecond infrared laser desorption probe. *Chem. Sci.* **2017**, *8* (9), 6508-6519.
23. Pirro, V.; Alfaro, C. M.; Jarmusch, A. K.; Hattab, E. M.; Cohen-Gadol, A. A.; Cooks, R. G., Intraoperative assessment of tumor margins during glioma resection by desorption electrospray ionization-mass spectrometry. *Proc. Natl. Acad. Sci. U. S. A.* **2017**, *114* (26), 6700-6705.
24. Eberlin, L. S.; Margulis, K.; Planell-Mendez, I.; Zare, R. N.; Tibshirani, R.; Longacre, T. A.; Jalali, M.; Norton, J. A.; Poultides, G. A., Pancreatic Cancer Surgical Resection Margins: Molecular Assessment by Mass Spectrometry Imaging. *PLoS Med* **2016**, *13* (8), e1002108.
25. Sans, M.; Zhang, J.; Lin, J. Q.; Feider, C. L.; Giese, N.; Breen, M. T.; Sebastian, K.; Liu, J.; Sood, A. K.; Eberlin, L. S., Performance of the MasSpec Pen for Rapid Diagnosis of Ovarian Cancer. *Clin Chem* **2019**, *65* (5), 674-683.
26. Zhang, J. L.; Rector, J.; Lin, J. Q.; Young, J. H.; Sans, M.; Katta, N.; Giese, N.; Yu, W. D.; Nagi, C.; Suliburk, J.; Liu, J. S.; Bensussan, A.; DeHoog, R. J.; Garza, K. Y.; Ludolph, B.; Sorace, A. G.; Syed, A.; Zahedivash, A.; Milner, T. E.; Eberlin, L. S., Nondestructive tissue analysis for ex vivo and in vivo cancer diagnosis using a handheld mass spectrometry system. *Sci. Transl. Med.* **2017**, *9* (406), ean3968.
27. Balog, J.; Sasi-Szabo, L.; Kinross, J.; Lewis, M. R.; Muirhead, L. J.; Veselkov, K.; Mirnezami, R.; Dezso, B.; Damjanovich, L.; Darzi, A.; Nicholson, J. K.; Takats, Z., Intraoperative Tissue Identification Using Rapid Evaporative Ionization Mass Spectrometry. *Sci. Transl. Med.* **2013**, *5* (194), 194ra93.
28. Schafer, K. C.; Szaniszló, T.; Gunther, S.; Balog, J.; Denes, J.; Keseru, M.; Dezso, B.; Toth, M.; Spengler, B.; Takats, Z., In Situ, Real-Time Identification of Biological Tissues by Ultraviolet and Infrared Laser Desorption Ionization Mass Spectrometry. *Anal. Chem.* **2011**, *83* (5), 1632-1640.
29. Keating, M. F.; Zhang, J.; Feider, C. L.; Retaillieu, S.; Reid, R.; Antaris, A.; Hart, B.; Tan, G.; Milner, T. E.; Miller, K.; Eberlin, L. S., Integrating the MasSpec Pen to the da Vinci Surgical System for In Vivo Tissue Analysis during a Robotic Assisted Porcine Surgery. *Anal Chem* **2020**.
30. Porcari, A. M.; Zhang, J. L.; Garza, K. Y.; Rodrigues-Peres, R. M.; Lin, J. Q.; Young, J. H.; Tibshirani, R.; Nagi, C.; Paiva, G. R.; Carter, S. A.; Sarian, L. O.; Eberlin, M. N.; Eberlin, L. S., Multicenter Study Using Desorption-Electrospray-Ionization-Mass-Spectrometry Imaging for Breast-Cancer Diagnosis. *Analytical Chemistry* **2018**, *90* (19), 11324-11332.

31. Feider, C. L.; Woody, S.; Ledet, S.; Zhang, J.; Sebastian, K.; Breen, M. T.; Eberlin, L. S., Molecular Imaging of Endometriosis Tissues using Desorption Electrospray Ionization Mass Spectrometry. *Sci. Rep.* **2019**, *9* (1), 15690.
32. Behne, M.; Wilke, H. J.; Harder, S., Clinical pharmacokinetics of sevoflurane. *Clin. Pharmacokinet.* **1999**, *36* (1), 13-26.
33. East, J. M.; Valentine, C. S. P.; Kanchev, E.; Blake, G. O., Sentinel lymph node biopsy for breast cancer using methylene blue dye manifests a short learning curve among experienced surgeons: a prospective tabular cumulative sum (CUSUM) analysis. *BMC Surg.* **2009**, *9*, 2.
34. Ali, I.; Wani, W. A.; Haque, A.; Saleem, K., Glutamic acid and its derivatives: candidates for rational design of anticancer drugs. *Future Med. Chem.* **2013**, *5* (8), 961-78.
35. Shenoy, N.; Creagan, E.; Witzig, T.; Levine, M., Ascorbic Acid in Cancer Treatment: Let the Phoenix Fly. *Cancer Cell* **2018**, *34* (5), 700-706.
36. Harris, I. S.; Treloar, A. E.; Inoue, S.; Sasaki, M.; Gorrini, C.; Lee, K. C.; Yung, K. Y.; Brenner, D.; Knobbe-Thomsen, C. B.; Cox, M. A.; Elia, A.; Berger, T.; Cescon, D. W.; Adeoye, A.; Brustle, A.; Molyneux, S. D.; Mason, J. M.; Li, W. Y.; Yamamoto, K.; Wakeham, A.; Berman, H. K.; Khokha, R.; Done, S. J.; Kavanagh, T. J.; Lam, C. W.; Mak, T. W., Glutathione and thioredoxin antioxidant pathways synergize to drive cancer initiation and progression. *Cancer Cell* **2015**, *27* (2), 211-22.
37. Zhang, D. Y.; Singhal, S.; Lee, J. Y. K., Optical Principles of Fluorescence-Guided Brain Tumor Surgery: A Practical Primer for the Neurosurgeon. *Neurosurgery* **2019**, *85* (3), 312-324.
38. Richter, J. C. O.; Haj-Hosseini, N.; Hallbeck, M.; Wardell, K., Combination of hand-held probe and microscopy for fluorescence guided surgery in the brain tumor marginal zone. *Photodiagnosis Photodyn. Ther.* **2017**, *18*, 185-192.
39. Alexander, J.; Gildea, L.; Balog, J.; Speller, A.; McKenzie, J.; Muirhead, L.; Scott, A.; Kontovounisios, C.; Rasheed, S.; Teare, J.; Hoare, J.; Veselkov, K.; Goldin, R.; Tekkis, P.; Darzi, A.; Nicholson, J.; Kinross, J.; Takats, Z., A novel methodology for in vivo endoscopic phenotyping of colorectal cancer based on real-time analysis of the mucosal lipidome: a prospective observational study of the iKnife. *Surg. Endosc.* **2017**, *31* (3), 1361-1370.

## **Chapter 5: Development of the MasSpec Pen for Rapid Evaluation of Surgical Margins During Breast Conserving Surgeries<sup>4</sup>**

### **INTRODUCTION**

Breast conserving surgery (BCS) is the standard of care option in the surgical management of women diagnosed with early stage breast cancer, including invasive ductal carcinoma (IDC). IDC is the most common type of breast cancer, representing approximately 80% of all breast cancer diagnoses. Effective and successful BCS for IDC entails resection of the tumor with a margin of normal tissue surrounding the excised specimen and is required to decrease local recurrence and prevent re-excision surgeries.<sup>1-3</sup> Surgical margins of the resected specimen are traditionally evaluated postoperatively by microscopic histopathological assessment of fixed tissue sections, with negative margins considered no tumor on ink for IDC.<sup>2</sup> However, clinical studies report positive margins in ~20-40% of breast conserving surgeries.<sup>2, 4-5</sup> As such, patients are recommended for additional surgery to ensure complete cancer removal, leading to increased risk of morbidity, patient anxiety, a less desirable aesthetic outcome, and increased health care costs.<sup>6-9</sup> Pathology<sup>10-11</sup>, spectroscopy<sup>12-13</sup>, and imaging<sup>14-15</sup>, among others<sup>16-17</sup>, based technologies have been developed to intraoperative margin evaluation, with clinical studies reporting re-excision rates as low as 4% when utilized.<sup>18</sup> Yet, these techniques are not routinely used as standard methods for intraoperative margin evaluation as they require specialized training for operation, preference and accuracy varies across institutions, and can be time and labor intensive.<sup>16, 19</sup>

---

<sup>4</sup> In preparation

Many technologies are currently being developed and evaluated for the intraoperative detection of breast cancer at the surgical margins during BCS, with the intent to reduce the number of re-excision surgeries.<sup>16-17</sup> Molecular based technologies, such as mass spectrometry (MS), offer the exciting opportunity to implement molecular information into the surgical environment to assist in decision making during surgical resection. MS has been successful in distinguishing normal tissue from cancerous lesions based on distinct molecular differences with high sensitivity and chemical specificity.<sup>20</sup> Desorption electrospray ionization (DESI) MS has been applied to the *ex vivo* analysis of normal and cancerous breast tissue sections, detecting molecular changes associated with the disease.<sup>21-23</sup> Capitalizing on this, several MS based approaches have been developed for the *in vivo* detection of various types of cancer, including breast cancer.<sup>24-25</sup> For example, rapid evaporative ionization mass spectrometry (REIMS) has been used to investigate alterations in the molecular information of frozen and fresh normal and cancerous breast tissue<sup>26-27</sup> and demonstrated intraoperative use in a proof of concept study.<sup>24</sup> While other MS devices have also been developed for *in vivo* cancer detection<sup>28-29</sup>, they have not been tested intraoperatively or applied to the detection of breast cancer.

We have developed a handheld and biocompatible MasSpec Pen device integrated to a mass spectrometer for direct and rapid molecular analysis of human tissue.<sup>25, 30-31</sup> Upon contact with tissue and press of a foot pedal, a discrete water droplet is delivered to the MasSpec Pen reservoir where it interacts with the tissue, gently extracting metabolites and lipids into the droplet. The droplet containing the extracted molecules is then transported into the mass spectrometer for molecular analysis. The MasSpec Pen has previously been

applied to the *ex vivo* molecular evaluation of various human cancers, including breast, lung, thyroid, and ovarian cancer, yielding a cross validation accuracy (CV) over 96% using the least absolute shrinkage and selection operator (Lasso).<sup>25</sup> More recently, the MasSpec Pen has been translated into an operating room (OR) for clinical feasibility testing during open human surgeries<sup>32</sup>, and a laparoscopic version has been evaluated for use during robotic-assisted surgery of a porcine model.<sup>31</sup> Here, we describe the application of the MasSpec Pen for the analysis of healthy breast and IDC tissues and build molecular classification models for disease prediction to evaluate its diagnostic performance for assessment of human banked, freshly excised, and *in vivo* breast tissue.

## **METHODS AND MATERIALS**

### **Banked tissue samples**

A total of 143 deidentified, banked frozen normal breast and IDC were retrospectively collected from the Cooperative Human Tissue Network (CHTN) under approved Institutional Review Board (IRB) protocol from 2016-2018. Tissue samples were stored at -80°C prior to MasSpec Pen analysis.

### **MasSpec Pen analysis of banked breast tissue samples**

The MasSpec Pen coupled to a Q Exactive mass spectrometer (Thermo Scientific) was used to analyze 79 healthy breast and 64 IDC tissue samples in four batches. Tissue samples were thawed in ambient conditions prior to MS analysis. Data was collected in the negative ion mode from  $m/z$  120-1800 using a resolving power of 140,000. For analyses performed in our laboratory, a tubing length of 1.5 m and a pen tip reservoir diameter of 2.7 mm was

used. Following MS analysis, a surgical ink stain was applied to the tissue to demarcate the region analyzed by the MasSpec Pen for a direct correlation of histology with the mass spectra. Samples were then immediately flash frozen in liquid nitrogen and sectioned at 5-10  $\mu$ M thickness with a CryoStar NX50 (Thermo Scientific) for pathological evaluation by C. N., a board-certified pathologist. Tandem MS of selected ions was performed on a Q Exactive HF mass spectrometer for ion identification.

### **Pathological evaluation of tissue sections**

Pathological evaluation of H&E stained tissue sections of each sample was performed to determine the tissue composition and histology within the analyzed region, which was demarcated with surgical ink. Evaluation was performed by C.N., and all tissue sections were assessed blindly. Normal breast tissue was typically composed of adipose and connective tissue as well luminal cells lining normal breast ducts. The major histological component of IDC tissues were tumor cells although lymphocytes, DCIS, and stroma were present as well. Histological features were carefully considered when extracting data to build classification models for disease prediction.

### **Intraoperative clinical testing of the MasSpec Pen during breast cancer surgeries**

The clinical study was conducted at Baylor St. Luke's Hospital (Houston, TX) from September 2018-June 2021 under approved IRB protocol from Baylor College of Medicine and The University of Texas at Austin. Patients were considered eligible for enrollment in our study if they were scheduled to undergo breast surgery, including lumpectomy or mastectomy procedures, independently of our study with S.A.C, A.T., or E.B.. Eligible

patients were identified at least one week prior to the scheduled surgery. On the day of the surgery, patients were informed of the study, and those who agreed to participate provided written consent. While a total of 20 patients agreed to enroll, MasSpec Pen data was collected only in 18 cases as there were last minute scheduling changes for Case 16 and 17 that prevented data acquisition.

A Q Exactive mass spectrometer (Thermo Scientific) equipped with the MasSpec Pen system was installed in an OR. The tubing length was increased to 4.5 m to fit the OR environment. Three to four autoclaved MasSpec Pen devices were placed in the surgical field for *in vivo* breast and lymph node analyses. An additional pen was placed next to the mass spectrometer, outside of the surgical field, and reserved for *ex vivo* analyses of freshly excised breast and lymph node specimens. Prior to the start of the surgery, UT research personnel connected one end of the tubing to the mass spectrometer. *In vivo* MasSpec Pen analyses were performed by attending surgeons S. A. C., A. T., and E. B., while *ex vivo* analyses were performed by C. P. and K. B. immediately following tissue resection. Data and results were not communicated to the surgical staff, and no statistical analysis or disease prediction was performed during the surgery.

### **Statistical analyses**

Three mass spectra were averaged and exported as a .csv file for each sample analyzed in our laboratory at UT. The data was imported into R studio for preprocessing and statistical analysis. The data was binned to 0.01  $m/z$ , and  $m/z$  values appearing in less than 10% of the data set were removed. Data was then background subtracted and normalized to the

total ion count. The least absolute shrinkage and selection operator (Lasso) was performed using the glmnet package in the R CRAN language library. Two classification models were built including a model for differentiation of healthy breast from IDC and a model for discriminating healthy nodes from nodes with IDC metastasis. The statistical classifiers were generated using data obtained from the MasSpec Pen analysis of tissue samples histologically validated by a pathologist (C.N.) via tissue sections. Training sets of samples were used to build each classifier, and model performance was evaluated using leave one out cross validation (LOOCV). The diagnostic performance of the normal breast vs IDC model was further assessed by predicting on a validation and independent test set of samples. Accuracy, sensitivity, and specificity for all prediction results were calculated based on agreement with pathological evaluation.

*In vivo* and *ex vivo* breast and lymph node data acquired in the OR were predicted on using the respective models. Lasso prediction results for *in vivo* tissue that were not surgically resected were compared to surgical gross assessment. Prediction results for *in vivo* and *ex vivo* data of the excised suspected tumor were compared to frozen section analysis, if performed, and postoperative pathological assessment.

## **RESULTS**

### **Molecular analysis and statistical prediction of banked breast tissue samples**

The MasSpec Pen was used to analyze 143 banked normal breast and IDC tissue samples to evaluate its potential for detecting IDC at the surgical margins of the primary specimen. We observed rich molecular profiles composed of a diverse array of metabolites and

complex glycerophospholipid (GP) species in normal breast and IDC mass spectral profiles (Figure 5.1A). For example, small metabolites including ascorbic acid ( $m/z$  175.203), hexose ( $m/z$  215.031), glutathione ( $m/z$  306.076), and glutamate ( $m/z$  146.046) were detected both tissue types. Various GP classes were also detected in healthy breast and IDC tissue, such as phosphatidylinositol (PI), phosphatidylethanolamine (PE), and phosphatidylserine (PS). Mass spectra obtained from IDC tissues were characterized by the high relative abundances of PI species such as PI 34:1 ( $m/z$  835.533), PI 36:1 ( $m/z$  863.565), and PI 38:3 ( $m/z$  887.565) while PS 36:1 ( $m/z$  788.544), PE O-38:5 ( $m/z$  750.544), and PI 38:4 ( $m/z$  885.549) were detected at higher relative abundances in normal breast tissue.

To evaluate if the molecular information obtained from normal breast and IDC banked tissue samples was distinct, we employed the Lasso statistical analysis method to select a sparse set of  $m/z$  features for disease prediction. Samples were categorized as normal or cancerous based on the histology of the region analyzed with the MasSpec Pen, as determined by the pathologist. The mass spectra collected in the first two batches were combined and randomly split into a training and validation set to build and validate the classification model (n=57 healthy breast, n=33 IDC). The Lasso model for IDC prediction was generated using a training set of 68 samples. The model exhibited a strong performance, achieving a sensitivity of 100%, specificity of 95.4%, and an overall agreement with pathology of 97.1% for LOOCV (Figure 5.1B). The predictive performance of the model was further evaluated by predicting on a validation set of 22 samples. Remarkably, an excellent sensitivity, specificity, and prediction accuracy of

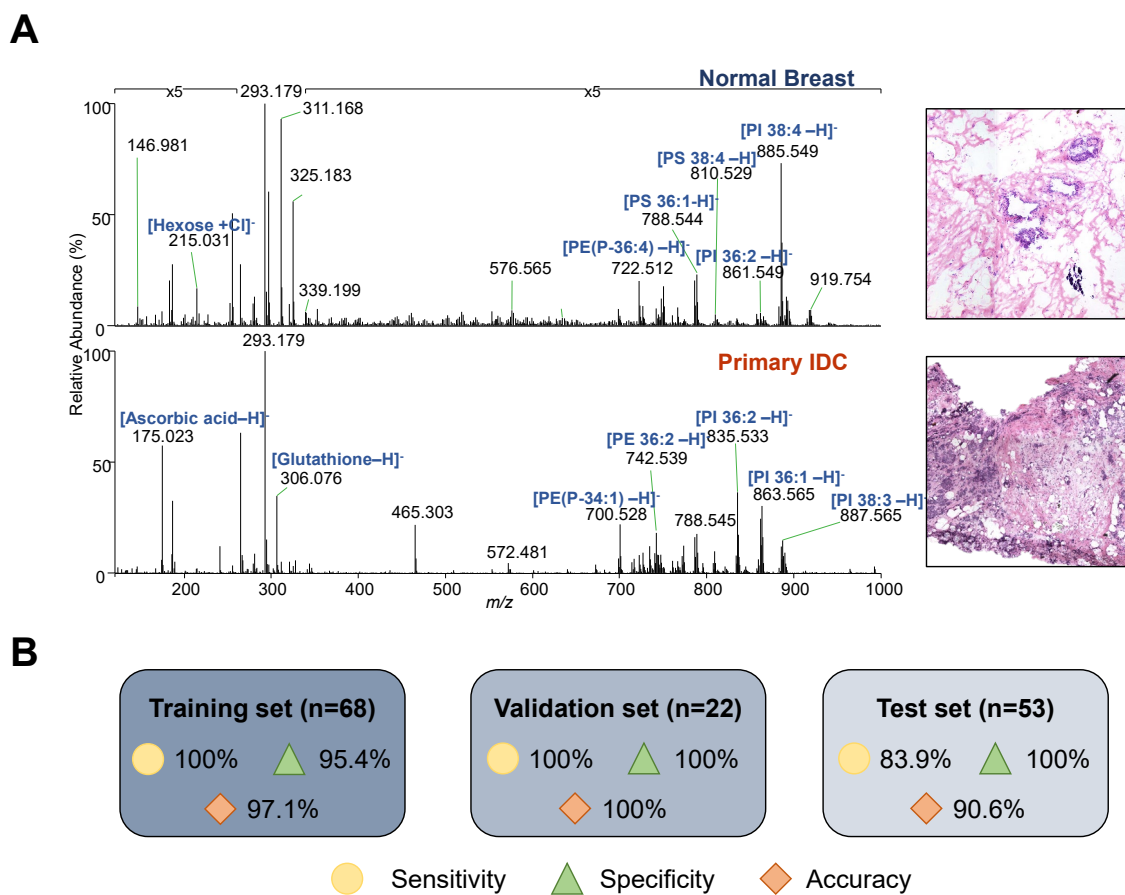


Figure 5.1: MasSpec Pen and statistical analysis of normal breast and primary IDC tissue.

A. Mass spectra from the MasSpec Pen analysis of normal breast tissue (top) and primary IDC tissue (bottom) with corresponding H&E stained images of the regions analyzed. B. Lasso prediction results for the IDC classification model. Sensitivity, specificity, and accuracy are shown for the training, validation, and test set.

100% as all samples were classified correctly in the validation set. We further evaluated the robustness of the classification model for the differentiating IDC from normal tissue by predicting on an independent test set comprised of 53 samples from batch three and four. Overall, sensitivity of 83.9%, a specificity of 100%, and 90.6% prediction accuracy was achieved, with five IDC samples classified as normal breast tissue. A summary of the classification results is included in Table 5.1. A total of seven metabolites and GP were selected to differentiate healthy breast tissue from IDC. Among those selected, hexose, PI 38:4 ( $m/z$  885.549), and two unidentified molecules at  $m/z$  268.801 and  $m/z$  373.04 were weighted toward healthy breast tissue, while ascorbic acid, PE 36:2 ( $m/z$  742.539), and PE 38:4 ( $m/z$  766.540) were selected as indicative of IDC.

### **Intraoperative MasSpec Pen analysis during breast cancer surgeries**

Toward the goal of evaluating the MasSpec Pen for intraoperative breast and lymph node tissue assessment, we installed the MasSpec Pen system in the OR for clinical testing during breast surgeries. The MasSpec Pen was used during 14 lumpectomy and 10 mastectomy surgeries treating patients with IDC as well as other conditions. During the surgeries, the attending surgeons performed *in vivo* analyses of tissue regions of interest which included surgical margins of the suspected tumor, normal breast tissue as determined by surgical gross assessment, and the surgical cavity following tissue resection. A BCM research personnel performed *ex vivo* analyses of the surgical margins of the freshly excised specimen, normal breast tissue removed during mastectomies. A total of 183 MasSpec Pen analyses were performed on breast tissue, including 80 *in vivo* and 103 *ex*

Table 5.1: Summary of the classification results for the training, validation and test sets of data.

Sample Set	Pathology	Model Prediction and Performance				
		Normal	Cancer	Sensitivity	Specificity	Accuracy
Training set	Normal	41	2	100.00%	95.35%	97.06%
	Cancer	0	25			
Validation set	Normal	14	0	100.00%	100.00%	100.00%
	Cancer	0	8			
Test set	Normal	22	0	83.87%	100.00%	90.57%
	Cancer	5	26			

*vivo* analyses. The molecular profiles obtained from intraoperative breast tissue analyses displayed various metabolite, fatty acid, and GP species, such as hexose ( $m/z$  215.032), ascorbic acid ( $m/z$  175.023), oleic acid ( $m/z$  281.248, PI 38:4 ( $m/z$  885.549), and PS 38:4 ( $m/z$  810.530) as shown in Figure 2. Similar species were observed in the mass spectra collected intraoperatively compared to those acquired from banked tissue in our laboratory. Interestingly, we observed higher relative abundances of chlorinated triacylglycerol (TG) species in the data collected intraoperatively. It is important to note, however, that fewer lipid species and generally, a relatively higher abundance of spectral noise, blood related species such as heme ( $m/z$  615.172) and hemoglobin (observed from  $m/z$  1200-1500), and Lymphazurin ( $m/z$  543.163), used for lymph node staging during SLNB, were observed in mass spectra collected intraoperatively. Of the 183 analyses collected intraoperatively, we evaluated the performance of the IDC classification model on 52 *in vivo* and 52 *ex vivo* analyses from 18 cases in an independent test set and achieved an 95.2% accuracy, with 99 of 104 predictions in agreement with final pathology reports. Note that the remaining 79 spectra did not yield any signal or a signal to noise above three was not observed for biological molecules and were thus excluded from the prediction.

## **DISCUSSION**

Achieving adequate negative margins for the primary tumor during BCS is strongly correlated with decreased local recurrence and is paramount to prevent re-excision surgeries, which have negative health and economic implications for the patient.<sup>1, 3</sup> While intraoperative surgical margin evaluation methodologies are currently available to

surgeons and clinicians, clinical and technical limitations have prevented their widespread in practice across institutions<sup>16, 19</sup>. In this study, we evaluated the ability of the MasSpec Pen to differentiate IDC from normal breast tissue by generating molecular classification models for IDC detection and translated the system to the OR assess performance for surgical margin evaluation on intraoperative data collected *in vivo* and from freshly excised breast specimen.

We applied the MasSpec Pen system to analyze 79 normal breast and 64 IDC banked frozen tissue samples, from which 68 were used in a training set to generate a classification model for discrimination of normal breast and IDC. An overall CV prediction accuracy of 97.1% was achieved, similar to what was achieved for the analysis of tissue sections by DESI-MS (~98%)<sup>21, 23</sup> and frozen and fresh specimens by REIMS (95.8%, n=260). Next, we evaluated the performance of the model on a validation set of 14 normal and 8 IDC tissue samples. Remarkably, all samples had a prediction result in agreement with pathology, with all IDC samples having a heterogenous histology of comprised of tumor cells intermixed with collagen, adipose tissue, and necrosis within the analyzed region. The robustness of the IDC model was further assessed by predicting on an independent test set of samples analyzed six months after the training and validation set data was collected. A total of five IDC samples were classified in disagreement with pathology while all normal breast tissue samples were correctly classified, resulting in an overall accuracy of 90.6%. Notably, three samples with an IDC cell concentration of 10-20% within the delineated analyzed region were correctly classified as cancer using the classification model. However, IDC sample 1161265 also displayed a low tumor cellularity

of ~5% intermingled with collagen within the region analyzed by the MasSpec Pen, and was classified as normal breast, suggesting that the MasSpec Pen has a tumor cell concentration limit of detection around 5-10% within a 2.7 mm diameter region. It is worth noting that the classification model was built using IDC samples with higher tumor cell concentrations ranging from >30%, potentially contributing to the misclassification of sample 1162165. Sample A423A is another IDC tissue classified as normal breast by the classification model, and the demarcated region of H&E stained tissue section displayed well-differentiated tumor cells. Well-differentiated tumor cells are slow growing, less aggressive, and undergo different metabolic changes compared to moderately- and poorly-differentiated tumors, possibly leading to the incorrect classification of the sample as normal breast tissue. Of note, a sample containing tumor cells as well as normal luminal cells in the analyzed region had a cancer prediction result. Collectively, the high performance achieved by the model demonstrate the robustness of the method for breast tissue assessment.

The classification model consisted of various lipid and metabolite species that have been previously reported to play key roles in cancer cell metabolism and detected in breast tissue by MS. For example, PI 38:4 was selected as a feature indicative of normal breast tissue. This biomolecule has been detected at higher relative abundances in normal breast tissue compared to breast cancer tissue in multiple DESI-MS studies.<sup>21,33</sup> Additionally, the chlorinated adduct of glucose was selected as predictive of normal breast tissue. Note that we have tentatively identified this molecule as glucose as tandem MS does not allow for the characterization of the structural isomer of hexose. In cancer cells, the rate of glucose

uptake is significantly increased and rapidly converted to lactate due to the Warburg effect.<sup>34</sup> As oxidative phosphorylation is more efficient at producing lactate, we suspect that glucose is present at higher relative abundances normal breast compared to IDC tissues. Two PE species, PE 36:2 and PE 38:4, were selected as indicative of IDC tissue, and PE 38:4 was found at a higher absolute abundance in breast cancer tissue relative to normal breast using quantitative LC-MS.<sup>35</sup> Polyunsaturated PE species in general have previously been detected at increased relative amounts in breast cancer tissue compared to normal breast, which corroborates our findings.<sup>36</sup>

The MasSpec Pen system was implemented into the surgical workflow for breast cancer and non-malignant lumpectomy and mastectomy procedures to demonstrate feasibility for *in vivo* and *ex vivo* tissue evaluation. Various GP and metabolite species detected in banked tissue as well as included in the IDC classification model were observed in the data obtained intraoperatively despite the detection of non-tissue specific molecules related to sentinel lymph node biopsies and anesthetics, peaks related to biological fluids, and an increase in spectral noise, showcasing the potential of the MasSpec Pen to detect important biomolecules involved in cell metabolism from *in vivo* and freshly excised tissues. The IDC classifier generated from banked tissue was then used to predict on an independent test set comprised of data obtained from 104 intraoperative MasSpec Pen analyses, resulting in an 95.2% overall agreement with final histopathological reports. For patient 6, for example, the MasSpec Pen was used to analyze the anterior margin of the suspected tumor from the left breast *in vivo* (three analyses) and *ex vivo* (three analyses) during a double breast lumpectomy. All analyses had a normal breast prediction, which

disagreed with intraoperative gross assessment of the surgical margins. Final postoperative histopathological pathology reports revealed that the anterior margin was negative for carcinoma, with a margin of 6 mm, confirming the prediction by our method. Additional case studies can be found in the SI. These results showcase the potential of the MasSpec Pen to evaluate for surgical margin evaluation and ultimately aid in the assessment of tissue during surgical resection.

This study has several limitations. First, the classification model was built using samples containing IDC as the major histological component and higher tumor cellularity and should be expanded to include samples with a ductal carcinoma in situ component, which has been reported to be present in up to 60% IDC cases<sup>37</sup>, and lower tumor cell concentration to more broadly evaluate the performance of the model for surgical margin assessment. For the pilot clinical study, final postoperative pathology revealed the surgical margins of resected tumor tissue was surrounded by a rim of normal breast tissue and was not physically exposed during the cancer surgeries (n=15). Thus, all MasSpec Pen analyses were performed on negative margins. The lack of IDC tissue exposed during the surgeries precluded the validation of our statistical classifier for the intraoperative detection of IDC; yet, the 95.2% overall agreement achieved for the negative margin analyses shows promise of the MasSpec Pen as an intraoperative method for tissue evaluation. Nevertheless, a larger patient cohort and multi-center studies are needed for further refinement and rigorous validation of the statistical classifier. While negative margins are considered no tumor on ink, the definition varies widely in practice among surgeons, pathologists, and institutions<sup>38-39</sup>, as well as for different types of breast cancer. Therefore, investigation into

the depth of MasSpec Pen solvent extraction is needed to expand the applications as well as increase usability at multiple institutions. The current design of the MasSpec Pen used in this study covers  $\sim 5.73$  mm<sup>2</sup> sampling area, meaning multiple MasSpec Pen analyses may be needed depending on tissue dimensions and coverage needs, which could increase the total time required for margin assessment via the MasSpec Pen. Further investigation into larger pen tip diameter, and thus larger area coverage, is needed to evaluate usability for surgical margin assessment.

## **CONCLUSION**

In conclusion, this study provides evidence that the MasSpec Pen can be used for rapid tissue assessment, exhibiting a strong and robust performance for discrimination of IDC from normal breast using banked tissue samples as well as showing promise for intraoperative use during breast surgeries. Although further refinement and validation of the methodology and classification model will be pursued, the work described here demonstrates the MasSpec Pen as a valuable tool to provide near real-time feedback to surgeons to aid in the assessment of specimen margins while operating, with potential to reduce secondary BCS surgeries and improve patient care and outcome.

## REFERENCES

1. Houssami, N.; Macaskill, P.; Marinovich, M. L.; Dixon, J. M.; Irwig, L.; Brennan, M. E.; Solin, L. J., Meta-analysis of the impact of surgical margins on local recurrence in women with early-stage invasive breast cancer treated with breast-conserving therapy. *Eur J Cancer* **2010**, *46* (18), 3219-32.
2. Moran, M. S.; Schnitt, S. J.; Giuliano, A. E.; Harris, J. R.; Khan, S. A.; Horton, J.; Klimberg, S.; Chavez-MacGregor, M.; Freedman, G.; Houssami, N.; Johnson, P. L.; Morrow, M., Society of Surgical Oncology-American Society for Radiation Oncology consensus guideline on margins for breast-conserving surgery with whole-breast irradiation in stages I and II invasive breast cancer. *Ann Surg Oncol* **2014**, *21* (3), 704-16.
3. Menes, T. S.; Tartter, P. I.; Bleiweiss, I.; Godbold, J. H.; Estabrook, A.; Smith, S. R., The consequence of multiple re-excisions to obtain clear lumpectomy margins in breast cancer patients. *Ann Surg Oncol* **2005**, *12* (11), 881-5.
4. Buchholz, T. A.; Somerfield, M. R.; Griggs, J. J.; El-Eid, S.; Hammond, M. E. H.; Lyman, G. H.; Mason, G.; Newman, L. A., Margins for Breast-Conserving Surgery With Whole-Breast Irradiation in Stage I and II Invasive Breast Cancer: American Society of Clinical Oncology Endorsement of the Society of Surgical Oncology/American Society for Radiation Oncology Consensus Guideline. *Journal of Clinical Oncology* **2014**, *32* (14), 1502-+.
5. McCahill, L. E.; Single, R. M.; Aiello Bowles, E. J.; Feigelson, H. S.; James, T. A.; Barney, T.; Engel, J. M.; Onitilo, A. A., Variability in reexcision following breast conservation surgery. *JAMA* **2012**, *307* (5), 467-75.
6. Olsen, M. A.; Nickel, K. B.; Margenthaler, J. A.; Wallace, A. E.; Mines, D.; Miller, J. P.; Fraser, V. J.; Warren, D. K., Increased Risk of Surgical Site Infection Among Breast-Conserving Surgery Re-excisions. *Ann Surg Oncol* **2015**, *22* (6), 2003-9.
7. Waljee, J. F.; Hu, E. S.; Newman, L. A.; Alderman, A. K., Predictors of re-excision among women undergoing breast-conserving surgery for cancer. *Ann Surg Oncol* **2008**, *15* (5), 1297-303.
8. Jung, W.; Kang, E.; Kim, S. M.; Kim, D.; Hwang, Y.; Sun, Y.; Yom, C. K.; Kim, S. W., Factors Associated with Re-excision after Breast-Conserving Surgery for Early-Stage Breast Cancer. *J Breast Cancer* **2012**, *15* (4), 412-9.
9. Pleijhuis, R. G.; Graafland, M.; de Vries, J.; Bart, J.; de Jong, J. S.; van Dam, G. M., Obtaining adequate surgical margins in breast-conserving therapy for patients with early-stage breast cancer: current modalities and future directions. *Ann Surg Oncol* **2009**, *16* (10), 2717-30.
10. Jorns, J. M.; Visscher, D.; Sabel, M.; Breslin, T.; Healy, P.; Daignaut, S.; Myers, J. L.; Wu, A. J., Intraoperative frozen section analysis of margins in breast conserving surgery significantly decreases reoperative rates: one-year experience at an ambulatory surgical center. *Am J Clin Pathol* **2012**, *138* (5), 657-69.

11. Esbona, K.; Li, Z.; Wilke, L. G., Intraoperative imprint cytology and frozen section pathology for margin assessment in breast conservation surgery: a systematic review. *Ann Surg Oncol* **2012**, *19* (10), 3236-45.
12. Allweis, T. M.; Kaufman, Z.; Lelcuk, S.; Pappo, I.; Karni, T.; Schneebaum, S.; Spector, R.; Schindel, A.; Hershko, D.; Zilberman, M.; Sayfan, J.; Berlin, Y.; Hadary, A.; Olsha, O.; Paran, H.; Gutman, M.; Carmon, M., A prospective, randomized, controlled, multicenter study of a real-time, intraoperative probe for positive margin detection in breast-conserving surgery. *Am J Surg* **2008**, *196* (4), 483-9.
13. Geha, R. C.; Taback, B.; Cadena, L.; Borden, B.; Feldman, S., A Single institution's randomized double-armed prospective study of lumpectomy margins with adjunctive use of the MarginProbe in nonpalpable breast cancers. *Breast J* **2020**, *26* (11), 2157-2162.
14. Moore, M. M.; Whitney, L. A.; Cerilli, L.; Imbrie, J. Z.; Bunch, M.; Simpson, V. B.; Hanks, J. B., Intraoperative ultrasound is associated with clear lumpectomy margins for palpable infiltrating ductal breast cancer. *Annals of Surgery* **2001**, *233* (6), 761-768.
15. Nguyen, F. T.; Zysk, A. M.; Chaney, E. J.; Kotynek, J. G.; Oliphant, U. J.; Bellafiore, F. J.; Rowland, K. M.; Johnson, P. A.; Boppart, S. A., Intraoperative evaluation of breast tumor margins with optical coherence tomography. *Cancer Res* **2009**, *69* (22), 8790-6.
16. Maloney, B. W.; McClatchy, D. M.; Pogue, B. W.; Paulsen, K. D.; Wells, W. A.; Barth, R. J., Review of methods for intraoperative margin detection for breast conserving surgery. *J Biomed Opt* **2018**, *23* (10), 1-19.
17. Gray, R. J.; Pockaj, B. A.; Garvey, E.; Blair, S., Intraoperative Margin Management in Breast-Conserving Surgery: A Systematic Review of the Literature. *Ann Surg Oncol* **2018**, *25* (1), 18-27.
18. Reyna, C.; DeSnyder, S. M., Intraoperative Margin Assessment in Breast Cancer Management. *Surg Oncol Clin N Am* **2018**, *27* (1), 155-165.
19. Nowikiewicz, T.; Srutek, E.; Glowacka-Mrotek, I.; Tarkowska, M.; Zyromska, A.; Zegarski, W., Clinical outcomes of an intraoperative surgical margin assessment using the fresh frozen section method in patients with invasive breast cancer undergoing breast-conserving surgery - a single center analysis. *Sci Rep* **2019**, *9* (1), 13441.
20. Ifa, D. R.; Eberlin, L. S., Ambient Ionization Mass Spectrometry for Cancer Diagnosis and Surgical Margin Evaluation. *Clin Chem* **2016**, *62* (1), 111-23.
21. Porcari, A. M.; Zhang, J. L.; Garza, K. Y.; Rodrigues-Peres, R. M.; Lin, J. Q.; Young, J. H.; Tibshirani, R.; Nagi, C.; Paiva, G. R.; Carter, S. A.; Sarian, L. O.; Eberlin, M. N.; Eberlin, L. S., Multicenter Study Using Desorption-Electrospray-Ionization-Mass-Spectrometry Imaging for Breast-Cancer Diagnosis. *Analytical Chemistry* **2018**, *90* (19), 11324-11332.
22. Calligaris, D.; Caragacianu, D.; Liu, X.; Norton, I.; Thompson, C. J.; Richardson, A. L.; Golshan, M.; Easterling, M. L.; Santagata, S.; Dillon, D. A.; Jolesz, F. A.; Agar, N. Y., Application

of desorption electrospray ionization mass spectrometry imaging in breast cancer margin analysis. *Proc Natl Acad Sci U S A* **2014**, *111* (42), 15184-9.

23. Guenther, S.; Muirhead, L. J.; Speller, A. V.; Golf, O.; Strittmatter, N.; Ramakrishnan, R.; Goldin, R. D.; Jones, E.; Veselkov, K.; Nicholson, J.; Darzi, A.; Takats, Z., Spatially resolved metabolic phenotyping of breast cancer by desorption electrospray ionization mass spectrometry. *Cancer Res* **2015**, *75* (9), 1828-37.

24. St John, E. R.; Balog, J.; McKenzie, J. S.; Rossi, M.; Covington, A.; Muirhead, L.; Bodai, Z.; Rosini, F.; Speller, A. V. M.; Shousha, S.; Ramakrishnan, R.; Darzi, A.; Takats, Z.; Leff, D. R., Rapid evaporative ionisation mass spectrometry of electrosurgical vapours for the identification of breast pathology: towards an intelligent knife for breast cancer surgery. *Breast Cancer Res* **2017**, *19* (1), 59.

25. Zhang, J.; Rector, J.; Lin, J. Q.; Young, J. H.; Sans, M.; Katta, N.; Giese, N.; Yu, W.; Nagi, C.; Suliburk, J.; Liu, J.; Bensussan, A.; DeHoog, R. J.; Garza, K. Y.; Ludolph, B.; Sorace, A. G.; Syed, A.; Zahedivash, A.; Milner, T. E.; Eberlin, L. S., Nondestructive tissue analysis for ex vivo and in vivo cancer diagnosis using a handheld mass spectrometry system. *Sci Transl Med* **2017**, *9* (406).

26. Balog, J.; Sasi-Szabo, L.; Kinross, J.; Lewis, M. R.; Muirhead, L. J.; Veselkov, K.; Mirnezami, R.; Dezso, B.; Damjanovich, L.; Darzi, A.; Nicholson, J. K.; Takats, Z., Intraoperative tissue identification using rapid evaporative ionization mass spectrometry. *Sci Transl Med* **2013**, *5* (194), 194ra93.

27. Schaefer, K.-C.; Denes, J.; Albrecht, K.; Szaniszló, T.; Balog, J.; Skoumal, R.; Katona, M.; Toth, M.; Balogh, L.; Takats, Z., In Vivo, In Situ Tissue Analysis Using Rapid Evaporative Ionization Mass Spectrometry. *Angewandte Chemie-International Edition* **2009**, *48* (44), 8240-8242.

28. Woolman, M.; Ferry, I.; Kuzan-Fischer, C. M.; Wu, M.; Zou, J.; Kiyota, T.; Isik, S.; Dara, D.; Aman, A.; Das, S.; Taylor, M. D.; Rutka, J. T.; Ginsberg, H. J.; Zarrine-Afsar, A., Rapid determination of medulloblastoma subgroup affiliation with mass spectrometry using a handheld picosecond infrared laser desorption probe. *Chem. Sci.* **2017**, *8* (9), 6508-6519.

29. Fatou, B.; Saudemont, P.; Leblanc, E.; Vinatier, D.; Mesdag, V.; Wisztorski, M.; Focsa, C.; Salzet, M.; Ziskind, M.; Fournier, I., In vivo Real-Time Mass Spectrometry for Guided Surgery Application. *Sci Rep* **2016**, *6*, 25919.

30. Sans, M.; Zhang, J.; Lin, J. Q.; Feider, C. L.; Giese, N.; Breen, M. T.; Sebastian, K.; Liu, J.; Sood, A. K.; Eberlin, L. S., Performance of the MasSpec Pen for Rapid Diagnosis of Ovarian Cancer. *Clin Chem* **2019**, *65* (5), 674-683.

31. Keating, M. F.; Zhang, J.; Feider, C. L.; Retailleau, S.; Reid, R.; Antaris, A.; Hart, B.; Tan, G.; Milner, T. E.; Miller, K.; Eberlin, L. S., Integrating the MasSpec Pen to the da Vinci Surgical System for In Vivo Tissue Analysis during a Robotic Assisted Porcine Surgery. *Anal Chem* **2020**, *92* (17), 11535-11542.

32. Zhang, J., Sans, M., DeHoog, R. J., Garza, K. Y., King, M. E., Fieder, C. L., Bensussan, A., Keating, M. F., Lin, J. Q., Povilaitis, S. C., Katta, N., Milner, T. E., Wendong, Y., Nagi, C., Dhingra, S., Pirko, C., Brahmabhatt, K. A., Van Buren, G., Carter, S. A., Thompson, A., Grogan, R. H., Suliburk, J., Eberlin, L. S., Clinical Translation and Evaluation of the MasSpec Pen Technology for Surgical Use. *Clinical Chemistry* **2021**.
33. Dill, A. L.; Ifa, D. R.; Manicke, N. E.; Ouyang, Z.; Cooks, R. G., Mass spectrometric imaging of lipids using desorption electrospray ionization. *J Chromatogr B Analyt Technol Biomed Life Sci* **2009**, *877* (26), 2883-9.
34. Liberti, M. V.; Locasale, J. W., The Warburg Effect: How Does it Benefit Cancer Cells? *Trends Biochem Sci* **2016**, *41* (3), 211-218.
35. Hilvo, M.; Denkert, C.; Lehtinen, L.; Muller, B.; Brockmoller, S.; Seppanen-Laakso, T.; Budczies, J.; Bucher, E.; Yetukuri, L.; Castillo, S.; Berg, E.; Nygren, H.; Sysi-Aho, M.; Griffin, J. L.; Fiehn, O.; Loibl, S.; Richter-Ehrenstein, C.; Radke, C.; Hyotylainen, T.; Kallioniemi, O.; Iljin, K.; Oresic, M., Novel theranostic opportunities offered by characterization of altered membrane lipid metabolism in breast cancer progression. *Cancer Res* **2011**, *71* (9), 3236-45.
36. Punnonen, K.; Hietanen, E.; Auvinen, O.; Punnonen, R., Phospholipids and fatty acids in breast cancer tissue. *J Cancer Res Clin Oncol* **1989**, *115* (6), 575-8.
37. Wu, S. G.; Zhang, W. W.; Sun, J. Y.; He, Z. Y., Prognostic value of ductal carcinoma in situ component in invasive ductal carcinoma of the breast: a Surveillance, Epidemiology, and End Results database analysis. *Cancer Manag Res* **2018**, *10*, 527-534.
38. Azu, M.; Abrahamse, P.; Katz, S. J.; Jagsi, R.; Morrow, M., What is an adequate margin for breast-conserving surgery? Surgeon attitudes and correlates. *Ann Surg Oncol* **2010**, *17* (2), 558-63.
39. Pilewskie, M.; Morrow, M., Margins in breast cancer: How much is enough? *Cancer* **2018**, *124* (7), 1335-1341.

## **Chapter 6: Rapid Screening of COVID-19 Disease Directly from Clinical Nasopharyngeal Swabs using the MasSpec Pen Technology<sup>5</sup>**

### **INTRODUCTION**

The novel coronavirus disease 2019 (COVID-19), caused by the severe acute respiratory syndrome coronavirus 2 (SARS-CoV-2), has presented an unprecedented global challenge to society and public health<sup>1-2</sup>. As vaccines have yet to be widely administered to the public, especially in resource-limited countries, and their effectiveness towards new variants are yet to be determined, mitigation of disease transmission relies heavily on the widespread availability of rapid COVID-19 tests exhibiting robust analytical performance and diagnostic metrics including adequate sensitivity, specificity, and low false-positive rates (FPR) and false-negative rates (FNR)<sup>3-4</sup>. Current diagnostic assays for COVID-19 are largely based on the detection of SARS-CoV-2 ribonucleic acid (RNA) via quantitative polymerase chain reaction (qPCR) analysis. PCR is a powerful and highly sensitive assay; yet, clinical laboratories have faced challenges in maintaining current demands due to limited availability of the specialized test reagents, instrumentation that have been overrun beyond their capabilities, and low throughput analyses<sup>5</sup>. Alternative diagnostic tests that have little to no reagent requirements and provide a rapid turnaround time are highly valuable for COVID-19 detection<sup>6</sup>. For example, serological tests targeting host antibodies have been deployed for COVID-19 diagnosis, yielding promising results<sup>7-8</sup>. Yet, the inability to diagnose early-stage or acute infections with antibody testing, along with potential cross-reactivity from prior infections by other pathogens presents a challenge for

---

<sup>5</sup> Submitted to Analytical Chemistry.

patient screening<sup>9</sup>. Antigen tests have been developed to rapidly identify active SARS-CoV-2 infections via the detection of the nucleocapsid protein antigen<sup>6</sup>. While antigen tests provide diagnosis in ~15 min, FNR of up to 40% have been reported due to higher limits of detection compared to PCR<sup>10-12</sup>. Alternative testing and screening methods capable of rapidly screening for COVID-19 disease are thus still needed to increase testing capacity and throughput.

COVID-19 tests targeting molecular species other than viral RNA are currently being evaluated as rapid screening methods prior to PCR analysis to mitigate viral outbreaks. Lipids present an interesting molecular target for identifying SARS-CoV-2 infection as these molecules are a major component of the viral envelope and are involved in key replication cycle processes, including the production of new virions<sup>13-14</sup>. Viral genetic material does not code for lipids but sequesters these molecules from their host cellular membranes during budding. The lipid composition of the host-derived viral envelope is known to be specific to the budding site<sup>15</sup> and quantitatively distinct from that of the host membrane and from other viruses<sup>16-19</sup>. Coronaviruses, for example, bud and derive their viral envelope lipids from the membrane of the host endoplasmic reticulum (ER)-Golgi intermediate complex<sup>16</sup>, whereas the influenza virus acquire their lipids from the host apical plasma membrane<sup>20</sup>. In a study by Van Genderen *et al*, the proportion of phosphatidylinositol (PI) in the viral membranes of coronavirus murine hepatitis virus (MHV) was found to be elevated by 4% compared to the host cells, and the ratio of phosphatidylserine (PS) to PI species was reduced by 12%<sup>21</sup>. Viral pathogens also remodel host lipid metabolism to enable replication during infection, altering the overall lipid

composition of infected host cells. For example, Yan *et al* described that fatty acids and glycerophospholipids were significantly elevated in human cells infected with the H-CoV 229E coronavirus compared to healthy cells<sup>22</sup>. Dysregulation of highly abundant glycerophospholipids in infected host cells and the unique lipid composition of the pathogen itself, therefore, represent a promising target for diagnostic tests.

Mass spectrometry (MS) is particularly suited to detect metabolites, lipids, and proteins from complex biological samples<sup>23-24</sup>. In particular, MS omics approaches have been successfully applied to study infectious diseases, targeting various biological molecules to identify bacterial and viral infections<sup>25-27</sup>. Recently, MS techniques have been explored to detect COVID-19 based on metabolite, lipid, and protein information<sup>28-34</sup>. For example, liquid chromatography MS and machine learning models have been used to identify proteomic and metabolic signatures in sera from COVID-19 patients with 93.5% accuracy for a training set of 31 samples<sup>31</sup>. Matrix-assisted laser desorption/ionization mass spectrometry (MALDI-MS) was also used to analyze extracts of nasal swabs<sup>29</sup> and plasma<sup>35</sup> to diagnose COVID-19. Ambient ionization MS and machine learning have been explored to detect SARS-CoV-2 infection based on fatty acid and lipid profiles<sup>30</sup>. De Silva *et al* used paper spray MS to analyze lysed cell extracts from 30 symptomatic COVID-19 positive and symptomatic negative patients, with 93.3% agreement with PCR based on 11 metabolites, fatty acids, and lipids<sup>30</sup> whereas Ford *et al* used desorption electrospray ionization (DESI) and laser desorption rapid evaporative ionization mass spectrometry (LD-REIMS) to analyze 70 nasal swabs, with accuracies over 84.0%<sup>32</sup>. As MS

technologies steadily advance towards clinical implementation, these studies showcase the potential of MS-based assays for screening and diagnosis of viral infections.

Here, we report a new design of the MasSpec Pen technology for the analysis of swabs and demonstrate its use for rapid and direct lipid analysis and potential for COVID-19 screening. We previously reported the development of the MasSpec Pen as a handheld device integrated to a mass spectrometer for direct and rapid molecular analysis of tissues<sup>36-37</sup>. While the handheld MasSpec Pen was designed as an easy-to-use device that enabled precise and efficient molecular analyses of sample surfaces using a solvent droplet, it precludes sufficient sampling and full area coverage of three-dimensional samples such as swab tips that contain heterogeneous adhesion and distribution of mucous secretion. To that end, we optimized the disposable device to enable uniform sampling of an entire swab tip via liquid extraction using common solvents, and thus efficient molecular extraction and analysis. The disposable sampling system was then directly integrated to an ESI source for sensitive detection of molecular ions. Using the MasSpec Pen-ESI MS system, we obtained rich lipid profiles from nasopharyngeal swabs and built statistical classification models to evaluate its prediction capabilities for COVID-19. Collectively, our study shows that direct analysis of clinical swabs with the MasSpec Pen-ESI MS technology is a potentially promising method for rapid screening of viral infections such as COVID-19.

## **METHODS AND MATERIALS**

### **Chemicals**

Cardiolipin (CL) 72:4, phosphatidylglycerol (PG) 36:2, and phosphatidylethanolamine (PE) 36:2 lipid standards were purchased from Avanti Polar Lipids (Alabaster, AL). PG and PE standards were dissolved in methanol at a concentration of 10  $\mu\text{M}$ , and the CL standard was dissolved in methanol at a concentration of 13  $\mu\text{M}$ .

### **Design and fabrication of the adapted MasSpec Pen-ESI system**

The MasSpec Pen polydimethylsiloxane (PDMS) swab sampling device was designed in CAD software and negative molds for the devices were fabricated using procedures previously described (Methods and Supplementary Materials)<sup>37</sup>. The sub-atmospheric pressure ESI source was built by modifying the housing of a commercially available atmospheric pressure chemical ionization (APCI) source (Agilent Technologies). Aluminum blocks and rubber gaskets were machined onto the source to create a vacuum seal when interfaced to the mass spectrometer, and a metal adapter was machined into the bottom of the aluminum block to connect a vacuum tube attached to an external rough pump (Edwards Vacuum). Additionally, a ceramic block was engineered and added to hold the lab-built ESI sprayer. The lab-built sprayer consists of a metal capillary (7 in, 0.62 in OD, 0.16 in ID, New England Small Tube Corporation) concentric with a ceramic tube (10 in, 0.125 in OD, 0.063 in ID, Omega Engineering, Inc.) through which  $\text{N}_2$  gas flows acting as a sheath gas, a plastic union tee (0.25 in, Legris) to which a gas tube is attached, and two neoprene rubber stoppers each machined with a hole to fit the ceramic tube or metal

capillary. A 1.5 m polytetrafluoroethylene (PTFE) tubing and silicone were used to connect the PDMS swab sampling port to the metal capillary of the lab-built sprayer.

### **Clinical nasopharyngeal swabs**

Nasopharyngeal swabs from symptomatic SARS-CoV-2 PCR positive and symptomatic and asymptomatic SARS-CoV-2 PCR negative individuals were collected from consented patients that were hospitalized with moderate or severe respiratory symptoms in two different hospitals (Santa Casa and Bragantino) as well as from asymptomatic volunteers at Integrated Unit of Pharmacology and Gastroenterology (UNIFAG) in the city of Bragança Paulista (São Paulo, Brazil), by the research team at the University of San Francisco (Bragança Paulista, Sao Paulo, Brazil). Approval from Institutional Review Board (IRB) was received for the study (protocol number 31573020.9.0000.5514, approved from May 29, 2020).

HydraFlock polyester swabs sterilized by gamma irradiation (Puritan Medical Products) were shipped to Brazil. A permit to import samples from Brazil to UT Austin was received from the Brazilian Health Regulatory Agency (ANVISA) and the Center for Disease Control and Prevention (CDC). Prior to shipment, all swabs were heat-inactivated in Brazil at 65°C for 30 min and kept at -20°C until the shipment in dry ice. Experiments were performed at the University of Texas at Austin under Biosafety Level 2 conditions. Swabs were handled by the principal investigator in the biosafety cabinet following biosafety protocols and requirements from the institutional biosafety committee.

Clinical sample collection began on July 17, 2020. Clinical diagnosis for the symptomatic patients and asymptomatic individuals was performed via RT-PCR analysis using a different clinical swab as part of their clinical care and independently of our study. Table 6.1 provides patient demographics information. As of October 21, 2020, swabs from 268 individuals have been collected in Brazil and shipped to and received by our laboratory at UT Austin where swabs were stored at  $-80^{\circ}\text{C}$  prior to analysis.

### **MasSpec Pen-ESI analysis and data acquisition**

Prior to the analysis, the swabs were removed from the  $-80^{\circ}\text{C}$  freezer and thawed to room temperature in a Class II biological safety cabinet for 15 min. To maximize safety measures, swabs were then heat-inactivated for 30 min at  $65^{\circ}\text{C}$ . Following heat inactivation, swabs were placed in the biological safety cabinet until cooled to room temperature. Swabs were stored in a refrigerator at  $4^{\circ}\text{C}$  until MasSpec Pen-ESI MS analysis. Swabs were analyzed within 3 days of heat inactivation.

Experiments were performed on two mass spectrometers, an LTQ Orbitrap XL and a Q Exactive HF mass spectrometer (Thermo Fisher Scientific). During MasSpec Pen-ESI MS analysis, the swab tips were inserted into the middle channel of the PDMS sampling device (Illustration 6.1). Upon the press of a foot pedal, a volume of  $167\ \mu\text{L}$  of  $\text{CHCl}_3:\text{MeOH}$  is delivered from the syringe pump to the middle channel containing the swab, interacting with and extracting molecules from the swab tip for 10 s. The entire process is controlled using programmed microcontrollers. A vacuum was then applied for

Table 6.1: Summary of patient demographics, clinical indications, and procedures.

Parameters	Symptomatic PCR Positive	Symptomatic PCR Negative	Asymptomatic PCR Negative	p-value
<b>Demographics</b>				
Number of patients, n	44	26	101	2.18E-06
Age range, y	(21, 84)	(26, 84)	(20, 89)	
Sex (female, male)	(16, 28)	(11, 15)	(58, 43)	
<b>Symptoms</b>				
Fever	19	12	-	1.0000
Cough	30	16	-	0.7602
Myalgia	9	2	-	0.2811
Sore throat	8	8	-	0.3590
Headache	12	1	-	0.0342
Dyspnea	29	18	-	0.9820
Tiredness/fatigue	3	2	-	1.0000
Loss of smell/taste	9	9	-	0.3045
Diarrhea	11	2	-	0.1386
None	-	-	101	-
<b>Chest CT Features</b>				
Ground-glass opacity	42	18	-	0.0024
Consolidations	21	14	-	0.8770
Crazy paving appearance	21	9	-	0.3659
Reticular pattern	6	6	-	0.5214
Pulmonary commitment degree	37	16	-	0.0410
Suggestive of viral infection	42	18	-	0.0024
<b>Underlying conditions</b>				
Systemic arterial hypertension	25	11	16	0.5765
Cardiovascular disease	6	4	2	1.0000
Obesity	10	1	22	0.0788
Diabetes	16	2	3	0.0178
Lung disease	4	5	8	0.3925
Chronic obstructive pulmonary disease	1	1	1	1.0000
Smoker/ex-smoker	3	3	6	0.8105
Asthma	2	2	2	0.9879

30 s to the PTFE tube to enable the transport of the solvent from the swab reservoir to the ESI source. Mass spectra were acquired for ~20-30 s.

Various swab tip materials were tested using the MasSpec Pen-ESI MS system, including nylon (Copan Diagnostics) and polyester flock (Puritan Medical Products) swabs. Each swab was dipped in a 13  $\mu\text{M}$  standard solution of CL 72:4 and analyzed using the MasSpec Pen-ESI system in the negative ion mode, with the mass spectrum of polyester flock swabs containing minimal interfering ions in the lipid range compared to nylon flock swabs. The interfering ions presented polymer-like distribution and were identified as repeating units of ethylene oxide. Additionally, solvents including methanol, isopropylalcohol, ethanol:ethylacetate (1:1, v/v),  $\text{CHCl}_3$ :MeOH (1:1, v/v), and  $\text{CHCl}_3$ :MeOH (2:1, v/v) were tested for compatibility with the MasSpec Pen-ESI MS system.

To evaluate the robustness of the MasSpec Pen-ESI MS system for the detection of lipids from gamma-irradiated polyester flock swabs, swabs dipped in 100  $\mu\text{L}$  of an equimolar (10  $\mu\text{M}$ ) lipid standard mixture of PE 36:2 ( $m/z$  742.540) and PG 36:2 ( $m/z$  773.539) were analyzed using  $\text{CHCl}_3$ :MeOH (1:1, v/v) as the solvent, yielding a relative standard deviation of 6.4% ( $n=10$ ).

To evaluate the effect of heat inactivation of the biological material on the swabs, swabs dipped in a mixture of PG and PE lipid standards were heat-treated for 30 min at 65°C ( $n=5$ ) to simulate heat-inactivation, while control swabs ( $n=5$ ) dipped in the same lipid mixture standard were not heat-treated, followed by analysis using the MasSpec Pen-ESI system.

## Statistical analysis

Seventy-five mass spectra were averaged and extracted for each sample analyzed. A mass filter of  $m/z$  400-1000 was applied, after binning and background subtraction. Data was normalized to the TIC, and peaks appearing in less than 50% of the entire data set for each classifier were removed during cross validation (CV). The least absolute shrinkage and selection operator (Lasso) statistical analysis was performed using the beta version of the glmnet package v4.1-2, using the exclude/filtering option in glmnet. The time elapsed between PCR and MS swab collection and days since symptom onset were used as selection criteria. Swabs that were collected for MS three days or more after PCR sample collection and beyond 14 days of symptom onset were excluded from the classifier. From the 268 individuals who had their swab samples collected, 171 met the criteria of the time interval to PCR-sample collection and days from symptoms onset. Demographic and clinical information for the patients from which the selected samples were obtained is provided in Table 6.1 and C6.1. Based on the selection criteria, two statistical classifiers were generated: 1) asymptomatic COVID-19 PCR negative (n= 101) vs COVID-19 symptomatic PCR positive (n=44) samples and 2) COVID-19 PCR negative (n=101 asymptomatic and n=26 symptomatic) vs COVID-19 symptomatic PCR positive. 10-fold CV was used with Lasso to generate predictive models. For Classifier 1, the data was randomly split into a training set (2/3 of data, n=97) and a validation set (1/3 of data, n=48). Additionally, we tested Classifier 1 on a withheld test set of PCR-negative symptomatic samples (n=26). The performance of the models were evaluated by measuring the predictive accuracy, sensitivity, specificity, negative predictive value (NPV), and positive

predictive value (PPV) which were calculated based on the agreement with PCR diagnosis. Statistical analysis were performed by K.Y.G., M.F.K., J.Q.L. and J.M.G., and independently verified by R.T..

The reproducibility of the MasSpec Pen-ESI system for swab analysis was quantified by calculating the relative standard deviation using the ratio of the intensities of lipid standards,  $m/z$  773.534 (PG 36:2)/ $m/z$  742.539 (PE 36:2) ( $n=10$ ). To evaluate the effect of heat inactivation on the stability of lipids, a t-test was performed on the intensities of two lipid standards,  $m/z$  742.639 and  $m/z$  773.533, extracted from swabs without heat inactivation ( $n=5$ ) and swabs heat-inactivated for 30 min at 65°C ( $n=5$ ) using the MasSpec Pen-ESI system. Lastly, descriptive statistics were also computed for clinical and demographic variables. Categorical variables were expressed as count (percentage), whereas continuous variables were expressed as median (25–75<sup>th</sup> percentiles). The chi-square test was used to compare categorical variables proportions, and the Mann–Whitney U-test was used to evaluate continuous data.

## RESULTS

### Design of the MasSpec Pen-ESI System

We previously developed the MasSpec Pen as a handheld device directly coupled to a mass spectrometer for direct analysis of tissues<sup>37</sup>. The PDMS pen tip was comprised of a solvent reservoir that held a solvent droplet in contact with a sample surface to enable efficient molecular extraction. While this design is intuitive for handheld use and well-suited for the analysis of tissue regions, the area covered by the reservoir opening (typically  $\sim 5.7$  mm<sup>2</sup>)

was insufficient for uniform sampling and analysis of the secretion covering the three-dimensional area of an entire swab tip. To enable sensitive and robust analysis of all the mucous secretion material in and on a swab tip, we thus redesigned and optimized the MasSpec Pen device, interface, and ionization system with the goal of ensuring direct and efficient sampling of the entire swab tip while maintaining the ease of use and rapid nature of the analysis of the original MasSpec Pen. The PDMS swab sampling device was integrated via PTFE tubing with a sub-atmospheric pressure ESI source for effective ionization and sensitive analysis of the extracted molecules (Illustration 6.1). Similar to the original MasSpec Pen PDMS tip, the PDMS sampling unit is designed with three conduits that connect to a middle reservoir that was widened to 5.5 mm diameter and ~22 mm height to enable an entire swab tip to be fully inserted (Illustration 6.1 insert). A PTFE tube connected to a syringe pump was then inserted into conduit 1 for the delivery of solvent to the middle reservoir, whereas a second PTFE tube was inserted into conduit 2 for solvent aspiration into the sub-atmospheric pressure ESI source. The swab analysis is then performed with minimal operational steps: after the swab is inserted into the middle swab reservoir, solvent is delivered to the reservoir through a PTFE tube connected to conduit 1 via the press of a foot pedal, where the solvent interacts with the entire swab tip for 10 s for analyte extraction. Following the extraction period, conduit 2 is opened for 30 s allowing the vacuum to aspirate solvent to the sprayer for ESI analysis. Within the ESI source, a lab-built sprayer promotes ionization of the molecules extracted within the solvent. Note that a sub-atmospheric pressure was set within the ESI housing, measured via the forevacuum pressure of the mass spectrometer (1.4-1.6 mbar), with the sole purpose

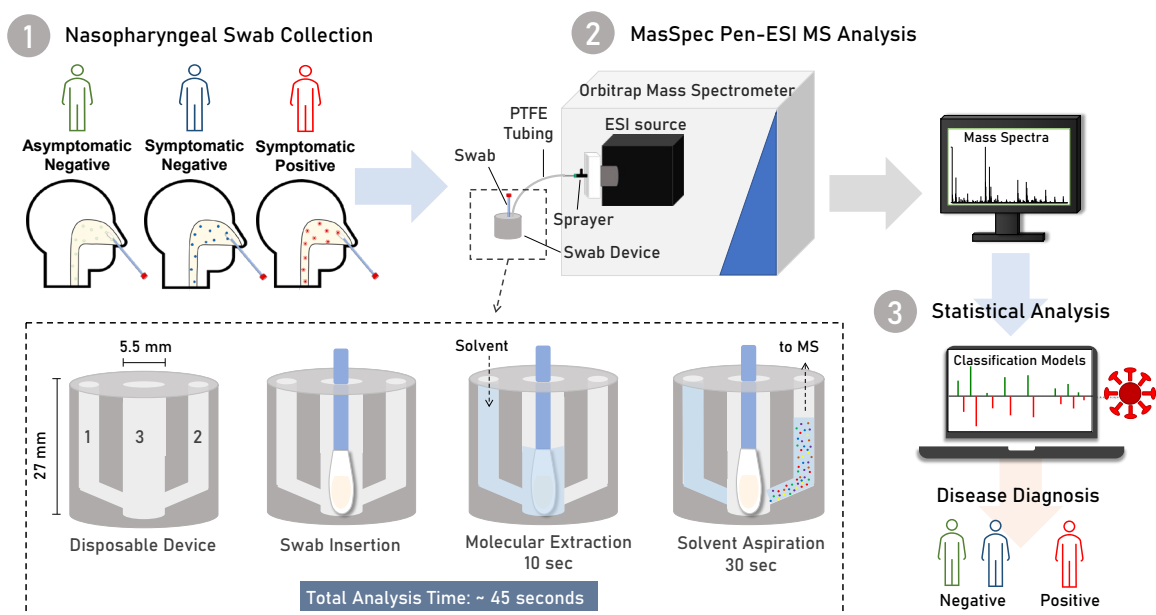


Illustration 6.1: Schematic of the MasSpec Pen-ESI-MS system for the diagnosis of COVID-19 infection.

Swabs acquired from symptomatic patients and asymptomatic individuals were analyzed by the MasSpec Pen-ESI MS platform and the mass spectra collected were used to build machine learning classification models for diagnosis of COVID-19. A zoom view of the design MS swab device and the steps for analysis. The insert shows two conduits for incoming solvent (1) and aspiration of the solvent containing the extracted molecules (2) and a middle reservoir (2). During analysis, the swab is inserted into the middle reservoir. Upon the press of a foot pedal, solvent is delivered to the middle reservoir to interact with the swab tip to extract molecules. After 10 sec the solvent containing the extracted molecules is transported the mass spectrometer for ESI analysis.

of enabling suction and thus transport of the solvent from the swab reservoir to the ESI sprayer.

### **Optimization of the MasSpec Pen-ESI system for swab analysis**

Using the MasSpec Pen-ESI system coupled to an LTQ XL mass spectrometer, we first evaluated commonly used medical polyester and nylon flock swabs sterilized with ethylene oxide or gamma irradiation for assay compatibility by dipping the swabs in a solution of cardiolipin (CL) 72:4 standard followed by analysis using MasSpec Pen-ESI MS. For the analysis of nylon flock swabs sterilized using ethylene oxide, a series of interfering ions identified as repeating units of ethylene oxide were observed from  $m/z$  350-1200 at a  $\sim 5.5$  fold ( $n=5$ ,  $m/z$  735.420) higher relative abundance compared to the CL standard ion of  $m/z$  727.510 (Figure 6.1), thus hindering the detection of the CL standard due to ion suppression. Yet, no polymer ions were observed in the mass spectra obtained from polyester flock swabs sterilized with gamma irradiation. Thus, all consecutive experiments including collection and analysis of clinical samples were therefore performed with polyester flock swabs sterilized by gamma irradiation to avoid polymer interference.

Next, solvent composition and the volume used to fill the reservoir were optimized to ensure the entire swab was saturated with solvent to efficiently extract molecules, as well as allow for consistent signal and ESI spray stability during the analysis. Different organic solvent systems with volumes ranging from 100  $\mu\text{L}$  to 200  $\mu\text{L}$  were evaluated, with a solvent volume of 167  $\mu\text{L}$  selected as optimal. Among the solvent systems tested,  $\text{CHCl}_3:\text{MeOH}$  (1:1, v/v) yielded the highest reproducibility (relative standard deviation of

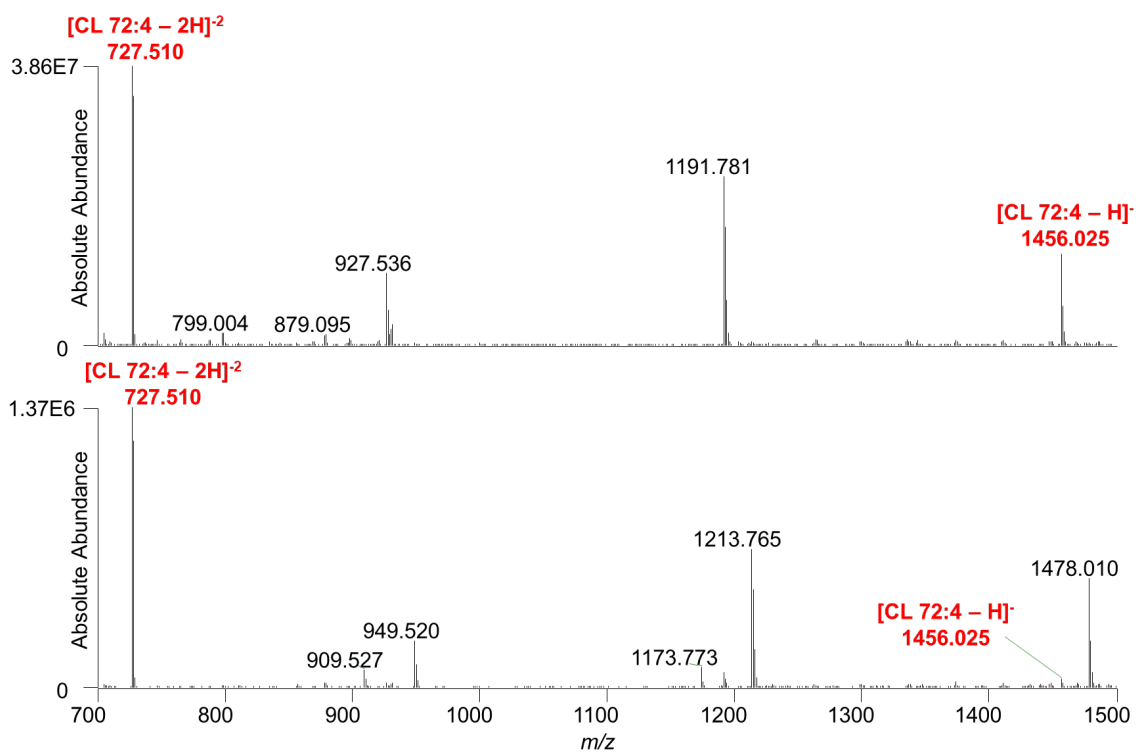


Figure 6.1: Comparison of mass spectra obtained using the MasSpec Pen with ESI or solvent assisted inlet ionization to analyze a 20 ppm CL 72:4 lipid standard.

The top mass spectrum shows data obtained using ESI and the bottom shows data collected using solvent-assisted inlet ionization. Singly and doubly charged CLs are labeled in red.

6.4% (n=10)) and spray stability (~20-30 s of ion signal) while minimizing the extraction and detection of interfering ions. Notably, a 25.5% (n=4) increase in signal intensity of lipids was achieved when compared to the traditional MasSpec Pen setup<sup>38</sup> (Figure E6.1), likely due to more efficient ionization and desolvation provided by ESI. Altogether, a total analysis time of 45 s or less per swab was achieved, which included 5 s of solvent delivery, 10 s of swab extraction time, and ~20-30 s droplet transport and ESI signal (Illustration 6.1). Lastly, we also evaluated if heat inactivation led to any substantial change or degradation to the lipids contained in the sample using PG and PE lipid standards (Figure 6.2). We found no statistical significance ( $p > 0.05$ ) in the mean intensity of the lipids detected from the heat-inactivated or control swabs, indicating that the inactivation process did not significantly alter lipid composition.

### **Molecular analysis of clinical nasopharyngeal swabs**

As Figure 6.3A shows, we observed rich molecular profiles composed of a diverse range of glycerophospholipid and lysolipid species in mass spectral profiles of symptomatic COVID-19 positive and negative swabs and asymptomatic healthy samples. Note that the  $m/z$  400-1000 range was used to avoid detection and ion suppression from non-biological interferences detected as ions of  $m/z < 400$  while enabling detection of a broad range of lipid species. Various ions tentatively identified lysoPE 16:0 ( $m/z$  452.278), lysoPE 18:0\_0:0 ( $m/z$  480.309), lysoPC 18:1 ( $m/z$  556.318) (Figure 6.3A), and cholesterol sulfate ( $m/z$  465.304) were observed in the  $m/z$  range 400-600. Additionally, molecules such as ceramide species including Cer 34:1 ( $m/z$  572.481), Cer 36:1 ( $m/z$  601.533), and Cer 42:2

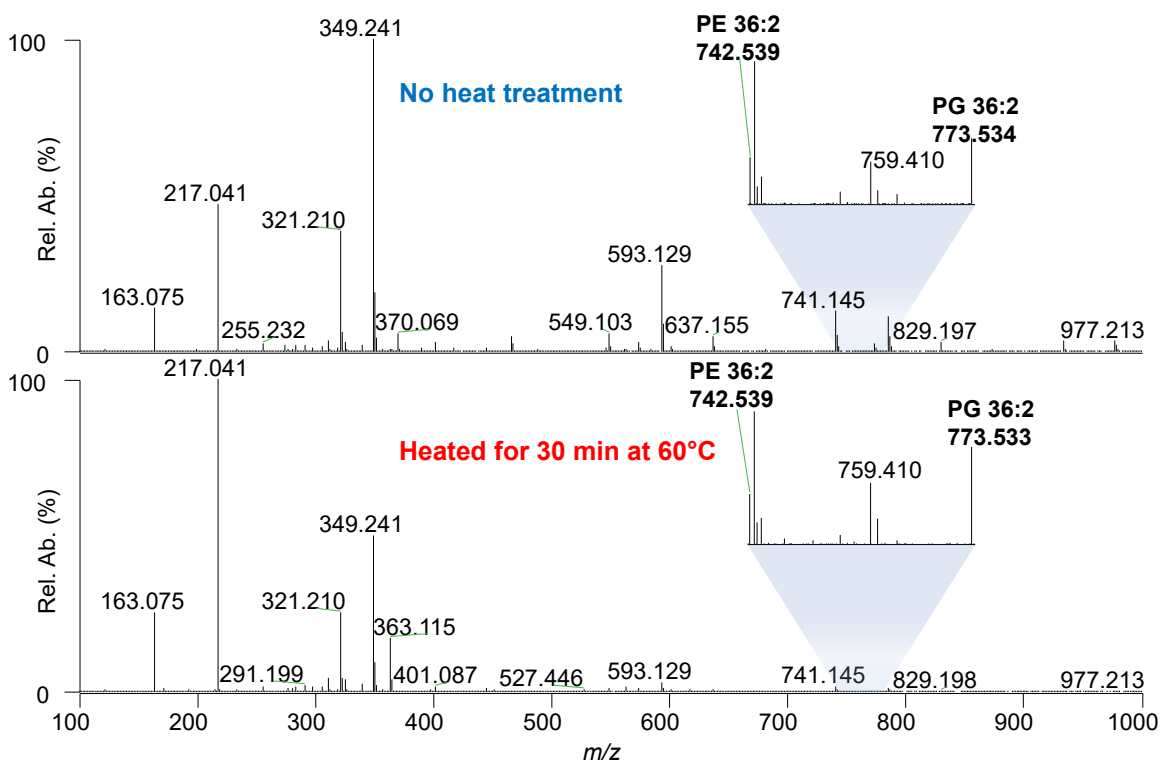


Figure 6.2: Comparison of mass spectra of swabs containing a 10  $\mu$ M PG 36:2 ( $m/z$  773.533) and PE 36:2 ( $m/z$  742.539) lipid standard mixture with and without heat inactivation.

The mass spectrum on top was obtained from the MasSpec Pen-ESI MS analysis of a swab without heat inactivation while the bottom shows the profile for a swab that had been heat-inactivated at 60°C for 30 min. Both insets are a zoom of  $m/z$  720-800 range to show the detection of the lipid standards.

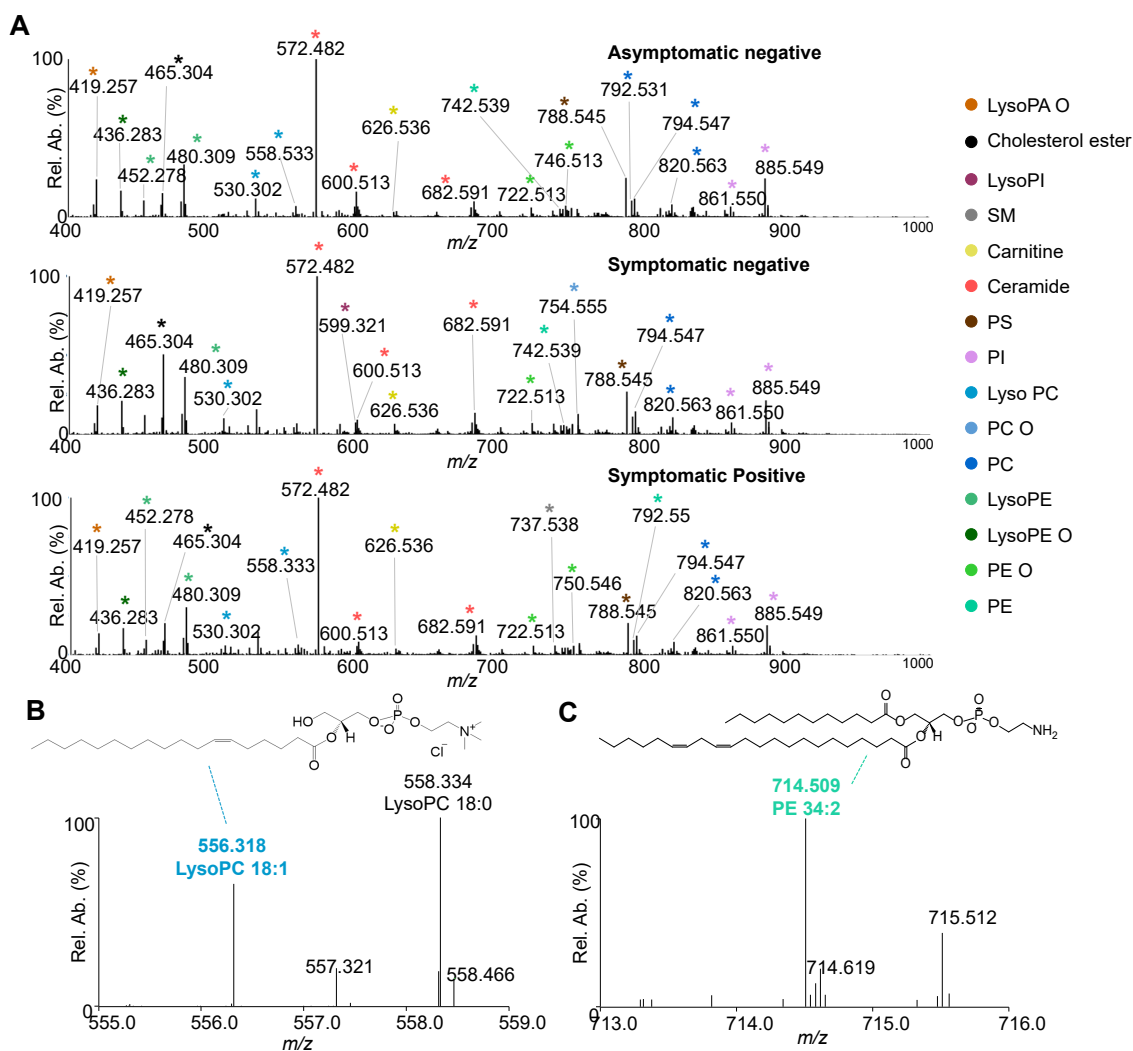


Figure 6.3: MasSpec Pen-ESI MS analysis of asymptomatic negative, symptomatic negative, and symptomatic positive samples.

A) Averaged spectra of all asymptomatic negative (n=101, top), symptomatic negative (n=26, middle), and symptomatic positive (n=44, bottom). Different colored peaks correspond to different lipid classes which are labeled in the legend. B) Zoom in of  $m/z$  range 555-559 to show the detection of lysoPC species including lysoPC 18:1 ( $m/z$  556.318) and 18:0 ( $m/z$  558.334) with the structure for lysoPC 18:1 shown in a mass spectra from a positive sample. C) Zoom in of  $m/z$  range 713-716 to show the detection of PE 34:2 ( $m/z$  714.509) and the corresponding structure in a mass spectra from a positive sample.

(*m/z* 682.591) as well as glycerophospholipids including PS 18:1\_18:0 (*m/z* 788.545), PI 20:4\_18:0 (*m/z* 885.550), and PE 34:2 (*m/z* 714.509) were observed (Figure 6.3C).

### **Statistical prediction of COVID-19 infection**

We next statistically evaluated if the molecular information obtained with the MasSpec Pen-ESI MS system was predictive of COVID-19 infection. We first employed the Lasso method to build a classification model to discriminate data obtained from symptomatic patients positive for COVID-19 (n=44) from asymptomatic individuals negative for COVID-19 (n=101), termed Classifier 1. The model exhibited a strong performance using 10-fold CV (n=97), yielding an area under the receiver operating characteristic (ROC) curve (AUC) of 0.852 (Figure 6.4A) and an accuracy of 83.5% (Figure 6.4C). A prediction probability value of 0.350 was selected as optimal threshold value for sample classification based on the ROC curve. Samples with a probability lower than 0.350 were classified as asymptomatic negative and those with a probability higher than 0.350 were classified as symptomatic positive (Figure 6.4B). Using this approach, a total of 58 out of 67 asymptomatic negative and 23 out of 30 symptomatic positive samples had a prediction result in agreement with PCR, resulting in 76.7% sensitivity and 86.6% specificity (Figure 6.4C). We also calculated the NPV and PPV to evaluate the ability of our statistical classifier to provide a predictive COVID-19 diagnosis that aligns with the true absence or presence of the disease. The model yielded an NPV of 89.2% and a PPV of 71.9%.

Next, we assessed the predictive performance of Classifier 1 using a validation set of 34 asymptomatic negative and 14 symptomatic positive samples. Only five

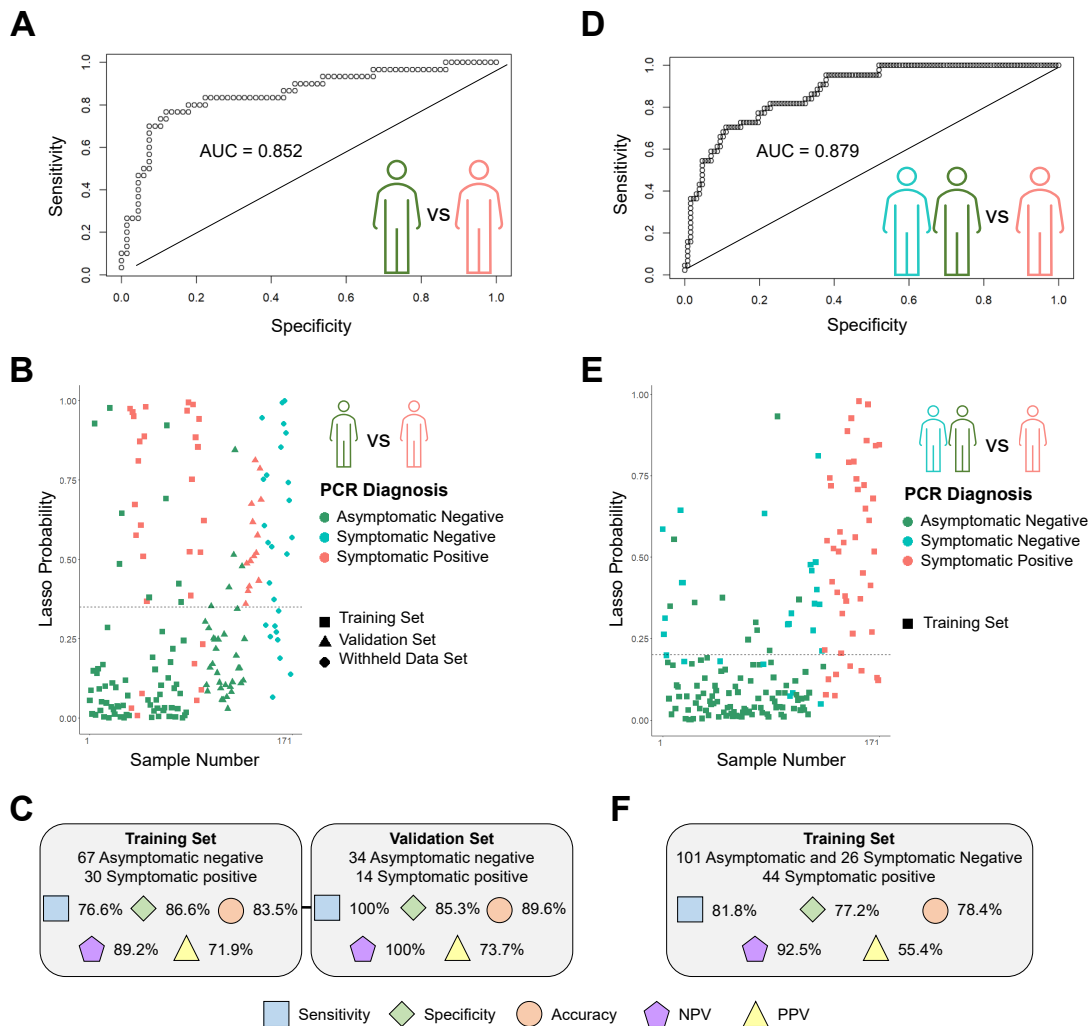


Figure 6.4: Statistical analysis results for Classification models 1 and 2.

Classifier 1, asymptomatic negative vs symptomatic positive, A) ROC curve, B) Plot of the classification probabilities for samples used in the training and validation set. The dashed line represents the cutoff value for classification as asymptomatic negative or symptomatic positive for COVID-19 (0.350). C) Sensitivity, specificity, accuracy, NPV, and PPV and for the training and validation set for Lasso Classifier 1. Classifier 2, negative vs positive, D) ROC curve, E) Plot of the classification probabilities for samples used in the training for Classifier 2. The dashed line represents the cutoff value for classification as negative or positive for COVID-19 (0.201). F) Sensitivity, specificity, accuracy, NPV, and PPV for the training set for Lasso Classifier 2.

asymptomatic negative samples were classified as positive in disagreement with PCR while all symptomatic positive samples were correctly classified, resulting in an overall agreement with PCR of 89.6%, a specificity of 85.3%, sensitivity of 100%, NPV of 100%, and PPV of 73.7%. We then used the classifier to predict on a withheld set of samples obtained from patients presenting respiratory symptoms similar to those associated with COVID-19 disease (n=26) but that had a negative PCR result (Table E6.1). A total of nine samples in the withheld set of data were classified as negative in agreement with PCR, whereas 17 samples were classified as positive, in disagreement with the PCR diagnosis. Out of these 17 patients, 12 had a chest computational tomography (CT) that was suggestive of viral infection, presenting ground-glass opacity (GGO) among other features such as consolidation and pulmonary commitment<sup>39</sup>. Table 6.2 provides a detailed summary of the classification results.

To more broadly evaluate performance for COVID-19 screening, we built a second classifier, termed Classifier 2, that combined the samples from the symptomatic negative patients (n=26) and the asymptomatic negative individuals (n=101) into a single negative class, whereas the positive class was comprised of samples from symptomatic positive patients (n=44). The predictive model was comprised of 41 *m/z* features and yielded an overall agreement with PCR of 78.4%, sensitivity of 81.8%, specificity of 77.2% (Figure 6.4F), and an AUC of 0.879 (Figure 6.4D). A prediction probability threshold of 0.201 was selected to maximize the sensitivity of Classifier 2 (Figure 6.4E). A total of 29 PCR negative samples were classified as positive by our method, among which 19 were from symptomatic patients that presented respiratory symptoms similar to those associated with

Table 6.2: Confusion matrices of the Lasso results for Classifiers 1 and 2.

Classification Model	Sample Set	PCR Diagnosis	Model Prediction and Performance								
			Negative	Positive	Sensitivity (%)	Specificity (%)	Accuracy (%)	NPV (%)	PPV (%)	FNR	FPR
Classifier 1: Asymptomatic Negative vs Symptomatic Positive	Training	Negative	58	9	76.7	86.6	83.5	89.2	71.9	23.3	13.4
		Positive	7	23							
	Validation	Negative	29	5	100.0	85.3	89.6	100.0	73.7	0.0	14.7
	Positive	0	14								
	Withheld Data	Negative	17	9	-	65.4	-	-	-		
Classifier 2: Asymptomatic + Symptomatic Negative vs Symptomatic Positive	Training	Negative	98	29	81.8	77.2	78.4	92.5	55.4	18.2	22.8
		Positive	8	36							

COVID-19 disease. We also noted that 13 of the 19 symptomatic negative samples classified as positive had chest CT results suggestive of viral infection.

Among the selected features used to build the several classification models, various lipids were selected to discriminate COVID-19 positive disease and negative diagnosis. For example, several PE and lysoPE species were selected as important for predicting negative status among the two classifiers generated, including lysoPE 20:0 ( $m/z$  508.341), and PE 34:2 ( $m/z$  714.508), (Figure 6.5). For Classifier 1, various ceramides such as Cer 42:3 ( $m/z$  680.576), Cer 42:2 ( $m/z$  682.591), Cer 43:3 ( $m/z$  694.592), Cer 44:5 ( $m/z$  700.587) were selected as characteristic of symptomatic positive COVID-19 infection by Lasso, whereas PE 38:2 ( $m/z$  770.571) and lysoPI ( $m/z$  619.289) were selected as indicative of asymptomatic negative samples (Figure 6.5A). Other species such as PE 50:9 ( $m/z$  976.619) and lysoPC 18:1 ( $m/z$  556.317) were selected as important for classification and weighted toward symptomatic positive COVID-19 disease for Classifier 1 and 2 (Figure 6.5A and B). LysoPS 18:1 ( $m/z$  522.284) and DG 40:6 ( $m/z$  808.504) were selected by Lasso as predictive of COVID-19 positive infection for Classifier 2 (Figure 6.5B). Table E6.2 provides the Lasso features selected for all statistical classifiers, the corresponding identifications, and mass errors.

The results from the descriptive statistical analysis performed to compare the clinical characteristics among the two symptomatic groups, symptomatic COVID-19 PCR positive and COVID-19 PCR negative subjects, are shown in Table 6.1. No association was found among the occurrence of symptoms and comorbidities with the PCR result.

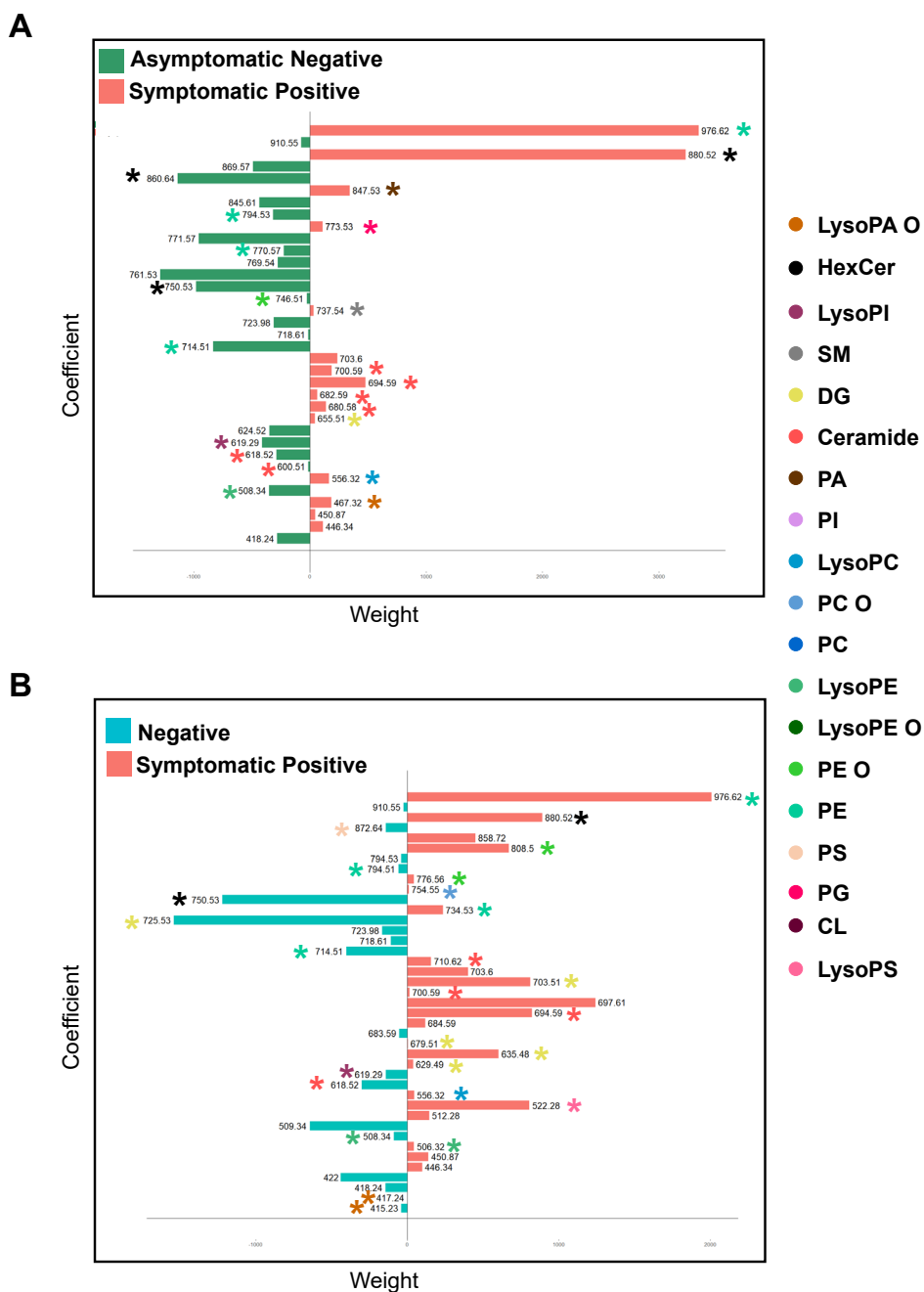


Figure 6.5: Lasso classification features.

Features ( $m/z$ ) selected as indicative of negative infection (negatively weighted values) and positive SARS-CoV-2 infection (positively weighted values) for A) Classifier 1 and B) Classifier 2. Tentatively identified features are color coded with asterisks corresponding to the identified lipid class.

These results indicate that there is no clinical difference detected by the symptomatic PCR-positive and symptomatic PCR-negative groups within the patients in our study.

## **DISCUSSION**

With the slow rollout of the COVID-19 vaccines, a recurring global surge in cases, and the discovery of variants with increased rates of transmission, the availability of alternative technologies that offer rapid analysis and screening for COVID-19 is highly desirable to meet unceasing testing demands. We describe herein the development of a robust MasSpec Pen-ESI MS system for rapid swab analysis and applied the technology to nasopharyngeal swabs in order to evaluate its usefulness for COVID-19 screening.

Modifications were made to the MasSpec Pen design and system to improve the performance and sensitivity for the analysis of swabs. Larger sampling area capabilities were attained to ensure that the three-dimensional clinical swabs with a sparse and heterogeneous distribution of biological materials were sampled in their entirety. The modified PDMS tip includes a hollow middle channel to fit a single swab tip that allowed the full covering and extraction of molecular information from the entire sample during analysis (Illustration 6.1), yielding direct, rapid, efficient, and uniform sampling of all the mucous secretion on the swab and largely mitigating bias in the data due to uneven sampling. Additionally, the use of ESI increased the ionization efficiency of extracted lipid molecules and improved the sensitivity for the untargeted molecular analysis of swabs, enabling detection of abundant ions and molecular profiles from the biological sample. Of note, while the total time per analysis of 45 seconds is remarkably fast compared to other

available molecular tests, additional system automation approaches are being explored to further expedite device swapping between samples and thus maximize testing throughput. Importantly, similar to the original handheld system, this design of the device for swab analysis maintains a small footprint, retains the ease-of-use and plug-and-play features disposability, and ability to perform rapid molecular analysis, and is compatible with multiple mass spectrometers fitted with ESI interfaces, potentially facilitating implementation in clinical laboratories already equipped with MS instrumentation.

We applied the MasSpec Pen-ESI MS system to analyze 244 nasopharyngeal swabs from COVID-19 positive and negative patients, from which 171 were used to build two statistical classifiers based on the lipid profiles obtained. Classifier 1 was built to evaluate the performance of our method in discriminating patients diagnosed as positive for COVID-19 infection by PCR from completely asymptomatic patients with a PCR negative result. The classifier was built using 145 samples and yielded a CV prediction accuracy of 83.5%, similar to what achieved in a study using metabolite and lipid information obtained from DESI-MS (86%, n=70) and LD-REIMS (84%, n=70) analysis of heat-inactivated swabs from negative patients with previous SARS-CoV-2 infection and symptomatic positive patients<sup>32</sup>. We evaluated Classifier 1 on a validation set of 34 asymptomatic PCR-negative and 14 symptomatic PCR-positive samples, yielding a specificity of 85.3%, or a low FPR of 14.7%, and most notably, a sensitivity of 100%, or low FNR of 0%. These results demonstrate the ability of the MasSpec Pen-ESI technology to detect alterations in the lipid profiles of symptomatic patients with an active SARS-CoV-2 viral infection when

compared to healthy individuals and to build classification models based on detected lipid species.

We then used Classifier 1 to predict on a withheld set samples obtained from 26 symptomatic patients hospitalized with moderate or severe symptoms including fever, cough, difficulty in breathing, but that received a negative PCR result for COVID-19 (Table E6.1). Nine of the symptomatic negative samples had a prediction result in agreement with PCR, while 17 symptomatic negative samples were classified as positive, in disagreement with PCR. Interestingly, 12 of the 17 symptomatic negative samples predicted as positive were obtained from patients showing GGO and consolidations in the chest CT scans, and five of the seven samples predicted as negative presented chest CT results indicative of being negative of viral infection. For example, sample 34 was obtained from a 76 year-old male patient that received a PCR negative diagnosis and was classified as positive by our method. This patient was experiencing cough, sore throat, and dyspnea, and had chest CT features suggestive of infection such as GGO, consolidations, and 50% pulmonary commitment. The patient was hospitalized in the intensive care unit for 13 days with the assistance of a mechanical ventilator until succumbing to death. Sample 108 was obtained from a 60-year-old female with preexisting conditions, including obesity and hypertension. She received a PCR negative diagnosis and was classified as positive by our method. Her symptoms included chest CT results suggestive of infection with GGO, consolidations, crazy-paving appearance, and pulmonary commitment (50%), as well as fever and low O<sub>2</sub> saturation levels (<95%). The patient was discharged from the hospital after nine days. Sample 242 was collected from a 28-year-old female who received a PCR

negative diagnosis and was also classified by our method as negative for viral infection. The patient was hospitalized for three days with symptoms including coughing, sore throat, and dyspnea, whereas her chest CT results were not indicative of an infection. Note that chest CT has been suggested as a fundamental tool for early diagnosis and monitoring of COVID-19 as it enables detection of lung alterations in symptomatic patients that are suggestive of viral infection<sup>40-43</sup>. In a recent study, a 90% sensitivity was reported for COVID-19 diagnosis based on GGO combined with other CT features<sup>44</sup>. Yet, chest CT is less specific than PCR and unable to distinguish between an active or previous SARS-CoV-2 infection or a different viral infection causing severe respiratory symptoms. It is also important to note that although PCR is the gold standard for COVID-19 detection and is highly accurate, several studies have reported a sensitivity of 80-90% (or FNR of 10-20%) for COVID-19 diagnosis using nasopharyngeal swabs<sup>45-47</sup>. Thus, while the results obtained on the withheld set of samples indicate that model built using symptomatic PCR positive and asymptomatic PCR negative samples and the selected predictive lipid species are more strongly associated with infection status when used to predict on independent data from symptomatic PCR negative patients, it is also possible that a proportion of the symptomatic PCR negative samples obtained from hospitalized patients may have inaccurate PCR results.

In order to more broadly evaluate the ability of our method to identify individuals negative for COVID-19 disease including symptomatic patients, we then built Classifier 2 using a training set of symptomatic positive samples (n=44) and a negative class (n=127) comprised of data from both symptomatic and asymptomatic PCR negative samples. As a

limited number of symptomatic negative samples were used in Classifier 2, only a training set of samples was used to assess the performance of the model for COVID-19 screening. Using CV, Classifier 2 yielded a 78.4% overall agreement with PCR results, 81.8% sensitivity (FNR of 18.2%), and 77.2% specificity (FPR of 22.8%), similar to what achieved for the training set of Classifier 1 despite the incorporation of symptomatic negative samples into the negative class. Of the 65 samples classified as positive by our method, 36 were from symptomatic positive samples, yielding a PPV value of 55.4%, meaning that for the prevalence of the disease in the cohort of patients evaluated (25.7%), 55.4% of patients with a positive prediction result by our method were also diagnosed as positive for COVID-19 by PCR. However, for the same disease prevalence, a high NPV of 92.5% was achieved, meaning that 92.5% of patients with a negative prediction by our method also received a negative PCR result for COVID-19. Thus, the high NPV value of 92.5% and the FNR of 18.2% achieved provides evidence that Classifier 2 can potentially identify individuals negative for SARS-CoV-2 infection and predict patients with SARS-CoV-2 infection as positive for the disease, respectively, both of which are paramount to halting the spread of the COVID-19 disease. While these results are encouraging, a larger cohort of samples is needed to validate the results by Classifiers 1 and 2 and further refine and improve the performance and robustness of the model for distinguishing symptomatic COVID-19 positive disease from symptomatic patients with other viral respiratory infections, such as the common cold and influenza.

Our statistical models were based on various classes of phospholipid species previously reported to play key roles in coronavirus virion production and replication<sup>21-22</sup>,

<sup>34</sup> and that are major components of host cellular membranes. The tentatively identified lipids included glycerophospholipids, such as ceramides, lysolipids, and PE. Among those, several lysoPC species including lysoPC 18:1 were selected as predictive of symptomatic COVID-19 positive disease. Interestingly, in a study by Yan *et al*, lysoPC species were detected at higher abundances in cells infected with the human coronavirus HCoV-229E, when compared to healthy cells, which substantiates our findings<sup>22</sup>. Yet, a recent study by Delafiori *et al* reported decreased abundances of lysoPC species in the serum of COVID-19 positive patients<sup>33</sup>. Across both classifiers, PE 50:9 was selected as indicative of COVID-19 with the highest weight toward the disease, while other PE species such as PE 34:2 was selected as indicative of being negative for COVID-19. Increased abundance of PE species were also recently reported by Ford *et al* in nasal swabs from COVID-19 positive patients<sup>32</sup>. Importantly, since our method does not enable deconvolution between the lipid signal arising from the virion or from host cells, we speculate that the species observed as indicative of COVID-19 are a major component of the virion cellular membrane and/or have increased abundances in host infected cells to enable replication of the virus. Thus, although lipid species represent promising detection targets for COVID-19, additional research is needed to elucidate the role of these species in COVID-19 disease and host response to the infection.

This study has a few limitations. Concerning clinical samples, the swabs for MS and PCR analysis were collected separately for hospitalized patients in our study, which could potentially lead to discrepancies in their diagnoses, especially considering the reported FNR of PCR analysis<sup>45-47</sup>. Viral load information was also unavailable for the

patients which prevented evaluation of a potential relationship between viral burden, molecular information, and diagnostic performance achieved. Heat-inactivation was also used in our study for all the clinical swabs, and thus, biosafety considerations in swab collection, storage, and inactivation steps are needed in future studies to facilitate sample collection and transport. Lastly, although our study was performed using a restricted population of individuals from Brazil, the promising results obtained warrants further investigation, and we expect that a larger cohort of patient samples including asymptomatic PCR positive patients and patients with other viral infections causing similar symptoms to COVID-19 will allow further refinement and validation of the classifiers for COVID-19 disease prediction using lipid information.

## **CONCLUSION**

In conclusion, the integration of a redesigned version of the disposable MasSpec Pen device provides a rapid MS-based screening method for COVID-19 disease directly from nasopharyngeal swabs. Modifications to the sampling unit and coupling to ESI enabled more effective and reproducible extraction and ionization of lipids from COVID-19 clinical nasal swabs using common solvent systems while maintaining the disposability and user-friendly features of the MasSpec Pen device. As the MasSpec Pen-ESI system has a small footprint and is compatible with various mass spectrometers, this system could be potentially implemented in clinical laboratories and testing facilities that are currently suited with MS instrumentation. The speed of analysis (~45 s/swab) combined with a relatively lower FNR compared to other FDA approved screening methods and high NPV

value achieved substantiate the potential of the technology as a rapid screening tool to identify individuals negative for COVID-19 infection prior to or when PCR is not readily available. While further refinement and testing of the methodology and statistical classifiers with larger sample cohorts will be pursued to improve analytical and diagnostic performance, the present results point to the MasSpec Pen-ESI MS system as a valuable approach for rapid screening of clinical swabs on a seconds-to-minutes time scale.

## REFERENCES

1. Huang, C.; Wang, Y.; Li, X.; Ren, L.; Zhao, J.; Hu, Y.; Zhang, L.; Fan, G.; Xu, J.; Gu, X.; Cheng, Z.; Yu, T.; Xia, J.; Wei, Y.; Wu, W.; Xie, X.; Yin, W.; Li, H.; Liu, M.; Xiao, Y.; Gao, H.; Guo, L.; Xie, J.; Wang, G.; Jiang, R.; Gao, Z.; Jin, Q.; Wang, J.; Cao, B., Clinical features of patients infected with 2019 novel coronavirus in Wuhan, China. *Lancet* **2020**, *395* (10223), 497-506.
2. Wu, F.; Zhao, S.; Yu, B.; Chen, Y. M.; Wang, W.; Song, Z. G.; Hu, Y.; Tao, Z. W.; Tian, J. H.; Pei, Y. Y.; Yuan, M. L.; Zhang, Y. L.; Dai, F. H.; Liu, Y.; Wang, Q. M.; Zheng, J. J.; Xu, L.; Holmes, E. C.; Zhang, Y. Z., A new coronavirus associated with human respiratory disease in China. *Nature* **2020**, *579* (7798), 265-+.
3. Mina, M. J.; Parker, R.; Larremore, D. B., Rethinking Covid-19 Test Sensitivity - A Strategy for Containment. *N Engl J Med* **2020**, *383* (22), e120.
4. Vandenberg, O.; Martiny, D.; Rochas, O.; van Belkum, A.; Kozlakidis, Z., Considerations for diagnostic COVID-19 tests. *Nat Rev Microbiol* **2020**.
5. Masterson, T. A.; Dill, A. L.; Eberlin, L. S.; Mattarozzi, M.; Cheng, L.; Beck, S. D.; Bianchi, F.; Cooks, R. G., Distinctive glycerophospholipid profiles of human seminoma and adjacent normal tissues by desorption electrospray ionization imaging mass spectrometry. *J Am Soc Mass Spectrom* **2011**, *22* (8), 1326-33.
6. Tromberg, B. J.; Schwetz, T. A.; Perez-Stable, E. J.; Hodes, R. J.; Woychik, R. P.; Bright, R. A.; Fleurence, R. L.; Collins, F. S., Rapid Scaling Up of Covid-19 Diagnostic Testing in the United States - The NIH RADx Initiative. *N Engl J Med* **2020**, *383* (11), 1071-1077.
7. Lisboa Bastos, M.; Tavaziva, G.; Abidi, S. K.; Campbell, J. R.; Haraoui, L. P.; Johnston, J. C.; Lan, Z.; Law, S.; MacLean, E.; Trajman, A.; Menzies, D.; Benedetti, A.; Ahmad Khan, F., Diagnostic accuracy of serological tests for covid-19: systematic review and meta-analysis. *BMJ* **2020**, *370*, m2516.
8. Miller, T. E.; Garcia Beltran, W. F.; Bard, A. Z.; Gogakos, T.; Anahtar, M. N.; Astudillo, M. G.; Yang, D.; Thierauf, J.; Fisch, A. S.; Mahowald, G. K.; Fitzpatrick, M. J.; Nardi, V.; Feldman, J.; Hauser, B. M.; Caradonna, T. M.; Marble, H. D.; Ritterhouse, L. L.; Turbett, S. E.; Batten, J.; Georgantas, N. Z.; Alter, G.; Schmidt, A. G.; Harris, J. B.; Gelfand, J. A.; Poznansky, M. C.; Bernstein, B. E.; Louis, D. N.; Dighe, A.; Charles, R. C.; Ryan, E. T.; Branda, J. A.; Pierce, V. M.; Murali, M. R.; Iafate, A. J.; Rosenberg, E. S.; Lennerz, J. K., Clinical sensitivity and interpretation of PCR and serological COVID-19 diagnostics for patients presenting to the hospital. *FASEB J* **2020**, *34* (10), 13877-13884.
9. Abbasi, J., The Promise and Peril of Antibody Testing for COVID-19. *JAMA* **2020**.
10. Mak, G. C. K.; Lau, S. S. Y.; Wong, K. K. Y.; Chow, N. L. S.; Lau, C. S.; Lam, E. T. K.; Chan, R. C. W.; Tsang, D. N. C., Evaluation of rapid antigen detection kit from the WHO Emergency Use List for detecting SARS-CoV-2. *J Clin Virol* **2021**, *134*, 104712.

11. Prince-Guerra, J. L.; Almendares, O.; Nolen, L. D.; Gunn, J. K. L.; Dale, A. P.; Buono, S. A.; Deutsch-Feldman, M.; Suppiah, S.; Hao, L.; Zeng, Y.; Stevens, V. A.; Knipe, K.; Pompey, J.; Atherstone, C.; Bui, D. P.; Powell, T.; Tamin, A.; Harcourt, J. L.; Shewmaker, P. L.; Medrzycki, M.; Wong, P.; Jain, S.; Tejada-Strop, A.; Rogers, S.; Emery, B.; Wang, H.; Petway, M.; Bohannon, C.; Folster, J. M.; MacNeil, A.; Salerno, R.; Kuhnert-Tallman, W.; Tate, J. E.; Thornburg, N. J.; Kirking, H. L.; Sheiban, K.; Kudrna, J.; Cullen, T.; Komatsu, K. K.; Villanueva, J. M.; Rose, D. A.; Neatherlin, J. C.; Anderson, M.; Rota, P. A.; Honein, M. A.; Bower, W. A., Evaluation of Abbott BinaxNOW Rapid Antigen Test for SARS-CoV-2 Infection at Two Community-Based Testing Sites - Pima County, Arizona, November 3-17, 2020. *MMWR Morb Mortal Wkly Rep* **2021**, *70* (3), 100-105.
12. West, C. P.; Montori, V. M.; Sampathkumar, P., COVID-19 Testing: The Threat of False-Negative Results. *Mayo Clin Proc* **2020**, *95* (6), 1127-1129.
13. Abu-Farha, M.; Thanaraj, T. A.; Qaddoumi, M. G.; Hashem, A.; Abubaker, J.; Al-Mulla, F., The Role of Lipid Metabolism in COVID-19 Virus Infection and as a Drug Target. *Int J Mol Sci* **2020**, *21* (10).
14. Caterino, M.; Gelzo, M.; Sol, S.; Fedele, R.; Annunziata, A.; Calabrese, C.; Fiorentino, G.; D'Abbraccio, M.; Dell'Isola, C.; Fusco, F. M.; Parrella, R.; Fabbrocini, G.; Gentile, I.; Andolfo, I.; Capasso, M.; Costanzo, M.; Daniele, A.; Marchese, E.; Polito, R.; Russo, R.; Missero, C.; Ruoppolo, M.; Castaldo, G., Dysregulation of lipid metabolism and pathological inflammation in patients with COVID-19. *Sci Rep* **2021**, *11* (1), 2941.
15. Ivanova, P. T.; Myers, D. S.; Milne, S. B.; McClaren, J. L.; Thomas, P. G.; Brown, H. A., Lipid Composition of the Viral Envelope of Three Strains of Influenza Virus—Not All Viruses Are Created Equal. *ACS Infectious Diseases* **2015**, *1* (9), 435-442.
16. Nayak, D. P.; Hui, E. K. W., The Role of Lipid Microdomains in Virus Biology. In *Membrane Dynamics and Domains: Subcellular Biochemistry*, Quinn, P. J., Ed. Springer US: Boston, MA, 2004; pp 443-491.
17. Quigley, J. P.; Rifkin, D. B.; Reich, E., Phospholipid composition of Rous sarcoma virus, host cell membranes and other enveloped RNA viruses. *Virology* **1971**, *46* (1), 106-116.
18. Kates, M.; Allison, A. C.; Tyrrell, D. A. J.; James, A. T., Lipids of influenza virus and their relation to those of the host cell. *Biochimica et Biophysica Acta* **1961**, *52* (3), 455-466.
19. Callens, N.; Brügger, B.; Bonnafous, P.; Drobecq, H.; Gerl, M. J.; Krey, T.; Roman-Sosa, G.; Rügenapf, T.; Lambert, O.; Dubuisson, J.; Rouillé, Y., Morphology and Molecular Composition of Purified Bovine Viral Diarrhea Virus Envelope. *PLoS Pathog* **2016**, *12* (3), e1005476-e1005476.
20. Dou, D.; Revol, R.; Ostbye, H.; Wang, H.; Daniels, R., Influenza A Virus Cell Entry, Replication, Virion Assembly and Movement. *Front Immunol* **2018**, *9*, 1581.

21. Van Genderen, I. L.; Godeke, G. J.; Rottier, P. J. M.; Van Meer, G., The phospholipid composition of enveloped viruses depends on the intracellular membrane through which they bud. *Biochemical Society Transactions* **1995**, *23* (3), 523-526.
22. Yan, B. P.; Chu, H.; Yang, D.; Sze, K. H.; Lai, P. M.; Yuan, S. F.; Shuai, H. P.; Wang, Y. X.; Kao, R. Y. T.; Chan, J. F. W.; Yuen, K. Y., Characterization of the Lipidomic Profile of Human Coronavirus-Infected Cells: Implications for Lipid Metabolism Remodeling upon Coronavirus Replication. *Viruses-Basel* **2019**, *11* (1).
23. Zhang, J.; Sans, M.; Garza, K. Y.; Eberlin, L. S., Mass Spectrometry Technologies to Advance Care for Cancer Patients in Clinical and Intraoperative Use. *Mass Spectrom Rev* **2020**.
24. Pu, F.; Chiang, S.; Zhang, W.; Ouyang, Z., Direct sampling mass spectrometry for clinical analysis. *Analyst* **2019**, *144* (4), 1034-1051.
25. Ho, Y. P.; Reddy, P. M., Identification of pathogens by mass spectrometry. *Clin Chem* **2010**, *56* (4), 525-36.
26. Ganova-Raeva, L. M.; Khudyakov, Y. E., Application of mass spectrometry to molecular diagnostics of viral infections. *Expert Rev Mol Diagn* **2013**, *13* (4), 377-88.
27. Mahmud, I.; Garrett, T. J., Mass Spectrometry Techniques in Emerging Pathogens Studies: COVID-19 Perspectives. *J Am Soc Mass Spectrom* **2020**, *31* (10), 2013-2024.
28. Nachtigall, F. M.; Pereira, A.; Trofymchuk, O. S.; Santos, L. S., Detection of SARS-CoV-2 in nasal swabs using MALDI-MS. *Nat Biotechnol* **2020**, *38* (10), 1168-1173.
29. Rocca, M. F.; Zintgraff, J. C.; Dattero, M. E.; Santos, L. S.; Ledesma, M.; Vay, C.; Prieto, M.; Benedetti, E.; Avaro, M.; Russo, M.; Nachtigall, F. M.; Baumeister, E., A combined approach of MALDI-TOF mass spectrometry and multivariate analysis as a potential tool for the detection of SARS-CoV-2 virus in nasopharyngeal swabs. *J Virol Methods* **2020**, *286*, 113991.
30. De Silva, I. W.; Nayek, S.; Singh, V.; Reddy, J.; Granger, J. K.; Verbeck, G. F., Paper spray mass spectrometry utilizing Teslin(R) substrate for rapid detection of lipid metabolite changes during COVID-19 infection. *Analyst* **2020**, *145* (17), 5725-5732.
31. Shen, B.; Yi, X.; Sun, Y.; Bi, X.; Du, J.; Zhang, C.; Quan, S.; Zhang, F.; Sun, R.; Qian, L.; Ge, W.; Liu, W.; Liang, S.; Chen, H.; Zhang, Y.; Li, J.; Xu, J.; He, Z.; Chen, B.; Wang, J.; Yan, H.; Zheng, Y.; Wang, D.; Zhu, J.; Kong, Z.; Kang, Z.; Liang, X.; Ding, X.; Ruan, G.; Xiang, N.; Cai, X.; Gao, H.; Li, L.; Li, S.; Xiao, Q.; Lu, T.; Zhu, Y.; Liu, H.; Chen, H.; Guo, T., Proteomic and Metabolomic Characterization of COVID-19 Patient Sera. *Cell* **2020**, *182* (1), 59-72 e15.
32. Ford, L.; Simon, D.; Balog, J.; Jiwa, N.; Higginson, J.; Jones, E.; Mason, S.; Wu, V.; Manoli, E.; Stavrakaki, S. M.; McKenzie, J.; McGill, D.; Koguna, H.; Kinross, J.; Takats, Z., Rapid detection of SARS-CoV2 by Ambient Mass Spectrometry Techniques. *medRxiv* **2020**, 2020.10.07.20207647.

33. Delafiori, J.; Navarro, L. C.; Siciliano, R. F.; de Melo, G. C.; Busanello, E. N. B.; Nicolau, J. C.; Sales, G. M.; de Oliveira, A. N.; Val, F. F. A.; de Oliveira, D. N.; Eguti, A.; Dos Santos, L. A.; Dalcoquio, T. F.; Bertolin, A. J.; Abreu-Netto, R. L.; Salsoso, R.; Baia-da-Silva, D.; Marcondes-Braga, F. G.; Sampaio, V. S.; Judice, C. C.; Costa, F. T. M.; Duran, N.; Perroud, M. W.; Sabino, E. C.; Lacerda, M. V. G.; Reis, L. O.; Favaro, W. J.; Monteiro, W. M.; Rocha, A. R.; Catharino, R. R., Covid-19 Automated Diagnosis and Risk Assessment through Metabolomics and Machine Learning. *Anal Chem* **2021**, *93* (4), 2471-2479.
34. Wu, D.; Shu, T.; Yang, X.; Song, J.-X.; Zhang, M.; Yao, C.; Liu, W.; Huang, M.; Yu, Y.; Yang, Q.; Zhu, T.; Xu, J.; Mu, J.; Wang, Y.; Wang, H.; Tang, T.; Ren, Y.; Wu, Y.; Lin, S.-H.; Qiu, Y.; Zhang, D.-Y.; Shang, Y.; Zhou, X., Plasma metabolomic and lipidomic alterations associated with COVID-19. *National Science Review* **2020**, *7* (7), 1157-1168.
35. Lazari, L. C.; De Rose Ghilardi, F.; Rosa-Fernandes, L.; Assis, D. M.; Nicolau, J. C.; Santiago, V. F.; Dalcoquio, T. F.; Angeli, C. B.; Bertolin, A. J.; Marinho, C. R. F.; Wrenger, C.; Durigon, E. L.; Siciliano, R. F.; Palmisano, G., Prognostic accuracy of MALDI mass spectrometric analysis of plasma in COVID-19. *medRxiv* **2020**, 2020.10.01.20205310.
36. Sans, M.; Zhang, J.; Lin, J. Q.; Feider, C. L.; Giese, N.; Breen, M. T.; Sebastian, K.; Liu, J.; Sood, A. K.; Eberlin, L. S., Performance of the MasSpec Pen for Rapid Diagnosis of Ovarian Cancer. *Clin Chem* **2019**, *65* (5), 674-683.
37. Zhang, J.; Rector, J.; Lin, J. Q.; Young, J. H.; Sans, M.; Katta, N.; Giese, N.; Yu, W.; Nagi, C.; Suliburk, J.; Liu, J.; Bensussan, A.; DeHoog, R. J.; Garza, K. Y.; Ludolph, B.; Sorace, A. G.; Syed, A.; Zahedivash, A.; Milner, T. E.; Eberlin, L. S., Nondestructive tissue analysis for ex vivo and in vivo cancer diagnosis using a handheld mass spectrometry system. *Sci Transl Med* **2017**, *9* (406).
38. Pagnotti, V. S.; Chubatyi, N. D.; McEwen, C. N., Solvent assisted inlet ionization: an ultrasensitive new liquid introduction ionization method for mass spectrometry. *Anal Chem* **2011**, *83* (11), 3981-5.
39. Kwee, T. C.; Kwee, R. M., Chest CT in COVID-19: What the Radiologist Needs to Know. *Radiographics* **2020**, *40* (7), 1848-1865.
40. Yang, W.; Sirajuddin, A.; Zhang, X.; Liu, G.; Teng, Z.; Zhao, S.; Lu, M., The role of imaging in 2019 novel coronavirus pneumonia (COVID-19). *Eur Radiol* **2020**, *30* (9), 4874-4882.
41. Ufuk, F.; Savas, R., Chest CT features of the novel coronavirus disease (COVID-19). *Turk J Med Sci* **2020**, *50* (4), 664-678.
42. Xie, X.; Zhong, Z.; Zhao, W.; Zheng, C.; Wang, F.; Liu, J., Chest CT for Typical Coronavirus Disease 2019 (COVID-19) Pneumonia: Relationship to Negative RT-PCR Testing. *Radiology* **2020**, *296* (2), E41-E45.
43. Feng, H.; Liu, Y.; Lv, M.; Zhong, J., A case report of COVID-19 with false negative RT-PCR test: necessity of chest CT. *Jpn J Radiol* **2020**, *38* (5), 409-410.

44. Hossein, H.; Ali, K. M.; Hosseini, M.; Sarveazad, A.; Safari, S.; Yousefifard, M., Value of chest computed tomography scan in diagnosis of COVID-19; a systematic review and meta-analysis. *Clin Transl Imaging* **2020**, 1-13.
45. Clerici, B.; Muscatello, A.; Bai, F.; Pavanello, D.; Orlandi, M.; Marchetti, G. C.; Castelli, V.; Casazza, G.; Costantino, G.; Podda, G. M., Sensitivity of SARS-CoV-2 Detection With Nasopharyngeal Swabs. *Front Public Health* **2020**, *8*, 593491.
46. Kucirka, L. M.; Lauer, S. A.; Laeyendecker, O.; Boon, D.; Lessler, J., Variation in False-Negative Rate of Reverse Transcriptase Polymerase Chain Reaction-Based SARS-CoV-2 Tests by Time Since Exposure. *Ann Intern Med* **2020**, *173* (4), 262-267.
47. He, J. L.; Luo, L.; Luo, Z. D.; Lyu, J. X.; Ng, M. Y.; Shen, X. P.; Wen, Z., Diagnostic performance between CT and initial real-time RT-PCR for clinically suspected 2019 coronavirus disease (COVID-19) patients outside Wuhan, China. *Respir Med* **2020**, *168*, 105980.

## Chapter 7: Conclusions and Perspectives

The development of ambient ionization MS methods greatly increased the accessibility of molecular information in clinical diagnostics beyond the current MS applications. The combination of the high performance achieved by MS with techniques requiring minimal sample preparation and processing as well as analysis in ambient conditions has enabled the *in situ* analysis of biological samples, showing promise for rapidly evaluating clinical samples in near real time through the detection of metabolic alterations characteristic of disease. Machine learning has also been implemented in the ambient ionization MS workflow to select features important for disease prediction and has potential to automate mass spectral interpretations for clinicians. Continuous effort is being made in the field to mitigate technical challenges faced when utilizing ambient ionization MS methods, focusing largely on improving the robustness and usability of these approaches. Nevertheless, extensive validation and multi-institutional studies using large cohorts of samples are needed to evaluate the robustness of and refine these methods for diagnostic and clinical applications. To that end, the studies described in this dissertation are aimed at assessing the reproducibility and evaluating clinical usability of ambient ionization MS methods for rapid evaluation of breast tissue specimens and screening of SARS-CoV-2 infections.

Ambient ionization MS technologies have been vastly explored for clinical applications, particularly in the field of oncology. The minimal sample preparation and processing steps and the elimination of vacuum chambers needed for sample analysis are attractive features for clinical translation. Yet very few studies have rigorously evaluated

the performance and reproducibility of ambient ionization methods for clinical diagnostics across multiple institutions. Chapter 2 of this dissertation is aimed at evaluating the robustness of DESI-MS imaging for the detection of IDC and breast cancer subtyping among a diverse patient population across two centers in the U.S. and Brazil. DESI-MS imaging analyses was performed at both institutions using two different DESI-MS platforms operated by different lab personnel. Statistical analysis was used to build classification models based on lipid information obtained in the U.S. by DESI-MS imaging to discriminate between normal breast tissue and IDC. The classification model was used to predict on an independent test set of samples analyzed in Brazil using a different mass spectrometer operated by a different lab personnel. Lipid information allowed for the successful discrimination of the two tissue types for the independent test set as well as negative and positive ER, PR, and HR status. While this study represents one of the first multi-center studies to investigate the robustness of ambient ionization MS for tissue evaluation and diagnosis, larger multi-institutional studies using commercially available DESI-MS instrumentation and LC-MS are needed to verify the trends in lipid species observed in this study. Recent advances to the commercially available DESI-MS instrumentation has decreased overall analysis time as well as improved the robustness of the DESI sprayer for tissue section analysis<sup>1</sup>, which is key to mitigating any intra-laboratory variability, facilitating clinical translation, and use as an alternative method to intraoperative frozen section analysis. Further, performing IHC on tissue sections following DESI-MS analysis should be incorporated into the workflow to refine the classification models for receptor status prediction as well as to evaluate the

usefulness of DESI-MS for molecular subtyping and treatment decision making.

Additional testing and validation of DESI-MS imaging will help provide insight into the usefulness of this technology for the clinical management of breast cancer patients.

Recent technical advances in the field of ambient ionization MS have focused on increasing the molecular coverage obtained by these technologies by incorporating ion mobility. Chapter 3 discusses the coupling of DESI-MS to FAIMS for the detection and imaging of multiply charged protein species up to 16 kDa directly from tissue sections, demonstrating feasibility for the first time using DESI-MS. The integration of FAIMS into the DESI-MS imaging workflow allowed for multi-modal imaging of proteins, lipids, and metabolites in tissue sections, which could prove useful for a more in depth investigation of healthy and diseased human tissue sections in future applications. While FAIMS enabled the detection of multiply charged molecules, it proved challenging to detect lower abundant proteins in biological tissue as smaller molecules not removed from the complex biological matrix during the organic solvent washing steps can compete with the proteins for charge and suppress the signal for the larger molecules. Additionally, FAIMS acts as an ion filter and ultimately further reduces the overall signal intensity of ions transmitted to the mass spectrometer. Although the protein coverage by DESI-MS remains inferior to LC-MS/MS of tissue extracts and MALDI-MS imaging experiments, recent improvements in the sensitivity of mass spectrometers and advancements in FAIMS instrumentation have increased the number of proteins detected by liquid extraction ambient ionization MS over 10-fold in biological tissue sections.<sup>2</sup> While DESI-MS has yet to be coupled to these higher resolution and performing

instrumentation for protein analysis, these improvements are a step toward alleviating some of the challenges experienced when utilizing ambient ionization MS for the detection of larger molecules in tissue samples.

The development of handheld ambient ionization MS-based technologies offers the exciting opportunity to incorporate the molecular assessment of human tissue specimens into the surgical workflow, bringing us closer than ever to translating these technologies from the research laboratory into the operating room. As discussed in Chapters 4 and 5, the MasSpec Pen is a biocompatible device that utilizes a discrete water droplet to extract molecular information directly from tissue samples in a matter of seconds. While extensive work has been done in our research lab to demonstrate the ability of the MasSpec Pen to distinguish between various types of banked normal and cancerous tissue, this technology was envisioned for the intraoperative molecular assessment human tissue during oncological surgical procedures, and therefore needs to be rigorously tested in a hospital setting. Chapter 4 describes the clinical translation of the MasSpec Pen system into the OR to evaluate feasibility of this technology for the intraoperative molecular analysis of human tissue and to better understand how it fits into the surgical workflow. MasSpec Pen data was collected during 100 surgeries for thyroid (n=75), breast (n=11), and pancreatic (n=14) cancer and nonmalignant conditions, showing qualitatively similar molecular profiles compared to those obtained from the *ex vivo* analysis of banked tissue samples. Although these results show feasibility of the MasSpec Pen for intraoperative molecular analysis of human tissue, additional considerations are needed to facilitate clinical translation of this technology. Packaging of

statistical classifiers into a user-friendly graphical user interface would allow complex mass spectra to be converted into disease prediction readouts that can be easily interpreted by clinicians and surgical staff. Additionally, integration of the MasSpec Pen to other ionization sources should be explored to decrease instrument contamination and improve the sensitivity of the method. The MasSpec Pen has recently been integrated with atmospheric chemical pressure ionization for forensics applications, showing a 200% increase in the signal compared to the ionization mechanism traditionally used with the MasSpec Pen.<sup>3</sup> Collectively, handheld MS-based devices show promise for intraoperatively evaluating human tissue on a seconds to minutes timescale, which is significantly faster than currently available intraoperative methods. However, these MS technologies are not intended to replace pathological evaluation of tissue specimens, which is currently the gold standard. Rather, they are envisioned as complimentary tools that can provide information complementary to final post-operative pathology to enable a more comprehensive evaluation of tissue specimens and to guide surgical resection. Continuous effort is aimed toward optimizing and refining handheld MS-based technologies for intraoperative and clinical use, ultimately working toward improving the surgical management of cancer patients.

Chapter 5 specifically focuses on refining the MasSpec Pen for intraoperative surgical margin evaluation during breast cancer surgeries. Although intraoperative surgical margin evaluation tools are currently available for surgical use, they are not widely implemented, resulting in a stagnant re-excision rate of ~20-40% over the last 10 years. As Chapter 5 describes, the MasSpec Pen is a promising solution for improving

intraoperative surgical margin evaluation, and potentially reducing the re-excision rate, as it can distinguish between IDC and normal breast tissue with over a 90% accuracy in an independent test set. The classification model built using *ex vivo* banked normal breast tissue and IDC data was used to predict on the mass spectra collected intraoperatively, resulting in a 95.2% agreement with final pathology. While these results are promising, all tissue sampled intraoperatively by the MasSpec Pen was negative for cancer as the tumor was not physically exposed in any of the cases. Thus, extensive validation of the classification model for IDC detection is still needed before implementation into a clinical environment. Future testing of this technology will focus on rigorously validating the performance of the statistical classifier for the detection of IDC at the surgical margins. Additionally, larger multi-institutional studies encompassing a diverse patient population will help evaluate the potential of the MasSpec Pen technology for the near real time detection of breast cancer and assessment of surgical margins and provide insight into its ability to reduce re-excision surgeries and improve patient care and outcome.

With the outbreak of the novel coronavirus COVID-19 so came the development of many techniques aimed at mitigating the spread of the virus. Chapter 6 of this dissertation describes the modification and application of the MasSpec Pen system for the analysis of clinical COVID-19 nasal swabs. Lipid information obtained from the analysis of asymptomatic negative, symptomatic negative, and symptomatic positive swabs was used to build classification models for COVID-19 status prediction, yielding ~80% agreement with PCR. Further testing and refinement of the methodology using large

sample sizes and asymptomatic negative samples is needed to improve the analytical and diagnostic performance as well as verify the diagnostic power of lipid information for COVID-19 diagnosis and screening. Nevertheless, the modifications to the sampling unit and coupling to ESI can broaden the applications of this technology to include the analysis medical swabs collected for other infections or diseases. As this method is coupled to ESI, quantitative analysis of pharmaceuticals and semiquantitative analysis of biological samples can now be explored with the MasSpec Pen technology, which was previously unattainable using solvent assisted inlet ionization. Additionally, the 3D printed materials used to make the sampling unit can be further modified to allow for the analysis of smaller or larger biological samples, including biofluids. The user-friendly features, small footprint, and compatibility with various benchtop mass spectrometers enable this system to potentially be implemented in clinical laboratories already equipped with MS instrumentation for various diagnostic applications.

Collectively, the studies described in Chapters 2-6 of this dissertation showcase the potential ambient ionization MS methodologies to address complex challenges in human health and disease diagnosis. Technological refinements and extensive testing validation in larger studies and clinical trials across multiple institutions will only provide more evidence of the benefits of incorporating ambient ionization MS approaches into clinical workflows for routine use. Although ambient ionization MS is relatively new compared to the MS methodologies currently used in a clinical lab, significant advancements have been made to make them more robust and versatile for clinical use, with the goal of improving patient care and outcome.

## REFERENCES

1. Tillner, J.; Wu, V.; Jones, E. A.; Pringle, S. D.; Karancsi, T.; Dannhorn, A.; Veselkov, K.; McKenzie, J. S.; Takats, Z., Faster, More Reproducible DESI-MS for Biological Tissue Imaging. *J. Am. Soc. Mass Spectrom.* **2017**, *28* (10), 2090-2098.
2. Griffiths, R. L.; Hughes, J. W.; Abbatiello, S. E.; Belford, M. W.; Styles, I. B.; Cooper, H. J., Comprehensive LESA Mass Spectrometry Imaging of Intact Proteins by Integration of Cylindrical FAIMS. *Anal Chem* **2020**, *92* (4), 2885-2890.
3. Feider, C. L.; Gatmaitan, A. N.; Hooper, T.; Chakraborty, A.; Gowda, P.; Buchanan, E.; Eberlin, L. S., Integrating the MasSpec Pen with Sub-Atmospheric Pressure Chemical Ionization for Rapid Chemical Analysis and Forensic Applications. *Anal Chem* **2021**.

# Appendices

## APPENDIX A: SUPPLEMENTARY MATERIAL FOR CHAPTER 2

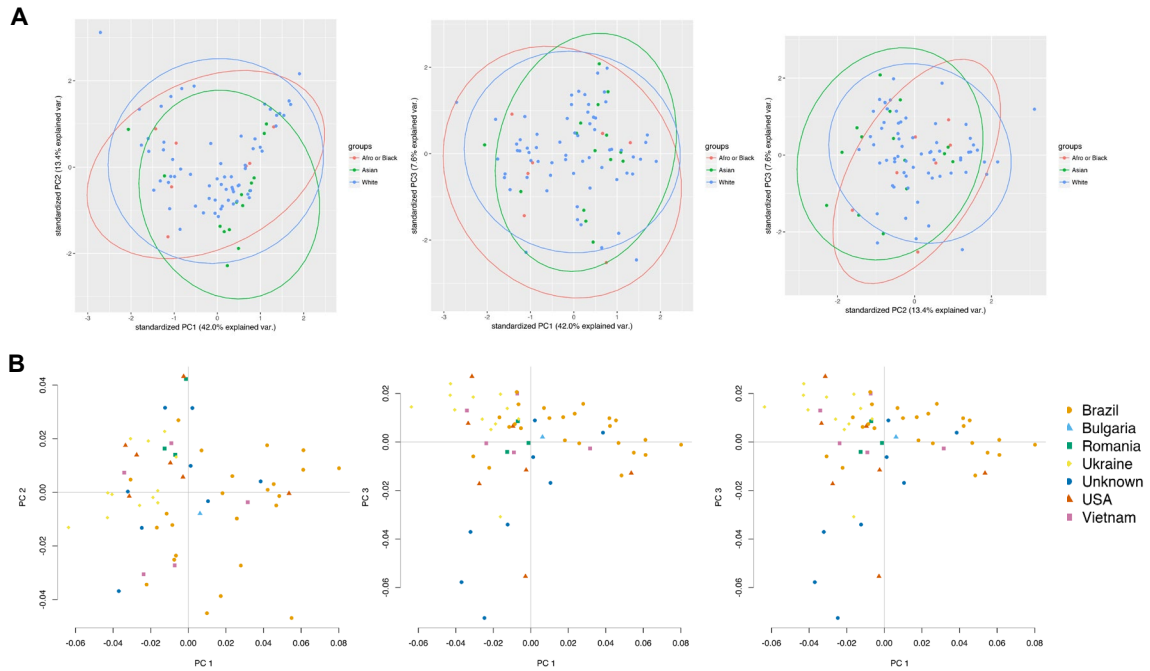


Figure A2.1: PCA analysis of normal breast tissue by race and ethnicity.

Projections of the mass spectra from normal breast tissue samples onto the first three principal components (PC) do not separate patients by A) race, or B) country of collection, as observed for the 2D PCA plot of PC1 versus PC2, 2D PCA plot of PC1 versus PC3, and 2D PCA plot of PC2 versus PC3.

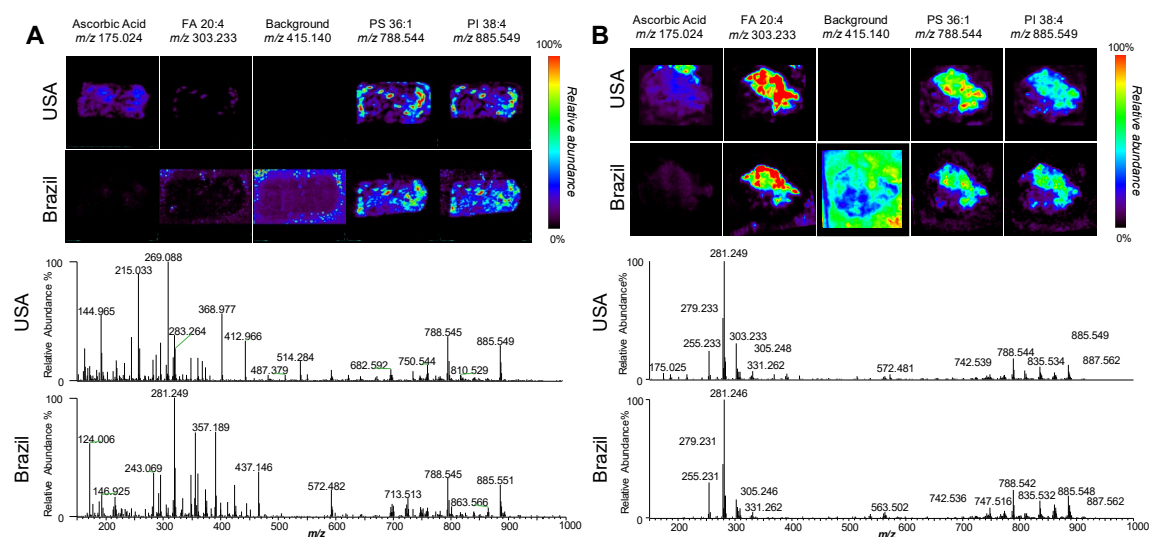


Figure A2.2: Negative ion mode DESI-MS ion images and mass spectra acquired in the USA and Brazil.

Negative ion mode DESI ion images and mass spectra of adjacent tissue sections of A) normal breast and B) breast IDC tissue samples analyzed in Brazil and the USA. PI: glycerophosphoinositol, PS: glycerophosphoserine, FA: fatty acid. Lipid species are described by number of fatty acid chain carbons and double bonds.

Table A2.1: Cosine similarity values of the data obtained in USA and Brazil for same Brazilian normal and cancer samples.

		<b>USA</b>	<b>USA</b>	<b>Brazil</b>	<b>Brazil</b>
		<b>normal</b>	<b>cancer</b>	<b>normal</b>	<b>cancer</b>
<b>m/z</b> <b>100-1200</b>	<b>USA normal</b>	1.00	0.73	0.51	0.57
	<b>USA cancer</b>	0.73	1.00	0.69	0.91
	<b>Brazil normal</b>	0.51	0.69	1.00	0.84
	<b>Brazil cancer</b>	0.57	0.91	0.84	1.00
<b>m/z</b> <b>700-1200</b>	<b>USA normal</b>	1.00	0.92	0.85	0.86
	<b>USA cancer</b>	0.92	1.00	0.72	0.92
	<b>Brazil normal</b>	0.85	0.72	1.00	0.82
	<b>Brazil cancer</b>	0.86	0.92	0.82	1.00

Table A2.2: Summary of Lasso prediction results for distinguishing between normal and IDC breast samples for USA training set, USA test set, and Brazil test set.

	Analysis	Pathologic Diagnosis	Lasso Results		Sensitivity (%)	Specificity (%)	Overall Agreement (%)
			Normal	Cancer			
<b>USA Training set</b>	<b>Per Pixel</b>	Normal	1049	36	97.6	96.7	97.6
		Cancer	417	17189			
	<b>Per Patient</b>	Normal	21	0	97.8	100.0	
		Cancer	1	44			
<b>USA Test Set</b>	<b>Per Pixel</b>	Normal	184	1	99.1	99.5	99.2
		Cancer	53	6120			
	<b>Per Patient</b>	Normal	6	0	100.0	100.0	
		Cancer	0	15			
<b>Brazil Test Set</b>	<b>Per Pixel</b>	Normal	2042	45	94.7	97.8	95.3
		Cancer	495	8795			
	<b>Per Patient</b>	Normal	18	0	96.2	100.0	
		Cancer	1	25			

## APPENDIX B: SUPPLEMENTARY MATERIAL FOR CHAPTER 3

Table B3.1: Comparison of the S/N of alpha globin in mouse kidney tissue sections detected by DESI-MS imaging with and without FAIMS

	<b>Signal*</b>	<b>Signal Std Dev</b>	<b>S/N*</b>	<b>S/N Std Dev</b>	<b>S/N RSD (%)</b>	<b>Variance</b>
<b>FAIMS</b>	773	83	32.1	2.5	7.8	63.6
<b>No FAIMS</b>	947	354	27.9	7.5	27	56.8

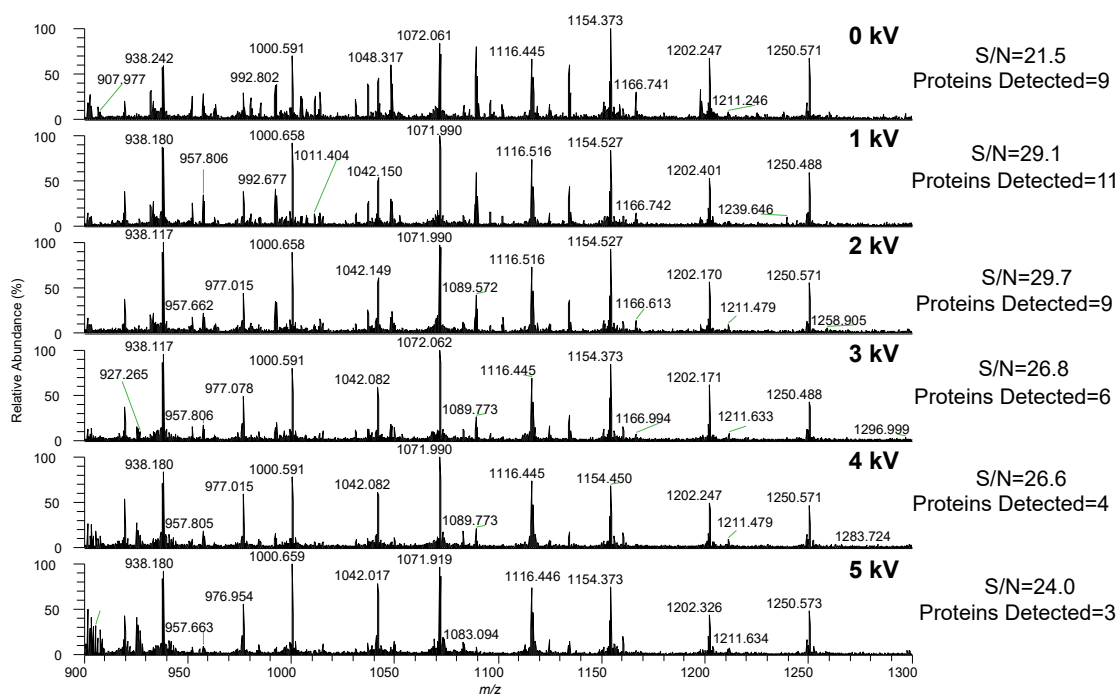


Figure B3.1: Comparison of the S/N and number of detected protein species at different spray voltages using DESI-FAIMS-MS.

Spectra are an average of 20 scans.

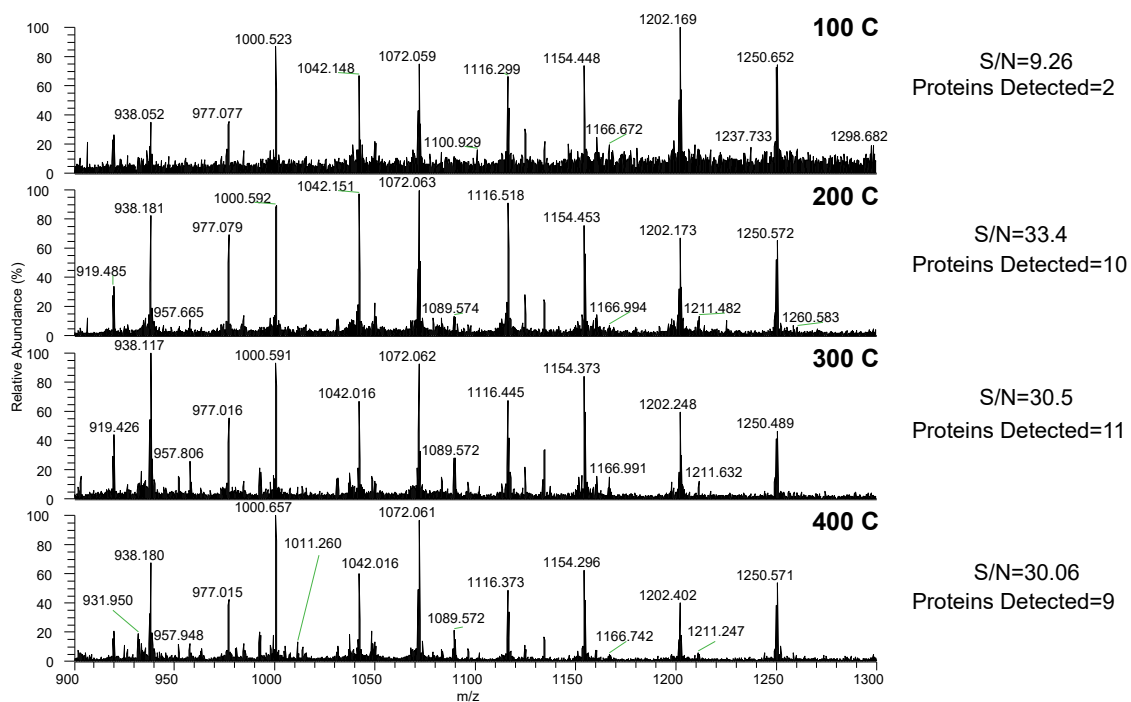


Figure B3.2: Comparison of the S/N and number of detected protein species at different inlet temperatures using DESI-FAIMS-MS.

Spectra are an average of 20 scans.

Table B3.2: Identified proteins and their corresponding sequence coverages for mouse brain, human ovary, and human breast tissue samples.

Proteins were either identified by top-down or bottom-up approaches.

Mouse brain						
Protein Identification	Accession Number	m/z	Charge State	Molecular Weight (Da)	Top Down Sequence Coverage (%)	Bottom Up Sequence Coverage (%)
6.8 kDa mitochondrial proteolipid	P56379	957.662	7	6,698	23	-
Cytochrome c oxidase subunit 6c	Q9CPQ1	1,048.44	8	8,469	36	-
Acyl-CoA-binding protein	P31786	901.931	11	10,000	41	57
V-type proton ATPase subunit G2	Q9WTT4	969.65	14	13,651	29	31
Myelin basic protein isoform 8	P04370-8	706.996	20	14,211	32	47
Alpha globin	Q91VB8	999.723	15	15,085	24	64
Beta globin	A8DUK4	1,042.22	15	15,784	20	75
Unidentified	--	1,096.75	6	6,567	--	--
Unidentified	--	992.68	8	7,929	--	--
Unidentified	--	1,166.87	8	9,320	--	--
Unidentified	--	985.173	11	10,818	--	--
Unidentified	--	1,031.29	11	12,357	--	--
Unidentified	--	1,053.78	13	13,680	--	--
Unidentified	--	707.667	20	14,127	--	--
Unidentified	--	943.358	14	14,140	--	--
Unidentified	--	936.307	16	14,957	--	--
Human Ovary						
Protein Identification	Accession Number	m/z	Charge State	Molecular Weight (Da)	Top Down Sequence Coverage (%)	Bottom-Up Sequence Coverage (%)
Protein S100A6	P06703	1,442.342	7	10,180	23 <sup>b</sup>	--
Hemoglobin subunit alpha	P69905	946.319	16	15,258	35 <sup>a</sup> , 52 <sup>b</sup>	50 <sup>a</sup> , 25 <sup>b</sup>
Hemoglobin subunit beta	P68871	1,058.765	15	15,998	27 <sup>a</sup> , 33 <sup>b</sup>	97 <sup>a</sup> , 50 <sup>b</sup>
Unidentified	--	1,161.080	13	15,085	--	--
Unidentified	--	1,110.289	7	7,760	--	--
Unidentified	--	945.378	16	15,100	--	--
Unidentified	--	1,070.282	14	14,960	--	--
Unidentified	--	1,166.091	10	11,645	--	--
Unidentified	--	1,077.288	14	15,072	--	--
Unidentified	--	1,082.162	14	15,137	--	--
Unidentified	--	1,055.761	15	15,813	--	--
Unidentified	--	1,057.761	15	15,841	--	--
Unidentified	--	1,069.502	15	16,018	--	--
Unidentified	--	1,099.843	15	16,472	--	--
Human Breast						
Protein Identification	Accession Number	m/z	Charge State	Molecular Weight (Da)	Top Down Sequence Coverage (%)	Bottom-Up Sequence Coverage (%)
Protein S100A6	P06703	1262.176	8	10,180	--	32 <sup>b</sup>
Protein S100A8	P05109	986.633	11	10,835	--	12 <sup>b</sup>
Protein S100A4	P26447	1058.893	11	11,279	--	9 <sup>b</sup>
Protein S100A11	P31949	1166.091	10	11,740	23 <sup>b</sup>	56 <sup>b</sup>
Galectin-1	P09382	1126.177	13	14,716	--	61 <sup>b</sup>
Profilin-1	P07737	1152.46	13	15,054	--	23 <sup>a</sup>
Hemoglobin subunit alpha	P69905	1009.405	15	15,258	36 <sup>a</sup> , 29 <sup>b</sup>	94 <sup>a</sup> , 29 <sup>b</sup>
Hemoglobin subunit beta	P68871	1058.763	15	15,998	34 <sup>a</sup> , 16 <sup>b</sup>	95 <sup>a</sup> , 16 <sup>b</sup>
Unidentified	--	1152.459	13	14,959	--	--
Unidentified	--	1077.284	14	15,058	--	--
Unidentified	--	1006.469	15	15,071	--	--
Unidentified	--	945.380	16	15,101	--	--
Unidentified	--	1010.600	15	15,138	--	--
Unidentified	--	1055.828	15	15,872	--	--
Unidentified	--	952.38	17	16,160	--	--
Unidentified	--	1156.181	14	16,163	--	--

<sup>a</sup> normal tissue

<sup>b</sup> cancerous tissue

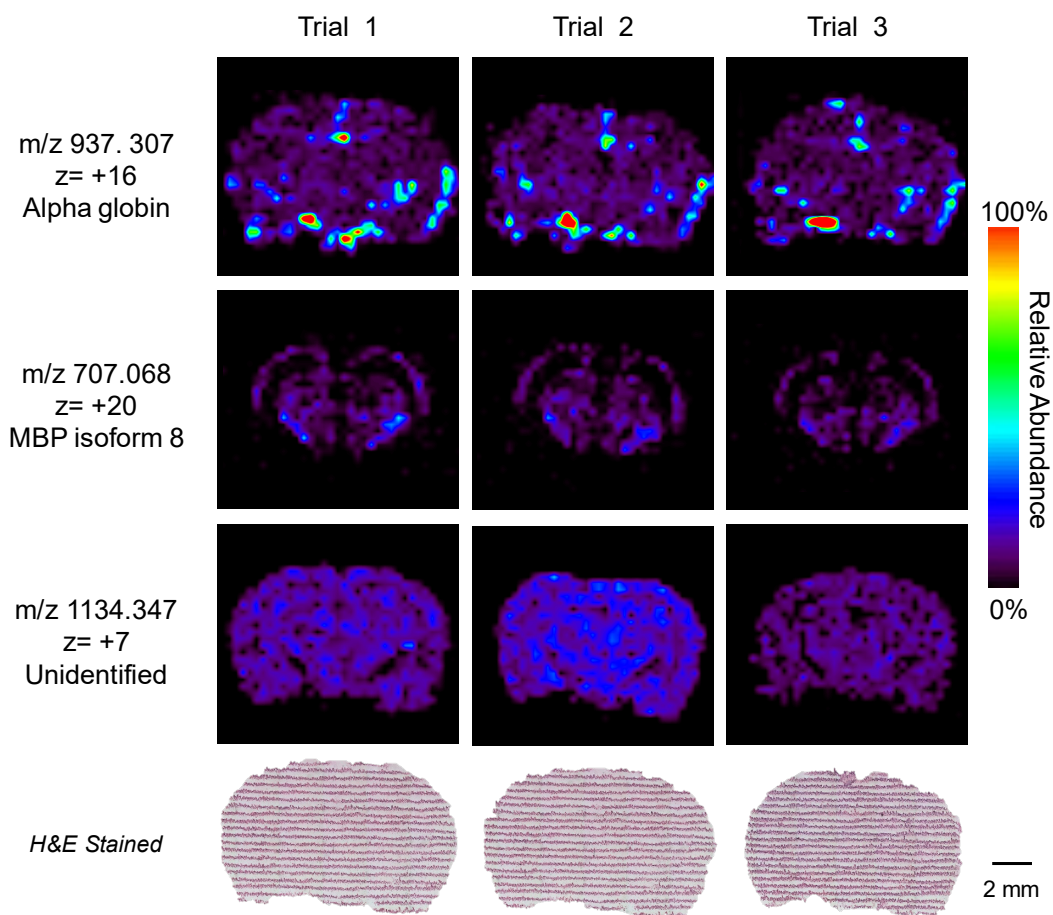


Figure B3.3: DESI-MS ion images of three serial mouse brain tissue sections. Reproducible ion intensities and protein distributions within the tissue provided by this method are shown. Optical H&E images shown are of the same tissue section analyzed.

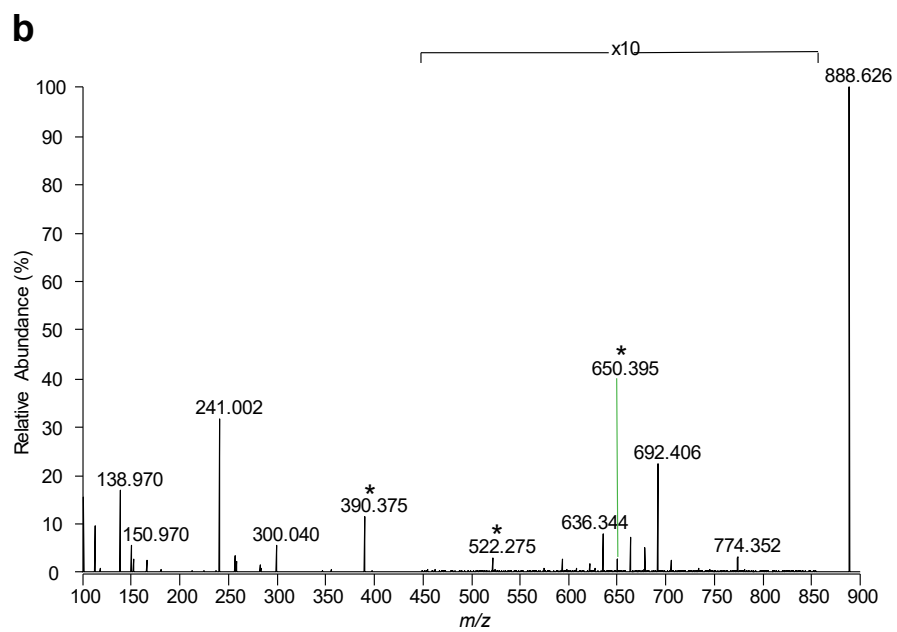
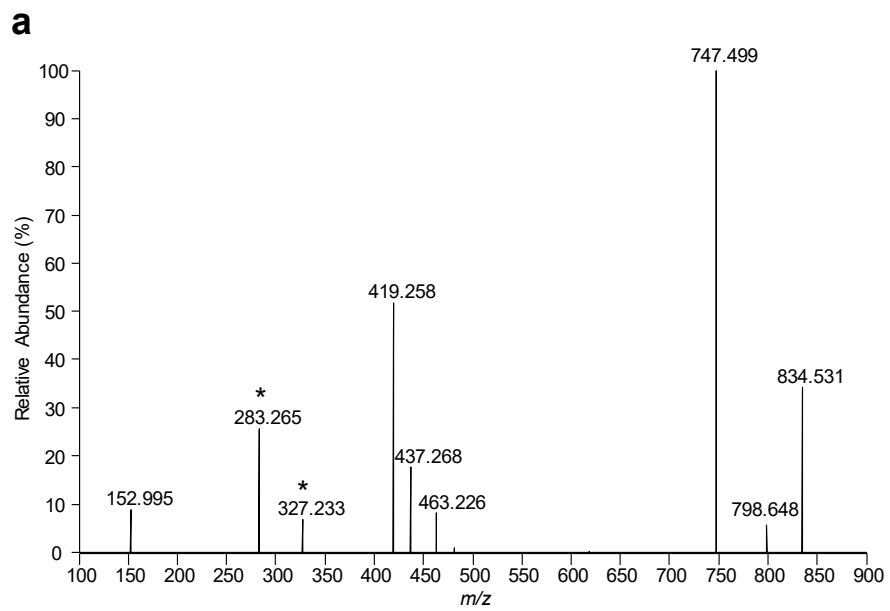


Figure B3.4: Representative negative ion mode MS/MS spectra of PS 40:6 and ST C24:1 obtained using DESI.

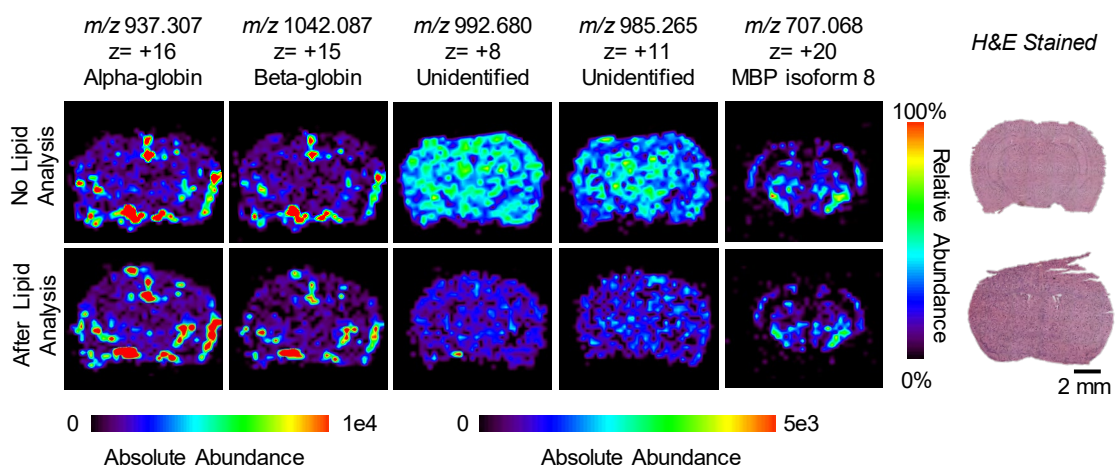


Figure B3.5: DESI-MS ion images of mouse brain tissue sections obtained both with and without previous analysis by DESI-MS imaging in negative ion mode.

A histologically compatible solvent system was used in the negative ion mode, showing minimal loss in protein signal intensity. Ion images are in the same scale. H&E stained images are of a serial mouse brain tissue section as protein conditions are not histologically compatible.

## APPENDIX C: SUPPLEMENTARY MATERIAL FOR CHAPTER 4

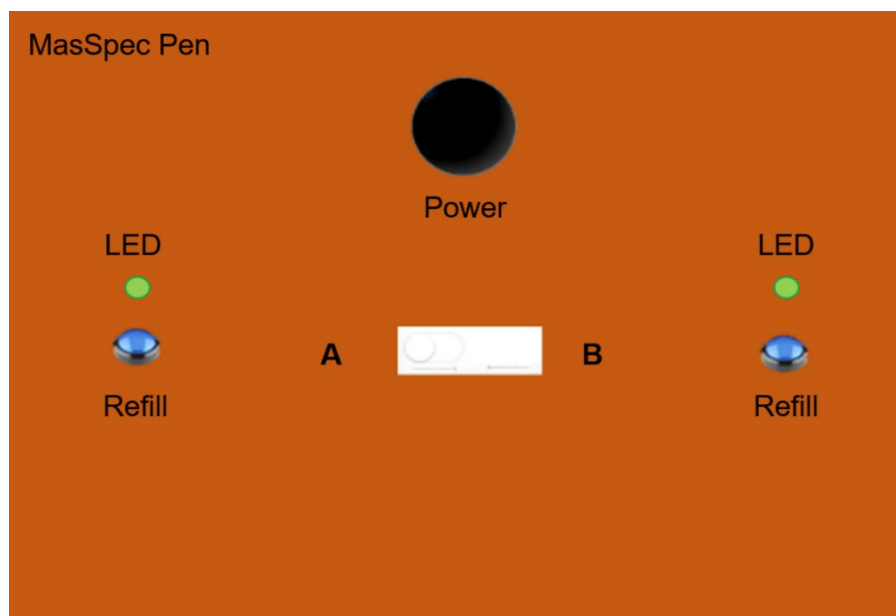


Figure C4.1: MasSpec Pen control interface front panel.

The control box is composed of four buttons which are power, A&B switch, and refill. LED lights were incorporated in the panel to indicate the status of “analysis” or “prime”.



Figure C4.2: Assembling of MasSpec Pen devices.

All the devices used intraoperatively were 3D printed and assembled in the laboratory at UT Austin. After assembly, each individual device was placed in sterile bag and sent to the hospital for autoclaving prior to surgical use.

Table C4.1: Cosine similarity results between the mass spectra obtained with different tubing lengths of the MasSpec Pen.

<b>Tubing Length</b>		
	<b>1.5 meters (n=4)</b>	<b>3.0 meters (n=4)</b>
<b>3.0 meters (n=4)</b>	0.91	--
<b>4.5 meters (n=4)</b>	0.92	0.97

Table C4.2: Droplet transport time from pen tip to mass spectrometer through various tubing lengths.

<b>Droplet Transport Time</b>		
	<b>Average (n=10) in seconds</b>	<b>Relative Standard Deviation (RSD)</b>
<b>1.5 meters</b>	3.8	12.4%
<b>3.0 meters</b>	5.8	11.5%
<b>4.5 meters</b>	7.5	5.2%

Table C4.3: Clinical and demographic information for the 100 patients included in this study.

Information on the analyses conducted with the MasSpec Pen, such as number of devices used, number of analyses, tissue samples analyzed and type of analysis (*in vivo* or *ex vivo*), is also provided. Patients IDs were defined according to the type of procedure (thyroidectomies – TH, parathyroidectomies – PT, BR – breast cancer surgery, PN – pancreatic cancer surgery).

DATE MM/YYYY Y	PATIENT ID	AGE	GENDER	ETHNICITY	RACE	PROCEDURE	INDICATION	MS	NUMBER	<i>IN VIVO</i> (Y/N)	<i>EX VIVO</i> (Y/N)	TISSUES ANALYZED
								PEN DEVICES USED	RMS PEN ANALYSES			
09/2018	TH0001	39	F	Not Hispanic or Latino	White or Caucasian	Right Hemithyroidectomy	Solitary Nodule	2	2	Y	Y	Thyroid
09/2018	TH0002	42	F	Not Hispanic or Latino	Black or African American	Total Thyroidectomy	Graves' Disease	2	9	Y	Y	Parathyroid, Thyroid
09/2018	TH0003	44	F	Hispanic or Latino	White or Caucasian	Right Hemithyroidectomy	Papillary Thyroid Cancer	2	8	Y	Y	Parathyroid, Thyroid
09/2018	PT0001	62	M	Not Hispanic or Latino	White or Caucasian	Right Inferior Parathyroidectomy	Primary Hyperparathyroidism	2	4	Y	N	Parathyroid, Thyroid
09/2018	PT0002	66	M	Not Hispanic or Latino	White or Caucasian	Left Superior Parathyroidectomy	Primary Hyperparathyroidism	2	5	Y	N	Parathyroid, Thyroid
09/2018	PT0003	56	F	Hispanic or Latino	White or Caucasian	Subtotal Parathyroidectomy	Secondary Hyperparathyroidism	1	1	Y	N	Parathyroid
09/2018	PN0001	73	M	Not Hispanic or Latino	White or Caucasian	Whipple	Pancreatic Adenocarcinoma	4	8	Y	Y	Lymph node, Pancreas
10/2018	BR0001	63	F	Not Hispanic or Latino	White or Caucasian	Right Mastectomy with SLNB	Grade III Intraductal Carcinoma	4	10	Y	Y	Lymph node, Breast
10/2018	TH0004	42	F	Hispanic or Latino	White or Caucasian	Right Hemithyroidectomy	Indeterminate nodule	1	5	Y	Y	Thyroid

10/2018	TH0005	66	M	Not Hispanic or Latino	White or Caucasian	Total Thyroidectomy	FAP with Multinodular Goiter	3	9	Y	Y	Thyroid
10/2018	PT0004	81	F	Not Hispanic or Latino	White or Caucasian	Left Inferior Parathyroidectomy, Thyroid Biopsy	Primary Hyperparathyroidism	2	6	Y	Y	Parathyroid, Thyroid
10/2018	PT0005	49	F	Not Hispanic or Latino	White or Caucasian	Subtotal Parathyroidectomy	Tertiary Hyperparathyroidism	3	12	Y	Y	Parathyroid, Thyroid
10/2018	TH0006	49	F	Not Hispanic or Latino	Black or African American	Left Hemithyroidectomy	Indeterminate nodule	3	7	Y	Y	Parathyroid, Thyroid
10/2018	TH0007	53	F	Not Hispanic or Latino	White or Caucasian	Left Hemithyroidectomy	Indeterminate nodule	2	5	Y	Y	Thyroid
10/2018	TH0008	28	F	Not Hispanic or Latino	White or Caucasian	Total Thyroidectomy	Toxic Multinodular Goiter	1	1	Y	N	Thyroid
10/2018	PN0002	69	F	Hispanic or Latino	Other	Whipple	Pancreatic Adenocarcinoma	3	4	Y	Y	Lymph node, Pancreas
10/2018	TH0009	29	F	Hispanic or Latino	White or Caucasian	Total Thyroidectomy	Papillary Thyroid Cancer	4	9	Y	Y	Parathyroid, Thyroid, Lymph node
10/2018	PT0006	68	F	Hispanic or Latino	Native Hawaiian or Other Pacific Islander	Right Parathyroidectomy	Primary Hyperparathyroidism	3	6	Y	Y	Parathyroid, Thyroid
10/2018	PT0007	46	F	Hispanic or Latino	White or Caucasian	Redo Parathyroidectomy	Primary Hyperparathyroidism	2	5	Y	N	Parathyroid, Thyroid
10/2018	PN0003	53	M	Hispanic or Latino	White or Caucasian	Laparoscopic Distal Pancreatectomy	IPMN	2	4	N	Y	Pancreas
10/2018	PT0008	48	M	Not Hispanic or Latino	Black or African American	Subtotal Parathyroidectomy	Tertiary Hyperparathyroidism	3	11	Y	Y	Parathyroid, Thyroid
10/2018	BR0002	58	F	Not Hispanic or Latino	White or Caucasian	Bilateral Mastectomy	Li Fraumeni Syndrome	1	2	N	Y	Breast

10/2018	BR0003	45	F	Hispanic or Latino	White or Caucasian	Right Breast Lumpectomy	Re-excision of + DCIS Margin	2	4	Y	Y	Breast
11/2018	PN0004	38	M	Hispanic or Latino	White or Caucasian	Whipple	Cholangiocarcinoma	2	4	Y	N	Pancreas, Bile Duct
11/2018	PN0005	77	F	Not Hispanic or Latino	White or Caucasian	Whipple	Pancreatic Adenocarcinoma	3	4	Y	N	Lymph Node, Pancreas
11/2018	PT0009	64	F	Not Hispanic or Latino	White or Caucasian	Parathyroidectomy	Primary Hyperparathyroidism	3	8	Y	Y	Parathyroid, Thyroid
11/2018	PT0010	55	F	Not Hispanic or Latino	White or Caucasian	Parathyroidectomy	Primary Hyperparathyroidism	2	5	Y	Y	Parathyroid
11/2018	PT0011	66	F	Not Hispanic or Latino	Black or African American	Subtotal Parathyroidectomy	Tertiary Hyperparathyroidism	1	2	N	Y	Parathyroid
11/2018	PT0012	58	F	Not Hispanic or Latino	White or Caucasian	Redo Parathyroidectomy	Primary Hyperparathyroidism	2	7	Y	N	Parathyroid, Thyroid
11/2018	TH0010	35	F	Not Hispanic or Latino	White or Caucasian	Total Thyroidectomy	Graves' Disease	3	6	Y	Y	Parathyroid, Thyroid
11/2018	PN0006	68	F	Not Hispanic or Latino	White or Caucasian	Whipple	Pancreatic Mass	4	7	Y	Y	Lymph Node, Pancreas, Bile Duct
11/2018	PT0013	60	F	Not Hispanic or Latino	White or Caucasian	Parathyroidectomy	Primary Hyperparathyroidism	2	8	Y	Y	Parathyroid, Thyroid
11/2018	PT0014	38	F	Not Hispanic or Latino	Black or African American	Parathyroidectomy	Primary Hyperparathyroidism	2	9	N	Y	Parathyroid
11/2018	TH0011	39	F	Not Hispanic or Latino	White or Caucasian	Total Thyroidectomy	Papillary Thyroid Cancer	3	8	Y	Y	Parathyroid, Thyroid, Lymph node
11/2018	PT0015	60	F	Not Hispanic or Latino	Other	Parathyroidectomy	Primary Hyperparathyroidism	3	8	Y	Y	Parathyroid, Thyroid
11/2018	PT0016	66	F	Not Hispanic or Latino	Black or African American	Redo Parathyroidectomy	Primary Hyperparathyroidism	2	5	Y	N	Parathyroid, Thyroid
11/2018	TH0012	33	F	Not Hispanic or Latino	Asian	Total Thyroidectomy	Right Sided Indeterminate nodule +	2	4	Y	Y	Parathyroid, Thyroid

							Hashimoto's					
11/2018	TH0013	45	F	Hispanic or Latino	White or Caucasian	Total Thyroidectomy	Graves' Disease	3	7	Y	Y	Parathyroid, Thyroid
11/2018	PT0017	67	M	Not Hispanic or Latino	Black or African American	Parathyroidectomy	Bilateral Inferior Parathyroid Adenomas	3	7	Y	Y	Parathyroid, Thyroid
12/2018	TH0014	40	F	Not Hispanic or Latino	White or Caucasian	Hemithyroidectomy	Thyroid Cyst	1	3	N	Y	Thyroid
12/2018	TH0015	70	M	Not Hispanic or Latino	White or Caucasian	Left Hemithyroidectomy	Follicular Adenoma	3	4	Y	Y	Parathyroid, Thyroid
12/2018	TH0016	32	M	Not Hispanic or Latino	Asian	Total Thyroidectomy	Graves' Disease	3	9	Y	Y	Parathyroid, Thyroid
12/2018	PT0018	39	M	Not Hispanic or Latino	White or Caucasian	Right Inferior Parathyroidectomy	Primary Hyperparathyroidism	3	9	Y	Y	Parathyroid, Thyroid
12/2018	PT0019	55	F	Not Hispanic or Latino	White or Caucasian	Right Inferior Parathyroidectomy	Primary Hyperparathyroidism	3	6	Y	Y	Parathyroid, Thyroid
12/2018	TH0017	64	M	Not Hispanic or Latino	White or Caucasian	Total Thyroidectomy	Papillary Thyroid Cancer	3	15	Y	Y	Parathyroid, Thyroid, Lymph Node
12/2018	PT0020	79	F	Not Hispanic or Latino	White or Caucasian	Parathyroidectomy	Primary Hyperparathyroidism	2	7	Y	Y	Parathyroid, Thyroid
12/2018	PT0021	56	F	Not Hispanic or Latino	White or Caucasian	Redo Parathyroidectomy	Tertiary Hyperparathyroidism	2	7	Y	N	Parathyroid, Thyroid
12/2018	TH0018	33	F	Not Hispanic or Latino	White or Caucasian	Right Hemithyroidectomy	Indeterminate nodule	3	10	Y	Y	Parathyroid, Thyroid
12/2018	TH0019	33	F	Not Hispanic or Latino	N/A	Right Hemithyroidectomy	Papillary Thyroid Cancer	3	9	Y	Y	Thyroid, Lymph Node
12/2018	TH0020	35	F	Not Hispanic or Latino	White or Caucasian and Black or African American	Total Thyroidectomy	Graves' Disease	3	7	Y	Y	Parathyroid, Thyroid

12/2018	PT0022	49	F	Not Hispanic or Latino	White or Caucasian	Parathyroidectomy	Primary Hyperparathyroidism	3	10	Y	Y	Parathyroid, Thyroid
12/2018	PN0007	70	F	Not Hispanic or Latino	White or Caucasian	Whipple	Pancreatic Adenocarcinoma	3	7	Y	Y	Lymph Node, Pancreas
12/2018	TH0021	58	M	Not Hispanic or Latino	Black or African American	Total Thyroidectomy	Graves' Disease	3	6	Y	Y	Parathyroid, Thyroid
12/2018	PT0023	66	F	Not Hispanic or Latino	Black or African American	Parathyroidectomy	Primary Hyperparathyroidism	3	10	Y	Y	Parathyroid, Thyroid
12/2018	PT0024	50	M	Hispanic or Latino	Black or African American	Parathyroidectomy	Primary Hyperparathyroidism	3	10	Y	Y	Parathyroid, Thyroid
12/2018	TH0022	54	F	Not Hispanic or Latino	Asian	Right Hemithyroidectomy	Indeterminate nodule	3	7	Y	Y	Lymph Node, Thyroid
12/2018	PT0025	68	F	Not Hispanic or Latino	White or Caucasian	Parathyroidectomy	Primary Hyperparathyroidism	3	7	Y	Y	Parathyroid, Thyroid
12/2018	PT0026	58	F	Not Hispanic or Latino	White or Caucasian	Redo Parathyroidectomy	Primary Hyperparathyroidism	3	6	Y	Y	Parathyroid, Thyroid
01/2019	PN0008	61	F	Hispanic or Latino	White or Caucasian	Whipple	Ampullary Mass	3	7	Y	Y	Lymph Node, Pancreas
01/2019	TH0023	48	F	Hispanic or Latino	N/A	Total Thyroidectomy	Papillary Thyroid Cancer	1	5	Y	Y	Thyroid
01/2019	PT0027	69	F	Not Hispanic or Latino	White or Caucasian	Parathyroidectomy	Primary Hyperparathyroidism	3	9	Y	Y	Parathyroid, Thyroid
01/2019	PT0028	31	M	Not Hispanic or Latino	White or Caucasian	Parathyroidectomy	Primary Hyperparathyroidism	3	9	Y	Y	Parathyroid, Thyroid
01/2019	PN0009	65	M	Not Hispanic or Latino	White or Caucasian	Whipple	Pancreatic Cyst	3	7	Y	Y	Lymph Node, Pancreas
01/2019	PN0010*	61	M	Not Hispanic or Latino	White or Caucasian	Whipple	Pancreatic Mass	0	0	NA	NA	NA
01/2019	TH0024	63	F	Not Hispanic or Latino	Black or African American	Total Thyroidectomy + Parathyroidectomy	Thyroid Neoplasm, Primary	4	12	Y	Y	Parathyroid, Thyroid, Lymph Node

							Hyperparat hyroidism					
02/2019	PN0011	57	M	Not Hispanic or Latino	White or Caucasian	Whipple	Pancreatic Mass	2	5	Y	Y	Pancreas
02/2019	PT0029	68	M	Not Hispanic or Latino	White or Caucasian	Parathyroidectomy	Primary Hyperparat hyroidism	3	7	Y	Y	Parathyroid, Thyroid
02/2019	PT0030	49	F	Not Hispanic or Latino	White or Caucasian	Parathyroidectomy	Primary Hyperparat hyroidism	2	3	Y	Y	Parathyroid
05/2019	PN0012	59	M	Not Hispanic or Latino	Black or African American	Whipple	Pancreatic Mass	2	4	Y	N	Lymph Node, Pancreas
05/2019	PT0031	65	F	Not Hispanic or Latino	White or Caucasian	Parathyroidectomy	Primary Hyperparat hyroidism	4	12	Y	Y	Parathyroid, Thyroid
05/2019	PT0032	52	F	Not Hispanic or Latino	White or Caucasian	Parathyroidectomy	Primary Hyperparat hyroidism	4	10	Y	Y	Parathyroid, Lymph Node
05/2019	PT0033	51	F	Not Hispanic or Latino	White or Caucasian	Redo Parathyroidectomy	Primary Hyperparat hyroidism	1	2	N	Y	Parathyroid
05/2019	PT0034	68	F	Not Hispanic or Latino	White or Caucasian	Parathyroidectomy	Primary Hyperparat hyroidism	3	6	Y	Y	Parathyroid, Thyroid
05/2019	TH0025	50	F	Not Hispanic or Latino	White or Caucasian	Right Hemithyroidectom y	Indetermina te nodule	3	10	Y	Y	Thyroid
05/2019	TH0026	49	F	Not Hispanic or Latino	Black or African American	Left Hemithyroidectom y	Indetermina te nodule	3	9	Y	Y	Parathyroid, Thyroid
05/2019	TH0027	35	F	Not Hispanic or Latino	Black or African American	Right Hemithyroidectom y	Indetermina te nodule	3	8	Y	Y	Thyroid
05/2019	PT0035	42	M	Not Hispanic or Latino	Black or African American	Subtotal Parathyroidectomy	Tertiary Hyperparat hyroidism	3	7	Y	Y	Parathyroid, Thyroid
05/2019	PN0013	64	F	Not Hispanic or Latino	White or Caucasian	Whipple	Pancreatic Mass	4	8	Y	Y	Lymph Node, Pancreas
05/2019	TH0028	34	F	Not Hispanic or Latino	Black or African American	Total Thyroidectomy	Toxic Multinodula r Goiter	3	8	Y	Y	Thyroid

05/2019	PT0036	51	F	Not Hispanic or Latino	White or Caucasian	Subtotal Parathyroidectomy	Tertiary Hyperparat hyroidism	3	9	Y	Y	Parathyroid, Thyroid
05/2019	TH0029	46	F	Not Hispanic or Latino	Black or African American	Right Hemithyroidectom y	Indetermina te nodule	2	9	Y	Y	Thyroid
05/2019	PT0037	44	F	Not Hispanic or Latino	White or Caucasian	Parathyroidectomy	Primary Hyperparat hyroidism	3	7	Y	Y	Parathyroid, Thyroid
05/2019	PT0038	65	F	Not Hispanic or Latino	Black or African American	Redo Parathyroidectomy	Primary Hyperparat hyroidism	3	10	Y	Y	Parathyroid, Thyroid
05/2019	TH0030	49	F	Not Hispanic or Latino	White or Caucasian	Right Hemithyroidectom y	Indetermina te nodule	3	4	Y	Y	Parathyroid, Thyroid
05/2019	TH0031	36	F	Not Hispanic or Latino	White or Caucasian	Completion Thyroidectomy	Papillary Thyroid Cancer	1	2	N	Y	Thyroid
05/2019	TH0032	26	F	Not Hispanic or Latino	White or Caucasian	Right Hemithyroidectom y	Indetermina te nodule	4	9	Y	Y	Lymph Node, Thyroid
005/2019	PT0039	80	F	Not Hispanic or Latino	White or Caucasian	Parathyroidectomy	Primary Hyperparat hyroidism	3	9	Y	Y	Parathyroid, Thyroid
07/2019	BR0004	60	F	Not Hispanic or Latino	White or Caucasian	Bilateral Mastectomy w/L Breast SNB	Invasive Ductal Carcinoma	1	4	Y	Y	Breast
07/2019	BR0005	48	F	Hispanic or Latino	White or Caucasian	Bilateral Mastectomy with R Axillary Dissection	Invasive Ductal Carcinoma	4	9	Y	Y	Lymph Node, Breast
07/2019	PN0014	52	F	Not Hispanic or Latino	White or Caucasian	Subtotal Pancreatectomy	Neuroendoc rine Tumor	3	3	Y	Y	Lymph Node, Pancreas, Liver
07/2019	PT0040	67	F	Hispanic or Latino	White or Caucasian	Parathyroidectomy	Primary Hyperparat hyroidism	3	16	Y	Y	Parathyroid
07/2019	PT0041	66	F	Not Hispanic or Latino	Black or African American	Parathyroidectomy	Primary Hyperparat hyroidism	3	9	Y	Y	Parathyroid, Thyroid
07/2019	BR0006	59	F	Not Hispanic or Latino	White or Caucasian	Bilateral Breast Lumpectomy w/Bilateral SNB	Infiltrating Lobular Carcinoma	5	24	Y	Y	Lymph Node, Breast
07/2019	BR0007	84	F	Not Hispanic or Latino	White or Caucasian	Right Breast Lumpectomy with	Infiltrating Carcinoma	3	5	Y	Y	Lymph Node, Breast

						Axillary Lymph Node Dissection	with Mixed Ductal And Lobular Features					
08/2019	BR0008	46	F	Hispanic or Latino	Native Hawaiian or Other Pacific Islander	Bilateral Total Mastectomy	Completion Mastectomy	2	5	Y	N	Breast
08/2019	TH0033	69	F	Not Hispanic or Latino	Asian	Total Thyroidectomy with Parathyroid Autotransplant	Toxic Multinodular Goiter	4	7	Y	Y	Parathyroid, Thyroid
08/2019	BR0009	65	F	Not Hispanic or Latino	White or Caucasian	Right Breast Lumpectomy	Infiltrating Ductal Carcinoma	3	7	Y	Y	Breast
08/2019	PT0042	38	M	Not Hispanic or Latino	White or Caucasian	Subtotal Parathyroidectomy	Primary Hyperparathyroidism	3	7	Y	Y	Parathyroid, Thyroid
08/2019	BR0010	49	F	Not Hispanic or Latino	White or Caucasian	Right Breast Lumpectomy w/SNB	Infiltrating Ductal Carcinoma	4	9	Y	Y	Lymph Node, Breast
08/2019	BR0011	58	F	Not Hispanic or Latino	Black or African American	Bilateral Breast Mastectomy w/L SNB	Infiltrating Ductal Carcinoma	6	18	Y	Y	Lymph Node, Breast

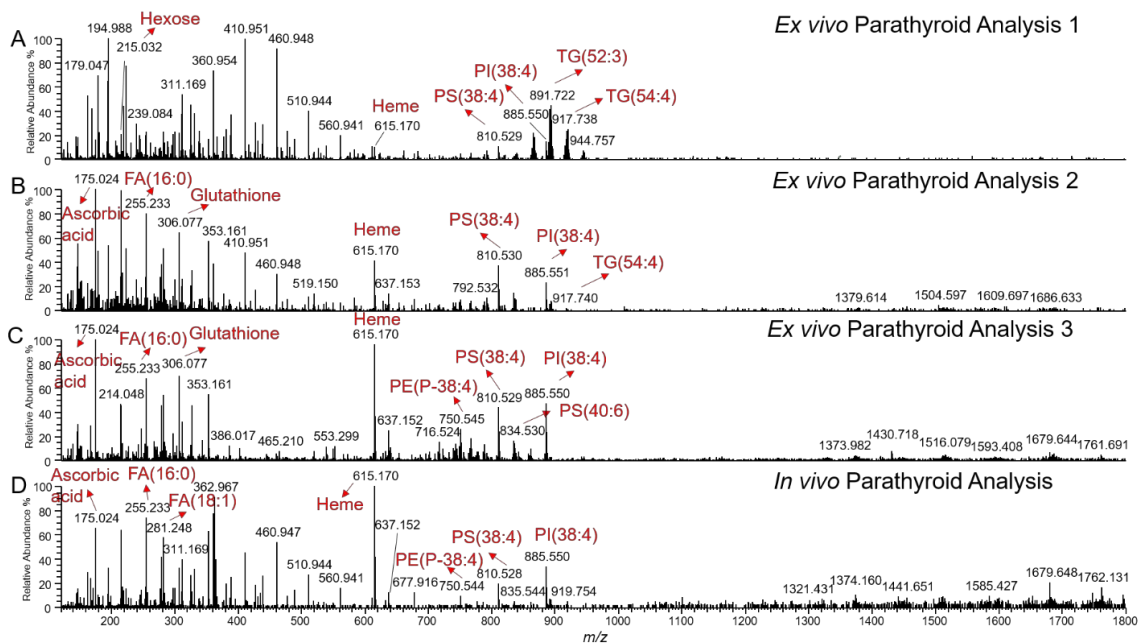


Figure C4.3: Comparison between mass spectra obtained *ex vivo* (A-C) and *in vivo* (D) from a parathyroid collected with the MasSpec Pen during a parathyroidectomy procedure for primary hyperparathyroidism (PT0010).

Several metabolites, including ascorbic acid and glutathione, as well as lipids species were detected in the mass spectra obtained from the three analyses performed with the same device. *In vivo* analysis of the same parathyroid gland was also performed prior to its excision, yielding a comparable molecular profile with high relative abundances of the same metabolites and lipid species detected *ex vivo*. Higher relative abundances of triacylglyceride species were observed in the first analysis, while a higher relative abundances of various metabolites, including ascorbic acid and glutathione, as well as glycerophosphoethanolamine, glycerophosphoserine, and glycerophosphoinositol lipid species, among others, were detected in the second and third analyses. The variations in the mass spectra profiles are likely due to sampling of different tissue regions within the gland, which were performed by the surgeon *in vivo* and by a surgical assistant *ex vivo* within the parathyroid specimen.

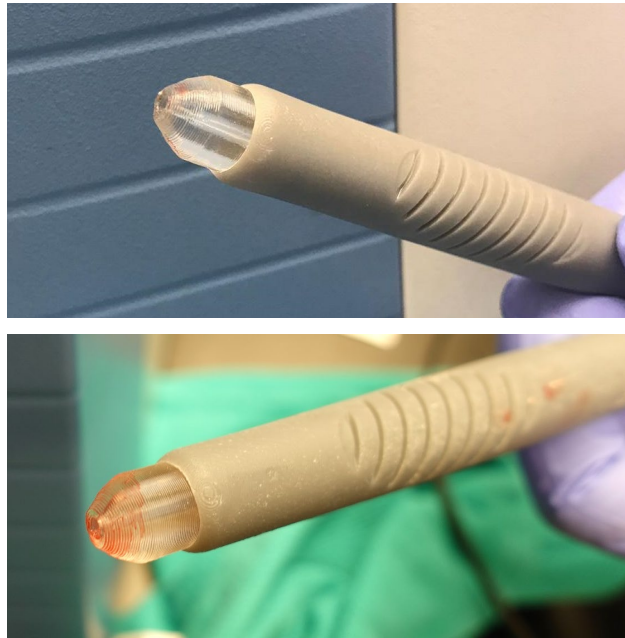


Figure C4.4: Images of two different MasSpec Pen devices after being used *in vivo* by surgeons for tissue analyses.

As observed in the images, while macroscopic blood staining was noted on the tissue contact portion of the device as expected (the extent of which varied depending on the amount of residual blood present at the tissue surface), tissue debris or tissue fragments were not visually observed on the pen tip nor within the tubing system by the surgical or research team.

Table C4.4: Proposed attributions, molecular formula, and mass error for the species annotated. Abbreviations: FA – fatty acid, PE – glycerophosphoethanolamine, PS – glycerophosphoserine, PI – glycerophosphoinositol, TG – triacylglycerol.

Detected <i>m/z</i>	Proposed Attribution	Proposed Molecular Formula	Mass Error (ppm)
124.006	Taurine	C <sub>2</sub> H <sub>6</sub> NO <sub>3</sub> S	3.6
126.904	Iodine	I	7.1
146.045	Glutamic Acid	C <sub>5</sub> H <sub>8</sub> NO <sub>4</sub>	5.5
167.021	Uric Acid	C <sub>5</sub> H <sub>3</sub> N <sub>4</sub> O <sub>3</sub>	3.0
175.024	Ascorbic Acid	C <sub>6</sub> H <sub>7</sub> O <sub>6</sub>	2.3
191.020	Citric Acid	C <sub>6</sub> H <sub>7</sub> O <sub>7</sub>	1.0
215.033	Hexose	C <sub>6</sub> H <sub>12</sub> O <sub>6</sub> Cl	-0.5
246.951	Hexafluoroisopropyl sulfonate	C <sub>3</sub> HO <sub>4</sub> F <sub>6</sub> S	-2.4
227.202	FA 14:0	C <sub>14</sub> H <sub>27</sub> O <sub>2</sub>	1.5
255.234	FA 16:0	C <sub>16</sub> H <sub>31</sub> O <sub>2</sub>	-2.7
279.234	FA 18:2	C <sub>18</sub> H <sub>31</sub> O <sub>2</sub>	-3.6
281.250	FA 18:1	C <sub>18</sub> H <sub>33</sub> O <sub>2</sub>	-3.9
283.265	FA 18:0	C <sub>18</sub> H <sub>35</sub> O <sub>2</sub>	-3.9
303.234	FA 20:4	C <sub>20</sub> H <sub>31</sub> O <sub>2</sub>	-4.3
306.078	Glutathione	C <sub>10</sub> H <sub>16</sub> N <sub>3</sub> O <sub>6</sub> S	-4.6
448.307	Chenodeoxyglycocholate	C <sub>26</sub> H <sub>42</sub> O <sub>5</sub> N	0.3
464.302	Glycocholate	C <sub>26</sub> H <sub>42</sub> O <sub>6</sub> N	0.5
498.290	Taurodeoxycholate	C <sub>26</sub> H <sub>44</sub> O <sub>6</sub> NS	1.0
514.285	Taurohyocholate	C <sub>26</sub> H <sub>44</sub> O <sub>7</sub> NS	1.2
543.164	Lymphazurin	C <sub>27</sub> H <sub>31</sub> N <sub>2</sub> O <sub>6</sub> S <sub>2</sub>	1.8
615.173	Heme	C <sub>34</sub> H <sub>31</sub> FeN <sub>4</sub> O <sub>4</sub>	-5.0

698.514	PE P-34:2	$C_{39}H_{73}NO_7P$	-2.0
700.532	PE P-34:1	$C_{39}H_{75}NO_7P$	4.8
714.511	PE 34:2	$C_{39}H_{73}NO_8P$	4.3
716.527	PE 34:1	$C_{39}H_{75}NO_8P$	4.8
722.517	PE P-36:4	$C_{41}H_{73}NO_7P$	-5.3
726.549	PE P-36:2	$C_{41}H_{77}NO_7P$	-5.8
738.512	PE 36:4	$C_{41}H_{73}NO_8P$	5.5
742.543	PE 36:2	$C_{41}H_{77}NO_8P$	-5.5
744.560	PE 36:1	$C_{41}H_{79}NO_8P$	6.9
750.549	PE P-38:4	$C_{43}H_{77}NO_7P$	-6.0
764.528	PE 38:5	$C_{43}H_{75}NO_8P$	5.8
766.543	PE 38:4	$C_{43}H_{77}NO_8P$	-5.3
770.575	PE 38:2	$C_{43}H_{81}NO_8P$	5.8
778.580	PE P-40:4	$C_{45}H_{81}NO_7P$	5.6
786.533	PS 36:2	$C_{42}H_{77}NO_{10}P$	-5.2
788.549	PS 36:1	$C_{42}H_{79}NO_{10}P$	-5.1
794.575	PE 40:4	$C_{45}H_{81}NO_8P$	5.6
810.533	PS 38:4	$C_{44}H_{77}NO_{10}P$	-5.2
834.533	PS 40:6	$C_{46}H_{77}NO_{10}P$	-4.8
835.537	PI 34:1	$C_{43}H_{80}O_{13}P$	-3.5
836.548	PS 40:5	$C_{46}H_{79}NO_{10}P$	3.9
857.523	PI 36:4	$C_{45}H_{78}O_{13}P$	-4.8
861.554	PI 36:2	$C_{45}H_{82}O_{13}P$	-5.1
883.539	PI 38:5	$C_{47}H_{80}O_{13}P$	5.4
885.555	PI 38:4	$C_{47}H_{82}O_{13}P$	-5.5
891.723	TG 52:3	$C_{55}H_{100}O_6Cl$	1.8

917.739	TG 54:4	$C_{57}H_{102}O_6Cl$	2.1
---------	---------	----------------------	-----

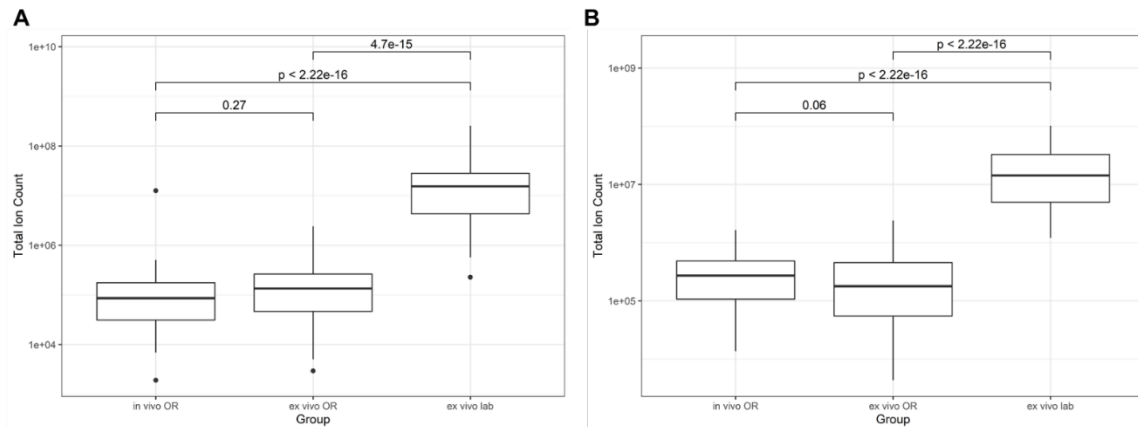


Figure C4.5: Comparison of total ion count values obtained from MasSpec Pen analyses in the operating room and laboratory setting for (A) breast and (B) thyroid specimens.

Total ion count values are provided as NL values from Orbitrap readings. Of note, the same Q Exactive™ Hybrid Quadrupole-Orbitrap™ mass spectrometer (Thermo Fisher Scientific) was used in the laboratory and in the OR. Data obtained *ex vivo* from frozen-thawed specimens in the laboratory (*ex vivo lab*) has been previously published (Zhang et. al STM 2017) (17). For breast, a total of 42 *in vivo* OR mass spectra, 31 *ex vivo* OR mass spectra, and 45 *ex vivo* laboratory mass spectra were considered. For thyroid, a total of 120 *in vivo* OR mass spectra, 71 *ex vivo* OR mass spectra, and 56 *ex vivo* laboratory mass spectra were considered. A Wilcoxon test was used to calculate p-values and are provided in the figure, showing significant differences in the total ion counts between intraoperative data and laboratory data but not between intraoperative *in vivo* and *ex vivo* mass spectra.

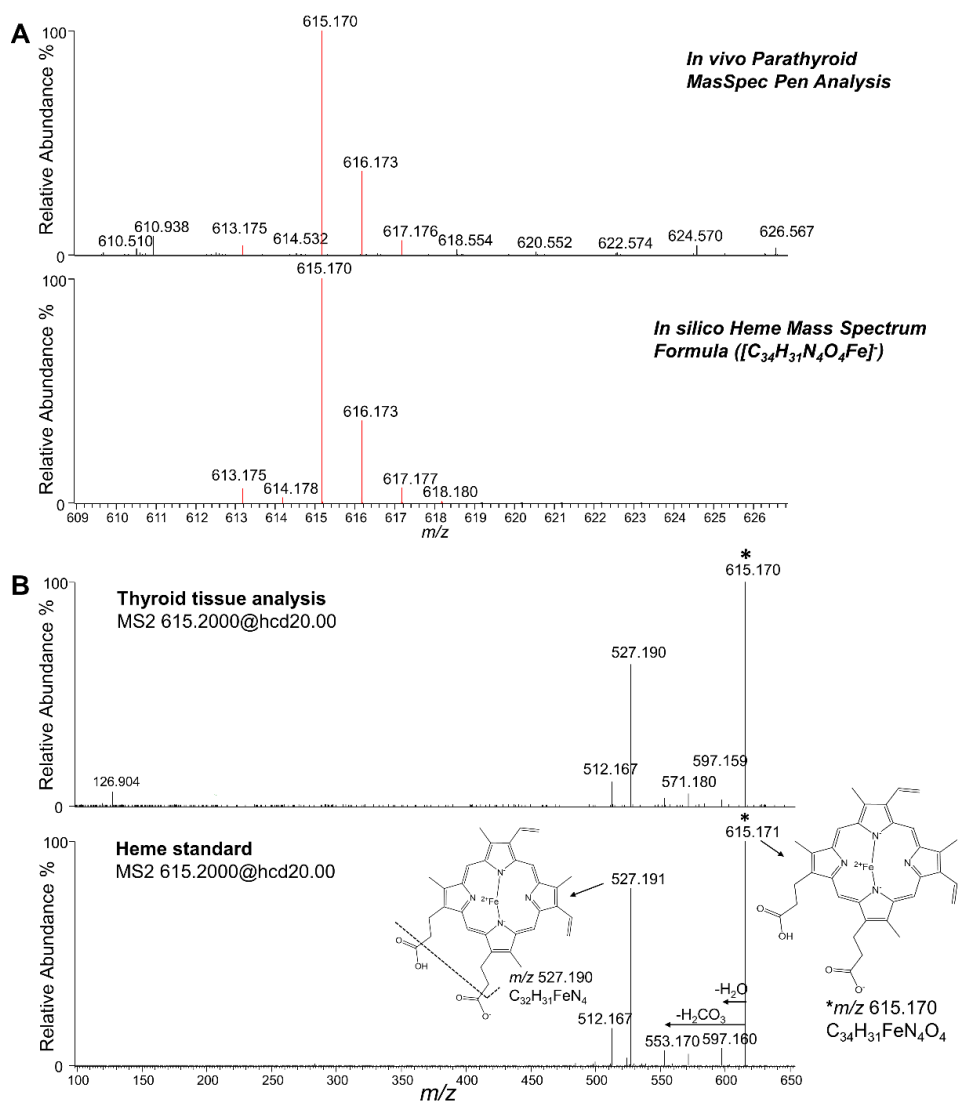


Figure C4.6: (A) Isotopic distribution of heme (on the top) observed *in vivo* from MasSpec Pen analysis of parathyroid tissue during a parathyroidectomy procedure for primary hyperparathyroidism (PT0012) and theoretical mass spectrum of heme (at the bottom) in negative ion mode using isotope simulation function available in Thermo XCalibur Qual Browser.

Tandem mass spectrum of  $m/z$  615.170 (on the top) from a thyroid tissue analysis by the MasSpec Pen and tandem mass spectrum of  $m/z$  615.171 (at the bottom) from heme standard by electrospray ionization (ESI) under higher-energy collisional dissociation (HCD) mode.

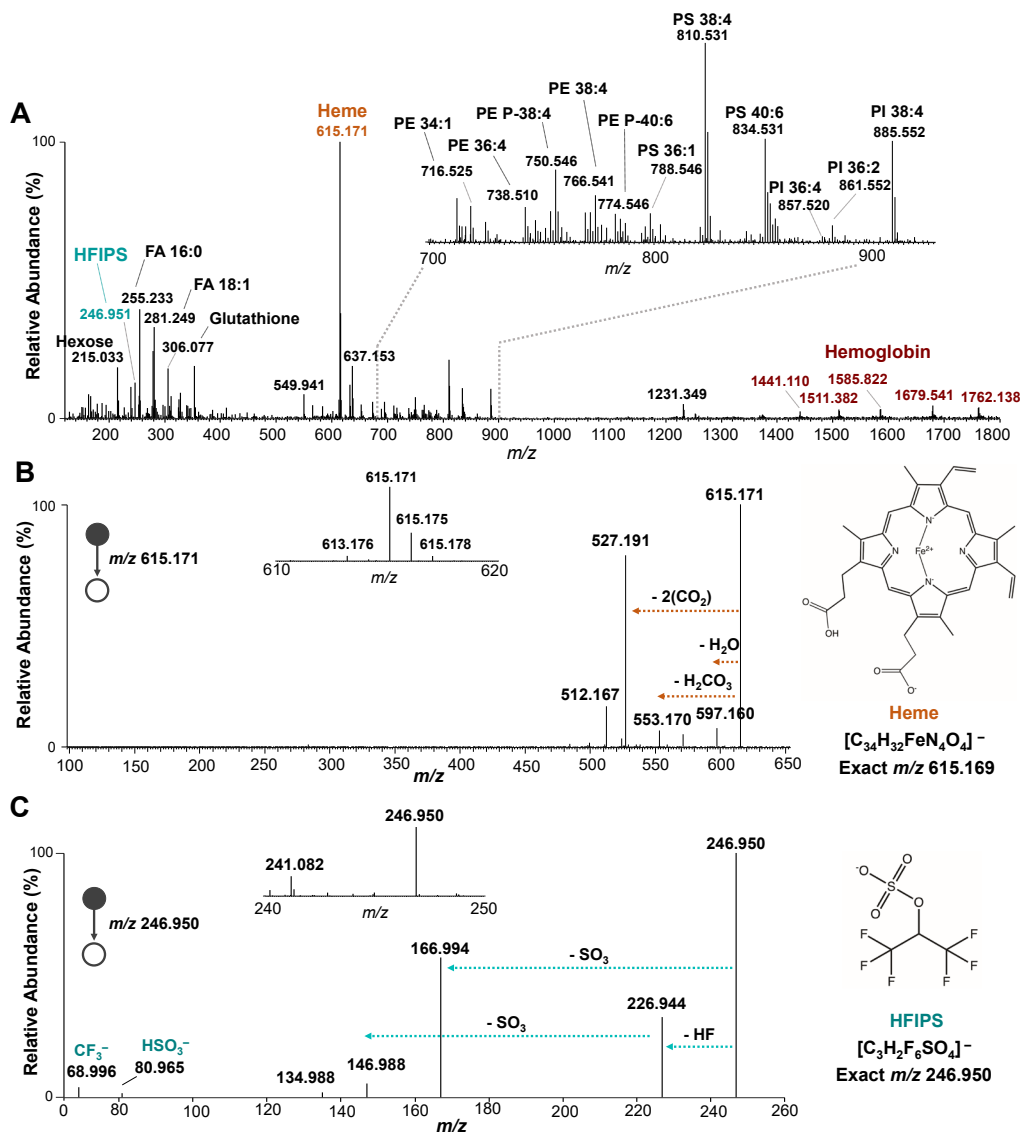


Figure C4.7: Detection and identification of heme and hexafluoroisopropyl sulfonate.

(A) *In vivo* mass spectrum obtained from MasSpec Pen analysis of a normal parathyroid specimen during parathyroidectomy procedure for primary hyperparathyroidism (PT0020). Despite the detection of heme at the highest relative abundance (100%) and the detection of multiply charged hemoglobin peaks, various metabolite and lipid species were still detected and identified, as annotated for selected ions in the mass spectra. (B) Identification of  $m/z$  615.171 as deprotonated heme by MS<sup>2</sup> experiment performed during analysis of a thyroid tissue by the MasSpec Pen. (C) Identification of  $m/z$  246.950 as deprotonated hexafluoroisopropyl sulfonate (HFIPS) by MS<sup>2</sup> performed on tissue.

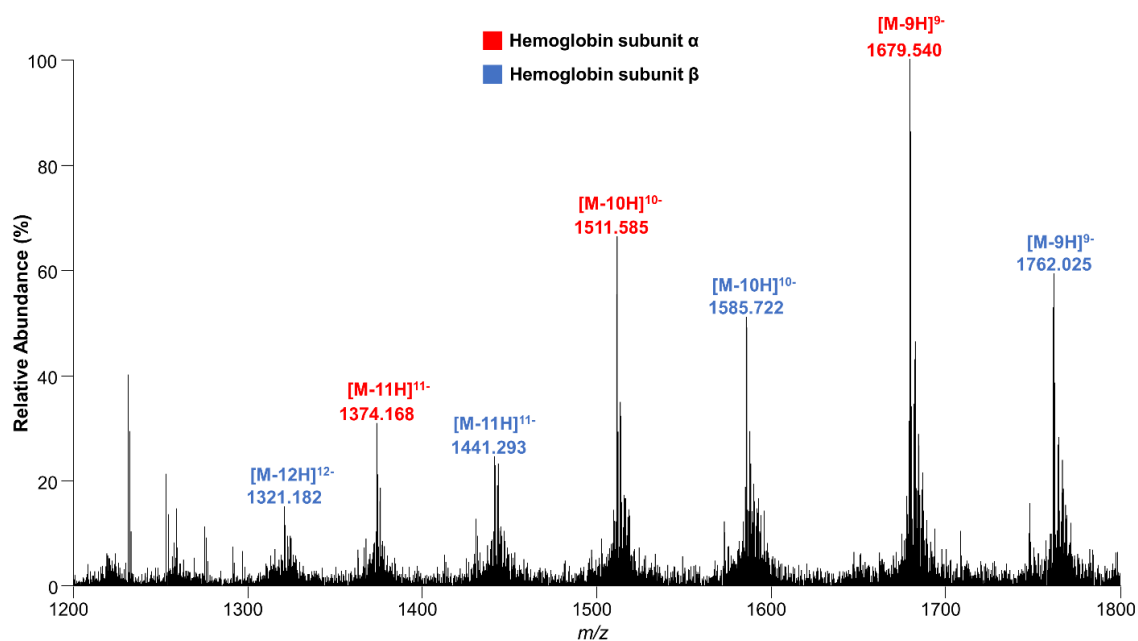


Figure C4.8: Multiply charged peaks detected from *in vivo* analysis of thyroid tissue using MasSpec Pen during a right hemithyroidectomy procedure of an indeterminate nodule (TH0025) were tentatively assigned as hemoglobin  $\alpha$  and hemoglobin  $\beta$  subunits.

Note that monoisotopic masses of human hemoglobin  $\alpha$  and hemoglobin  $\beta$  subunits (without the initiator methionine) are 15116 and 15857, respectively.

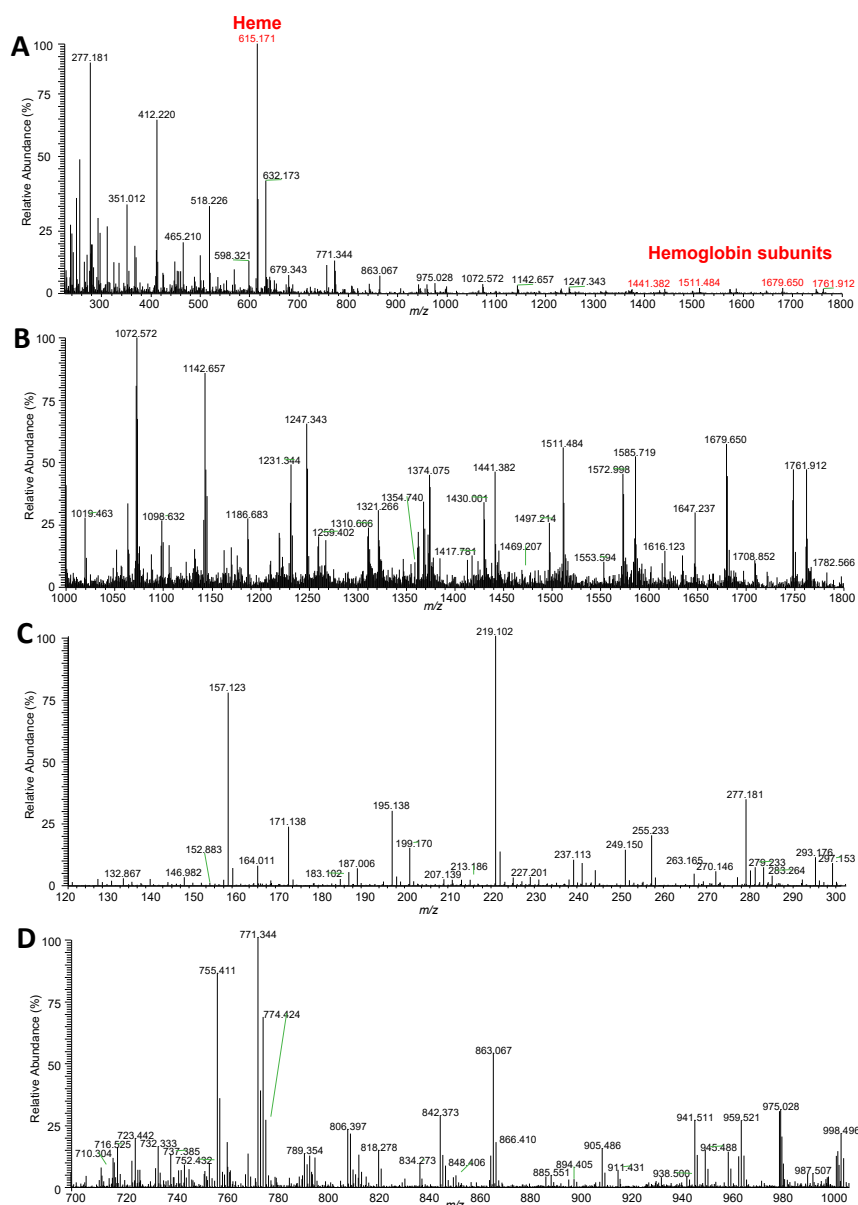


Figure C4.9: Negative ion mode mass spectra obtained of 10  $\mu\text{L}$  of human blood deposited onto a glass slide and analyzed with the MasSpec Pen. (A)  $m/z$  220-1800 range showing detection of heme and hemoglobin peaks, (B) zoom in  $m/z$  1000-1800 showing detecting of multiply charged hemoglobin peaks, (C) zoom in  $m/z$  120-300 where metabolites and fatty acids are normally detected, (D) zoom in  $m/z$  700-1000 where complex lipids are often detected. **Note:** These experiments were performed in the lab with a HF Q Exactive Orbitrap mass spectrometer and used the same experimental conditions for OR tissue analysis.

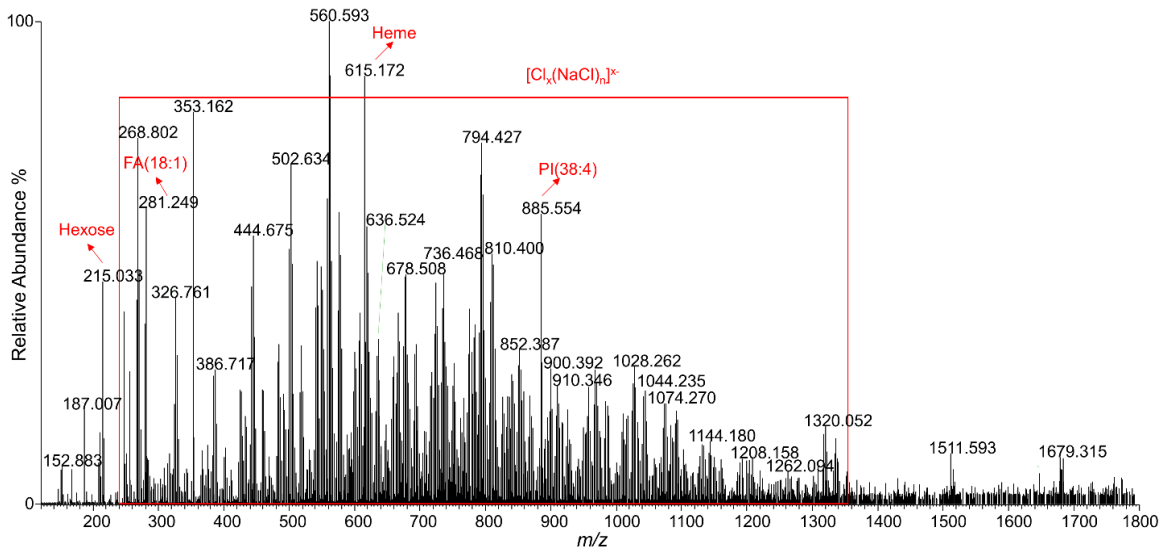


Figure C4.10: MasSpec Pen *in vivo* analysis of a thyroid nodule during a total thyroidectomy and parathyroidectomy for a thyroid neoplasm and primary hyperparathyroidism (TH0024), showing interferences in the mass spectrum resulting from saline irrigation.

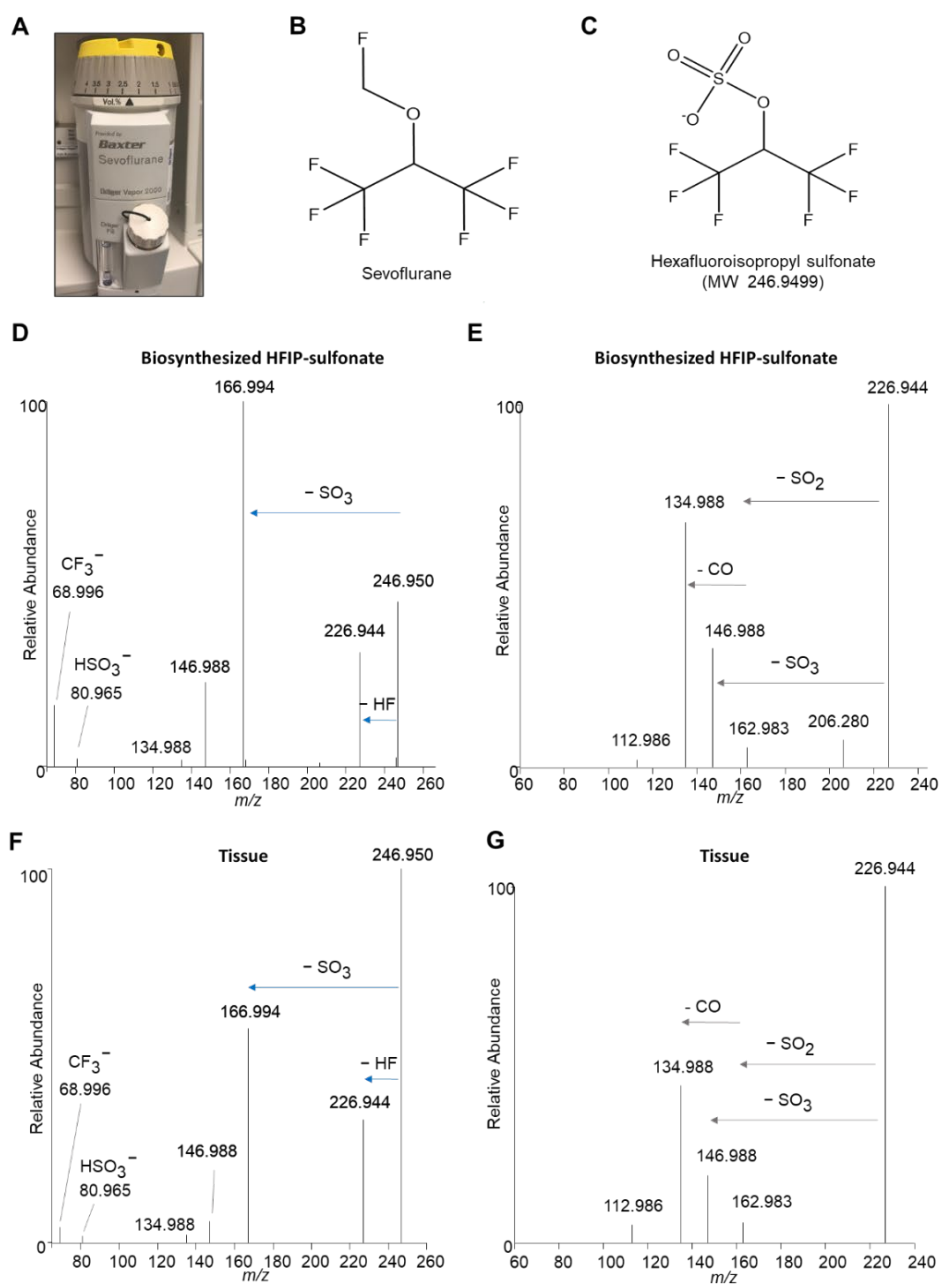


Figure C4.11: Identification of  $m/z$  246.950 as hexafluoroisopropyl sulfonate (HFIPS).

(A) Sevoflurane tank used for anesthesia during the surgeries described in this study. (B) Structure of sevoflurane. (C) Structure of HFIPS. MS<sup>2</sup> (D) and MS<sup>3</sup> (E) of biosynthesized HFIPS. MS<sup>2</sup> (F) and MS<sup>3</sup> (G) of HFIPS detected from endometriosis tissue by DESI-MS.

## APPENDIX E: SUPPLEMENTARY MATERIAL FOR CHAPTER 6

Table E6.1: Demographic and detailed clinical information for the 26 symptomatic negative patients

Original Class	ID#	Gender	Age	RT-PCR (Observed)	Prediction (Classifier 1)	Hospitalization Days	ICU days	Mechanical Ventilation Days	Outcome
Symptomatic Negative	30	F	35	NEG	POS	2	0	0	Discharged
Symptomatic Negative	34	M	76	NEG	POS	15	13	11	Death
Symptomatic Negative	36	M	73	NEG	POS	3	0	0	Discharged
Symptomatic Negative	45	F	50	NEG	POS	13	0	0	Discharged
Symptomatic Negative	68	F	76	NEG	POS	3	0	0	Discharged
Symptomatic Negative	71	F	49	NEG	POS	4	0	0	Discharged
Symptomatic Negative	92	F	69	NEG	POS	29	19	19	Death
Symptomatic Negative	93	M	68	NEG	POS	7	0	0	Discharged
Symptomatic Negative	96	M	76	NEG	POS	5	0	0	Discharged
Symptomatic Negative	97	M	67	NEG	POS	5	0	0	Discharged
Symptomatic Negative	101	F	27	NEG	POS	1	0	0	Discharged
Symptomatic Negative	108	F	60	NEG	POS	9	0	0	Discharged
Symptomatic Negative	111	M	50	NEG	POS	2	0	0	Discharged
Symptomatic Negative	116	F	78	NEG	NEG	8	0	0	Discharged
Symptomatic Negative	149	M	66	NEG	POS	7	0	0	Discharged
Symptomatic Negative	151	M	47	NEG	POS	7	0	0	Discharged
Symptomatic Negative	152	M	66	NEG	POS	4	0	0	Death
Symptomatic Negative	156	F	81	NEG	NEG	3	0	0	Discharged
Symptomatic Negative	193	F	57	NEG	POS	6	0	0	Discharged
Symptomatic Negative	240	M	68	NEG	NEG	10	0	0	Discharged
Symptomatic Negative	242	M	28	NEG	NEG	3	0	0	Discharged
Symptomatic Negative	263	M	71	NEG	POS	6	0	0	Discharged
Symptomatic Negative	264	M	26	NEG	POS	2	0	0	Discharged
Symptomatic Negative	265	M	83	NEG	NEG	3	0	0	Discharged
Symptomatic Negative	266	M	84	NEG	POS	2	0	0	Discharged
Symptomatic Negative	267	F	52	NEG	NEG	64	0	0	Discharged

Original Class	ID#	Chest CT Suggestive of viral infection	Chest CT Findings					
			Ground-Glass Opacity	Consolidations	Crazy Paving Appearance	Reticular Pattern	Presence of Pulmonary Commitment	% of Pulmonary Commitment
Symptomatic Negative	30	YES	YES	NO	NO	NO	YES	25-50
Symptomatic Negative	34	YES	YES	NO	NO	NO	YES	50
Symptomatic Negative	36	YES	YES	YES	YES	YES	YES	20-50
Symptomatic Negative	45	YES	YES	YES	YES	YES	YES	50
Symptomatic Negative	68	NO	NO	NO	NO	NO	NO	0
Symptomatic Negative	71	YES	YES	NO	NO	NO	YES	50
Symptomatic Negative	92	YES	YES	NO	NO	NO	YES	30-50
Symptomatic Negative	93	YES	YES	YES	NO	NO	YES	60
Symptomatic Negative	96	YES	YES	NO	YES	YES	YES	20-50
Symptomatic Negative	97	YES	YES	YES	YES	YES	YES	30
Symptomatic Negative	101	YES	YES	NO	NO	NO	NO	0
Symptomatic Negative	108	YES	YES	YES	YES	YES	YES	50
Symptomatic Negative	111	YES	YES	NO	NO	NO	YES	50-80
Symptomatic Negative	116	NO	NO	NO	NO	NO	NO	0
Symptomatic Negative	149	YES	YES	NO	NO	NO	YES	50-70
Symptomatic Negative	151	YES	YES	YES	NO	NO	YES	50-80
Symptomatic Negative	152	YES	YES	YES	NO	NO	YES	50
Symptomatic Negative	156	NO	NO	NO	NO	NO	NO	-
Symptomatic Negative	193	YES	YES	YES	NO	NO	YES	50-80
Symptomatic Negative	240	NO	NO	NO	NO	NO	NO	0
Symptomatic Negative	242	NO	NO	NO	NO	NO	NO	0
Symptomatic Negative	263	NO	NO	YES	NO	NO	NO	0
Symptomatic Negative	264	YES	YES	NO	NO	NO	NO	0
Symptomatic Negative	265	NO	NO	NO	NO	NO	NO	0
Symptomatic Negative	266	NO	NO	NO	NO	NO	NO	0
Symptomatic Negative	267	YES	YES	YES	YES	YES	YES	20-50

Original Class	ID#	Reported Symptoms										Other Information		
		Fever	Cough	Myalgia	Sore Throat	Headache	Coryza	Dyspnea	Loss of smell/taste	O2 Saturation < 95%	COPD presence	Smoker or Ex-smoker	Asthma	
Symptomatic Negative	30	YES	YES	NO	NO	NO	NO	NO	NO	NO	YES	NO	NO	NO
Symptomatic Negative	34	NO	YES	NO	YES	NO	NO	NO	NO	NO	NO	NO	NO	NO
Symptomatic Negative	36	YES	NO	NO	NO	NO	NO	NO	NO	YES	NO	NO	NO	NO
Symptomatic Negative	45	NO	NO	YES	NO	NO	NO	NO	NO	NO	NO	NO	NO	NO
Symptomatic Negative	68	YES	NO	NO	NO	NO	NO	YES	NO	YES	NO	NO	NO	NO
Symptomatic Negative	71	YES	NO	NO	YES	NO	NO	YES	NO	YES	NO	NO	NO	NO
Symptomatic Negative	92	NO	NO	NO	NO	NO	NO	NO	NO	NO	NO	NO	NO	NO
Symptomatic Negative	93	NO	YES	NO	NO	NO	NO	YES	NO	NO	NO	NO	NO	NO
Symptomatic Negative	96	NO	YES	NO	NO	NO	NO	NO	NO	NO	NO	YES	YES	NO
Symptomatic Negative	97	YES	NO	NO	YES	NO	NO	NO	NO	NO	NO	NO	NO	NO
Symptomatic Negative	101	YES	NO	NO	NO	NO	NO	NO	NO	NO	NO	NO	NO	YES
Symptomatic Negative	108	NO	YES	NO	NO	NO	NO	NO	NO	YES	NO	NO	NO	NO
Symptomatic Negative	111	NO	YES	NO	NO	NO	NO	YES	NO	YES	NO	NO	NO	NO
Symptomatic Negative	116	NO	NO	NO	NO	NO	NO	YES	NO	NO	NO	NO	NO	NO
Symptomatic Negative	149	NO	NO	NO	YES	NO	NO	NO	NO	NO	NO	NO	NO	NO
Symptomatic Negative	151	NO	YES	NO	YES	NO	YES	YES	NO	YES	NO	NO	NO	NO
Symptomatic Negative	152	YES	NO	NO	NO	NO	NO	YES	NO	NO	NO	NO	YES	NO
Symptomatic Negative	156	NO	YES	NO	YES	NO	NO	NO	NO	NO	NO	NO	NO	YES
Symptomatic Negative	193	YES	NO	YES	NO	NO	NO	YES	NO	YES	NO	NO	NO	NO
Symptomatic Negative	240	YES	YES	NO	NO	NO	YES	YES	NO	NO	NO	NO	YES	NO
Symptomatic Negative	242	NO	YES	NO	YES	NO	YES	NO	NO	NO	NO	NO	NO	NO
Symptomatic Negative	263	YES	YES	NO	NO	NO	NO	YES	NO	NO	NO	NO	NO	NO
Symptomatic Negative	264	YES	YES	NO	YES	NO	NO	YES	NO	NO	NO	NO	NO	NO
Symptomatic Negative	265	YES	YES	NO	NO	NO	NO	NO	NO	NO	NO	NO	NO	NO
Symptomatic Negative	266	YES	YES	NO	NO	NO	NO	NO	NO	NO	NO	NO	NO	NO
Symptomatic Negative	267	NO	YES	NO	NO	NO	NO	YES	NO	NO	NO	NO	NO	NO

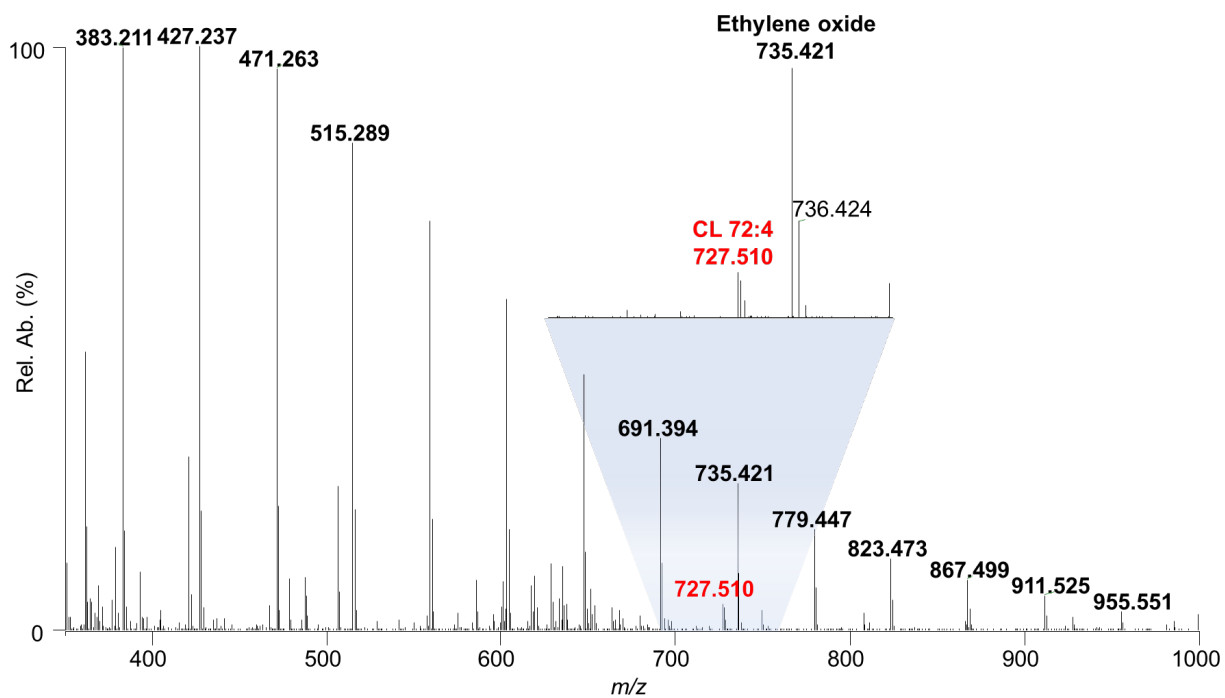


Figure E6.1: Representative mass spectrum from the MasSpec Pen-ESI MS analysis of a nylon flock swab dipped in 20 ppm CL 72:4 ( $m/z$  727.510) lipid standard.

The doubly charged CL species are labeled in red while the repeating units of ethylene oxide are labeled in black.

Table E6.2: Observed  $m/z$ , mass error, and identification for the features selected by Lasso for Classifier 1 and 2.

Identifications are based on high mass accuracy and/or tandem MS measurements.

Lasso Feature	Observed $m/z$	Theoretical $m/z$	Mass Error	Attribution	Formula
415.23	415.226	415.2255	1.204	LPA O-18:4	C21H37O6P [M-H]-
417.24	417.241	417.2412	- 0.479	LPA O-18:3	C21H39O6P [M-H]-
418.24	418.244	418.2445	- 1.195	Isotope of LPA O-18:3, $m/z$ 417.241	C21H39O6P [M-H]-
422	421.997	-	-	Unidentified	-
446.34	446.336	-	-	Isotope of $m/z$ 445.333, unidentified	-
450.87	450.874	-	-	Unidentified	-
467.32	467.316	467.3143	3.638	LPA O-20:0	
506.32	506.324	506.3252	- 2.370	LPE 20:1	C25H50NO7P [M-H]-
508.34	508.341	508.3409	0.197	LPE 20:0	C25H52NO7P [M-H]-
509.34	509.344	509.3442	- 0.393	Isotope of LPE 20:0	C25H52NO7P [M-H]-
512.28	512.283	512.2864	-	Unidentified	-
522.28	522.284	522.2838	0.383	LPS 18:1	C24H46NO9P [M-H]-
556.32	556.318	556.3176	0.719	LPC 18:1	C26H52NO7P
600.51	600.514	600.5128	1.998	Cer 36:1	C36H71NO3 [M+Cl]-
618.52	618.524	618.5234	0.970	Cer 36:0	C36H73NO4 [M+Cl]-
619.29	619.289	619.2889	0.161	LPI 20:4	C29H49O12P [M-H]-
624.52	624.522	-	-	Unidentified	-
629.49	629.492	629.4917	0.477	DG 34:1	C37H70O5 [M+Cl]-
635.48	635.482	635.4812	1.259	DG O-36:5	C39H68O4 [M+Cl]-
655.51	655.508	655.5074	0.915	DG 36:2	C39H72O5 [M+Cl]-
679.51	679.507	679.5074	- 0.589	DG O-38:5	C41H72O5 [M+Cl]-
680.58	680.576	680.5754	0.882	Cer 42:3	C42H79NO3 [M+Cl]-
682.59	682.591	682.5911	- 0.147	Cer 42:2	C42H81NO3 [M+Cl]-

683.59	683.594	683.5944	- 0.585	Isotope of m/z 682.591, Cer 42:2	C42H81NO3 [M+Cl]-
684.59	684.588	684.5881	- 0.146	Isotope of m/z 682.591, Cer 42:3	C42H81NO4 [M+Cl]-
694.59	694.592	694.5911	1.296	Cer 43:3	C43H81NO3 [M+Cl]-
697.61	697.61	-	-	Unidentified	-
700.59	700.587	700.5886	- 2.284	Cer 44:5	C44H79NO5 [M+Cl]-
703.51	703.507	703.5074	- 0.569	DG 40:6	C43H72O5 [M+Cl]-
703.6	703.603	-	-	Unidentified	-
710.62	710.623	710.6224	0.844	Cer 44:2	C44H85NO3 [M+Cl]-
714.51	714.508	714.5079	0.140	PE 34:2	C39H74NO8P [M-H]-
718.61	718.613	-	-	Unidentified	-
723.98	723.981	723.9805	0.691	Isotope of m/z 723.479, CL 72:8	C81H142O17P2 [M- 2H]2-
725.53	725.533	725.5362	- 4.411	DG 42:7	C45H74O7 [M-H]-
734.53	734.534	734.5342	- 0.272	PE 34:0	C39H78NO9P [M-H]-
737.54	737.537	737.5370	0.000	SM 34:1	C39H79N2O6P [M+Cl]-
746.51	746.513	746.5130	0.000	PE O-38:7	C43H74NO7P [M-H]-
750.53	750.528	750.5292	- 1.599	HexCer 34:1	C49H77NO9 [M+Cl]-
754.55	754.554	754.5523	2.253	PC O-32:0	C40H82NO7P [M+Cl]-
761.53	761.534	761.532	2.626	Isotope of m/z 760.529, PE O- 39:7	C44H76NO7P [M-H]-
769.54	769.535	769.5389	-	Unidentified	-
770.57	770.570	770.5705	- 0.649	PE 38:2	C43H82NO8P [M- H]-
771.57	771.573	771.574	- 1.296	Isotope of m/z 770.570, PE 38:2	C43H82NO8P [M- H]-
773.53	773.534	773.5338	0.259	PG 36:2	C42H79O10P [M-H]-
776.56	776.559	776.5600	- 1.288	PE O-40:6	C45H80NO7P [M-H]-
794.51	794.508	794.5108	- 3.524	PE 36:2	C41H78NO9P [M+Cl]-

794.53	794.529	-	-	Unidentified	-
808.5	808.504	808.5054	- 1.732	PE O-40:8	C45H76NO7P [M+Cl]-
845.61	845.610	845.611	- 1.183	Isotope of m/z 844.607, PS 40:1	C46H88NO10P [M- H]-
847.53	847.529	847.5283	0.826	PA 48:12	C51H77O8P [M-H]-
858.72	858.723	-	-	Unidentified	-
860.64	860.638	860.6388	- 0.930	HexCer 42:2	C48H91NO9 [M+Cl]-
869.57	869.569	869.5662	3.220	Isotope of m/z 868.563, PC 40:6	C48H84NO8P [M+Cl]-
872.64	872.638	872.6386	- 0.688	PS 42:1	C48H92NO10P [M- H]-
880.52	880.519	880.5195	- 0.568	HexCer 32:3	C44H79NO14 [M+Cl]-
910.55	914.584	914.5845	- 0.547	Isotope of m/z 913.585, PI 40:4	C49H87O13P [M-H]-
976.62	976.619	976.6204	- 1.434	PE 50:9	C55H92NO9P [M+Cl]-

## Bibliography

### CHAPTER 1

1. Jannetto, P. J.; Fitzgerald, R. L., Effective Use of Mass Spectrometry in the Clinical Laboratory. *Clin Chem* **2016**, *62* (1), 92-8.
2. Banerjee, S., Empowering Clinical Diagnostics with Mass Spectrometry. *ACS Omega* **2020**, *5* (5), 2041-2048.
3. Ombrone, D.; Giocaliere, E.; Forni, G.; Malvagia, S.; la Marca, G., Expanded newborn screening by mass spectrometry: New tests, future perspectives. *Mass Spectrom Rev* **2016**, *35* (1), 71-84.
4. Ismail, I. T.; Showalter, M. R.; Fiehn, O., Inborn Errors of Metabolism in the Era of Untargeted Metabolomics and Lipidomics. *Metabolites* **2019**, *9* (10).
5. Tsuchida, S.; Umemura, H.; Nakayama, T., Current Status of Matrix-Assisted Laser Desorption/Ionization-Time-of-Flight Mass Spectrometry (MALDI-TOF MS) in Clinical Diagnostic Microbiology. *Molecules* **2020**, *25* (20).
6. Hou, T. Y.; Chiang-Ni, C.; Teng, S. H., Current status of MALDI-TOF mass spectrometry in clinical microbiology. *J Food Drug Anal* **2019**, *27* (2), 404-414.
7. Kostrzewa, M., Application of the MALDI Biotyper to clinical microbiology: progress and potential. *Expert Rev Proteomics* **2018**, *15* (3), 193-202.
8. Takats, Z.; Wiseman, J. M.; Gologan, B.; Cooks, R. G., Mass spectrometry sampling under ambient conditions with desorption electrospray ionization. *Science* **2004**, *306* (5695), 471-3.
9. Garg, U.; Zhang, Y. V., Mass Spectrometry in Clinical Laboratory: Applications in Therapeutic Drug Monitoring and Toxicology. *Methods Mol Biol* **2016**, *1383*, 1-10.
10. Ifa, D. R.; Eberlin, L. S., Ambient Ionization Mass Spectrometry for Cancer Diagnosis and Surgical Margin Evaluation. *Clin Chem* **2016**, *62* (1), 111-23.
11. Feider, C. L.; Krieger, A.; DeHoog, R. J.; Eberlin, L. S., Ambient Ionization Mass Spectrometry: Recent Developments and Applications. *Anal Chem* **2019**, *91* (7), 4266-4290.
12. Zhang, J.; Sans, M.; Garza, K. Y.; Eberlin, L. S., Mass Spectrometry Technologies to Advance Care for Cancer Patients in Clinical and Intraoperative Use. *Mass Spectrom Rev* **2020**.
13. Bardin, E. E.; Cameron, S. J. S.; Perdones-Montero, A.; Hardiman, K.; Bolt, F.; Alton, E.; Bush, A.; Davies, J. C.; Takats, Z., Metabolic Phenotyping and Strain Characterisation of *Pseudomonas aeruginosa* Isolates from Cystic Fibrosis Patients Using Rapid Evaporative Ionisation Mass Spectrometry. *Sci Rep* **2018**, *8* (1), 10952.
14. Pirro, V.; Llor, R. S.; Jarmusch, A. K.; Alfaro, C. M.; Cohen-Gadol, A. A.; Hattab, E. M.; Cooks, R. G., Analysis of human gliomas by swab touch spray-mass spectrometry: applications to intraoperative assessment of surgical margins and presence of oncometabolites. *Analyst* **2017**, *142* (21), 4058-4066.

15. Garza, K. Y.; Feider, C. L.; Klein, D. R.; Rosenberg, J. A.; Brodbelt, J. S.; Eberlin, L. S., Desorption Electrospray Ionization Mass Spectrometry Imaging of Proteins Directly from Biological Tissue Sections. *Anal Chem* **2018**, *90* (13), 7785-7789.
16. Towers, M. W.; Karancsi, T.; Jones, E. A.; Pringle, S. D.; Claude, E., Optimised Desorption Electrospray Ionisation Mass Spectrometry Imaging (DESI-MSI) for the Analysis of Proteins/Peptides Directly from Tissue Sections on a Travelling Wave Ion Mobility Q-ToF. *J Am Soc Mass Spectrom* **2018**.
17. Eberlin, L. S.; Ferreira, C. R.; Dill, A. L.; Ifa, D. R.; Cheng, L.; Cooks, R. G., Nondestructive, histologically compatible tissue imaging by desorption electrospray ionization mass spectrometry. *Chembiochem* **2011**, *12* (14), 2129-32.
18. Porcari, A. M.; Zhang, J. L.; Garza, K. Y.; Rodrigues-Peres, R. M.; Lin, J. Q.; Young, J. H.; Tibshirani, R.; Nagi, C.; Paiva, G. R.; Carter, S. A.; Sarian, L. O.; Eberlin, M. N.; Eberlin, L. S., Multicenter Study Using Desorption-Electrospray-Ionization-Mass-Spectrometry Imaging for Breast-Cancer Diagnosis. *Analytical Chemistry* **2018**, *90* (19), 11324-11332.
19. Guenther, S.; Muirhead, L. J.; Speller, A. V.; Golf, O.; Strittmatter, N.; Ramakrishnan, R.; Goldin, R. D.; Jones, E.; Veselkov, K.; Nicholson, J.; Darzi, A.; Takats, Z., Spatially resolved metabolic phenotyping of breast cancer by desorption electrospray ionization mass spectrometry. *Cancer Res* **2015**, *75* (9), 1828-37.
20. Calligaris, D.; Caragacianu, D.; Liu, X.; Norton, I.; Thompson, C. J.; Richardson, A. L.; Golshan, M.; Easterling, M. L.; Santagata, S.; Dillon, D. A.; Jolesz, F. A.; Agar, N. Y., Application of desorption electrospray ionization mass spectrometry imaging in breast cancer margin analysis. *Proc Natl Acad Sci U S A* **2014**, *111* (42), 15184-9.
21. Doria, M. L.; McKenzie, J. S.; Mroz, A.; Phelps, D. L.; Speller, A.; Rosini, F.; Strittmatter, N.; Golf, O.; Veselkov, K.; Brown, R.; Ghaem-Maghami, S.; Takats, Z., Epithelial ovarian carcinoma diagnosis by desorption electrospray ionization mass spectrometry imaging. *Scientific Reports* **2016**, *6*, 11.
22. Sans, M.; Gharpure, K.; Tibshirani, R.; Zhang, J.; Liang, L.; Liu, J.; Young, J. H.; Dood, R. L.; Sood, A. K.; Eberlin, L. S., Metabolic Markers and Statistical Prediction of Serous Ovarian Cancer Aggressiveness by Ambient Ionization Mass Spectrometry Imaging. *Cancer Res* **2017**, *77* (11), 2903-2913.
23. Zhang, J.; Feider, C. L.; Nagi, C.; Yu, W.; Carter, S. A.; Suliburk, J.; Cao, H. S. T.; Eberlin, L. S., Detection of Metastatic Breast and Thyroid Cancer in Lymph Nodes by Desorption Electrospray Ionization Mass Spectrometry Imaging. *J. Am. Soc. Mass Spectrom.* **2017**, *28* (6), 1166-1174.
24. DeHoog, R. J.; Zhang, J.; Alore, E.; Lin, J. Q.; Yu, W.; Woody, S.; Almendariz, C.; Lin, M.; Engelsman, A. F.; Sidhu, S. B.; Tibshirani, R.; Suliburk, J.; Eberlin, L. S., Preoperative metabolic classification of thyroid nodules using mass spectrometry imaging of fine-needle aspiration biopsies. *Proc Natl Acad Sci U S A* **2019**, *116* (43), 21401-21408.
25. Cooks, R. G.; Alfaro, C.; Jarmusch, A.; Pirro, V.; Baird, Z.; Hattab, E.; Cohen-Gadol, A. In *Intrasurgical diagnosis of human brain tumor tissue and surgical margin characterization by DESI-MS*, American Chemical Society: 2017; pp ANYL-284.

26. Eberlin, L. S.; Dill, A. L.; Golby, A. J.; Ligon, K. L.; Wiseman, J. M.; Cooks, R. G.; Agar, N. Y., Discrimination of human astrocytoma subtypes by lipid analysis using desorption electrospray ionization imaging mass spectrometry. *Angew Chem Int Ed Engl* **2010**, *49* (34), 5953-6.
27. Jarmusch, A. K.; Pirro, V.; Baird, Z.; Hattab, E. M.; Cohen-Gadol, A. A.; Cooks, R. G., Lipid and metabolite profiles of human brain tumors by desorption electrospray ionization-MS. *Proc. Natl. Acad. Sci. U. S. A.* **2016**, *113* (6), 1486-1491.
28. Banerjee, S.; Zare, R. N.; Tibshirani, R. J.; Kunder, C. A.; Nolley, R.; Fan, R.; Brooks, J. D.; Sonn, G. A., Diagnosis of prostate cancer by desorption electrospray ionization mass spectrometric imaging of small metabolites and lipids. *Proc. Natl. Acad. Sci. U. S. A.* **2017**, *114* (13), 3334-3339.
29. Kerian, K. S.; Jarmusch, A. K.; Pirro, V.; Koch, M. O.; Masterson, T. A.; Cheng, L.; Cooks, R. G., Differentiation of prostate cancer from normal tissue in radical prostatectomy specimens by desorption electrospray ionization and touch spray ionization mass spectrometry. *Analyst* **2015**, *140* (4), 1090-1098.
30. Eberlin, L. S.; Dill, A. L.; Costa, A. B.; Ifa, D. R.; Cheng, L.; Masterson, T.; Koch, M.; Ratliff, T. L.; Cooks, R. G., Cholesterol sulfate imaging in human prostate cancer tissue by desorption electrospray ionization mass spectrometry. *Anal Chem* **2010**, *82* (9), 3430-4.
31. Eberlin, L. S.; Tibshirani, R. J.; Zhang, J.; Longacre, T. A.; Berry, G. J.; Bingham, D. B.; Norton, J. A.; Zare, R. N.; Poultides, G. A., Molecular assessment of surgical-resection margins of gastric cancer by mass-spectrometric imaging. *Proc Natl Acad Sci U S A* **2014**, *111* (7), 2436-41.
32. Schafer, K. C.; Denes, J.; Albrecht, K.; Szaniszló, T.; Balog, J.; Skoumal, R.; Katona, M.; Toth, M.; Balogh, L.; Takats, Z., In vivo, in situ tissue analysis using rapid evaporative ionization mass spectrometry. *Angew Chem Int Ed Engl* **2009**, *48* (44), 8240-2.
33. Balog, J.; Sasi-Szabo, L.; Kinross, J.; Lewis, M. R.; Muirhead, L. J.; Veselkov, K.; Mirnezami, R.; Dezso, B.; Damjanovich, L.; Darzi, A.; Nicholson, J. K.; Takats, Z., Intraoperative tissue identification using rapid evaporative ionization mass spectrometry. *Sci Transl Med* **2013**, *5* (194), 194ra93.
34. Zhang, J.; Rector, J.; Lin, J. Q.; Young, J. H.; Sans, M.; Katta, N.; Giese, N.; Yu, W.; Nagi, C.; Suliburk, J.; Liu, J.; Bensussan, A.; DeHoog, R. J.; Garza, K. Y.; Ludolph, B.; Sorace, A. G.; Syed, A.; Zahedivash, A.; Milner, T. E.; Eberlin, L. S., Nondestructive tissue analysis for ex vivo and in vivo cancer diagnosis using a handheld mass spectrometry system. *Sci Transl Med* **2017**, *9* (406).
35. Keating, M. F.; Zhang, J.; Feider, C. L.; Retailleau, S.; Reid, R.; Antaris, A.; Hart, B.; Tan, G.; Milner, T. E.; Miller, K.; Eberlin, L. S., Integrating the MasSpec Pen to the da Vinci Surgical System for In Vivo Tissue Analysis during a Robotic Assisted Porcine Surgery. *Anal Chem* **2020**, *92* (17), 11535-11542.
36. St John, E. R.; Balog, J.; McKenzie, J. S.; Rossi, M.; Covington, A.; Muirhead, L.; Bodai, Z.; Rosini, F.; Speller, A. V. M.; Shousha, S.; Ramakrishnan, R.; Darzi, A.; Takats, Z.; Leff, D. R., Rapid evaporative ionisation mass spectrometry of electrosurgical vapours for the identification of

breast pathology: towards an intelligent knife for breast cancer surgery. *Breast Cancer Res* **2017**, *19* (1), 59.

37. Woolman, M.; Ferry, I.; Kuzan-Fischer, C. M.; Wu, M.; Zou, J.; Kiyota, T.; Isik, S.; Dara, D.; Aman, A.; Das, S.; Taylor, M. D.; Rutka, J. T.; Ginsberg, H. J.; Zarrine-Afsar, A., Rapid determination of medulloblastoma subgroup affiliation with mass spectrometry using a handheld picosecond infrared laser desorption probe. *Chem. Sci.* **2017**, *8* (9), 6508-6519.

38. Phelps, D. L.; Balog, J.; Gildea, L. F.; Bodai, Z.; Savage, A.; El-Bahrawy, M. A.; Speller, A. V.; Rosini, F.; Kudo, H.; McKenzie, J. S.; Brown, R.; Takats, Z.; Ghaem-Maghani, S., The surgical intelligent knife distinguishes normal, borderline and malignant gynaecological tissues using rapid evaporative ionisation mass spectrometry (REIMS). *Br J Cancer* **2018**, *118* (10), 1349-1358.

39. Fatou, B.; Saudemont, P.; Leblanc, E.; Vinatier, D.; Mesdag, V.; Wisztorski, M.; Focsa, C.; Salzter, M.; Ziskind, M.; Fournier, I., In vivo Real-Time Mass Spectrometry for Guided Surgery Application. *Scientific Reports* **2016**, *6*.

40. Sans, M.; Zhang, J.; Lin, J. Q.; Giese, N.; Liu, J.; Sood, A. K.; Eberlin, L. S., Evaluating the Performance of the MasSpec Pen for Rapid Diagnosis of Ovarian Cancer. *Clinical Chemistry under review*.

41. Mason, S.; Manoli, E.; Poynter, L.; Alexander, J.; Paizs, P.; Adebessin, A.; Goldin, R.; Darzi, A.; Takats, Z.; Kinross, J., Mass spectrometry transanal minimally invasive surgery (MS-TAMIS) to promote organ preservation in rectal cancer. *Surg Endosc* **2020**, *34* (8), 3618-3625.

42. Yaziji, H.; Barry, T., Diagnostic Immunohistochemistry: what can go wrong? *Adv Anat Pathol* **2006**, *13* (5), 238-46.

43. Sarsby, J.; Griffiths, R. L.; Race, A. M.; Bunch, J.; Randall, E. C.; Creese, A. J.; Cooper, H. J., Liquid Extraction Surface Analysis Mass Spectrometry Coupled with Field Asymmetric Waveform Ion Mobility Spectrometry for Analysis of Intact Proteins from Biological Substrates. *Anal Chem* **2015**, *87* (13), 6794-800.

44. Feider, C. L.; Elizondo, N.; Eberlin, L. S., Ambient Ionization and FAIMS Mass Spectrometry for Enhanced Imaging of Multiply Charged Molecular Ions in Biological Tissues. *Anal Chem* **2016**, *88* (23), 11533-11541.

45. Griffiths, R. L.; Creese, A. J.; Race, A. M.; Bunch, J.; Cooper, H. J., LESA FAIMS Mass Spectrometry for the Spatial Profiling of Proteins from Tissue. *Anal Chem* **2016**, *88* (13), 6758-66.

46. Guevremont, R., High-field asymmetric waveform ion mobility spectrometry (FAIMS). *Can. J. Anal. Sci. Spectrosc.* **2004**, *49* (3), 105-113.

47. Cooper, H. J., To What Extent is FAIMS Beneficial in the Analysis of Proteins? *J Am Soc Mass Spectrom* **2016**, *27* (4), 566-77.

48. Houssami, N.; Marinovich, M. L., Margins in Breast-Conserving Surgery for Early Breast Cancer: How Much is Good Enough? *Curr Breast Cancer R* **2016**, *8* (2), 127-134.

49. Pilewskie, M.; Morrow, M., Margins in breast cancer: How much is enough? *Cancer* **2018**, *124* (7), 1335-1341.

50. Cabioglu, N.; Hunt, K. K.; Sahin, A. A.; Kuerer, H. M.; Babiera, G. V.; Singletary, S. E.; Whitman, G. J.; Ross, M. I.; Ames, F. C.; Feig, B. W.; Buchholz, T. A.; Meric-Bernstam, F., Role for intraoperative margin assessment in patients undergoing breast-conserving surgery. *Ann Surg Oncol* **2007**, *14* (4), 1458-71.
51. Bakhshandeh, M.; Tutuncuoglu, S. O.; Fischer, G.; Masood, S., Use of imprint cytology for assessment of surgical margins in lumpectomy specimens of breast cancer patients. *Diagn Cytopathol* **2007**, *35* (10), 656-9.
52. Weber, W. P.; Engelberger, S.; Viehl, C. T.; Zanetti-Dallenbach, R.; Kuster, S.; Dirnhofer, S.; Wruk, D.; Oertli, D.; Marti, W. R., Accuracy of frozen section analysis versus specimen radiography during breast-conserving surgery for nonpalpable lesions. *World J Surg* **2008**, *32* (12), 2599-606.
53. Dener, C.; Inan, A.; Sen, M.; Demirci, S., Intraoperative Frozen Section for Margin Assessment in Breast Conserving Surgery. *Scand J Surg* **2009**, *98* (1), 34-40.
54. Pleijhuis, R. G.; Graafland, M.; de Vries, J.; Bart, J.; de Jong, J. S.; van Dam, G. M., Obtaining adequate surgical margins in breast-conserving therapy for patients with early-stage breast cancer: current modalities and future directions. *Ann Surg Oncol* **2009**, *16* (10), 2717-30.
55. Fisher, S.; Yasui, Y.; Dabbs, K.; Winget, M., Re-excision and survival following breast conserving surgery in early stage breast cancer patients: a population-based study. *BMC Health Serv Res* **2018**, *18* (1), 94.

## CHAPTER 2

1. Koboldt, D. C.; Fulton, R. S.; McLellan, M. D.; Schmidt, H.; Kalicki-Veizer, J.; McMichael, J. F.; Fulton, L. L.; Dooling, D. J.; Ding, L.; Mardis, E. R.; Wilson, R. K.; Ally, A.; Balasundaram, M.; Butterfield, Y. S. N.; Carlsen, R.; Carter, C.; Chu, A.; Chuah, E.; Chun, H.-J. E.; Coope, R. J. N.; Dhalla, N.; Guin, R.; Hirst, C.; Hirst, M.; Holt, R. A.; Lee, D.; Li, H. I.; Mayo, M.; Moore, R. A.; Mungall, A. J.; Pleasance, E.; Robertson, A. G.; Schein, J. E.; Shafiei, A.; Sipahimalani, P.; Slobodan, J. R.; Stoll, D.; Tam, A.; Thiessen, N.; Varhol, R. J.; Wye, N.; Zeng, T.; Zhao, Y.; Birol, I.; Jones, S. J. M.; Marra, M. A.; Cherniack, A. D.; Saksena, G.; Onofrio, R. C.; Pho, N. H.; Carter, S. L.; Schumacher, S. E.; Tabak, B.; Hernandez, B.; Gentry, J.; Huy, N.; Crenshaw, A.; Ardlie, K.; Beroukhim, R.; Winckler, W.; Getz, G.; Gabriel, S. B.; Meyerson, M.; Chin, L.; Park, P. J.; Kucherlapati, R.; Hoadley, K. A.; Auman, J. T.; Fan, C.; Turman, Y. J.; Shi, Y.; Li, L.; Topal, M. D.; He, X.; Chao, H.-H.; Prat, A.; Silva, G. O.; Iglesia, M. D.; Zhao, W.; Usary, J.; Berg, J. S.; Adams, M.; Booker, J.; Wu, J.; Gulabani, A.; Bodenheimer, T.; Hoyle, A. P.; Simons, J. V.; Soloway, M. G.; Mose, L. E.; Jefferys, S. R.; Balu, S.; Parker, J. S.; Hayes, D. N.; Perou, C. M.; Malik, S.; Mahurkar, S.; Shen, H.; Weisenberger, D. J.; Triche, T., Jr.; Lai, P. H.; Bootwalla, M. S.; Maglinte, D. T.; Berman, B. P.; Van den Berg, D. J.; Baylin, S. B.; Laird, P. W.; Creighton, C. J.; Donehower, L. A.; Getz, G.; Noble, M.; Voet, D.; Saksena, G.; Gehlenborg, N.; DiCara, D.; Zhang, J.; Zhang, H.; Wu, C.-J.; Liu, S. Y.; Lawrence, M. S.; Zou, L.; Sivachenko, A.; Lin, P.; Stojanov, P.; Jing, R.; Cho, J.; Sinha, R.; Park, R. W.; Nazaire, M.-D.; Robinson, J.; Thorvaldsdottir, H.; Mesirov, J.; Park, P. J.; Chin, L.; Reynolds, S.; Kreisberg, R. B.; Bernard, B.; Bressler, R.; Erkkila, T.; Lin, J.; Thorsson, V.; Zhang, W.; Shmulevich, I.; Ciriello, G.; Weinhold, N.; Schultz, N.; Gao, J.; Cerami, E.; Gross, B.; Jacobsen, A.; Sinha, R.; Aksoy, B. A.; Antipin, Y.; Reva, B.; Shen, R.; Taylor, B. S.; Ladanyi, M.; Sander, C.; Anur, P.; Spellman, P. T.; Lu, Y.; Liu, W.; Verhaak, R. R. G.; Mills, G. B.; Akbani, R.; Zhang, N.; Broom, B. M.; Casant, T. D.; Wakefield, C.; Unruh, A. K.; Baggerly, K.; Coombes, K.; Weinstein, J. N.; Haussler, D.; Benz, C. C.; Stuart, J. M.; Benz, S. C.; Zhu, J.; Szeto, C. C.; Scott, G. K.; Yau, C.; Paul, E. O.; Carlin, D.; Wong, C.; Sokolov, A.; Thusberg, J.; Mooney, S.; Sam, N.; Goldstein, T. C.; Ellrott, K.; Grifford, M.; Wilks, C.; Ma, S.; Craft, B.; Yan, C.; Hu, Y.; Meerzaman, D.; Gastier-Foster, J. M.; Bowen, J.; Ramirez, N. C.; Black, A. D.; Pyatt, R. E.; White, P.; Zmuda, E. J.; Frick, J.; Lichtenberg, T.; Brookens, R.; George, M. M.; Gerken, M. A.; Harper, H. A.; Leraas, K. M.; Wise, L. J.; Tabler, T. R.; McAllister, C.; Barr, T.; Hart-Kothari, M.; Tarvin, K.; Saller, C.; Sandusky, G.; Mitchell, C.; Iacocca, M. V.; Brown, J.; Rabeno, B.; Czerwinski, C.; Petrelli, N.; Dolzhansky, O.; Abramov, M.; Voronina, O.; Potapova, O.; Marks, J. R.; Suchorska, W. M.; Murawa, D.; Kycler, W.; Ibbs, M.; Korski, K.; Spsychala, A.; Murawa, P.; Brzezinski, J. J.; Perz, H.; Lazniak, R.; Teresiak, M.; Tatka, H.; Leporowska, E.; Bogusz-Czerniewicz, M.; Malicki, J.; Mackiewicz, A.; Wiznerowicz, M.; Xuan Van, L.; Kohl, B.; Nguyen Viet, T.; Thorp, R.; Nguyen Van, B.; Sussman, H.; Bui Duc, P.; Hajek, R.; Nguyen Phi, H.; Tran Viet The, P.; Huynh Quyet, T.; Khan, K. Z.; Penny, R.; Mallery, D.; Curley, E.; Shelton, C.; Yena, P.; Ingle, J. N.; Couch, F. J.; Lingle, W. L.; King, T. A.; Gonzalez-Angulo, A. M.; Mills, G. B.; Dyer, M. D.; Liu, S.; Meng, X.; Patangan, M.; Waldman, F.; Stoeppler, H.; Rathmell, W. K.; Thorne, L.; Huang, M.; Boice, L.; Hill, A.; Morrison, C.; Gaudioso, C.; Bshara, W.; Daily, K.; Egea, S. C.; Pegram, M. D.; Gomez-Fernandez, C.; Dhir, R.; Bhargava, R.; Brufsky, A.; Shriver, C. D.; Hooke, J. A.; Campbell, J. L.; Mural, R. J.; Hu, H.; Somiari, S.; Larson, C.; Deyarmin, B.; Kvecher, L.; Kovatich, A. J.; Ellis, M. J.; King, T. A.; Hu, H.; Couch, F. J.; Mural, R. J.; Stricker, T.; White, K.; Olopade, O.; Ingle, J. N.; Luo, C.; Chen, Y.; Marks, J. R.; Waldman, F.; Wiznerowicz, M.; Bose, R.; Chang, L.-W.; Beck, A. H.; Gonzalez-Angulo, A. M.; Pihl, T.; Jensen, M.; Sfeir, R.; Kahn, A.; Chu, A.; Kothiyal, P.; Wang, Z.; Snyder, E.; Pontius, J.; Ayala, B.; Backus, M.; Walton, J.; Baboud, J.; Berton, D.; Nicholls, M.; Srinivasan,

D.; Raman, R.; Girshik, S.; Kigonya, P.; Alonso, S.; Sanbhadti, R.; Barletta, S.; Pot, D.; Sheth, M.; Demchok, J. A.; Shaw, K. R. M.; Yang, L.; Eley, G.; Ferguson, M. L.; Tarnuzzer, R. W.; Zhang, J.; Dillon, L. A. L.; Buetow, K.; Fielding, P.; Ozenberger, B. A.; Guyer, M. S.; Sofia, H. J.; Palchik, J. D.; Canc Genome Atlas, N., Comprehensive molecular portraits of human breast tumours. *Nature* **2012**, *490* (7418), 61-70.

2. Jemal, A.; Bray, F.; Center, M. M.; Ferlay, J.; Ward, E.; Forman, D., Global Cancer Statistics. *Ca-a Cancer Journal for Clinicians* **2011**, *61* (2), 69-90.

3. Esserman, L. J.; Berry, D. A.; DeMichele, A.; Carey, L.; Davis, S. E.; Buxton, M.; Hudis, C.; Gray, J. W.; Perou, C.; Yau, C.; Livasy, C.; Krontiras, H.; Montgomery, L.; Tripathy, D.; Lehman, C.; Liu, M. C.; Olopade, O. I.; Rugo, H. S.; Carpenter, J. T.; Dressler, L.; Chhieng, D.; Singh, B.; Mies, C.; Rabban, J.; Chen, Y. Y.; Giri, D.; van 't Veer, L.; Hylton, N., Pathologic complete response predicts recurrence-free survival more effectively by cancer subset: results from the I-SPY 1 TRIAL--CALGB 150007/150012, ACRIN 6657. *Journal of clinical oncology : official journal of the American Society of Clinical Oncology* **2012**, *30* (26), 3242-9.

4. Kos, Z.; Dabbs, D. J., Biomarker assessment and molecular testing for prognostication in breast cancer. *Histopathology* **2016**, *68* (1), 70-85.

5. Perou, C. M.; Sorlie, T.; Eisen, M. B.; van de Rijn, M.; Jeffrey, S. S.; Rees, C. A.; Pollack, J. R.; Ross, D. T.; Johnsen, H.; Akslén, L. A.; Fluge, O.; Pergamenschikov, A.; Williams, C.; Zhu, S. X.; Lonning, P. E.; Borresen-Dale, A. L.; Brown, P. O.; Botstein, D., Molecular portraits of human breast tumours. *Nature* **2000**, *406* (6797), 747-52.

6. Perou, C. M., Molecular stratification of triple-negative breast cancers. *The oncologist* **2010**, *15* Suppl 5, 39-48.

7. Sorlie, T.; Perou, C. M.; Tibshirani, R.; Aas, T.; Geisler, S.; Johnsen, H.; Hastie, T.; Eisen, M. B.; van de Rijn, M.; Jeffrey, S. S.; Thorsen, T.; Quist, H.; Matese, J. C.; Brown, P. O.; Botstein, D.; Lonning, P. E.; Borresen-Dale, A. L., Gene expression patterns of breast carcinomas distinguish tumor subclasses with clinical implications. *Proceedings of the National Academy of Sciences of the United States of America* **2001**, *98* (19), 10869-74.

8. Yaziji, H.; Barry, T., Diagnostic immunohistochemistry: What can go wrong? *Advances in Anatomic Pathology* **2006**, *13* (5), 238-246.

9. Hicks, D. G.; Tubbs, R. R., Assessment of the HER2 status in breast cancer by fluorescence in situ hybridization: a technical review with interpretive guidelines. *Hum Pathol* **2005**, *36* (3), 250-61.

10. Furrer, D.; Sanschagrin, F.; Jacob, S.; Diorio, C., Advantages and disadvantages of technologies for HER2 testing in breast cancer specimens. *Am J Clin Pathol* **2015**, *144* (5), 686-703.

11. Frampton, G. M.; Fichtenholtz, A.; Otto, G. A.; Wang, K.; Downing, S. R.; He, J.; Schnall-Levin, M.; White, J.; Sanford, E. M.; An, P.; Sun, J.; Juhn, F.; Brennan, K.; Iwanik, K.; Maillet, A.; Buell, J.; White, E.; Zhao, M.; Balasubramanian, S.; Terzic, S.; Richards, T.; Banning, V.;

Garcia, L.; Mahoney, K.; Zwirko, Z.; Donahue, A.; Beltran, H.; Mosquera, J. M.; Rubin, M. A.; Dogan, S.; Hedvat, C. V.; Berger, M. F.; Pusztai, L.; Lechner, M.; Boshoff, C.; Jarosz, M.; Vietz, C.; Parker, A.; Miller, V. A.; Ross, J. S.; Curran, J.; Cronin, M. T.; Stephens, P. J.; Lipson, D.; Yelensky, R., Development and validation of a clinical cancer genomic profiling test based on massively parallel DNA sequencing. *Nat. Biotechnol.* **2013**, *31* (11), 1023-+.

12. Alexandrov, L. B.; Nik-Zainal, S.; Wedge, D. C.; Aparicio, S.; Behjati, S.; Biankin, A. V.; Bignell, G. R.; Bolli, N.; Borg, A.; Borresen-Dale, A. L.; Boyault, S.; Burkhardt, B.; Butler, A. P.; Caldas, C.; Davies, H. R.; Desmedt, C.; Eils, R.; Eyfjord, J. E.; Foekens, J. A.; Greaves, M.; Hosoda, F.; Hutter, B.; Ilcic, T.; Imbeaud, S.; Imielinski, M.; Jager, N.; Jones, D. T. W.; Jones, D.; Knappskog, S.; Kool, M.; Lakhani, S. R.; Lopez-Otin, C.; Martin, S.; Munshi, N. C.; Nakamura, H.; Northcott, P. A.; Pajic, M.; Papaemmanuil, E.; Paradiso, A.; Pearson, J. V.; Puente, X. S.; Raine, K.; Ramakrishna, M.; Richardson, A. L.; Richter, J.; Rosenstiel, P.; Schlesner, M.; Schumacher, T. N.; Span, P. N.; Teague, J. W.; Totoki, Y.; Tutt, A. N. J.; Valdes-Mas, R.; van Buuren, M. M.; van 't Veer, L.; Vincent-Salomon, A.; Waddell, N.; Yates, L. R.; Zucman-Rossi, J.; Futreal, P. A.; McDermott, U.; Lichter, P.; Meyerson, M.; Grimmond, S. M.; Siebert, R.; Campo, E.; Shibata, T.; Pfister, S. M.; Campbell, P. J.; Stratton, M. R.; Australian Pancreatic Canc, G.; Consortium, I. B. C.; Consortium, I. M.-S.; PedBrain, I., Signatures of mutational processes in human cancer. *Nature* **2013**, *500* (7463), 415-+.

13. Budczies, J.; Brockmoller, S. F.; Muller, B. M.; Barupal, D. K.; Richter-Ehrenstein, C.; Kleine-Tebbe, A.; Griffin, J. L.; Oresic, M.; Dietel, M.; Denkert, C.; Fiehn, O., Comparative metabolomics of estrogen receptor positive and estrogen receptor negative breast cancer: alterations in glutamine and beta-alanine metabolism. *Journal of proteomics* **2013**, *94*, 279-288.

14. Heeren, R. M. A., Getting the picture: The coming of age of imaging MS. **2015**, *377*, 672–680.

15. Golf, O.; Strittmatter, N.; Karancsi, T.; Pringle, S. D.; Speller, A. V.; Mroz, A.; Kinross, J. M.; Abbassi-Ghadi, N.; Jones, E. A.; Takats, Z., Rapid evaporative ionization mass spectrometry imaging platform for direct mapping from bulk tissue and bacterial growth media. *Analytical chemistry* **2015**, *87* (5), 2527-34.

16. Laskin, J.; Heath, B. S.; Roach, P. J.; Cazares, L.; Semmes, O. J., Tissue Imaging Using Nanospray Desorption Electrospray Ionization Mass Spectrometry. *Analytical chemistry* **2011**, *84* (1), 141-148.

17. Walsh, C. M.; Reschke, B. R.; Fortney, J.; Piktel, D.; Razunguzwa, T. T.; Powell, M. J.; Gibson, L. F., A novel laser ablation electrospray ionization mass spectrometry (LAESI-MS) platform for biomarker discovery in cancer cells. *Cancer Research* **2012**, *72* (8), Abstract 4793.

18. Hsu, C.-C.; Dorrestein, P. C., Visualizing life with ambient mass spectrometry. *Current Opinion in Biotechnology* **2015**, *31*, 24-34.

19. Laskin, J.; Lanekoff, I., Ambient Mass Spectrometry Imaging Using Direct Liquid Extraction Techniques. *Analytical chemistry* **2015**, *88* (1), 52-73.

20. Kawashima, M.; Iwamoto, N.; Kawaguchi-Sakita, N.; Sugimoto, M.; Ueno, T.; Mikami, Y.; Terasawa, K.; Sato, T. A.; Tanaka, K.; Shimizu, K.; Toi, M., High-resolution imaging mass spectrometry reveals detailed spatial distribution of phosphatidylinositols in human breast cancer. *Cancer science* **2013**, *104* (10), 1372-9.
21. Tata, A.; Woolman, M.; Ventura, M.; Bernards, N.; Ganguly, M.; Gribble, A.; Shrestha, B.; Bluemke, E.; Ginsberg, H. J.; Vitkin, A.; Zheng, J.; Zarrine-Afsar, A., Rapid Detection of Necrosis in Breast Cancer with Desorption Electrospray Ionization Mass Spectrometry. *Scientific Reports* **2016**, *6*:35374.
22. Guo, S.; Wang, Y.; Zhou, D.; Li, Z., Significantly increased monounsaturated lipids relative to polyunsaturated lipids in six types of cancer microenvironment are observed by mass spectrometry imaging. *Scientific Reports*, *Published online: 5 August 2014*; | *doi:10.1038/srep05959* **2014**.
23. Bluestein, B. M.; Morrish, F.; Graham, D. J.; Guenthoer, J.; Hockenbery, D.; Porter, P. L.; Gamble, L. J., An unsupervised MVA method to compare specific regions in human breast tumor tissue samples using ToF-SIMS. *The Analyst* **2016**, *141* (6), 1947-57.
24. Rauser, S.; Marquardt, C.; Balluff, B.; Deininger, S. O.; Albers, C.; Belau, E.; Hartmer, R.; Suckau, D.; Specht, K.; Ebert, M. P.; Schmitt, M.; Aubele, M.; Hofler, H.; Walch, A., Classification of HER2 receptor status in breast cancer tissues by MALDI imaging mass spectrometry. *J Proteome Res* **2010**, *9* (4), 1854-63.
25. Mao, X.; He, J.; Li, T.; Lu, Z.; Sun, J.; Meng, Y.; Abliz, Z.; Chen, J., Application of imaging mass spectrometry for the molecular diagnosis of human breast tumors. *Sci Rep* **2016**, *6*, 21043.
26. Guenther, S.; Muirhead, L. J.; Speller, A. V. M.; Golf, O.; Strittmatter, N.; Ramakrishnan, R.; Goldin, R. D.; Jones, E.; Veselkov, K.; Nicholson, J.; Darzi, A.; Takats, Z., Spatially Resolved Metabolic Phenotyping of Breast Cancer by Desorption Electrospray Ionization Mass Spectrometry. *Cancer Research* **2015**, *75* (9), 1828-1837.
27. Alberici, R. M.; Simas, R. C.; Sanvido, G. B.; Romao, W.; Lalli, P. M.; Benassi, M.; Cunha, I. B. S.; Eberlin, M. N., Ambient mass spectrometry: bringing MS into the "real world". *Analytical and Bioanalytical Chemistry* **2010**, *398* (1), 265-294.
28. Ifa, D. R.; Eberlin, L. S., Ambient Ionization Mass Spectrometry for Cancer Diagnosis and Surgical Margin Evaluation. *Clinical Chemistry* **2016**, *62* (1), 111-123.
29. Dill, A. L.; Ifa, D. R.; Manicke, N. E.; Zheng, O.; Cooks, R. G., Mass spectrometric imaging of lipids using desorption electrospray ionization. *Journal of Chromatography B-Analytical Technologies in the Biomedical and Life Sciences* **2009**, *877* (26), 2883-2889.
30. Calligaris, D.; Caragacianu, D.; Liu, X.; Norton, I.; Thompson, C. J.; Richardson, A. L.; Golshan, M.; Easterling, M. L.; Santagata, S.; Dillon, D. A.; Jolesz, F. A.; Agar, N. Y. R., Application of desorption electrospray ionization mass spectrometry imaging in breast cancer margin analysis. *Proc. Natl. Acad. Sci. U. S. A.* **2014**, *111* (42), 15184-15189.

31. Zhang, J.; Feider, C. L.; Nagi, C.; Yu, W.; Carter, S. A.; Suliburk, J.; Cao, H. S.; Eberlin, L. S., Detection of Metastatic Breast and Thyroid Cancer in Lymph Nodes by Desorption Electrospray Ionization Mass Spectrometry Imaging. *Journal of the American Society for Mass Spectrometry* **2017**, *28* (6), 1166-1174.
32. Huo, D. Z.; Hu, H.; Rhie, S. K.; Gamazon, E. R.; Cherniack, A. D.; Liu, J. F.; Yoshimatsu, T. F.; Pitt, J. J.; Hoadley, K. A.; Troester, M.; Ru, Y. B.; Lichtenberg, T.; Sturtz, L. A.; Shelley, C. S.; Benz, C. C.; Mills, G. B.; Laird, P. W.; Shriver, C. D.; Perou, C. M.; Olopade, O. I., Comparison of Breast Cancer Molecular Features and Survival by African and European Ancestry in The Cancer Genome Atlas. *Jama Oncology* **2017**, *3* (12), 1654-1662.
33. Michels, K. B.; Mohllajee, A. R.; Roset-Bahmanyar, E.; Beehler, G. P.; Moysich, K. B., Diet and breast cancer - A review of the prospective observational studies. *Cancer* **2007**, *109* (12), 2712-2749.
34. Dill, A. L.; Eberlin, L. S.; Costa, A. B.; Ifa, D. R.; Cooks, R. G., Data quality in tissue analysis using desorption electrospray ionization. *Anal Bioanal Chem* **2011**, *401* (6), 1949-61.
35. Eberlin, L. S.; Ferreira, C. R.; Dill, A. L.; Ifa, D. R.; Cheng, L.; Cooks, R. G., Non-Destructive, Histologically Compatible Tissue Imaging by Desorption Electrospray Ionization Mass Spectrometry. *ChemBioChem* **2011**, *12* (14), 2129-2132.
36. Bokhart, M. T.; Nazari, M.; Garrard, K. P.; Muddiman, D. C., MSiReader v1.0: Evolving Open-Source Mass Spectrometry Imaging Software for Targeted and Untargeted Analyses. *Journal of the American Society for Mass Spectrometry* **2018**, *29* (1), 8-16.
37. O'Brien, K. M.; Cole, S. R.; Tse, C. K.; Perou, C. M.; Carey, L. A.; Foulkes, W. D.; Dressler, L. G.; Geradts, J.; Millikan, R. C., Intrinsic Breast Tumor Subtypes, Race, and Long-Term Survival in the Carolina Breast Cancer Study. *Clinical Cancer Research* **2010**, *16* (24), 6100-6110.
38. Eberlin, L. S.; Tibshirani, R. J.; Zhang, J.; Longacre, T. A.; Berry, G. J.; Bingham, D. B.; Norton, J. A.; Zare, R. N.; Poultides, G. A., Molecular assessment of surgical-resection margins of gastric cancer by mass-spectrometric imaging. *Proc Natl Acad Sci U S A* **2014**, *111* (7), 2436-41.
39. Sans, M.; Gharpure, K.; Tibshirani, R.; Zhang, J.; Liang, L.; Liu, J.; Young, J. H.; Dood, R. L.; Sood, A. K.; Eberlin, L. S., Metabolic Markers and Statistical Prediction of Serous Ovarian Cancer Aggressiveness by Ambient Ionization Mass Spectrometry Imaging. *Cancer Res* **2017**, *77* (11), 2903-2913.
40. Cairns, R. A.; Harris, I. S.; Mak, T. W., Regulation of cancer cell metabolism. *Nature Reviews Cancer* **2011**, *11* (2), 85-95.
41. Chughtai, K.; Jiang, L.; Greenwood, T. R.; Glunde, K.; Heeren, R. M., Mass spectrometry images acylcarnitines, phosphatidylcholines, and sphingomyelin in MDA-MB-231 breast tumor models. *Journal of lipid research* **2013**, *54* (2), 333-44.

42. Baumann, J.; Sevinsky, C.; Conklin, D. S., Lipid biology of breast cancer. *Biochim. Biophys. Acta Mol. Cell Biol. Lipids* **2013**, *1831* (10), 1509-1517.
43. Baenke, F.; Peck, B.; Miess, H.; Schulze, A., Hooked on fat: the role of lipid synthesis in cancer metabolism and tumour development. *Dis Model Mech* **2013**, *6* (6), 1353-63.
44. Calligaris, D.; Caragacianu, D.; Liu, X.; Norton, I.; Thompson, C. J.; Richardson, A. L.; Golshan, M.; Easterling, M. L.; Santagata, S.; Dillon, D. A.; Jolesz, F. A.; Agar, N. Y., Application of desorption electrospray ionization mass spectrometry imaging in breast cancer margin analysis. *Proc Natl Acad Sci U S A* **2014**, *111* (42), 15184-9.
45. Guenther, S.; Muirhead, L. J.; Speller, A. V.; Golf, O.; Strittmatter, N.; Ramakrishnan, R.; Goldin, R. D.; Jones, E.; Veselkov, K.; Nicholson, J.; Darzi, A.; Takats, Z., Spatially resolved metabolic phenotyping of breast cancer by desorption electrospray ionization mass spectrometry. *Cancer Res* **2015**, *75* (9), 1828-37.
46. Mertens, B. J. A., Proteomic diagnosis competition: Design, concepts, participants and first results. **2009**, *72* (5), 785-790.
47. Dekker, T. J.; Balluff, B. D.; Jones, E. A.; Schone, C. D.; Schmitt, M.; Aubele, M.; Kroep, J. R.; Smit, V. T.; Tollenaar, R. A.; Mesker, W. E.; Walch, A.; McDonnell, L. A., Multicenter matrix-assisted laser desorption/ionization mass spectrometry imaging (MALDI MSI) identifies proteomic differences in breast-cancer-associated stroma. *J Proteome Res* **2014**, *13* (11), 4730-8.
48. Dill, A. L.; Eberlin, L. S.; Costa, A. B.; Ifa, D. R.; Cooks, R. G., Data quality in tissue analysis using desorption electrospray ionization. *Analytical and Bioanalytical Chemistry* **2011**, *401* (6), 1949-1961.
49. Burstein, H. J., The distinctive nature of HER2-positive breast cancers. *New England Journal of Medicine* **2005**, *353* (16), 1652-1654.
50. Buckley, N. E.; Forde, C.; McArt, D. G.; Boyle, D. P.; Mullan, P. B.; James, J. A.; Maxwell, P.; McQuaid, S.; Salto-Tellez, M., Quantification of HER2 heterogeneity in breast cancer-implications for identification of sub-dominant clones for personalised treatment. *Scientific Reports* **2016**, *6*.
51. Wesola, M.; Jelen, M., A Comparison of IHC and FISH Cytogenetic Methods in the Evaluation of HER2 Status in Breast Cancer. *Advances in clinical and experimental medicine : official organ Wroclaw Medical University* **2015**, *24* (5), 899-903.

### CHAPTER 3

1. Schwamborn, K.; Caprioli, R. M., MALDI imaging mass spectrometry--painting molecular pictures. *Mol Oncol* **2010**, *4* (6), 529-38.
2. Wu, C.; Dill, A. L.; Eberlin, L. S.; Cooks, R. G.; Ifa, D. R., Mass spectrometry imaging under ambient conditions. *Mass Spectrom Rev* **2013**, *32* (3), 218-43.
3. Kriegsmann, M.; Casadonte, R.; Kriegsmann, J.; Dienemann, H.; Schirmacher, P.; Kobarg, J. H.; Schwamborn, K.; Stenzinger, A.; Warth, A.; Weichert, W., Reliable Entity Subtyping in Non-small Cell Lung Cancer by Matrix-assisted Laser Desorption/Ionization Imaging Mass Spectrometry on Formalin-fixed Paraffin-embedded Tissue Specimens. *Molecular & Cellular Proteomics* **2016**, *15* (10), 3081-3089.
4. Ifa, D. R.; Eberlin, L. S., Ambient Ionization Mass Spectrometry for Cancer Diagnosis and Surgical Margin Evaluation. *Clin Chem* **2016**, *62* (1), 111-23.
5. Calligaris, D.; Caragacianu, D.; Liu, X. H.; Norton, I.; Thompson, C. J.; Richardson, A. L.; Golshan, M.; Easterling, M. L.; Santagata, S.; Dillon, D. A.; Jolesz, F. A.; Agar, N. Y. R., Application of desorption electrospray ionization mass spectrometry imaging in breast cancer margin analysis. *Proc. Natl. Acad. Sci. U. S. A.* **2014**, *111* (42), 15184-15189.
6. Guenther, S.; Muirhead, L. J.; Speller, A. V.; Golf, O.; Strittmatter, N.; Ramakrishnan, R.; Goldin, R. D.; Jones, E.; Veselkov, K.; Nicholson, J.; Darzi, A.; Takats, Z., Spatially resolved metabolic phenotyping of breast cancer by desorption electrospray ionization mass spectrometry. *Cancer Res* **2015**, *75* (9), 1828-37.
7. Dill, A. L.; Ifa, D. R.; Manicke, N. E.; Ouyang, Z.; Cooks, R. G., Mass spectrometric imaging of lipids using desorption electrospray ionization. *J Chromatogr B Analyt Technol Biomed Life Sci* **2009**, *877* (26), 2883-9.
8. Sans, M.; Gharpure, K.; Tibshirani, R.; Zhang, J.; Liang, L.; Liu, J.; Young, J. H.; Dood, R. L.; Sood, A. K.; Eberlin, L. S., Metabolic Markers and Statistical Prediction of Serous Ovarian Cancer Aggressiveness by Ambient Ionization Mass Spectrometry Imaging. *Cancer Res* **2017**, *77* (11), 2903-2913.
9. Doria, M. L.; McKenzie, J. S.; Mroz, A.; Phelps, D. L.; Speller, A.; Rosini, F.; Strittmatter, N.; Golf, O.; Veselkov, K.; Brown, R.; Ghaem-Maghani, S.; Takats, Z., Epithelial ovarian carcinoma diagnosis by desorption electrospray ionization mass spectrometry imaging. *Scientific Reports* **2016**, *6*, 11.
10. Jarmusch, A. K.; Pirro, V.; Baird, Z.; Hattab, E. M.; Cohen-Gadol, A. A.; Cooks, R. G., Lipid and metabolite profiles of human brain tumors by desorption electrospray ionization-MS. *Proc. Natl. Acad. Sci. U. S. A.* **2016**, *113* (6), 1486-1491.
11. Eberlin, L. S.; Norton, I.; Orringer, D.; Dunn, I. F.; Liu, X. H.; Ide, J. L.; Jarmusch, A. K.; Ligon, K. L.; Jolesz, F. A.; Golby, A. J.; Santagata, S.; Agar, N. Y. R.; Cooks, R. G., Ambient mass

spectrometry for the intraoperative molecular diagnosis of human brain tumors. *Proc. Natl. Acad. Sci. U. S. A.* **2013**, *110* (5), 1611-1616.

12. Honarvar, E.; Venter, A. R., Ammonium Bicarbonate Addition Improves the Detection of Proteins by Desorption Electrospray Ionization Mass Spectrometry. *J Am Soc Mass Spectrom* **2017**, *28* (6), 1109-1117.

13. Shin, Y. S.; Drolet, B.; Mayer, R.; Dolence, K.; Basile, F., Desorption electrospray ionization-mass spectrometry of proteins. *Anal Chem* **2007**, *79* (9), 3514-8.

14. Ambrose, S.; Housden, N. G.; Gupta, K.; Fan, J.; White, P.; Yen, H. Y.; Marcoux, J.; Kleanthous, C.; Hopper, J. T. S.; Robinson, C. V., Native Desorption Electrospray Ionization Liberates Soluble and Membrane Protein Complexes from Surfaces. *Angew Chem Int Ed Engl* **2017**, *56* (46), 14463-14468.

15. Hsu, C. C.; Chou, P. T.; Zare, R. N., Imaging of Proteins in Tissue Samples Using Nanospray Desorption Electrospray Ionization Mass Spectrometry. *Anal. Chem.* **2015**, *87* (22), 11171-11175.

16. Griffiths, R. L.; Creese, A. J.; Race, A. M.; Bunch, J.; Cooper, H. J., LESA FAIMS Mass Spectrometry for the Spatial Profiling of Proteins from Tissue. *Anal. Chem.* **2016**, *88* (13), 6758-6766.

17. Feider, C. L.; Elizondo, N.; Eberlin, L. S., Ambient Ionization and FAIMS Mass Spectrometry for Enhanced Imaging of Multiply Charged Molecular Ions in Biological Tissues. *Anal. Chem.* **2016**, *88*, 11533-11541.

18. Klein, D. R.; Holden, D. D.; Brodbelt, J. S., Shotgun Analysis of Rough-Type Lipopolysaccharides Using Ultraviolet Photodissociation Mass Spectrometry. *Anal Chem* **2016**, *88* (1), 1044-51.

19. Li, Q.; Lex, R. K.; Chung, H.; Giovanetti, S. M.; Ji, Z.; Ji, H.; Person, M. D.; Kim, J.; Vokes, S. A., The Pluripotency Factor NANOG Binds to GLI Proteins and Represses Hedgehog-mediated Transcription. *The Journal of Biological Chemistry* **2016**, *291* (13), 7171-7182.

20. Seeley, E. H.; Oppenheimer, S. R.; Mi, D.; Chaurand, P.; Caprioli, R. M., Enhancement of protein sensitivity for MALDI imaging mass spectrometry after chemical treatment of tissue sections. *Journal of the American Society for Mass Spectrometry* **2008**, *19* (8), 1069-1077.

21. Eberlin, L. S.; Ferreira, C. R.; Dill, A. L.; Ifa, D. R.; Cooks, R. G., Desorption electrospray ionization mass spectrometry for lipid characterization and biological tissue imaging. *Biochim Biophys Acta* **2011**, *1811* (11), 946-60.

22. Takats, Z.; Wiseman, J. M.; Cooks, R. G., Ambient mass spectrometry using desorption electrospray ionization (DESI): instrumentation, mechanisms and applications in forensics, chemistry, and biology. *J Mass Spectrom* **2005**, *40* (10), 1261-75.

23. Guevremont, R., High-field asymmetric waveform ion mobility spectrometry (FAIMS). *Can. J. Anal. Sci. Spectrosc.* **2004**, *49* (3), 105-113.
24. Swearingen, K. E.; Moritz, R. L., High-field asymmetric waveform ion mobility spectrometry for mass spectrometry-based proteomics. *Expert Review of Proteomics* **2012**, *9* (5), 505-517.
25. Page, J. S.; Kelly, R. T.; Tang, K.; Smith, R. D., Ionization and transmission efficiency in an electrospray ionization-mass spectrometry interface. *J Am Soc Mass Spectrom* **2007**, *18* (9), 1582-90.
26. Klein, D. R.; Holden, D. D.; Brodbelt, J. S., Shotgun Analysis of Rough-Type Lipopolysaccharides Using Ultraviolet Photodissociation Mass Spectrometry. *Analytical Chemistry* **2016**, *88* (1), 1044-1051.
27. Hanrieder, J.; Oskar, K.; Brittebo, E. B.; Malmberg, P.; Ewing, A. G., Probing the lipid chemistry of neurotoxin-induced hippocampal lesions using multimodal imaging mass spectrometry. *Surf. Interface Anal.* **2014**, *46*, 375-378.
28. Chughtai, S.; Chughtai, K.; Cillero-Pastor, B.; Kiss, A.; Agrawal, P.; MacAleese, L.; Heeren, R. M. A., A multimodal mass spectrometry imaging approach for the study of musculoskeletal tissues. *Int. J. Mass Spectrom.* **2012**, *325*, 150-160.
29. Marshall, P.; Toteu-Djomte, V.; Bareille, P.; Perry, H.; Brown, G.; Baumert, M.; Biggadike, K., Correlation of Skin Blanching and Percutaneous Absorption for Glucocorticoid Receptor Agonists by Matrix-Assisted Laser Desorption Ionization Mass Spectrometry Imaging and Liquid Extraction Surface Analysis with Nanoelectrospray Ionization Mass Spectrometry. *Analytical Chemistry* **2010**, *82* (18), 7787-7794.
30. Eberlin, L. S.; Liu, X.; Ferreira, C. R.; Santagata, S.; Agar, N. Y.; Cooks, R. G., Desorption electrospray ionization then MALDI mass spectrometry imaging of lipid and protein distributions in single tissue sections. *Anal Chem* **2011**, *83* (22), 8366-71.
31. Eberlin, L. S.; Ferreira, C. R.; Dill, A. L.; Ifa, D. R.; Cheng, L.; Cooks, R. G., Nondestructive, histologically compatible tissue imaging by desorption electrospray ionization mass spectrometry. *Chembiochem* **2011**, *12* (14), 2129-32.
32. Bresnick, A. R.; Weber, D. J.; Zimmer, D. B., S100 proteins in cancer. *Nat Rev Cancer* **2015**, *15* (2), 96-109.
33. Delcourt, V.; Franck, J.; Leblanc, E.; Narducci, F.; Robin, Y. M.; Gimeno, J. P.; Quanico, J.; Wisztorski, M.; Kobeissy, F.; Jacques, J. F.; Roucou, X.; Salzet, M.; Fournier, I., Combined Mass Spectrometry Imaging and Top-down Microproteomics Reveals Evidence of a Hidden Proteome in Ovarian Cancer. *EBioMedicine* **2017**, *21*, 55-64.
34. Cross, S. S.; Hamdy, F. C.; Deloulme, J. C.; Rehman, I., Expression of S100 proteins in normal human tissues and common cancers using tissue microarrays: S100A6, S100A8, S100A9 and S100A11 are all overexpressed in common cancers. *Histopathology* **2005**, *46* (3), 256-69.

35. McKiernan, E.; McDermott, E. W.; Evoy, D.; Crown, J.; Duffy, M. J., The role of S100 genes in breast cancer progression. *Tumor Biol* **2011**, *32* (3), 441-450.
36. Sanders, M. E.; Dias, E. C.; Xu, B. J.; Mobley, J. A.; Billheimer, D.; Roder, H.; Grigorieva, J.; Dowsett, M.; Arteaga, C. L.; Caprioli, R. M., Differentiating proteomic biomarkers in breast cancer by laser capture microdissection and MALDI MS. *J Proteome Res* **2008**, *7* (4), 1500-7.
37. Grosset, A. A.; Labrie, M.; Vladoiu, M. C.; Yousef, E. M.; Gaboury, L.; St-Pierre, Y., Galectin signatures contribute to the heterogeneity of breast cancer and provide new prognostic information and therapeutic targets. *Oncotarget* **2016**, *7* (14), 18183-203.
38. Kompauer, M.; Heiles, S.; Spengler, B., Atmospheric pressure MALDI mass spectrometry imaging of tissues and cells at 1.4- $\mu\text{m}$  lateral resolution. *Nat Methods* **2017**, *14* (1), 90-96.
39. Palma, C. D.; Grassi, M. L.; Thome, C. H.; Ferreira, G. A.; Albuquerque, D.; Pinto, M. T.; Melo, F. U. F.; Kashima, S.; Covas, D. T.; Pitteri, S. J.; Faca, V. M., Proteomic Analysis of Epithelial to Mesenchymal Transition (EMT) Reveals Cross-talk between SNAIL and HDAC1 Proteins in Breast Cancer Cells. *Molecular & Cellular Proteomics* **2016**, *15* (3), 906-917.

## CHAPTER 4

1. Yokoyama, Y.; Nimura, Y.; Nagino, M., Advances in the treatment of pancreatic cancer: Limitations of surgery and evaluation of new therapeutic strategies. *Surg. Today* **2009**, *39* (6), 466-475.
2. Jaafar, H., Intra-Operative Frozen Section Consultation: Concepts, Applications and Limitations. *Malays. J. Med. Sci.* **2006**, *13* (1), 4-12.
3. Lee, K.; Yoon, K.; Lee, J.; Lee, H.; Kim, J.; Kim, S. I.; Cho, Y. U.; Park, B. W.; Park, H. S.; Alshahrani, M. A., The potential role of frozen sections of tumors in decision making of axillary procedure in breast conserving surgery for DCIS at preoperative diagnosis. *Breast* **2019**, *44*, S119-S119.
4. Orosco, R. K.; Tapia, V. J.; Califano, J. A.; Clary, B.; Cohen, E. E. W.; Kane, C.; Lippman, S. M.; Messer, K.; Molinolo, A.; Murphy, J. D.; Pang, J.; Sacco, A.; Tringale, K. R.; Wallace, A.; Nguyen, Q. T., Positive Surgical Margins in the 10 Most Common Solid Cancers. *Sci. Rep.* **2018**, *8*.
5. Gal, A. A.; Cagle, P. T., The 100-year anniversary of the description of the frozen section procedure. *J. Am. Med. Assoc.* **2005**, *294* (24), 3135-3137.
6. Hughes, D. T.; White, M. L.; Miller, B. S.; Gauger, P. G.; Burney, R. E.; Doherty, G. M., Influence of prophylactic central lymph node dissection on postoperative thyroglobulin levels and radioiodine treatment in papillary thyroid cancer. *Surgery* **2010**, *148* (6), 1100-6; discussion 1006-7.
7. Buchholz, T. A.; Somerfield, M. R.; Griggs, J. J.; El-Eid, S.; Hammond, M. E. H.; Lyman, G. H.; Mason, G.; Newman, L. A., Margins for Breast-Conserving Surgery With Whole-Breast Irradiation in Stage I and II Invasive Breast Cancer: American Society of Clinical Oncology Endorsement of the Society of Surgical Oncology/American Society for Radiation Oncology Consensus Guideline. *Journal of Clinical Oncology* **2014**, *32* (14), 1502-+.
8. Moran, M. S.; Schnitt, S. J.; Giuliano, A. E.; Harris, J. R.; Khan, S. A.; Horton, J.; Klimberg, S.; Chavez-MacGregor, M.; Freedman, G.; Houssami, N.; Johnson, P. L.; Morrow, M., Society of Surgical Oncology-American Society for Radiation Oncology Consensus Guideline on Margins for Breast-Conserving Surgery With Whole-Breast Irradiation in Stages I and II Invasive Breast Cancer. *Journal of Clinical Oncology* **2014**, *32* (14), 1507-+.
9. King, T. A.; Sakr, R.; Patil, S.; Gurevich, I.; Stempel, M.; Sampson, M.; Morrow, M., Clinical management factors contribute to the decision for contralateral prophylactic mastectomy. *J. Clin. Oncol.* **2011**, *29* (16), 2158-64.
10. Stummer, W.; Pichlmeier, U.; Meinel, T.; Wiestler, O. D.; Zanella, F.; Hans-Jürgen, R.; Grp, A.-G. S., Fluorescence-guided surgery with 5-aminolevulinic acid for resection of malignant glioma: a randomised controlled multicentre phase III trial. *Lancet Oncol.* **2006**, *7* (5), 392-401.

11. Jermyn, M.; Mok, K.; Mercier, J.; Desroches, J.; Pichette, J.; Saint-Arnaud, K.; Bernstein, L.; Guiot, M. C.; Petrecca, K.; Leblond, F., Intraoperative brain cancer detection with Raman spectroscopy in humans. *Sci. Transl. Med.* **2015**, *7* (274), 274ra19.
12. Kut, C.; Chaichana, K. L.; Xi, J. F.; Raza, S. M.; Ye, X. B.; McVeigh, E. R.; Rodriguez, F. J.; Quinones-Hinojosa, A.; Li, X. D., Detection of human brain cancer infiltration ex vivo and in vivo using quantitative optical coherence tomography. *Science Translational Medicine* **2015**, *7* (292).
13. Rajaram, N.; Aramil, T. J.; Lee, K.; Reichenberg, J. S.; Nguyen, T. H.; Tunnell, J. W., Design and validation of a clinical instrument for spectral diagnosis of cutaneous malignancy. *Applied Optics* **2010**, *49* (2), 142-152.
14. Orringer, D. A.; Pandian, B.; Niknafs, Y. S.; Hollon, T. C.; Boyle, J.; Lewis, S.; Garrard, M.; Hervey-Jumper, S. L.; Garton, H. J. L.; Maher, C. O.; Heth, J. A.; Sagher, O.; Wilkinson, D. A.; Snuderl, M.; Venneti, S.; Ramkissoon, S. H.; McFadden, K. A.; Fisher-Hubbard, A.; Lieberman, A. P.; Johnson, T. D.; Xie, X. S.; Trautman, J. K.; Freudiger, C. W.; Camelo-Piragua, S., Rapid intraoperative histology of unprocessed surgical specimens via fibre-laser-based stimulated Raman scattering microscopy. *Nat. Biomed. Eng.* **2017**, *1* (2), 0027.
15. Banerjee, S.; Zare, R. N.; Tibshirani, R. J.; Kunder, C. A.; Nolley, R.; Fan, R.; Brooks, J. D.; Sonn, G. A., Diagnosis of prostate cancer by desorption electrospray ionization mass spectrometric imaging of small metabolites and lipids. *Proc. Natl. Acad. Sci. U. S. A.* **2017**, *114* (13), 3334-3339.
16. Calligaris, D.; Caragacianu, D.; Liu, X. H.; Norton, I.; Thompson, C. J.; Richardson, A. L.; Golshan, M.; Easterling, M. L.; Santagata, S.; Dillon, D. A.; Jolesz, F. A.; Agar, N. Y. R., Application of desorption electrospray ionization mass spectrometry imaging in breast cancer margin analysis. *Proc. Natl. Acad. Sci. U. S. A.* **2014**, *111* (42), 15184-15189.
17. Calligaris, D.; Feldman, D. R.; Norton, I.; Olubiyi, O.; Changelian, A. N.; Machaidze, R.; Vestal, M. L.; Laws, E. R.; Dunn, I. F.; Santagata, S.; Agar, N. Y. R., MALDI mass spectrometry imaging analysis of pituitary adenomas for near-real-time tumor delineation. *Proc. Natl. Acad. Sci. U. S. A.* **2015**, *112* (32), 9978-9983.
18. Fatou, B.; Saudemont, P.; Leblanc, E.; Vinatier, D.; Mesdag, V.; Wisztorski, M.; Focsa, C.; Salzet, M.; Ziskind, M.; Fournier, I., In vivo Real-Time Mass Spectrometry for Guided Surgery Application. *Sci Rep* **2016**, *6*, 25919.
19. Woolman, M.; Kuzan-Fischer, C. M.; Ferry, I.; Kiyota, T.; Luu, B.; Wu, M. G.; Munoz, D. G.; Das, S.; Aman, A.; Taylor, M. D.; Rutka, J. T.; Ginsberg, H. J.; Zarrine-Afsar, A., Picosecond Infrared Laser Desorption Mass Spectrometry Identifies Medulloblastoma Subgroups on Intrasurgical Timescales. *Cancer Res.* **2019**, *79* (9), 2426-2434.
20. Ogrinc, N.; Saudemont, P.; Balog, J.; Robin, Y. M.; Gimeno, J. P.; Pascal, Q.; Tierny, D.; Takats, Z.; Salzet, M.; Fournier, I., Water-assisted laser desorption/ionization mass spectrometry for minimally invasive in vivo and real-time surface analysis using SpiderMass. *Nat. Protoc.* **2019**, *14* (11), 3162-3182.

21. Balog, J.; Kumar, S.; Alexander, J.; Golf, O.; Huang, J. Z.; Wiggins, T.; Abbassi-Ghadi, N.; Enyedi, A.; Kacska, S.; Kinross, J.; Hanna, G. B.; Nicholson, J. K.; Takats, Z., In Vivo Endoscopic Tissue Identification by Rapid Evaporative Ionization Mass Spectrometry (REIMS). *Angew. Chem. Int. Ed.* **2015**, *54* (38), 11059-11062.
22. Woolman, M.; Ferry, I.; Kuzan-Fischer, C. M.; Wu, M. G.; Zou, J.; Kiyota, T.; Isik, S.; Dara, D.; Aman, A.; Das, S.; Taylor, M. D.; Rutka, J. T.; Ginsberg, H. J.; Zarrine-Afsar, A., Rapid determination of medulloblastoma subgroup affiliation with mass spectrometry using a handheld picosecond infrared laser desorption probe. *Chem. Sci.* **2017**, *8* (9), 6508-6519.
23. Pirro, V.; Alfaro, C. M.; Jarmusch, A. K.; Hattab, E. M.; Cohen-Gadol, A. A.; Cooks, R. G., Intraoperative assessment of tumor margins during glioma resection by desorption electrospray ionization-mass spectrometry. *Proc. Natl. Acad. Sci. U. S. A.* **2017**, *114* (26), 6700-6705.
24. Eberlin, L. S.; Margulis, K.; Planell-Mendez, I.; Zare, R. N.; Tibshirani, R.; Longacre, T. A.; Jalali, M.; Norton, J. A.; Poultsides, G. A., Pancreatic Cancer Surgical Resection Margins: Molecular Assessment by Mass Spectrometry Imaging. *PLoS Med* **2016**, *13* (8), e1002108.
25. Sans, M.; Zhang, J.; Lin, J. Q.; Feider, C. L.; Giese, N.; Breen, M. T.; Sebastian, K.; Liu, J.; Sood, A. K.; Eberlin, L. S., Performance of the MasSpec Pen for Rapid Diagnosis of Ovarian Cancer. *Clin Chem* **2019**, *65* (5), 674-683.
26. Zhang, J. L.; Rector, J.; Lin, J. Q.; Young, J. H.; Sans, M.; Katta, N.; Giese, N.; Yu, W. D.; Nagi, C.; Suliburk, J.; Liu, J. S.; Bensussan, A.; DeHoog, R. J.; Garza, K. Y.; Ludolph, B.; Sorace, A. G.; Syed, A.; Zahedivash, A.; Milner, T. E.; Eberlin, L. S., Nondestructive tissue analysis for ex vivo and in vivo cancer diagnosis using a handheld mass spectrometry system. *Sci. Transl. Med.* **2017**, *9* (406), ean3968.
27. Balog, J.; Sasi-Szabo, L.; Kinross, J.; Lewis, M. R.; Muirhead, L. J.; Veselkov, K.; Mirnezami, R.; Dezso, B.; Damjanovich, L.; Darzi, A.; Nicholson, J. K.; Takats, Z., Intraoperative Tissue Identification Using Rapid Evaporative Ionization Mass Spectrometry. *Sci. Transl. Med.* **2013**, *5* (194), 194ra93.
28. Schafer, K. C.; Szaniszló, T.; Gunther, S.; Balog, J.; Denes, J.; Keseru, M.; Dezso, B.; Toth, M.; Spengler, B.; Takats, Z., In Situ, Real-Time Identification of Biological Tissues by Ultraviolet and Infrared Laser Desorption Ionization Mass Spectrometry. *Anal. Chem.* **2011**, *83* (5), 1632-1640.
29. Keating, M. F.; Zhang, J.; Feider, C. L.; Retailleau, S.; Reid, R.; Antaris, A.; Hart, B.; Tan, G.; Milner, T. E.; Miller, K.; Eberlin, L. S., Integrating the MasSpec Pen to the da Vinci Surgical System for In Vivo Tissue Analysis during a Robotic Assisted Porcine Surgery. *Anal Chem* **2020**.
30. Porcari, A. M.; Zhang, J. L.; Garza, K. Y.; Rodrigues-Peres, R. M.; Lin, J. Q.; Young, J. H.; Tibshirani, R.; Nagi, C.; Paiva, G. R.; Carter, S. A.; Sarian, L. O.; Eberlin, M. N.; Eberlin, L. S., Multicenter Study Using Desorption-Electrospray-Ionization-Mass-Spectrometry Imaging for Breast-Cancer Diagnosis. *Analytical Chemistry* **2018**, *90* (19), 11324-11332.

31. Feider, C. L.; Woody, S.; Ledet, S.; Zhang, J.; Sebastian, K.; Breen, M. T.; Eberlin, L. S., Molecular Imaging of Endometriosis Tissues using Desorption Electrospray Ionization Mass Spectrometry. *Sci. Rep.* **2019**, *9* (1), 15690.
32. Behne, M.; Wilke, H. J.; Harder, S., Clinical pharmacokinetics of sevoflurane. *Clin. Pharmacokinet.* **1999**, *36* (1), 13-26.
33. East, J. M.; Valentine, C. S. P.; Kanchev, E.; Blake, G. O., Sentinel lymph node biopsy for breast cancer using methylene blue dye manifests a short learning curve among experienced surgeons: a prospective tabular cumulative sum (CUSUM) analysis. *BMC Surg.* **2009**, *9*, 2.
34. Ali, I.; Wani, W. A.; Haque, A.; Saleem, K., Glutamic acid and its derivatives: candidates for rational design of anticancer drugs. *Future Med. Chem.* **2013**, *5* (8), 961-78.
35. Shenoy, N.; Creagan, E.; Witzig, T.; Levine, M., Ascorbic Acid in Cancer Treatment: Let the Phoenix Fly. *Cancer Cell* **2018**, *34* (5), 700-706.
36. Harris, I. S.; Treloar, A. E.; Inoue, S.; Sasaki, M.; Gorrini, C.; Lee, K. C.; Yung, K. Y.; Brenner, D.; Knobbe-Thomsen, C. B.; Cox, M. A.; Elia, A.; Berger, T.; Cescon, D. W.; Adeoye, A.; Brustle, A.; Molyneux, S. D.; Mason, J. M.; Li, W. Y.; Yamamoto, K.; Wakeham, A.; Berman, H. K.; Khokha, R.; Done, S. J.; Kavanagh, T. J.; Lam, C. W.; Mak, T. W., Glutathione and thioredoxin antioxidant pathways synergize to drive cancer initiation and progression. *Cancer Cell* **2015**, *27* (2), 211-22.
37. Zhang, D. Y.; Singhal, S.; Lee, J. Y. K., Optical Principles of Fluorescence-Guided Brain Tumor Surgery: A Practical Primer for the Neurosurgeon. *Neurosurgery* **2019**, *85* (3), 312-324.
38. Richter, J. C. O.; Haj-Hosseini, N.; Hallbeck, M.; Wardell, K., Combination of hand-held probe and microscopy for fluorescence guided surgery in the brain tumor marginal zone. *Photodiagnosis Photodyn. Ther.* **2017**, *18*, 185-192.
39. Alexander, J.; Gildea, L.; Balog, J.; Speller, A.; McKenzie, J.; Muirhead, L.; Scott, A.; Kontovounisios, C.; Rasheed, S.; Teare, J.; Hoare, J.; Veselkov, K.; Goldin, R.; Tekkis, P.; Darzi, A.; Nicholson, J.; Kinross, J.; Takats, Z., A novel methodology for in vivo endoscopic phenotyping of colorectal cancer based on real-time analysis of the mucosal lipidome: a prospective observational study of the iKnife. *Surg. Endosc.* **2017**, *31* (3), 1361-1370.

## CHAPTER 5

1. Houssami, N.; Macaskill, P.; Marinovich, M. L.; Dixon, J. M.; Irwig, L.; Brennan, M. E.; Solin, L. J., Meta-analysis of the impact of surgical margins on local recurrence in women with early-stage invasive breast cancer treated with breast-conserving therapy. *Eur J Cancer* **2010**, *46* (18), 3219-32.
2. Moran, M. S.; Schnitt, S. J.; Giuliano, A. E.; Harris, J. R.; Khan, S. A.; Horton, J.; Klimberg, S.; Chavez-MacGregor, M.; Freedman, G.; Houssami, N.; Johnson, P. L.; Morrow, M., Society of Surgical Oncology-American Society for Radiation Oncology consensus guideline on margins for breast-conserving surgery with whole-breast irradiation in stages I and II invasive breast cancer. *Ann Surg Oncol* **2014**, *21* (3), 704-16.
3. Menes, T. S.; Tartter, P. I.; Bleiweiss, I.; Godbold, J. H.; Estabrook, A.; Smith, S. R., The consequence of multiple re-excisions to obtain clear lumpectomy margins in breast cancer patients. *Ann Surg Oncol* **2005**, *12* (11), 881-5.
4. Buchholz, T. A.; Somerfield, M. R.; Griggs, J. J.; El-Eid, S.; Hammond, M. E. H.; Lyman, G. H.; Mason, G.; Newman, L. A., Margins for Breast-Conserving Surgery With Whole-Breast Irradiation in Stage I and II Invasive Breast Cancer: American Society of Clinical Oncology Endorsement of the Society of Surgical Oncology/American Society for Radiation Oncology Consensus Guideline. *Journal of Clinical Oncology* **2014**, *32* (14), 1502-+.
5. McCahill, L. E.; Single, R. M.; Aiello Bowles, E. J.; Feigelson, H. S.; James, T. A.; Barney, T.; Engel, J. M.; Onitilo, A. A., Variability in reexcision following breast conservation surgery. *JAMA* **2012**, *307* (5), 467-75.
6. Olsen, M. A.; Nickel, K. B.; Margenthaler, J. A.; Wallace, A. E.; Mines, D.; Miller, J. P.; Fraser, V. J.; Warren, D. K., Increased Risk of Surgical Site Infection Among Breast-Conserving Surgery Re-excisions. *Ann Surg Oncol* **2015**, *22* (6), 2003-9.
7. Waljee, J. F.; Hu, E. S.; Newman, L. A.; Alderman, A. K., Predictors of re-excision among women undergoing breast-conserving surgery for cancer. *Ann Surg Oncol* **2008**, *15* (5), 1297-303.
8. Jung, W.; Kang, E.; Kim, S. M.; Kim, D.; Hwang, Y.; Sun, Y.; Yom, C. K.; Kim, S. W., Factors Associated with Re-excision after Breast-Conserving Surgery for Early-Stage Breast Cancer. *J Breast Cancer* **2012**, *15* (4), 412-9.
9. Pleijhuis, R. G.; Graafland, M.; de Vries, J.; Bart, J.; de Jong, J. S.; van Dam, G. M., Obtaining adequate surgical margins in breast-conserving therapy for patients with early-stage breast cancer: current modalities and future directions. *Ann Surg Oncol* **2009**, *16* (10), 2717-30.
10. Jorns, J. M.; Visscher, D.; Sabel, M.; Breslin, T.; Healy, P.; Daignaut, S.; Myers, J. L.; Wu, A. J., Intraoperative frozen section analysis of margins in breast conserving surgery significantly decreases reoperative rates: one-year experience at an ambulatory surgical center. *Am J Clin Pathol* **2012**, *138* (5), 657-69.

11. Esbona, K.; Li, Z.; Wilke, L. G., Intraoperative imprint cytology and frozen section pathology for margin assessment in breast conservation surgery: a systematic review. *Ann Surg Oncol* **2012**, *19* (10), 3236-45.
12. Allweis, T. M.; Kaufman, Z.; Lelcuk, S.; Pappo, I.; Karni, T.; Schneebaum, S.; Spector, R.; Schindel, A.; Hershko, D.; Zilberman, M.; Sayfan, J.; Berlin, Y.; Hadary, A.; Olsha, O.; Paran, H.; Gutman, M.; Carmon, M., A prospective, randomized, controlled, multicenter study of a real-time, intraoperative probe for positive margin detection in breast-conserving surgery. *Am J Surg* **2008**, *196* (4), 483-9.
13. Geha, R. C.; Taback, B.; Cadena, L.; Borden, B.; Feldman, S., A Single institution's randomized double-armed prospective study of lumpectomy margins with adjunctive use of the MarginProbe in nonpalpable breast cancers. *Breast J* **2020**, *26* (11), 2157-2162.
14. Moore, M. M.; Whitney, L. A.; Cerilli, L.; Imbrie, J. Z.; Bunch, M.; Simpson, V. B.; Hanks, J. B., Intraoperative ultrasound is associated with clear lumpectomy margins for palpable infiltrating ductal breast cancer. *Annals of Surgery* **2001**, *233* (6), 761-768.
15. Nguyen, F. T.; Zysk, A. M.; Chaney, E. J.; Kotynek, J. G.; Oliphant, U. J.; Bellafiore, F. J.; Rowland, K. M.; Johnson, P. A.; Boppart, S. A., Intraoperative evaluation of breast tumor margins with optical coherence tomography. *Cancer Res* **2009**, *69* (22), 8790-6.
16. Maloney, B. W.; McClatchy, D. M.; Pogue, B. W.; Paulsen, K. D.; Wells, W. A.; Barth, R. J., Review of methods for intraoperative margin detection for breast conserving surgery. *J Biomed Opt* **2018**, *23* (10), 1-19.
17. Gray, R. J.; Pockaj, B. A.; Garvey, E.; Blair, S., Intraoperative Margin Management in Breast-Conserving Surgery: A Systematic Review of the Literature. *Ann Surg Oncol* **2018**, *25* (1), 18-27.
18. Reyna, C.; DeSnyder, S. M., Intraoperative Margin Assessment in Breast Cancer Management. *Surg Oncol Clin N Am* **2018**, *27* (1), 155-165.
19. Nowikiewicz, T.; Srutek, E.; Glowacka-Mrotek, I.; Tarkowska, M.; Zyromska, A.; Zegarski, W., Clinical outcomes of an intraoperative surgical margin assessment using the fresh frozen section method in patients with invasive breast cancer undergoing breast-conserving surgery - a single center analysis. *Sci Rep* **2019**, *9* (1), 13441.
20. Ifa, D. R.; Eberlin, L. S., Ambient Ionization Mass Spectrometry for Cancer Diagnosis and Surgical Margin Evaluation. *Clin Chem* **2016**, *62* (1), 111-23.
21. Porcari, A. M.; Zhang, J. L.; Garza, K. Y.; Rodrigues-Peres, R. M.; Lin, J. Q.; Young, J. H.; Tibshirani, R.; Nagi, C.; Paiva, G. R.; Carter, S. A.; Sarian, L. O.; Eberlin, M. N.; Eberlin, L. S., Multicenter Study Using Desorption-Electrospray-Ionization-Mass-Spectrometry Imaging for Breast-Cancer Diagnosis. *Analytical Chemistry* **2018**, *90* (19), 11324-11332.
22. Calligaris, D.; Caragacianu, D.; Liu, X.; Norton, I.; Thompson, C. J.; Richardson, A. L.; Golshan, M.; Easterling, M. L.; Santagata, S.; Dillon, D. A.; Jolesz, F. A.; Agar, N. Y., Application

of desorption electrospray ionization mass spectrometry imaging in breast cancer margin analysis. *Proc Natl Acad Sci U S A* **2014**, *111* (42), 15184-9.

23. Guenther, S.; Muirhead, L. J.; Speller, A. V.; Golf, O.; Strittmatter, N.; Ramakrishnan, R.; Goldin, R. D.; Jones, E.; Veselkov, K.; Nicholson, J.; Darzi, A.; Takats, Z., Spatially resolved metabolic phenotyping of breast cancer by desorption electrospray ionization mass spectrometry. *Cancer Res* **2015**, *75* (9), 1828-37.

24. St John, E. R.; Balog, J.; McKenzie, J. S.; Rossi, M.; Covington, A.; Muirhead, L.; Bodai, Z.; Rosini, F.; Speller, A. V. M.; Shousha, S.; Ramakrishnan, R.; Darzi, A.; Takats, Z.; Leff, D. R., Rapid evaporative ionisation mass spectrometry of electrosurgical vapours for the identification of breast pathology: towards an intelligent knife for breast cancer surgery. *Breast Cancer Res* **2017**, *19* (1), 59.

25. Zhang, J.; Rector, J.; Lin, J. Q.; Young, J. H.; Sans, M.; Katta, N.; Giese, N.; Yu, W.; Nagi, C.; Suliburk, J.; Liu, J.; Bensussan, A.; DeHoog, R. J.; Garza, K. Y.; Ludolph, B.; Sorace, A. G.; Syed, A.; Zahedivash, A.; Milner, T. E.; Eberlin, L. S., Nondestructive tissue analysis for ex vivo and in vivo cancer diagnosis using a handheld mass spectrometry system. *Sci Transl Med* **2017**, *9* (406).

26. Balog, J.; Sasi-Szabo, L.; Kinross, J.; Lewis, M. R.; Muirhead, L. J.; Veselkov, K.; Mirnezami, R.; Dezso, B.; Damjanovich, L.; Darzi, A.; Nicholson, J. K.; Takats, Z., Intraoperative tissue identification using rapid evaporative ionization mass spectrometry. *Sci Transl Med* **2013**, *5* (194), 194ra93.

27. Schaefer, K.-C.; Denes, J.; Albrecht, K.; Szaniszló, T.; Balog, J.; Skoumal, R.; Katona, M.; Toth, M.; Balogh, L.; Takats, Z., In Vivo, In Situ Tissue Analysis Using Rapid Evaporative Ionization Mass Spectrometry. *Angewandte Chemie-International Edition* **2009**, *48* (44), 8240-8242.

28. Woolman, M.; Ferry, I.; Kuzan-Fischer, C. M.; Wu, M.; Zou, J.; Kiyota, T.; Isik, S.; Dara, D.; Aman, A.; Das, S.; Taylor, M. D.; Rutka, J. T.; Ginsberg, H. J.; Zarrine-Afsar, A., Rapid determination of medulloblastoma subgroup affiliation with mass spectrometry using a handheld picosecond infrared laser desorption probe. *Chem. Sci.* **2017**, *8* (9), 6508-6519.

29. Fatou, B.; Saudemont, P.; Leblanc, E.; Vinatier, D.; Mesdag, V.; Wisztorski, M.; Focsa, C.; Salzet, M.; Ziskind, M.; Fournier, I., In vivo Real-Time Mass Spectrometry for Guided Surgery Application. *Sci Rep* **2016**, *6*, 25919.

30. Sans, M.; Zhang, J.; Lin, J. Q.; Feider, C. L.; Giese, N.; Breen, M. T.; Sebastian, K.; Liu, J.; Sood, A. K.; Eberlin, L. S., Performance of the MasSpec Pen for Rapid Diagnosis of Ovarian Cancer. *Clin Chem* **2019**, *65* (5), 674-683.

31. Keating, M. F.; Zhang, J.; Feider, C. L.; Retailleau, S.; Reid, R.; Antaris, A.; Hart, B.; Tan, G.; Milner, T. E.; Miller, K.; Eberlin, L. S., Integrating the MasSpec Pen to the da Vinci Surgical System for In Vivo Tissue Analysis during a Robotic Assisted Porcine Surgery. *Anal Chem* **2020**, *92* (17), 11535-11542.

32. Zhang, J., Sans, M., DeHoog, R. J., Garza, K. Y., King, M. E., Fieder, C. L., Bensussan, A., Keating, M. F., Lin, J. Q., Povilaitis, S. C., Katta, N., Milner, T. E., Wendong, Y., Nagi, C., Dhingra, S., Pirko, C., Brahmabhatt, K. A., Van Buren, G., Carter, S. A., Thompson, A., Grogan, R. H., Suliburk, J., Eberlin, L. S., Clinical Translation and Evaluation of the MasSpec Pen Technology for Surgical Use. *Clinical Chemistry* **2021**.
33. Dill, A. L.; Ifa, D. R.; Manicke, N. E.; Ouyang, Z.; Cooks, R. G., Mass spectrometric imaging of lipids using desorption electrospray ionization. *J Chromatogr B Analyt Technol Biomed Life Sci* **2009**, *877* (26), 2883-9.
34. Liberti, M. V.; Locasale, J. W., The Warburg Effect: How Does it Benefit Cancer Cells? *Trends Biochem Sci* **2016**, *41* (3), 211-218.
35. Hilvo, M.; Denkert, C.; Lehtinen, L.; Muller, B.; Brockmoller, S.; Seppanen-Laakso, T.; Budczies, J.; Bucher, E.; Yetukuri, L.; Castillo, S.; Berg, E.; Nygren, H.; Sysi-Aho, M.; Griffin, J. L.; Fiehn, O.; Loibl, S.; Richter-Ehrenstein, C.; Radke, C.; Hyotylainen, T.; Kallioniemi, O.; Iljin, K.; Oresic, M., Novel theranostic opportunities offered by characterization of altered membrane lipid metabolism in breast cancer progression. *Cancer Res* **2011**, *71* (9), 3236-45.
36. Punnonen, K.; Hietanen, E.; Auvinen, O.; Punnonen, R., Phospholipids and fatty acids in breast cancer tissue. *J Cancer Res Clin Oncol* **1989**, *115* (6), 575-8.
37. Wu, S. G.; Zhang, W. W.; Sun, J. Y.; He, Z. Y., Prognostic value of ductal carcinoma in situ component in invasive ductal carcinoma of the breast: a Surveillance, Epidemiology, and End Results database analysis. *Cancer Manag Res* **2018**, *10*, 527-534.
38. Azu, M.; Abrahamse, P.; Katz, S. J.; Jagsi, R.; Morrow, M., What is an adequate margin for breast-conserving surgery? Surgeon attitudes and correlates. *Ann Surg Oncol* **2010**, *17* (2), 558-63.
39. Pilewskie, M.; Morrow, M., Margins in breast cancer: How much is enough? *Cancer* **2018**, *124* (7), 1335-1341.

## CHAPTER 6

1. Huang, C.; Wang, Y.; Li, X.; Ren, L.; Zhao, J.; Hu, Y.; Zhang, L.; Fan, G.; Xu, J.; Gu, X.; Cheng, Z.; Yu, T.; Xia, J.; Wei, Y.; Wu, W.; Xie, X.; Yin, W.; Li, H.; Liu, M.; Xiao, Y.; Gao, H.; Guo, L.; Xie, J.; Wang, G.; Jiang, R.; Gao, Z.; Jin, Q.; Wang, J.; Cao, B., Clinical features of patients infected with 2019 novel coronavirus in Wuhan, China. *Lancet* **2020**, 395 (10223), 497-506.
2. Wu, F.; Zhao, S.; Yu, B.; Chen, Y. M.; Wang, W.; Song, Z. G.; Hu, Y.; Tao, Z. W.; Tian, J. H.; Pei, Y. Y.; Yuan, M. L.; Zhang, Y. L.; Dai, F. H.; Liu, Y.; Wang, Q. M.; Zheng, J. J.; Xu, L.; Holmes, E. C.; Zhang, Y. Z., A new coronavirus associated with human respiratory disease in China. *Nature* **2020**, 579 (7798), 265-+.
3. Mina, M. J.; Parker, R.; Larremore, D. B., Rethinking Covid-19 Test Sensitivity - A Strategy for Containment. *N Engl J Med* **2020**, 383 (22), e120.
4. Vandenberg, O.; Martiny, D.; Rochas, O.; van Belkum, A.; Kozlakidis, Z., Considerations for diagnostic COVID-19 tests. *Nat Rev Microbiol* **2020**.
5. Masterson, T. A.; Dill, A. L.; Eberlin, L. S.; Mattarozzi, M.; Cheng, L.; Beck, S. D.; Bianchi, F.; Cooks, R. G., Distinctive glycerophospholipid profiles of human seminoma and adjacent normal tissues by desorption electrospray ionization imaging mass spectrometry. *J Am Soc Mass Spectrom* **2011**, 22 (8), 1326-33.
6. Tromberg, B. J.; Schwetz, T. A.; Perez-Stable, E. J.; Hodes, R. J.; Woychik, R. P.; Bright, R. A.; Fleurence, R. L.; Collins, F. S., Rapid Scaling Up of Covid-19 Diagnostic Testing in the United States - The NIH RADx Initiative. *N Engl J Med* **2020**, 383 (11), 1071-1077.
7. Lisboa Bastos, M.; Tavaziva, G.; Abidi, S. K.; Campbell, J. R.; Haraoui, L. P.; Johnston, J. C.; Lan, Z.; Law, S.; MacLean, E.; Trajman, A.; Menzies, D.; Benedetti, A.; Ahmad Khan, F., Diagnostic accuracy of serological tests for covid-19: systematic review and meta-analysis. *BMJ* **2020**, 370, m2516.
8. Miller, T. E.; Garcia Beltran, W. F.; Bard, A. Z.; Gogakos, T.; Anahtar, M. N.; Astudillo, M. G.; Yang, D.; Thierauf, J.; Fisch, A. S.; Mahowald, G. K.; Fitzpatrick, M. J.; Nardi, V.; Feldman, J.; Hauser, B. M.; Caradonna, T. M.; Marble, H. D.; Ritterhouse, L. L.; Turbett, S. E.; Batten, J.; Georgantas, N. Z.; Alter, G.; Schmidt, A. G.; Harris, J. B.; Gelfand, J. A.; Poznansky, M. C.; Bernstein, B. E.; Louis, D. N.; Dighe, A.; Charles, R. C.; Ryan, E. T.; Branda, J. A.; Pierce, V. M.; Murali, M. R.; Iafate, A. J.; Rosenberg, E. S.; Lennerz, J. K., Clinical sensitivity and interpretation of PCR and serological COVID-19 diagnostics for patients presenting to the hospital. *FASEB J* **2020**, 34 (10), 13877-13884.
9. Abbasi, J., The Promise and Peril of Antibody Testing for COVID-19. *JAMA* **2020**.
10. Mak, G. C. K.; Lau, S. S. Y.; Wong, K. K. Y.; Chow, N. L. S.; Lau, C. S.; Lam, E. T. K.; Chan, R. C. W.; Tsang, D. N. C., Evaluation of rapid antigen detection kit from the WHO Emergency Use List for detecting SARS-CoV-2. *J Clin Virol* **2021**, 134, 104712.

11. Prince-Guerra, J. L.; Almendares, O.; Nolen, L. D.; Gunn, J. K. L.; Dale, A. P.; Buono, S. A.; Deutsch-Feldman, M.; Suppiah, S.; Hao, L.; Zeng, Y.; Stevens, V. A.; Knipe, K.; Pompey, J.; Atherstone, C.; Bui, D. P.; Powell, T.; Tamin, A.; Harcourt, J. L.; Shewmaker, P. L.; Medrzycki, M.; Wong, P.; Jain, S.; Tejada-Strop, A.; Rogers, S.; Emery, B.; Wang, H.; Petway, M.; Bohannon, C.; Folster, J. M.; MacNeil, A.; Salerno, R.; Kuhnert-Tallman, W.; Tate, J. E.; Thornburg, N. J.; Kirking, H. L.; Sheiban, K.; Kudrna, J.; Cullen, T.; Komatsu, K. K.; Villanueva, J. M.; Rose, D. A.; Neatherlin, J. C.; Anderson, M.; Rota, P. A.; Honein, M. A.; Bower, W. A., Evaluation of Abbott BinaxNOW Rapid Antigen Test for SARS-CoV-2 Infection at Two Community-Based Testing Sites - Pima County, Arizona, November 3-17, 2020. *MMWR Morb Mortal Wkly Rep* **2021**, *70* (3), 100-105.
12. West, C. P.; Montori, V. M.; Sampathkumar, P., COVID-19 Testing: The Threat of False-Negative Results. *Mayo Clin Proc* **2020**, *95* (6), 1127-1129.
13. Abu-Farha, M.; Thanaraj, T. A.; Qaddoumi, M. G.; Hashem, A.; Abubaker, J.; Al-Mulla, F., The Role of Lipid Metabolism in COVID-19 Virus Infection and as a Drug Target. *Int J Mol Sci* **2020**, *21* (10).
14. Caterino, M.; Gelzo, M.; Sol, S.; Fedele, R.; Annunziata, A.; Calabrese, C.; Fiorentino, G.; D'Abbraccio, M.; Dell'Isola, C.; Fusco, F. M.; Parrella, R.; Fabbrocini, G.; Gentile, I.; Andolfo, I.; Capasso, M.; Costanzo, M.; Daniele, A.; Marchese, E.; Polito, R.; Russo, R.; Missero, C.; Ruoppolo, M.; Castaldo, G., Dysregulation of lipid metabolism and pathological inflammation in patients with COVID-19. *Sci Rep* **2021**, *11* (1), 2941.
15. Ivanova, P. T.; Myers, D. S.; Milne, S. B.; McClaren, J. L.; Thomas, P. G.; Brown, H. A., Lipid Composition of the Viral Envelope of Three Strains of Influenza Virus—Not All Viruses Are Created Equal. *ACS Infectious Diseases* **2015**, *1* (9), 435-442.
16. Nayak, D. P.; Hui, E. K. W., The Role of Lipid Microdomains in Virus Biology. In *Membrane Dynamics and Domains: Subcellular Biochemistry*, Quinn, P. J., Ed. Springer US: Boston, MA, 2004; pp 443-491.
17. Quigley, J. P.; Rifkin, D. B.; Reich, E., Phospholipid composition of Rous sarcoma virus, host cell membranes and other enveloped RNA viruses. *Virology* **1971**, *46* (1), 106-116.
18. Kates, M.; Allison, A. C.; Tyrrell, D. A. J.; James, A. T., Lipids of influenza virus and their relation to those of the host cell. *Biochimica et Biophysica Acta* **1961**, *52* (3), 455-466.
19. Callens, N.; Brügger, B.; Bonnafous, P.; Drobecq, H.; Gerl, M. J.; Krey, T.; Roman-Sosa, G.; Rügenapf, T.; Lambert, O.; Dubuisson, J.; Rouillé, Y., Morphology and Molecular Composition of Purified Bovine Viral Diarrhea Virus Envelope. *PLoS Pathog* **2016**, *12* (3), e1005476-e1005476.
20. Dou, D.; Revol, R.; Ostbye, H.; Wang, H.; Daniels, R., Influenza A Virus Cell Entry, Replication, Virion Assembly and Movement. *Front Immunol* **2018**, *9*, 1581.

21. Van Genderen, I. L.; Godeke, G. J.; Rottier, P. J. M.; Van Meer, G., The phospholipid composition of enveloped viruses depends on the intracellular membrane through which they bud. *Biochemical Society Transactions* **1995**, *23* (3), 523-526.
22. Yan, B. P.; Chu, H.; Yang, D.; Sze, K. H.; Lai, P. M.; Yuan, S. F.; Shuai, H. P.; Wang, Y. X.; Kao, R. Y. T.; Chan, J. F. W.; Yuen, K. Y., Characterization of the Lipidomic Profile of Human Coronavirus-Infected Cells: Implications for Lipid Metabolism Remodeling upon Coronavirus Replication. *Viruses-Basel* **2019**, *11* (1).
23. Zhang, J.; Sans, M.; Garza, K. Y.; Eberlin, L. S., Mass Spectrometry Technologies to Advance Care for Cancer Patients in Clinical and Intraoperative Use. *Mass Spectrom Rev* **2020**.
24. Pu, F.; Chiang, S.; Zhang, W.; Ouyang, Z., Direct sampling mass spectrometry for clinical analysis. *Analyst* **2019**, *144* (4), 1034-1051.
25. Ho, Y. P.; Reddy, P. M., Identification of pathogens by mass spectrometry. *Clin Chem* **2010**, *56* (4), 525-36.
26. Ganova-Raeva, L. M.; Khudyakov, Y. E., Application of mass spectrometry to molecular diagnostics of viral infections. *Expert Rev Mol Diagn* **2013**, *13* (4), 377-88.
27. Mahmud, I.; Garrett, T. J., Mass Spectrometry Techniques in Emerging Pathogens Studies: COVID-19 Perspectives. *J Am Soc Mass Spectrom* **2020**, *31* (10), 2013-2024.
28. Nachtigall, F. M.; Pereira, A.; Trofymchuk, O. S.; Santos, L. S., Detection of SARS-CoV-2 in nasal swabs using MALDI-MS. *Nat Biotechnol* **2020**, *38* (10), 1168-1173.
29. Rocca, M. F.; Zintgraff, J. C.; Dattero, M. E.; Santos, L. S.; Ledesma, M.; Vay, C.; Prieto, M.; Benedetti, E.; Avaro, M.; Russo, M.; Nachtigall, F. M.; Baumeister, E., A combined approach of MALDI-TOF mass spectrometry and multivariate analysis as a potential tool for the detection of SARS-CoV-2 virus in nasopharyngeal swabs. *J Virol Methods* **2020**, *286*, 113991.
30. De Silva, I. W.; Nayek, S.; Singh, V.; Reddy, J.; Granger, J. K.; Verbeck, G. F., Paper spray mass spectrometry utilizing Teslin(R) substrate for rapid detection of lipid metabolite changes during COVID-19 infection. *Analyst* **2020**, *145* (17), 5725-5732.
31. Shen, B.; Yi, X.; Sun, Y.; Bi, X.; Du, J.; Zhang, C.; Quan, S.; Zhang, F.; Sun, R.; Qian, L.; Ge, W.; Liu, W.; Liang, S.; Chen, H.; Zhang, Y.; Li, J.; Xu, J.; He, Z.; Chen, B.; Wang, J.; Yan, H.; Zheng, Y.; Wang, D.; Zhu, J.; Kong, Z.; Kang, Z.; Liang, X.; Ding, X.; Ruan, G.; Xiang, N.; Cai, X.; Gao, H.; Li, L.; Li, S.; Xiao, Q.; Lu, T.; Zhu, Y.; Liu, H.; Chen, H.; Guo, T., Proteomic and Metabolomic Characterization of COVID-19 Patient Sera. *Cell* **2020**, *182* (1), 59-72 e15.
32. Ford, L.; Simon, D.; Balog, J.; Jiwa, N.; Higginson, J.; Jones, E.; Mason, S.; Wu, V.; Manoli, E.; Stavrakaki, S. M.; McKenzie, J.; McGill, D.; Koguna, H.; Kinross, J.; Takats, Z., Rapid detection of SARS-CoV2 by Ambient Mass Spectrometry Techniques. *medRxiv* **2020**, 2020.10.07.20207647.

33. Delafiori, J.; Navarro, L. C.; Siciliano, R. F.; de Melo, G. C.; Busanello, E. N. B.; Nicolau, J. C.; Sales, G. M.; de Oliveira, A. N.; Val, F. F. A.; de Oliveira, D. N.; Eguti, A.; Dos Santos, L. A.; Dalcoquio, T. F.; Bertolin, A. J.; Abreu-Netto, R. L.; Salsoso, R.; Baia-da-Silva, D.; Marcondes-Braga, F. G.; Sampaio, V. S.; Judice, C. C.; Costa, F. T. M.; Duran, N.; Perroud, M. W.; Sabino, E. C.; Lacerda, M. V. G.; Reis, L. O.; Favaro, W. J.; Monteiro, W. M.; Rocha, A. R.; Catharino, R. R., Covid-19 Automated Diagnosis and Risk Assessment through Metabolomics and Machine Learning. *Anal Chem* **2021**, *93* (4), 2471-2479.
34. Wu, D.; Shu, T.; Yang, X.; Song, J.-X.; Zhang, M.; Yao, C.; Liu, W.; Huang, M.; Yu, Y.; Yang, Q.; Zhu, T.; Xu, J.; Mu, J.; Wang, Y.; Wang, H.; Tang, T.; Ren, Y.; Wu, Y.; Lin, S.-H.; Qiu, Y.; Zhang, D.-Y.; Shang, Y.; Zhou, X., Plasma metabolomic and lipidomic alterations associated with COVID-19. *National Science Review* **2020**, *7* (7), 1157-1168.
35. Lazari, L. C.; De Rose Ghilardi, F.; Rosa-Fernandes, L.; Assis, D. M.; Nicolau, J. C.; Santiago, V. F.; Dalcoquio, T. F.; Angeli, C. B.; Bertolin, A. J.; Marinho, C. R. F.; Wrenger, C.; Durigon, E. L.; Siciliano, R. F.; Palmisano, G., Prognostic accuracy of MALDI mass spectrometric analysis of plasma in COVID-19. *medRxiv* **2020**, 2020.10.01.20205310.
36. Sans, M.; Zhang, J.; Lin, J. Q.; Feider, C. L.; Giese, N.; Breen, M. T.; Sebastian, K.; Liu, J.; Sood, A. K.; Eberlin, L. S., Performance of the MasSpec Pen for Rapid Diagnosis of Ovarian Cancer. *Clin Chem* **2019**, *65* (5), 674-683.
37. Zhang, J.; Rector, J.; Lin, J. Q.; Young, J. H.; Sans, M.; Katta, N.; Giese, N.; Yu, W.; Nagi, C.; Suliburk, J.; Liu, J.; Bensussan, A.; DeHoog, R. J.; Garza, K. Y.; Ludolph, B.; Sorace, A. G.; Syed, A.; Zahedivash, A.; Milner, T. E.; Eberlin, L. S., Nondestructive tissue analysis for ex vivo and in vivo cancer diagnosis using a handheld mass spectrometry system. *Sci Transl Med* **2017**, *9* (406).
38. Pagnotti, V. S.; Chubatyi, N. D.; McEwen, C. N., Solvent assisted inlet ionization: an ultrasensitive new liquid introduction ionization method for mass spectrometry. *Anal Chem* **2011**, *83* (11), 3981-5.
39. Kwee, T. C.; Kwee, R. M., Chest CT in COVID-19: What the Radiologist Needs to Know. *Radiographics* **2020**, *40* (7), 1848-1865.
40. Yang, W.; Sirajuddin, A.; Zhang, X.; Liu, G.; Teng, Z.; Zhao, S.; Lu, M., The role of imaging in 2019 novel coronavirus pneumonia (COVID-19). *Eur Radiol* **2020**, *30* (9), 4874-4882.
41. Ufuk, F.; Savas, R., Chest CT features of the novel coronavirus disease (COVID-19). *Turk J Med Sci* **2020**, *50* (4), 664-678.
42. Xie, X.; Zhong, Z.; Zhao, W.; Zheng, C.; Wang, F.; Liu, J., Chest CT for Typical Coronavirus Disease 2019 (COVID-19) Pneumonia: Relationship to Negative RT-PCR Testing. *Radiology* **2020**, *296* (2), E41-E45.
43. Feng, H.; Liu, Y.; Lv, M.; Zhong, J., A case report of COVID-19 with false negative RT-PCR test: necessity of chest CT. *Jpn J Radiol* **2020**, *38* (5), 409-410.

44. Hossein, H.; Ali, K. M.; Hosseini, M.; Sarveazad, A.; Safari, S.; Yousefifard, M., Value of chest computed tomography scan in diagnosis of COVID-19; a systematic review and meta-analysis. *Clin Transl Imaging* **2020**, 1-13.
45. Clerici, B.; Muscatello, A.; Bai, F.; Pavanello, D.; Orlandi, M.; Marchetti, G. C.; Castelli, V.; Casazza, G.; Costantino, G.; Podda, G. M., Sensitivity of SARS-CoV-2 Detection With Nasopharyngeal Swabs. *Front Public Health* **2020**, *8*, 593491.
46. Kucirka, L. M.; Lauer, S. A.; Laeyendecker, O.; Boon, D.; Lessler, J., Variation in False-Negative Rate of Reverse Transcriptase Polymerase Chain Reaction-Based SARS-CoV-2 Tests by Time Since Exposure. *Ann Intern Med* **2020**, *173* (4), 262-267.
47. He, J. L.; Luo, L.; Luo, Z. D.; Lyu, J. X.; Ng, M. Y.; Shen, X. P.; Wen, Z., Diagnostic performance between CT and initial real-time RT-PCR for clinically suspected 2019 coronavirus disease (COVID-19) patients outside Wuhan, China. *Respir Med* **2020**, *168*, 105980.

## CHAPTER 7

1. Tillner, J.; Wu, V.; Jones, E. A.; Pringle, S. D.; Karancsi, T.; Dannhorn, A.; Veselkov, K.; McKenzie, J. S.; Takats, Z., Faster, More Reproducible DESI-MS for Biological Tissue Imaging. *J. Am. Soc. Mass Spectrom.* **2017**, *28* (10), 2090-2098.
2. Griffiths, R. L.; Hughes, J. W.; Abbatiello, S. E.; Belford, M. W.; Styles, I. B.; Cooper, H. J., Comprehensive LESA Mass Spectrometry Imaging of Intact Proteins by Integration of Cylindrical FAIMS. *Anal Chem* **2020**, *92* (4), 2885-2890.
3. Feider, C. L.; Gatmaitan, A. N.; Hooper, T.; Chakraborty, A.; Gowda, P.; Buchanan, E.; Eberlin, L. S., Integrating the MasSpec Pen with Sub-Atmospheric Pressure Chemical Ionization for Rapid Chemical Analysis and Forensic Applications. *Anal Chem* **2021**.

## **Vita**

Kyana Garza was born and raised in Sugar Land, TX. She received her B.S. in Chemistry from the University of St. Thomas in Houston, making her a first-generation college graduate. In 2016, she began her graduate studies in Analytical Chemistry at the University of Texas at Austin under the supervision of Prof. Livia S. Eberlin.

Permanent email address: [kygarza@comcast.net](mailto:kygarza@comcast.net)

This dissertation was typed by Kyana Y. Garza.